Removal of bias in global seismic magnitude determinations

Mehdi Rezapour

A thesis submitted in fulfilment of the requirements
for the degree of Doctor of Philosophy
to the
University of Edinburgh
1999

Abstract

Bias in global seismic magnitude determinations caused by inadequacies in distance/depth calibration functions is reduced, by developing new formulae for surface-wave magnitude M_s, and new distance/depth calibration terms for body-wave magnitude m_b. Bias in M_s and m_b is investigated using the complete ISC and NEIC datasets between 1978 and 1993. Analysis of the ISC dataset shows that the density function for magnitude against frequency for M_s values is smooth but significantly asymmetric. While that for m_b appears to be symmetric and close to normally distributed, this is shown not to be the case. Examination of M_s : m_b for this dataset reveals some anomalous earthquakes which plot as explosions according to the M_s : m_b discriminant. Also, the frequency-distance plot for reported surface wave amplitude observations exhibits detailed structure of the body-wave amplitude-distance curve at all distances. This censoring via the body waves represents a large deficit in the number of potentially usable surface-wave amplitude observations, particularly in the P-wave shadow zone for $120° < \Delta < 100°$.

To reduce bias in surface-wave magnitude two new formulae are proposed, with constants obtained using all ISC data:

$$M_s^e = \log(A/T)_{max} + 1.155\log(\Delta) + 4.269$$
$$M_s^t = \log(A/T)_{max} + \tfrac{1}{3}\log(\Delta) + \tfrac{1}{2}\log(\sin\Delta) + 0.0046\Delta + 5.370.$$

For M_s^e the conventional logarithmic dependence of the distance correction is retained, while for M_s^t the theoretically-known relationship for the dispersion and geometrical spreading contributions is exploited. Comparison of these formulae with other work confirms the inadequacy of the distance-dependence term in the Gutenberg (1945) and Prague formulae. The M_s^e formula, as well as that of Herak and Herak (1993), gives less bias at all epicentral distances to within the scatter of the observed dataset. M_s^t provides an improved overall distance correction, especially beyond Δ=145° and provides the basis for regionalising M_s distance correction in the futuer. It is shown that evidence of Airy-phase distance decay predominates at shorter distances ($\Delta \leq 30°$). Assuming 20-second surface waves with $U = 3.6$ km/s, a globally-averaged apparent Q^{-1} of 0.00192±0.00026 ($Q \approx 500$) is obtained for Rayleigh waves.

Comparison of the M_s versus $\log M_0$ relation when using M_s^t and M_s^{Prague} shows that there

is significantly less scatter in $\log M_0$ for a given M_s when M_s^t is used, and that the slope of M_s against $\log M_0$ does not tend to 1.0 towards smaller magnitudes. This suggests that previous claims of M_s data supporting a theoretical slope of 1.0 towards small magnitudes may not be justified. Conclusions of Ekström and Dziewonski (1988) and Abercrombie (1994) about anomalies in estimated M_s values in regions such as the New-Hebrides and Tonga-Kermadec are reexamined; it is shown that when using M_s^t values, most of the anomaly is removed, and it is concluded that the remainder is more likely to be path effect. To reduce the depth bias in M_s, a depth correction term of $\delta M_s = 0.0025h$ is obtained for earthquakes with depth range of 10–60 km. An empirical non-linear relationship between surface-wave magnitude and seismic moment is obtained using magnitude data determined by applying M_s^t for M_s determination, together with CMT M_0 values. This relation is compared with other global linear and non-linear relations.

New empirical global depth-distance correction terms $B(\Delta, h)$ for body-wave magnitude are determined using the values of scalar moment M_0 in the Harvard CMT Catalogue. Application to the ISC dataset shows that estimated m_b is then independent of distance and focal depth, and provides unbiased estimates of m_b, by comparison with other published depth-distance functions. Comparison of event magnitudes m_b calculated using the commonly-used Gutenberg-Richter (1956) calibration terms with those of this study, shows that the new correction terms increase small magnitudes and decrease large magnitudes. Comparison of the standard deviation of m_b values for single events using different depth-distance correction terms shows that the Gutenberg-Richter standard deviations are consistently larger than those of Veith-Clawson (1972), Lilwall (1987), and this study.

Also, for further improvement in M_s determination by taking account of the path effects, the collapsing of surface-wave seismograms to a standard distance using standard oceanic and continental dispersion functions is examined. This shows that the collapse of surface-wave seismograms to a standard distance is only possible with a velocity model specific to each path.

The studies reported here are important in the removal of magnitude bias. Bias in magnitude estimates is caused by incorrect allowance for any effects other than earthquake strength, directly affecting the results of any study in which magnitude data are used. Hence these studies have important implications in seismicity studies, explosion yield estimation, seismic source identification and the estimation of seismic moments of historical earthquakes (using an empirical relation between magnitude and seismic moment) for which only magnitudes are available.

Acknowledgements

I would like to thank my supervisors, Robert Pearce, Ian Main, and David Bowers, for their advice and encouragement throughout my project. Thanks especially to Robert Pearce for his tolerance in dealing with my questions/requests and many fruitful discussions at any time even at weekends.

I am grateful to Professor Alan Douglas at Blacknest for his help and encouragement on many occasions. Thanks to all the staff at Blacknest and ISC for providing ISC Catalogue data used in this thesis. Thanks to the Institute of Geophysics of Tehran University and the IRIS Data Management Centre for ILPA and other waveform data, although eventually ILPA data were not used in this project.

Many thanks for computing support from Shane Voss, Ian Chisholm, Justin MacNeil and all at Edinburgh University Computer Support. Thanks to all postgraduates for their support. Also, I express my appreciation to all those in the Department of Geology and Geophysics who directly or indirectly helped me throughout my time in Edinburgh.

Special thanks have to go to my family, Zahra, Maryam, and Mona which without their support I would not be able to complete this thesis. Lastly, but no means least, thanks to my father, relations, and friends for their love and support.

This project was funded by a scholarship from the Ministry of Culture and Higher Education of Iran, Award Number 42/65515–1373/05/04. Supplementary support was provided through AWE Blacknest.

Contents

Inclusions (inside back cover)

Rezapour, M. and R. G. Pearce (1998). Bias in surface wave magnitude M_s due to inadequate distance corrections, *Bull. Seism. Soc. Am.* **88**, 43–61.

Rezapour, M. and R. G. Pearce (1998). Relation between seismic moment M_0 and surface wave magnitude M_s. *Bull. Seism. Soc. Am.* in revision.

List of Figures

List of Tables

List of Abbreviations

CLVD	Compensated Linear Vector Dipole
CMT	Centroid Moment Tensor
CNTBT	Comprehensive Nuclear Test Ban Treaty
ERI	Earthquake Research Institute
IASPEI	International Association of Seismology and Physics of the Earth's Interior
ILPA	Iranian Long Period Array
IRIS	Incorporated Research Institutions for Seismology
ISC	International Seismological Centre
LP	Long Period
LRSM	Long Range Seismic Measurement
LVZ	Low Velocity Zone
NEIC	National Earthquake Information Center
PDE	Preliminary Determination of Epicentres
PREM	Preliminary Reference Earth Model
RRMSE	Root Residual Mean Square Error
RSSE	Residual Sum Square Error
SCR	Stable Continental Regions
SP	Short Period
SRO	Seismic Research Observatory
STS	Semipalatinsk Test Site
USGS	United States Geological Survey
WWSSN	World Wide Standard Seismograph Network

Chapter 1

Introduction

The original project proposal was on surface wave studies of paths across Iran to constrain seismic velocities using the Iranian Long Period Array (ILPA). ILPA is a seven element three component array of 60 km aperture which was installed in 1976. After a lengthy study of Iranian seismology and investigations of various data sources for ILPA, it became clear that the archived ILPA data were not sufficient to achieve the proposal goals. Only three of seven array elements are available for most time periods. The project was then revised to focus on global seismic magnitude determinations using Catalogue data from the International Seismological Centre (ISC) and waveform data from the Incorporated Research Institutions for Seismology (IRIS) Data Management Centre.

Prior to instrumental recording, "intensity" was used for describing and comparisons of earthquakes size. Earthquake intensity scales, especially the Rossi-Forel and various versions of the Mercalli scale, were used almost universally to measure earthquake size for about 50 years. The earthquake intensity is a subjective parameter that is based on an assessment of visible effects (damage) and it depends on factors other than actual size of the earthquake. A number of different intensity scales have been set up during the current century. Intensity scale is important in specifying building codes, and for estimating the magnitude of historical earthquakes.

Richter (1935) set up a "magnitude scale" of earthquake which based on measurement on instrumental recording. Magnitude M is a measure of earthquake size determined from the amplitude and period of a certain type of seismic wave using an empirical formula which contains several constants whose values are chosen to maximise internal consistency between different observations. During the past 60 years several variations of magnitude scale were developed. The advantage of magnitude scale is simple function of amplitude of displacement on seismogram. There is a limitation in the use of any magnitude scale for the quantification of earthquakes because magnitude is not completely related to source physics. Nevertheless, magnitude scales are so widely used that it is difficult to imagine that they would be easily

abandoned. Moreover, archived magnitude data provide the only quantitative determinations of size for most historical earthquakes.

A more physically meaningful measurement of earthquake size "seismic moment" was introduced into seismology in the middle of this century. Seismic moment rests on the equivalence between elastic dislocation and the double-couple force system (Burridge and Knopoff, 1964; Haskell, 1964). In an earthquake fault, dislocation is equivalent to a distribution of double couples on the fault surface whose total moment is $M_0 = \mu A\bar{u}$, where μ is the rigidity of the medium, A is the fault surface area, and $\bar{u}$ is the average dislocation. (In this thesis M_0 is expressed in c.g.s units i.e., dyne-cm following normal seismological practice.) Seismologists nowadays consider the seismic moment to be a more reliable measure of earthquake size, and because of progress in seismological theory and digital instrumentation, moment estimates are made routinely. However, values are available only since 1977, and only for a limited number of larger earthquakes.

Most studies in earthquake seismology use magnitude data as a guide to the strength of an earthquake. So biases in magnitude estimates, caused by incorrect allowance for any effects other than earthquake strength, directly affect the result of any study in which magnitude data are used. Such uses cover a wide range of seismology. Reduction of bias when comparing recent data (for which seismic moments can be determined) with historical data (for which only magnitudes can be determined) will improve estimates of the size of historical earthquakes, improve discrimination between earthquakes and nuclear explosions, and will give us a better measure of the overall rate of seismic energy release.

There are two primary motivations behind the work presented in this thesis. First, the $M_s : m_b$ criterion is a widely-used seismic discriminant between earthquakes and nuclear explosions, and it has potential to identify underground nuclear explosions prohibited by the Comprehensive Nuclear Test Ban Treaty (CNTBT). Secondly, the quantification of earthquake size requires a parameter which has a physical basis (e.g., seismic moment); such parameters for historical earthquakes must usually be derived from archived magnitude data. As the body of global magnitude data increases with the passage of time, there is more scope for understanding, and hence allowing for, magnitude bias and scatter e.g., due to inadequate calibration function, systematic errors in the instrument response calibration, radiation pattern effects, non-uniform station coverage, etc.

The main aim of this thesis is to re-investigate the bias in determination of body-wave and surface-wave magnitudes, using a large ISC dataset. Figure 1.1 shows the epicentres of 110,225 earthquakes located by ISC between 1978 and 1993 which are used in this study. The magnitude scales, the main sources of magnitude bias, and dataset used are described in Chapter 2. A comparison of magnitudes reported by the ISC and NEIC (National Earthquake Information Centre) global agencies is included.

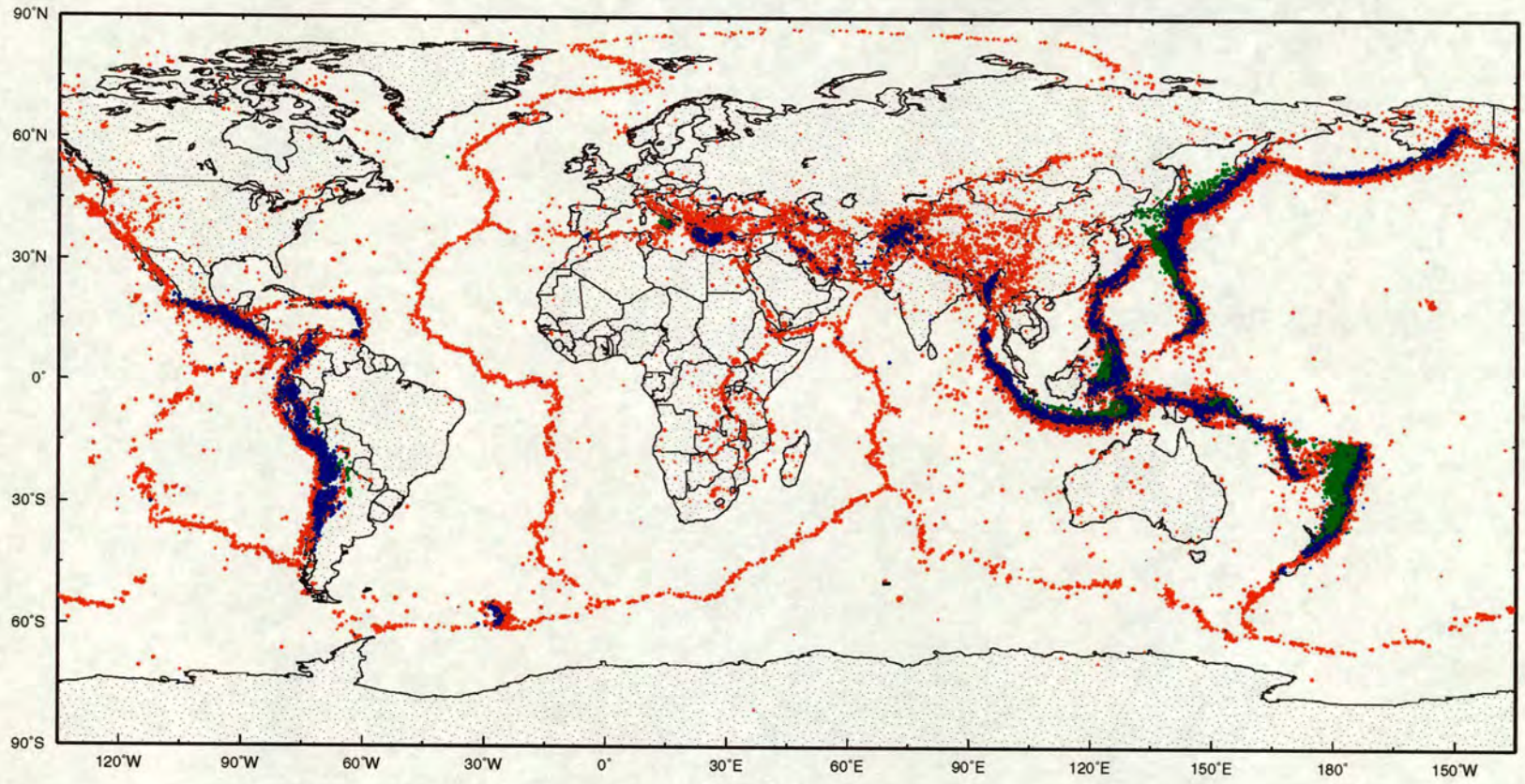

Figure 1.1. 110,225 earthquakes that have been located by the ISC between 1978 and 1993. Red, blue, and green circles represent shallow ($h < 70$ km), intermediate ($70 \leq h \leq 300$ km), and deep ($h > 300$ km) earthquakes respectively. The size of each circle is proportional to value of body-wave magnitude; the largest symbol corresponds to a body-wave magnitude of 6.8.

The M_s : m_b criterion has turned out to be the most robust criterion for distinguishing between earthquakes and explosions. This discriminant is based on the observation that for a given m_b, explosions have a much smaller M_s than earthquakes. One disadvantage of the M_s : m_b criterion is the problem of the anomalous earthquakes which plot in or near the explosion population. This includes a discussion about the density function for magnitude against frequency for both M_s and m_b values, and similarity of magnitude-frequency distribution to a normal distribution. The M_s : m_b criterion for ISC data and some anomalous earthquakes are discussed.

It is generally assumed that the quality and the quantity of global earthquake catalogues such as the ISC and NEIC is improving with time because of advances in recording techniques, and increased station coverage. These catalogues contain progressively smaller events and uncertainties in the epicentre, depth, and origin times are reduced. However, in the last two/three decades the magnitude formulae or their calibration functions have not been changed, because of an understandable desire to maintain consistency in the magnitude determination procedure. The causes of bias in magnitude determination are identified in Chapter 2. In Chapter 3 bias in surface-wave magnitude M_s due to the distance calibration function is highlighted with some theoretical arguments. Then a new approach for determining a distance calibration function for M_s is demonstrated. This assumes a logarithmic distance dependence of surface-wave magnitudes, and takes account of those parts of the distance dependence, such as geometrical spreading and anelastic attenuation, whose distance dependence is known from theory. This approach introduces a new formula for M_s that combines theoretical constraints with the traditional empirical approach of M_s. These formulae are compared with each other and with the formulae of Gutenberg (1945a), "Prague" (Vaněk *et al.*, 1962), Marshall and Basham (1972), and Herak and Herak (1993). The efficiency of application of the new M_s formula is examined for distances $\Delta < 20°$ and $\Delta > 160°$. Also, the effect of station instruments on M_s determination, is considered, and magnitude residuals are determined for individual stations. The remaining sources of scatter and bias in M_s are then discussed.

The seismology research group at Harvard routinely determine the seismic moment of almost all earthquakes with $M_s \gtrsim 5.5$ using the Centroid Moment Tensor (CMT) method. CMT solutions are available for most moderate to large earthquakes for 1977-present. To extend seismic moment estimation to archived data (for which only magnitude are available) an empirical relationship between magnitudes and seismic moment is required. In Chapter 4 the relationship between magnitude scale (surface-wave) with scalar seismic moment is studied using published seismic moments from the CMT Catalogue. In this chapter recalculated magnitudes using the Prague formula and M_s^t formula (which is developed in Chapter 3) are used, and linearity or nonlinearity between seismic moment and surface-wave magnitude (using M_s^{Prague} and M_s^t

values) is investigated. This includes reexamination of conclusions of Ekström and Dziewonski (1988) and Abercrombie (1994) about anomaly in M_s values of different regions. Also, the depth effect in the determination of surface-wave magnitude is discussed and a depth correction term is given for earthquakes with a focal depth of 10 to 60 km. The regression analysis is made for earthquakes common to the ISC and CMT catalogues. The nonlinear relation of regression fit is compared with other global relationships between M_s and $\log M_0$.

Chapter 5 begins with a discussion of the depth-distance calibration terms of Gutenberg and Richter (1956) for m_b determination which is currently used by ISC and NEIC. This includes briefly a description of some other distance or depth-distance calibration terms such as those of Veith and Clawson (1972), Christoskov *et al.* (1979), Nortmann and Duda (1982), Marshall *et al.* (1986), and Lilwall (1987b). Then a new set of depth-distance terms for m_b is presented using seismic moments from the Harvard CMT Catalogue. The new depth-distance calibration terms obtained in this study and other calibration terms are compared by applying them to an ISC dataset. Also, correlation of values of m_b using different depth-distance terms with $\log M_0$ is discussed. The values of m_b using Gutenberg-Richter and the new calibration terms are compared for seven subduction areas (Kurile, Japan, Mariana Trench, South-West Pacific, South Pacific, Tonga, and South America). In Chapter 5 station corrections are determined from residuals, and effect of using station corrections on magnitude residuals over epicentral distance is discussed. Then empirical relation between m_b and nuclear explosion yield at two nuclear test sites is compared.

Chapter 6 begins with a brief discussion of theoretical background about surface-waves. Then the idea of collapsing surface-wave seismogram to a standard distance, by removal of a standard dispersion or a specific dispersion curve is examined.

A brief summary of the main results of this thesis is given in Chapter 7.

Chapter 2

Magnitude scales and bias in magnitude determination

2.1 Introduction

The concept of seismic magnitude scale is complicated by the many different scales that have been introduced to accommodate different situations, such as (1) the use of teleseismic surface waves and body waves, (2) extension of the scale to intermediate and deep earthquakes, (3) changes in seismic instrumentation, and (4) extension of the scale to very small and very large earthquakes. Moreover, the standard magnitude estimates (such as M_L, m_b, and M_s) are meaningless for very large events (Aki, 1967; Kanamori, 1978a) as the scale becomes saturated.

During the last 50 years several variations of magnitude scales were developed. All of the modern magnitude scales are refinements of the original Richter scale. Earthquake magnitudes are both convenient and widely available, although the idea is based solely on an empirical relationship. Development of magnitude formulae is essentially based on a compromise between theory and observations (Båth, 1981). As Båth, (1981) stated the magnitude scale could be developed if magnitude formulae consider not only ratio of amplitude/period, distance, focal depth, but also the source properties (radiation pattern, and spectra), the path properties (anelastic attenuation, geometrical spreading, dispersion) and the receiver properties (tectonic, structure, instrumentation). Following Båth, (1981) M can be expressed as:

$$M = M(A/T, \Delta, h, K, P, R) \tag{2.1}$$

where A/T is amplitude/period ratio and is measured from a seismogram, Δ=distance, and h=depth can be estimated given the hypocentre, and K, P, and R are source, path, and receiver properties respectively. Measuring K, P, and R is difficult and has often been ignored in majority of magnitude scales.

Earthquake magnitude is routinely estimated by large data centres, such as the ISC, the NEIC of the US Geological Survey, and by many national networks and at individual stations. In order to avoid microseismic noise ($T \sim 6$ sec) it is normally estimated in two frequency bands: high-frequency body-waves with periods around 1 sec (for m_b) and low-frequency surface-waves with periods around 20 sec (for M_s). However, the period of the wave with maximum ground motion depends upon the source spectrum, the source mechanism, the source depth, the dispersion characteristics and the absorption properties of the propagation path, and the instrumental response of the seismograph.

Excellent reviews on various magnitude scales are available in the literature e.g., Båth (1981). In this chapter I will therefore summarise most of the salient points regarding different magnitude scales, and the main sources of magnitude bias. Then, after describing the dataset which will be used in this study, magnitudes estimated by the global agencies such as ISC and NEIC are compared. This includes a discussion about the density function for magnitude against frequency for the distribution of m_b and M_s in the ISC catalogue. Also, the $M_s : m_b$ relationship, using ISC data, and some anomalous earthquakes, are considered.

2.2 Local magnitude, M_L

In 1935 Richter defined the local magnitude scale M_L as a measure of earthquake size in southern California, as the logarithm of the maximum amplitude measured in microns on the record of a horizontal-component standard torsion seismograph, for an instrument located 100 km from the earthquake epicentre. A calibration curve is used so that amplitudes recorded from earthquakes at an arbitrary epicentral distance can be reduced to that expected at 100 km. M_L is determined from the maximum amplitude on a Wood-Anderson seismogram (with the free period of 0.8 sec, a maximum magnification of 2800, and a damping ratio 0.8) using the formula

$$M_L = \log A(\Delta) + B_L(\Delta) + S_c, \tag{2.2}$$

where A is the vectorial sum of the maximum trace amplitudes on the horizontal seismograms in millimetres, Δ is the epicentral distance in kilometres, $B_L(\Delta)$ is the calibrating function and S_c is the station correction. $B_L(\Delta) = -\log A_0(\Delta; M_L = 0)$ where $A_0(\Delta; M_L = 0)$ is the maximum trace amplitude in millimetres for a magnitude-zero event at distance Δ. Richter assumed that all earthquakes in southern California occur at a common depth, so that $B_L(\Delta)$ does not depend on the focal depth. It is clear that $B_L(\Delta)$ values for each region differ according to the regional structure, and that the period at which A is measured will differ according to the seismograph type. The predominant period of waves used is usually 0.5 – 3.0 sec.

Richter introduced the universally accepted basis of magnitude as proportional to log(ampli-

tude). However, there was no absolute scaling between the maximum amplitudes on instruments with different frequency responses, and the correction for distance was constrained to be logarithmic, without theoretical justification. Scales obtained from different instruments can be matched at one magnitude level, but they will then diverge at other levels (Scheidegger, 1985).

2.3 Body-wave scales, m_B, m_b

2.3.1 Gutenberg-Richter, m_B

Gutenberg (1945b) introduced a body-wave magnitude, m_B, based on various seismic phases such as P, PP, and S from shallow-focus earthquakes, and calibrated it to agree with M_s:

$$m_B = \log(A/T) + Q(\Delta) + 0.1(m_B - 7) + S_c, \tag{2.3}$$

where A is the maximum amplitude on the seismogram in microns for body waves with period about $12 \leq T \leq 0.5$ sec, Δ is the epicentral distance in degrees and S_c is the station correction. The amplitude-distance correction $Q(\Delta)$ was developed by a combination of theory and observation and included the effects of both geometrical spreading and anelastic attenuation (Båth, 1981). In order to reach agreement between m_B and M_s, it was necessary to include in equation (2.3) a correction term $0.1(m_B - 7)$ for P-wave phases, which for very large earthquakes was replaced with $0.2(m_B - 7)$. Gutenberg adjusted m_B to coincide with his surface wave magnitude scale (Gutenberg, 1945a) near $M = 7$. Gutenberg (1945c) developed the body wave scale, to include earthquakes of any focal depth. So for both shallow and deep events m_B is applicable. In 1956 Gutenberg-Richter provided improved values of the calibration function $Q(\Delta, h)$ for PH, PZ, PPH, PPZ, and SH in graphs and tables. In Chapter 5 the Gutenberg-Richter calibration terms for m_b determination will be discussed.

For m_B measurement, various types of seismograph including short- and long-period mechanical instruments and some electro-mechanical instruments were used; usually the period of waves used ranges from 0.5 to 12 sec (Kanamori 1983). Therefore the Gutenberg-Richter (1956) calibration for body-waves was based on medium-period seismographs. Though details of seismographs employed were never published, it can be assumed that primarily Wiechert- and Galitzin- type instruments were used (Miyamura 1982). In a multiple-rupture earthquake, m_B (classical) represents the energy of main rupture, and the modern m_b (see section 2.3.2) represents the energy of first rupture (Miyamura 1982).

2.3.2 Current determination of body-wave magnitude, m_b

Since the World-Wide Standard Seismograph Network (WWSSN) was installed in early 1960's, the body wave magnitude m_b has been determined routinely, mainly from the WWSSN short period vertical component seismograms at a period of about 1 sec. In this scale the maximum amplitude during the first few seconds of the P-wave arrival only is used, so for large earthquakes it represents the size of an earthquake at the beginning rather than the total size, and the m_b scale was not regressed against the existing scale. In spite of the essential difference in the period and measurement of amplitude, m_b is now calculated from a revised form of equation (2.3) i.e., without the $0.1(m_B - 7)$ term, and using $Q(\Delta, h)$.

Global agencies such as the ISC and NEIC report body-wave magnitude m_b for a number of shallow, intermediate, and deep earthquakes in their bulletins. Both the ISC and the NEIC use a formula in their determination of m_b as

$$m_b = \frac{1}{n}\sum_{i=1}^{n}[Q(\Delta_i, h) + q_i] - 3, \tag{2.4}$$

where n is the number of observations, Q is the depth-distance factor (from Gutenberg-Richter (1956), Figure 5), and q_i is log(amplitude in nanometers/period in sec) at the ith station. Amplitudes are measured from the first few cycles of the P-wave on the vertical seismogram of a short-period instrument with periods $T \leq 3$ sec. In the ISC Catalogue observations at distances less than 21° or more than 100° are excluded from the calculation of m_b. The NEIC uses a 25% truncation in the mean of individual station values.

The Commission of Practice of IASPEI (International Association of Seismology and Physics of the Earth's Interior) at Durham in 1977, recommended measuring the maximum amplitude of P-waves up to 25 sec or more from the P for m_b, so as to truly represent the mean rupture for large earthquakes, especially in representing the total wave energy of shallow and deep earthquakes (Miyamura 1983). But to maintain consistency of m_b, the ISC uses only $T \leq 3$ sec for determination of event magnitude.

2.4 Surface-wave scales, M_s

2.4.1 Gutenberg formula

Surface-wave magnitude was originally defined by Gutenberg (1945a) as the first attempt to measure the strength of shallow earthquakes at teleseismic distances. As such it was an extension of the local magnitude scale, M_L, introduced by Richter (1935) for estimating the size of regional earthquakes in Southern California. The M_s scale is based on 20 sec period surface waves from shallow earthquakes in the distance range $15° \leq \Delta \leq 130°$. The final formula of

Gutenberg (1945a) is:

$$M_s^{Gutenberg} = \log A + 1.656 \log \Delta + 1.818 + S_c, \tag{2.5}$$

where S_c is a station correction, Δ is the epicentral distance in degrees and A is the maximum amplitude on the horizontal component seismogram in microns for a surface-wave with a period of about 20 sec. The amplitude A is defined as $(A_N^2 + A_E^2)^{1/2}$, where A_N is the maximum on the $N - S$ component and A_E the maximum on the $E - W$ component; also in this case the period T is defined as $T = \frac{T_E + T_N}{2}$. If only one component is available, its amplitude is multiplied by $\sqrt{2}$ for use in equation (2.5). Most of the events used for the calibration of m_B and $M_s^{Gutenberg}$ scales were around $M_L = 6$, so these two scales approximately agree at $M_L \sim 6$.

$M_s^{Gutenberg}$ was originally designed to use amplitude data from horizontal seismographs, but when vertical component systems came into general use, it became common practice to measure amplitudes on the vertical component.

2.4.2 Prague formula

In 1960 and 1961, Czechoslovakian and Soviet seismologists met and developed a formula (the Prague formula) from the 14 station-dependent surface wave magnitude formulae detailed in Lienkaemper (1984). Vaněk *et al.* (1962) proposed the so-called "Prague formula":

$$M_s^{Prague} = \log (A/T)_{max} + 1.66 \log \Delta + 3.3, \tag{2.6}$$

where A is the vertical or resultant horizontal amplitude in microns and T is the mean period in sec and Δ in degrees. In equation (2.6) $(A/T)_{max}$ is the maximum of all A/T (amplitude/period) values of wave groups on a record. However, it is not clear whether all the seismic stations which report data to the ISC measure $(A/T)_{max}$ or (A_{max}/T). In practice it seems improbable that $\log(A/T)_{max}$ and $\log(A_{max}/T)$ will differ greatly for classical long-period observations, though the difference may be very large on broad band seismograms, which are of course becoming more common. The Prague formula employed a geographic average of various distance-normalising terms, and incorporated T in the formula to account for those cases, particularly for continental propagation and using broad band (Kirnos-type) seismographs, for which the maximum trace amplitude does not occur at a period near 20 sec (Marshall and Basham 1972).

The recommendations on magnitude made by the IASPEI Assembly at Zürich in 1967 (Båth, 1981) concerned surface-wave magnitude determination using the Prague formula with conditions $20° \leq \Delta \leq 160°$, and 17 sec $\leq T \leq$23 sec for shallow earthquakes with a calculated depth $h \leq 50$ km. The ISC uses the Prague formula for shallow events with a calculated depth

of $h \leq 60$ km in the distance range 20° to 160° and in the period range 10 sec $\leq T \leq$ 60 sec. ISC uses either the vertical component or the vector sum of the horizontals, but NEIC uses only the vertical component.

Since the above scales were established, a large number of other scales have been introduced for different regions. For detailed discussion on the different scales and relations between them see Båth (1981). Different scales may represent fundamentally different properties of the source. Since seismic waves at a given period may represent, if not very accurately, the source spectrum at that period, the difference in the period is more fundamental than that in the wave type (Kanamori,1983). Magnitude scales have been grouped by Kanamori (1983) according to the period as shown in Table 2.1

2.4.3 Modified M_s formulae

Several authors have pointed out difficulties with the above scales for $\Delta \leq 20°$ (e.g., von Seggern, 1970; Evernden, 1971). A modification of the Prague formula applicable to closer ranges was proposed by Marshall and Basham (1972). They suggested a modified formula for M_s as:

$$M_s = \log A_{max} + B'(\Delta) + P(T) + 3, \tag{2.7}$$

where A is the maximum amplitude in microns of the Raleigh wave train, $B'(\Delta)$ is a tabulated epicentral distance correction term and $P(T)$ is the path correction varying with the period of the wave measured, and tabulated for continental lithosphere of North-America and Eurasia, oceanic lithosphere, and mixed continental-oceanic lithospheric structures. Marshall and Basham proposed that for distances up to 25° the distance dependence term, $B'(\Delta)$, is proportional to $0.8\log(\Delta)$, and at large teleseismic distances is the same as Gutenberg's distance ($1.66\log(\Delta)$) dependence term. Marshall and Basham have adjusted the absolute level of $B'(\Delta)$, so that magnitude determinations give results essentially the same as the Gutenberg and Prague formulae at large epicentral distances.

Herak and Herak (1993) found a new empirical formula for determining M_s as:

$$M_s = \log(A/T) + 1.094\log(\Delta) + 4.429, \tag{2.8}$$

based on an analysis of surface wave magnitudes of 250 selected earthquakes published in the ISC and NEIC Catalogues. They conclude that the Prague formula is inappropriate for magnitude determination because of bias in the distance calibration function.

The general form of most formulae for determining surface-wave magnitude has remained

Table 2.1. Magnitude scales (after Kanamori, 1983).

scale	T (sec)	λ_{max} (km)	Related scales
M_L	$0.1 \sim 3$	10	m_{bLg}
M_s	~ 20	70	$M_{GR}, M_R, M_D, M_Z, M_V, M_{JMA}$
m_B	$0.5 \sim 12$	70	
m_b	~ 1	10	m_{bLg}
Moment magnitude	$10 \sim \infty$	∞	M_M, M_w, M_E, M_t
M_C	–	–	
M_I	–	–	M_K

Notation

T	Period
λ_{max}	Maximum wave length
M_L	Local magnitude, Richter (1935)
M_s	Surface-wave magnitude, Gutenberg (1945a)
m_B	Body-wave magnitude, Gutenberg(1945b), Gutenberg and Richter (1956)
m_b	Short-period body-wave magnitude reported in "Earthquake Data Report" and "Bulletin of International Seismological Centre"
m_{bLg}	Lg-wave magnitude, e.g., Nuttli (1973)
M_{GR}	Magnitude used in Gutenberg and Richter(1954)
M_R	Magnitude used in Richter (1958)
M_D	Magnitude used in Duda (1965)
M_Z	Surface-wave magnitude determined from the vertical-component seismograms (e.g., Earthquake Data Reports)
M_V	Surface-wave magnitude defined by Vaněk *et al.* (1962)
M_{JMA}	Magnitude scale used by the Japan Meteorological Agency
M_M	Moment magnitude by Brune and Engen (1969)
M_w	Moment magnitude by Kanamori (1977)
M_E	Strain-energy magnitude (Moment magnitude) by Purcaru and Berckhemer (1978)
M_t	Tsunami magnitude regressed against M_w, Abe (1979)
M_C	Coda (or duration magnitude), e.g., Bisztricsany (1959), Tsumura (1967), Real and Teng (1973)
M_I	Magnitude determined from intensity data and macro-seismic data, e.g., Nuttli and Zollweg (1974), Nuttli *et al.*, (1979), Utsu (1979)
M_k	Kawasumi (1951)

as:

$$M_s = \log(A/T) + B(\Delta) + C, \tag{2.9}$$

where $B(\Delta)$ is a correction for the decay of amplitude with distance, and C is a correction for effect of the station structure or path correction etc., which in some formulae has been omitted. In Chapter 3 a M_s formula similar to equation (2.9) will be computed, using a much larger ISC dataset.

2.5 Theoretical relationship involving seismic energy and magnitude

The magnitude scale measures earthquake size in a relative manner. It compares large and small earthquakes quantitatively, but indicates little about the physical properties of their sources. Fundamental interest in the magnitude scale arises primarily from direct relationship between magnitude and the total elastic-wave energy of an earthquake. Magnitude is obviously related to the energy which is radiated from earthquake sources in the form of elastic waves. Part of the original potential energy of strain stored in the rock must go into mechanical work, as in raising crustal blocks against gravity, or in crushing material in the fault zone; and part must be dissipated as heat (Richter, 1958).

Following Gutenberg and Richter, (1956) the seismic energy of a wave propagating with velocity c can be expressed as

$$E = 2\pi^3 h^2 ct\rho(A/T)^2, \tag{2.10}$$

where A, T, and t are the amplitude recorded at the free surface, the period, and the duration of wave group (which hence contains $n = t/T$ waves) respectively. h is focal depth, and ρ is the density of the medium. Assuming $c = 3.4$ km/s for S-waves, applying a factor $\frac{3}{2}$ to allow for half as much energy in P-waves (Eq. (2.10) dealt with the maximum energy which at short distance are S-waves; the energy of P-waves must be added which is assumed to be half of the S-waves (Gutenberg and Richter, 1956)), $\rho = 2.7\text{g/cm}^3$, and $h = 16$ km (a probable focal depth in southern California), equation (2.10) becomes

$$\log E = 12.34 + 2\log(A/T) + \log t. \tag{2.11}$$

Gutenberg and Richter (1956) obtained the following empirical relations for earthquakes in southern California,

$$\log t = -1 + 0.4\log(A/T), \tag{2.12}$$

$$\log(A/T) = m_B - 2.3, \tag{2.13}$$

$$M_s = 1.59m_B - 3.97. \tag{2.14}$$

Therefore, by substituting equations (2.13) and (2.12) into equation (2.11) we have

$$\log E = 5.8 + 2.4m_B \quad \text{(E in ergs)}. \tag{2.15}$$

Also, by substituting (2.14) into (2.15), the $E : M_s$ relation becomes

$$\log E = 1.5M_s + 11.8. \tag{2.16}$$

If M_s is increased by 1.0 in (2.16), E is magnified by a factor of $10^{1.5}$, i.e., approximately 32. In other words, the seismic energy of an $M_s = 6$ earthquake is about 32 times as large as that of an $M_s = 5$ earthquake, and is about 1000 times that of an $M_s = 4$ earthquake.

Båth (1958) integrated the surface-wave trains to establish the relation between the surface-wave energy and M_s. Combining this relation with a relation between surface-wave energy and the radiated energy, Båth (1958) introduced the relation

$$\log E = 1.44M_s + 12.24. \tag{2.17}$$

Obviously, the energy calculation in equations (2.15), (2.16) and (2.17) suffers from all the problems of magnitude determination (saturation, etc.). Equation (2.17) gives the radiated wave energy (E_R) which is very similar to equation (2.16). M_s represents the level of the energy spectrum at 20 seconds while E_R represents the spectrum over the entire frequency band. Energy is a well-defined physical quantity, but this does not mean that the estimated energy, as introduced above, is of high precision. Many assumptions have been made in the derivation of the kinetic energy of waves, e.g., the wave-form has been greatly simplified, the azimuthal effect of wave radiation, attenuation during propagation, and wave behaviour near the surface, etc. have been ignored. Even if these factors are taken into account to determine an accurate measurement of the kinetic energy, the more essential question of whether or not this particular quantity can accurately represent all the energy produced by a seismic source must still be considered.

2.6 Seismic moment

While magnitude is a convenient way to measure earthquake size from seismograms, a more physically meaningful measurement of earthquake size is given by the seismic moment. The

concept of seismic moment is important in connection with the long period spectra of earthquakes (Aki, 1972) and with the accumulated seismic displacement in an extended fault zone (Brune, 1968). Seismic moment is perhaps the most fundamental parameter that can be used to measure the accurate strength of an earthquake caused by fault slip. In addition, it is not dependent on station azimuth because the calculation takes the radiation pattern into account. The general expression for seismic moment due to slip u over a fault area A in a medium of rigidity μ (with both u and μ varying over the fault) is

$$M_0 = \int_A \mu u dA, \tag{2.18}$$

where μ is rigidity modulus of the faulted medium and u is the slip, and the integration is over the fault area A. Assuming constant μ, the average slip $\bar{u}$ is defined to give

$$M_0 = \mu A \bar{u}. \tag{2.19}$$

This is equivalent to the value of the moment of force of each couple of the double-couple stress field, since if a fault of dimensions $L \times W (L > W)$ is considered so that $A = LW$, then the elastic strain release, $\epsilon \approx \bar{u}/W$ and the stress release $(\sigma_{\text{initial}} - \sigma_{\text{final}})$ is

$$\sigma = \mu \bar{u}/W = M_0/AW \quad \Rightarrow \quad M_0 = A\sigma W. \tag{2.20}$$

The shearing force across the fault plane is $A\sigma$ (stress $\times$ area) and the lever arm of this force is W, that is, the moment of the stress field may be represented by forces at $W/2$ on either side of fault.

Measured values of M_0 range from about 10^{30} dyne-cm (1960 Chilean earthquake, 1964 Alaskan earthquake) down to around 10^{12} dyne-cm for micro-earthquakes, and 10^5 dyne-cm for micro-fractures in laboratory experiments on loaded rock samples. The first estimate of seismic moment was made by Aki (1966) for the Niigata earthquake of 1964, using long-period Love-waves observed by the World-Wide Standard Seismograph Network.

2.7 Moment magnitude

The seismic moment represents the size of an earthquake only at a period much longer than the source process time (~source dimension/shear velocity), so it represents the long-period end of the source spectrum (Kanamori, 1983). Several studies have indicated that it is possible to determine the spectral shape from the long-period end of the spectrum. Kanamori (1977) used this concept and a very simple model proposed by Orowan (1960) (final stress is equal to frictional stress), and obtained a relation $E_R = \frac{\Delta\sigma M_0}{2\mu}$ (in which the stress drop $\Delta\sigma = \sigma_0$ is complete) between the radiated energy E_R which corresponds to the integral of the square

of the source velocity spectrum over the entire frequency band, and the seismic moment M_0. If we assume that average stress drop is constant and equal to about 30 bar (which is nearly constant at 20–60 bars for large earthquake, Kanamori 1978b), and μ equal to 300 kbar, these yield $E_R = \frac{M_0}{2\times 10^4}$ (1 bar $= 10^5$ Nm^{-2} $= 10^6$ dynes cm^{-2}).

Kanamori (1983) showed that the energy computed from the seismic moment by $E_R = \frac{\Delta\sigma M_0}{2\mu}$ for shallow and deep events is in good agreement respectively with the empirical relations of (2.16) and (2.15), and he defined a magnitude scale (called moment magnitude) for shallow and deep earthquakes respectively as:

$$\log M_0 = 1.5M_w + 16.1 \quad \text{for shallow earthquakes,} \tag{2.21}$$

$$\log M_0 = 2.4m_w + 10.1 \quad \text{for deep and intermediate earthquakes,} \tag{2.22}$$

where seismic moment M_0 is in dyne-cm. Actually the relation (2.21), was obtained by Hanks and Kanamori in 1979, which is remarkably consistent with the M_0—M_s relationship which is empirically defined by Purcaru and Berckhemer (1978) for the range of moderate to large earthquakes i.e., $5 \lesssim M_s \lesssim 7.5$:

$$\log M_0 = 1.5M_s + (16.1 \pm 0.1), \tag{2.23}$$

and the M_0—M_L relationship empirically defined by Thatcher and Hanks (1973) for southern California earthquakes ($5 \lesssim M_L \lesssim 7$):

$$\log M_0 = 1.5M_L + 16.0. \tag{2.24}$$

Hanks and Kanamori (1979) introduced a single moment magnitude from equations (2.21), (2.23), and (2.24) as

$$M_w = \frac{2}{3}\log M_0 + 10.7. \tag{2.25}$$

which is uniformly valid with respect to $3 \lesssim M_L \lesssim 7.5$, $5 \lesssim M_s \lesssim 7.5$, and larger M_w at larger magnitudes (Hanks and Kanamori, 1979). Equation (2.25) is extensively used in the seismology literature.

Equation (2.21) essentially represents the $\log M_0$—M_s dependence for ordinary constant strain-drop moderate to large earthquakes and, in this case, M_0 can be predicted from M_s or vice versa. M_w (moment magnitude) indeed agrees well with M_s for smaller than a magnitude of ~ 8. This magnitude scale M_w represents the total wave energy released by an earthquake. In order to compare the magnitude of deep events with those for shallow earthquakes, m_w can be converted to M_w by using the standard relation between m_B and M_s. The inverse of

equation (2.21) therefore provides a means of estimating M_0 when only M_s is known, i.e., for historical earthquakes, that is important in evaluating the seismic risk or estimating of rates of seismic deformation. Many workers pointed to the uncertainty associated with this estimate, specially for very large earthquakes.

2.8 Saturation of magnitude scales

All instrumental magnitude scales suffer from saturation at high magnitudes. The seismic energy in the far-field spectrum of earthquakes concentrates at frequencies below a limit called the corner frequency, which decreases as the source dimensions of the earthquake increase. For very large earthquakes the corner frequency can fall below below 0.05 Hz. The most common magnitude scale i.e., m_b and even M_s then suffer and become unrepresentative of true earthquake size, because the majority of the energy is at lower frequencies. This happens for M_s at approximately $M_s = 8.0$ and for m_b at about 6.5 (Reiter, 1990). Figures 2.1a and 2.1b, show schematic seismograms of broad-band and narrow-band seismometers respectively.

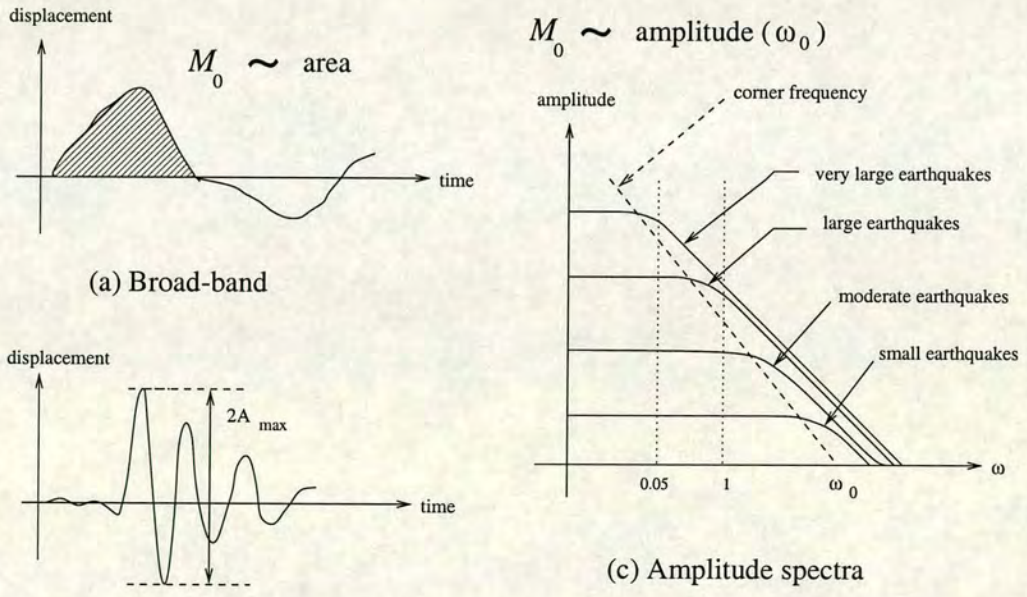

(a) Broad-band

(b) Narrow-band

(c) Amplitude spectra

Figure 2.1. Cartoon of a broad- and a narrow- band seismogram with a schematic far-field amplitude spectrum.

Also, a schematic far-field amplitude spectrum is shown in Figure 2.1c. Both of m_b and M_s scales are saturated for very large earthquakes on narrow band seismograms, but on broad band

seismograph do not saturate.

If the corner frequency becomes lower than 0.05 Hz (equivalent to a corner period of 20 sec) this affects the IASPEI formula used for M_s (Prague formula with $17 \leq T \leq 23$ sec). The consequence is that even the 20 sec surface-wave magnitude M_s will suffer from saturation at its upper levels, leading to values which are biased to low values. Several efforts have been made to remedy this shortcoming such as introduction of the moment magnitude scale M_w. The corner frequency is a consequence of taking the Fourier transform of the signal radiated from an extended fault plane, which generates a radiated plane of non-zero duration due to delay introduced by propagation of the rupture over the fault. Thus the corner frequency is inversely proportional to fault length.

The moment magnitude M_w, which is based on seismic moment M_0, is perhaps the best currently-available measure of earthquake size. Figure 2.2 shows a comparison of moment magnitude with some other magnitude scales. In construction of these curves the results of many works contributed, for detail see Heaton *et al.*, (1986). It is important to note how

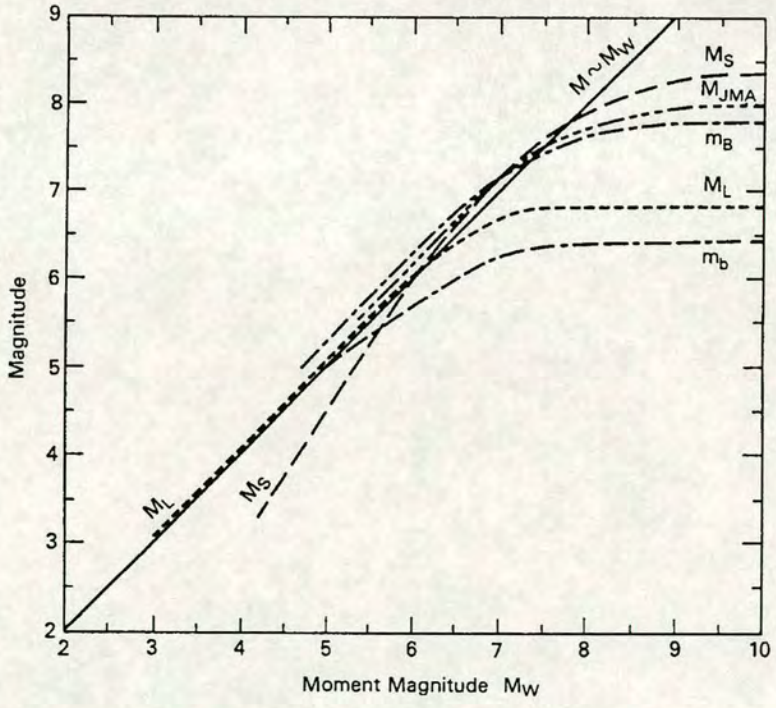

Figure 2.2. A comparison of moment magnitude with other magnitude scales (after Heaton *et al.*, 1986).

the different magnitude scales saturate, or stop increasing with increasing earthquake size or

moment M_0. This occurs because each magnitude scale, with the exception of moment magnitude, is determined using a seismic wave of a particular period and wavelength. Seismic waves whose wavelengths are much smaller than the earthquake source, do not increase in amplitude linearly with earthquake size. Thus m_b, which uses P-waves of about one second period and less than 10 km wavelength, does not truly represent the energy release from faults whose rupture dimensions are tens of kilometres or greater. Also, M_s, which uses surface waves of about 20 sec period or 70 km wavelength, does not represent the energy release from faults whose rupture dimensions are hundreds of kilometres. Except for M_s values of less than about 5.5, all the magnitude scales approach, and become approximately equal to, moment magnitude below their respective saturation points.

Both the 1906 San Francisco and the 1960 Chile earthquakes, have M_s estimated at about 8.3. The fault rupture area of the 1906 San Francisco earthquake was estimated at 5800 km^2, while that of the 1960 Chile earthquake was associated with a fault rupture area of about 35 times greater than the 1906 San Francisco earthquake. For the 1906 earthquake, a moment magnitude of about 8 is computed, while for the 1960 Chile earthquake it is estimated at about 9.5 (Reiter, 1990).

As a result of differences in magnitude scales, differences in recording systems, and the complexities and variations of source, and rupture characteristics, a scatter in magnitude values is obtained for the same earthquake.

2.9 Sources of systematic bias and scatters in magnitude

Magnitudes of earthquakes determined using traditional methods show systematic deviations, dependent on tectonic setting, from accurate estimates of earthquake size. There are many possible factors that create systematic bias in determination of magnitudes. Some of the important systematic factors which might lead to such bias include:

- Systematic errors in the distance or depth-distance calibration functions.
- Radiation pattern effects (different focal mechanism, i.e., focal depth and faulting geometry effects).
- Anelastic attenuation effects (different propagation paths, e.g., oceanic and continental paths between source and station).
- Systematic errors in the instrument response calibration.
- Non-uniform station coverage on land and ocean.
- Systematic errors in reading parameters on seismograms by different operators.

- Effect of lens structures near the receivers (focusing and defocusing).

Also, some of the important factors which create scatter in magnitudes are:

- Variety of recording conditions (differing seismograph systems).
- Differences in near-station wave speed between stations.
- Errors in the determination of depths.
- Noisy seismograms.
- Radiation pattern effects.
- Absence of a truncation in the averaging method (mean magnitude).

Removing the bias of some of the above factors, e.g., correction for the radiation pattern, is difficult to carry out uniformly for a large archived dataset, but reduction of error for some of them is possible. The distance or depth-distance calibration functions include the most important factors in decaying seismic energy during propagating i.e., anelastic attenuation and geometrical spreading effects. Therefore, in this thesis attention to reduce systematic errors caused by inappropriate distance and depth calibration functions is emphasised.

2.10 ISC Bulletin data

For the investigation of the distance/depth-distance calibration function for M_s and m_b determination, studying the $M_s : m_b$ criterion and the relationship between magnitude and seismic moment, and for a global comparison of magnitudes reported by the ISC and the NEIC, the ISC dataset from 1978 (when consistent ISC M_s determination began) to 1993 are used. Data are used from all earthquakes for which the ISC uses its own determination in the ISC Catalogue (i.e., where the ISC location is the "prime" location). Therefore the 16 years of the ISC data which includes the NEIC Catalogue are used here to achieve the objectives of this thesis. There are 110,720 events in that period for which the ISC has determined m_b, 420 of them have been identified as nuclear explosion, and 75 events have been identified as chemical explosion or events associated with mine blasting etc. The total of this data set will be used in Chapter 5 to consider body-wave calibration terms. The distribution of maximum azimuth gap for all of 110,225 earthquakes is shown in Figure 2.3. As this Figure shows, about more than 89.6% of data have a maximum azimuth gap of greater than 120°.

In the ISC, for 22,080 earthquakes with a calculated depth of $h \leq 60$ km, $\overline{M_s}$ have been reported between 1978 and 1993, of which 10,894 have more than two contributing stations. In the next chapter this sub-set of the data will be used to correct the surface-wave distance

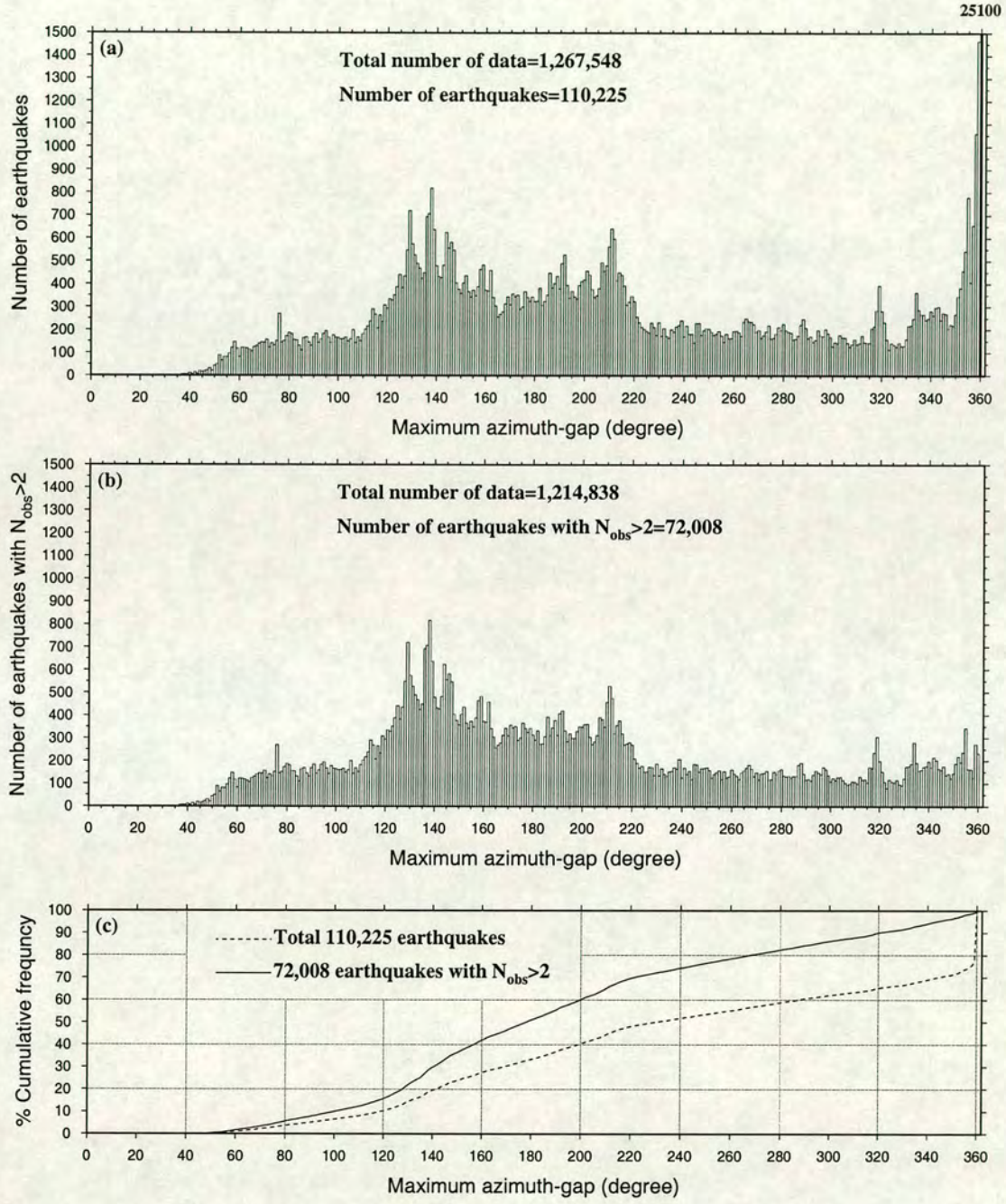

Figure 2.3. Distribution of maximum azimuth-gap for 110,225 earthquakes which have reported m_b data to the ISC from 1978 to 1993. (a) For all of 110,225 earthquakes. (b) For 72,008 earthquakes in which more than two stations contributed to the mean m_b ($\overline{m_b^{ISC}}$). (c) The same as (a) and (b) but for cumulative frequency. In (a) number of events with azimuth-gap of 360 degrees (i.e., with only one contributing station), increases to 25,100 (black bar).

calibration function. Because these data are used frequently in this thesis, the distribution of some parameters such as amplitude, period, and maximum azimuth gap, within this subset of the data are now briefly studied.

Figure 2.4 shows the distribution of amplitude and period values among the observations. As in the data of Douglas *et al* (1981b) a predominance of "round number" values in A and T are observed for the ISC data; this is evident from the peaks at multiples of 0.1 micron and 2 sec in amplitude and period respectively in Figure 2.4a. This is made clear in the magnified section of Figure 2.4a, shown in Figure 2.4b. It is known that the most important source of this type of effect is associated with the analyst and recording system. In particular, many WWSSN stations recorded at 0.5 mm/sec while many analysts read times to the nearest millimetre. This measurement practice results in various preferred $\log(A/T)$ values. The effect of this on larger magnitude values is insignificant, but the effect becomes progressively larger towards smaller magnitudes. For example, it seems the precision of most amplitude measurements is ± 0.05 micron. For a measured value of 0.1 micron with a positive error ($M_s \approx 4, \Delta = 100°$) it implies a positive error of 0.18 magnitude units, whereas at 0.01 micron with a positive error ($M_s \approx 3, \Delta = 100°$) this gives a positive error of 0.8 magnitude units.

Figure 2.5 shows the distribution of maximum azimuth gap (maximum azimuth gap of stations which contributed to $\overline{M_s^{ISC}}$) for this dataset. As Figure 2.5c shows, about 87% of data have an azimuth gap greater than 120°. To reduce the effect of radiation pattern of source in the determination of magnitude, a well-distributed network of stations for global determination of magnitude is important. However, in reality the distribution of networks and earthquakes is not random. For example most stations are situated on land, and earthquake belts commonly form at plate boundaries. In future, station coverage may be improved by the installation of stations on some ocean sites, but such sites are known to suffer from high seismic noise levels.

It is well known that azimuthal variation in surface wave radiation pattern contributes significantly to the scatter in amplitude observed in M_s^{STA}. For example Haskell (1963) showed that in a homogeneous medium the azimuthal (ϕ) dependence of the Rayleigh wave displacements are functions of $\sin\phi$, $\cos\phi$, $\cos 2\phi$, and $\sin 2\phi$ with coefficients which are functions of dip and slip-angle of the fault. He showed that radiation of Rayleigh waves from a 45° dip-slip fault has a minimum amplitude in the strike direction and a maximum amplitude in the direction perpendicular to the strike. Bowers (1997), by connecting the similarity of observed/synthetic Rayleigh wave amplitudes from the October 30, 1994, $M_s = 4.7$ seismic disturbance in South Africa to Haskell's result, distinguished the fault plane from the auxiliary plane. For all the reasons cited above, the estimation of M_s values (event magnitude) based on very limited azimuthal coverage may be unreliable.

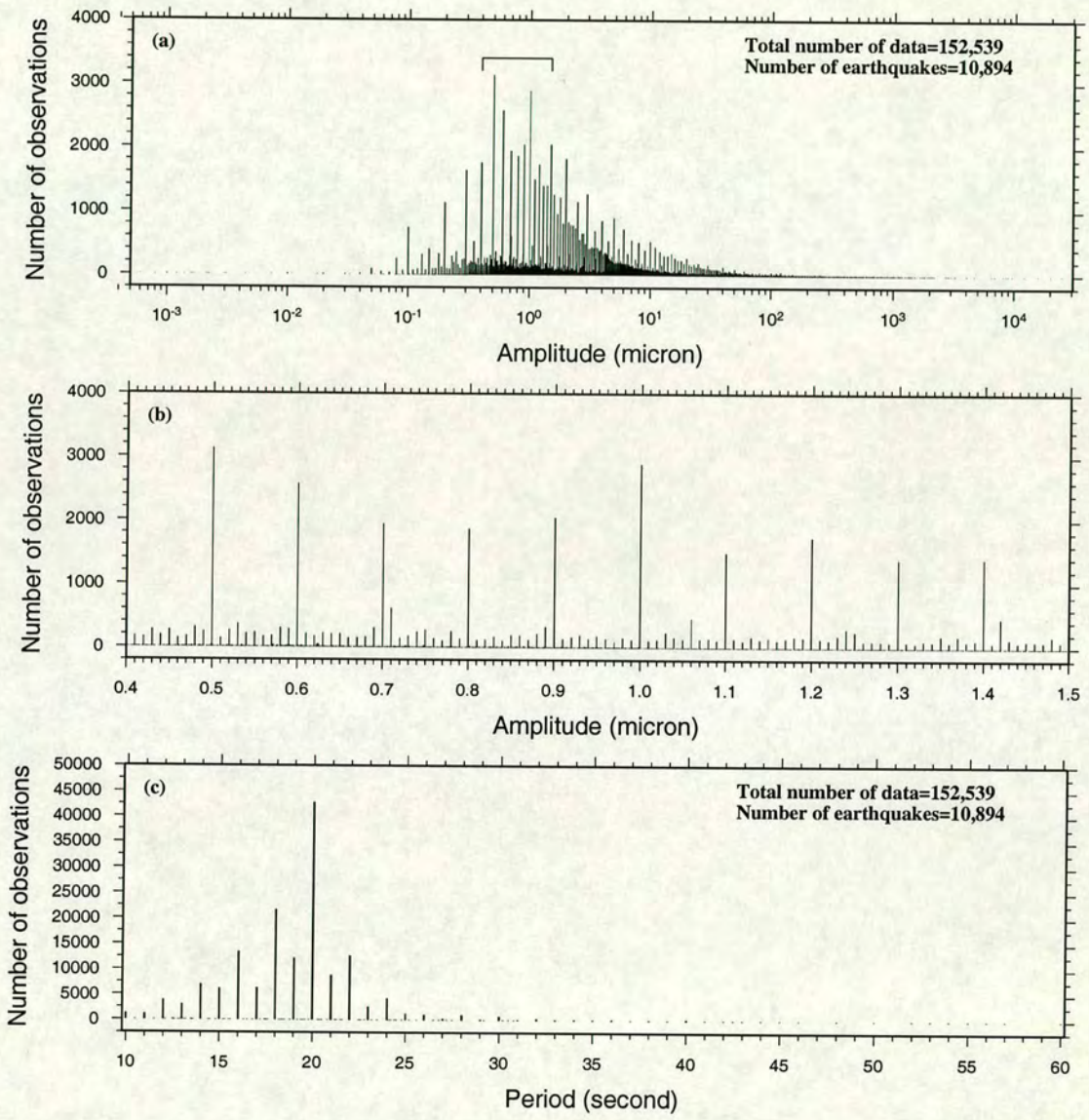

Figure 2.4. Histograms of measured amplitude and period of surface waves for all observations of earthquakes for which three or more reported observations have been used in the calculation of M_s^{ISC}. (a) For amplitude (in microns) on logarithmic scale. (b) For a small part of the amplitude range identified in Figure 2.4a, plotted on a linear scale for more clarity. (c) For period in seconds.

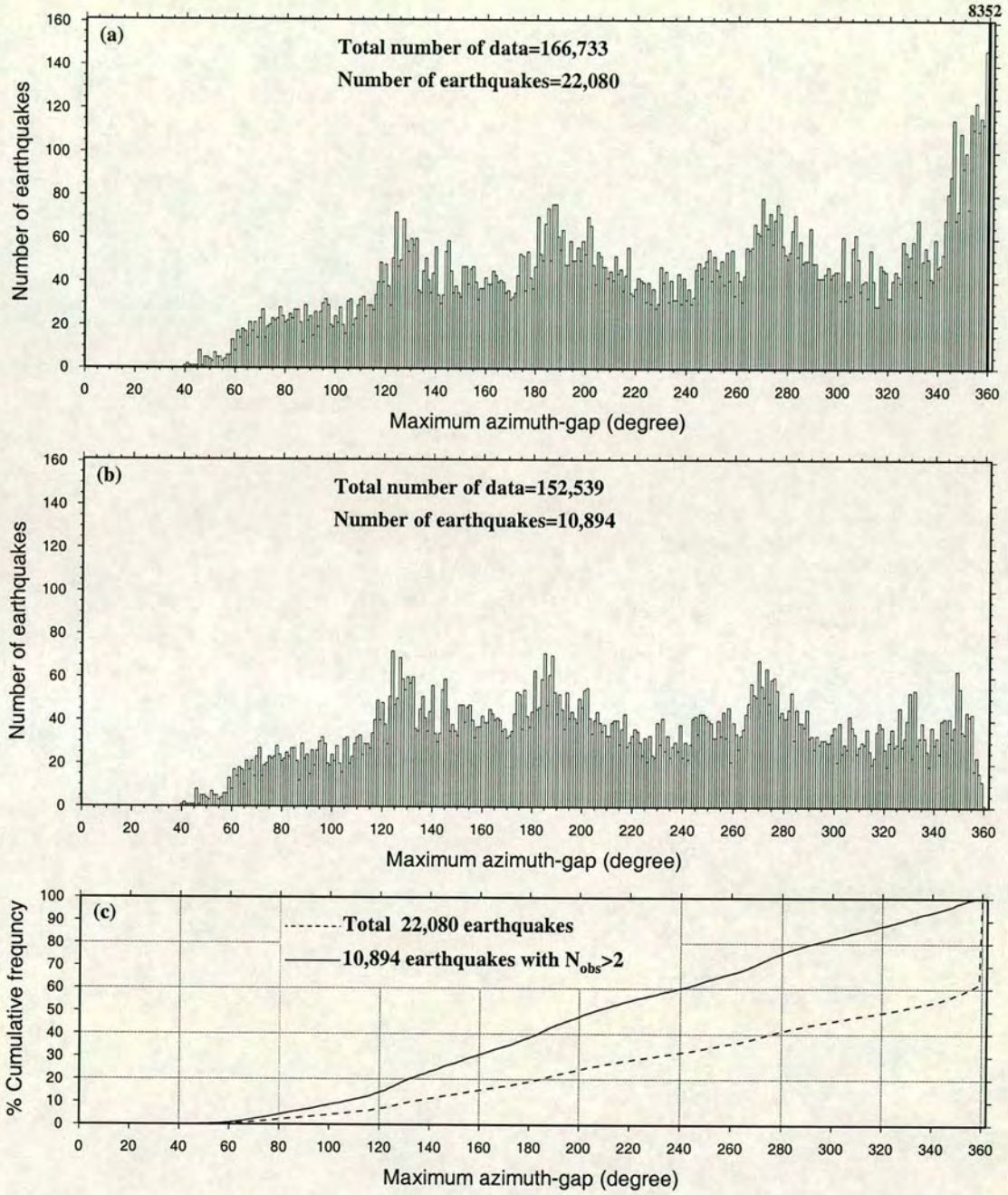

Figure 2.5. Distribution of maximum azimuth-gap of stations that the ISC has used in determining event-magnitude M_s for earthquakes with computed depth $h \leq 60$ km for which M_s data have been reported to the ISC from 1978 to 1993. (a) For all of 22,080 such earthquakes. (b) For the 10,894 such earthquakes for which more than two stations have contributed to the mean M_s ($\overline{M_s^{ISC}}$). (c) The same as (a) and (b) for cumulative frequency. In (a) the number of earthquakes with azimuth-gap of 360 degrees (i.e., with only one contributing station), increases to 8552 (black bar).

2.11 Comparison of magnitudes determined by ISC and NEIC

Magnitude (m_b or M_s) is a parameter which has a large variation due to radiation pattern at source, attenuation along the path, crustal effects etc. For some events the variation of estimated magnitude at individual stations (magnitude residual) is as large as two magnitude units(!). The reliability of estimated magnitude for an event depends on the number of stations (with a reasonable azimuthal coverage) which contributed to the mean magnitude. Especially for small events (with low magnitude), which are recorded by only a few seismic stations at teleseismic distances, the possible bias because of radiation pattern at source should be assessed. In the ISC Catalogue the number of stations which are used in estimating the mean magnitude of an event are generally greater than those used in the NEIC Catalogue. The NEIC uses a 25% truncation in the averaging method, but, the ISC does not impose any restriction in calculating mean magnitude. This raises the possibility of a further source of systematic bias, mainly for small events. In this section magnitudes determined by ISC and NEIC are compared without attention to the number of stations which they have used in the estimation of their event magnitudes.

The M_s : m_b statistics can be used for comparison of source properties only over a limited range of magnitudes, since the relationship is not linear over a large magnitude range. Figure 2.6 shows a comparison of magnitudes determined by the ISC and the NEIC. Each graph includes those earthquakes (i.e., excluding events reported as explosions) for which both the relevant two parameters are reported. ISC and NEIC compute M_s for earthquakes with a computed depth h of $\leq$60 km and <50 km respectively. To improve comparability, a limit of h <50 km is imposed for both agencies.

Many authors have given linear approximations to the relation between surface-wave and body-wave magnitudes. However, there is a great deal of scatter about the straight lines because of large variations, both random and systematic, in the empirical signals. These may be caused by differences in recording apparatus, the non-uniform distribution of seismic stations, and differences in the method of determination of magnitudes (Prozorov and Hudson, 1974).

In Figures 2.6a and 2.6b, M_s versus m_b has been plotted for ISC and NEIC data respectively. Regression lines have been determined assuming the same variance in M_s and m_b (using the method of York (1966) to account for uncertainties in both abscissa and ordinate), as:

$$M_s^{ISC} = (1.8782 \pm 0.0222) m_b^{ISC} - (4.6046 \pm 0.1102), \tag{2.26}$$

$$M_s^{NEIC} = (1.8030 \pm 0.0216) m_b^{NEIC} - (4.3655 \pm 0.1101). \tag{2.27}$$

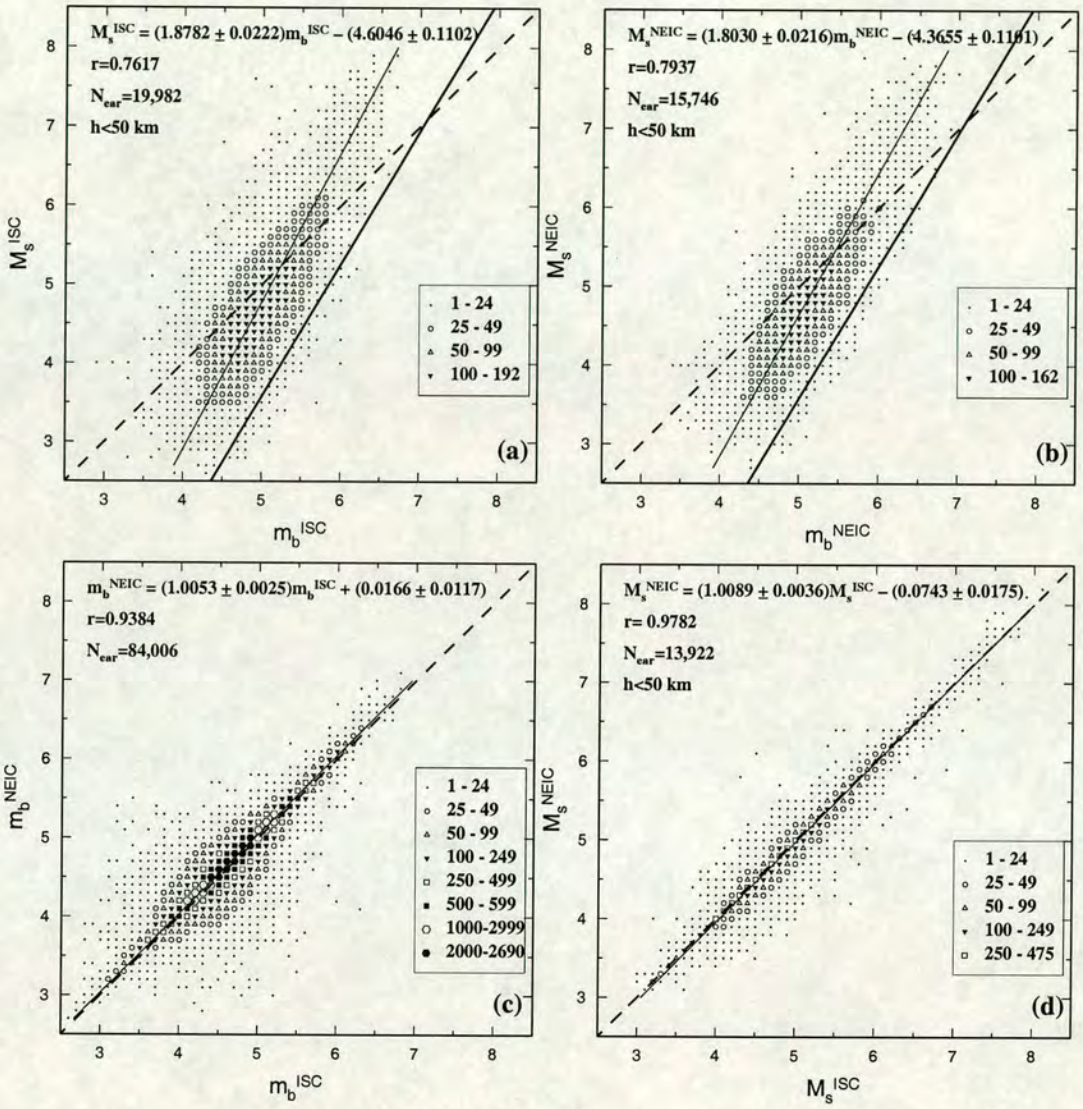

Figure 2.6. Relation between body-wave magnitude and surface-wave magnitude for earthquakes reported by ISC and NEIC from 1978 to 1993. (a) and (b) show surface-wave magnitude against body-wave magnitude. In (c) m_b^{ISC} vs m_b^{NEIC} and in (d) M_s^{ISC} vs M_s^{NEIC} is shown. Each plot includes all events for which the relevant two parameters have been reported, and for which the ISC provides the "prime" location. In each case a dashed line shows the locus of equality, and the regression line is shown by a thin solid line. r=correlation coefficient; N_{ear}=number of earthquakes; h=depth. Symbols indicate the number of data points as shown. In (a) and (b) the thick solid line shows the equation of $m_b = 0.595M_s + 2.872$ which Nowroozi, (1986) proposed as a discrimination line for earthquakes and underground nuclear explosions.

Error of parameters in these regressions is one standard deviation (1 SD). Due to the progressive increase in network sensitivity, the regression coefficient and regression constant in the linear regression line between M_s and m_b change significantly over time; this would be expected even if a magnitude cutoff and minimum number of reporting stations are imposed, because of the evolution of the global network. From the regression lines in Figures 2.6a and 2.6b it is seen that in the ISC Catalogue, the values are equal at magnitude (M) about 5.2; for $M < 5.2$ surface-wave magnitude is less than body-wave magnitude, while for $M > 5.2$ the reverse is true. In the NEIC Catalogue the values are equal at magnitude about 5.4. The correlation in Figure 2.6b (NEIC) is a little better than in Figure 2.6a (ISC).

In Figures 2.6a and 2.6b, when only earthquakes common to the ISC NEIC dataset are included (13,903 earthquakes) the regression lines do not change significantly.

In Figures 2.6c and Figure 2.6d a comparison is made between data for the two agencies, separately for body wave and surface wave magnitudes. The equations of the regression lines in Figures 2.6c and Figure 2.6d are

$$m_b^{NEIC} = (1.0053 \pm 0.0025) m_b^{ISC} + (0.0166 \pm 0.0117), \tag{2.28}$$

$$M_s^{NEIC} = (1.0089 \pm 0.0036) M_s^{ISC} - (0.0743 \pm 0.0175). \tag{2.29}$$

In both Figures 2.6c and 2.6d the correlation is good, but it seems that for body-wave magnitude the correlation is higher for the NEIC than for the ISC. For surface-wave magnitude the reverse is true. The correlation coefficient in equation (2.29) is higher than in equation (2.28). Constraining $h < 50$ km in Figure 2.6c does not reduce the scatter. Although there are some small differences between the ISC and NEIC magnitudes, it can be concluded that there is no major difference between these agencies for this presentation of the global earthquake data.

In the determination of M_s there is no depth correction either by the ISC or the NEIC. The absence of a depth correction introduces a bias in M_s. Alternatively, a poorly-constrained depth correction itself may be introduced bias in M_s value (when a depth correction is applied for M_s). Figure 2.7 compares the depths for 84,006 earthquakes (data set used in Figure 2.6c) determined by the ISC and NEIC between 1978 and 1993. The lack of good correlation, evident from Figure 2.7a, makes it clear that the errors in calculated depth for both ISC and NEIC are large. In Figures 2.7b and 2.7c the black bars are dominated by artificial depth assignments by agencies for earthquakes whose depths are poorly determined or negative (i.e., depth equal to 0, 10, and 33 km for ISC and depth equal to 10, and 33 km for NEIC). The ISC procedure for some earthquakes is to adopt a conventional depth of 33 or 0 km in the final hypocentre inversion, whereas NEIC routinely restrains oceanic foci to a depth of 10 km, rather than the ISC conventional value of 33 km, (Adams *et al.*, 1982).

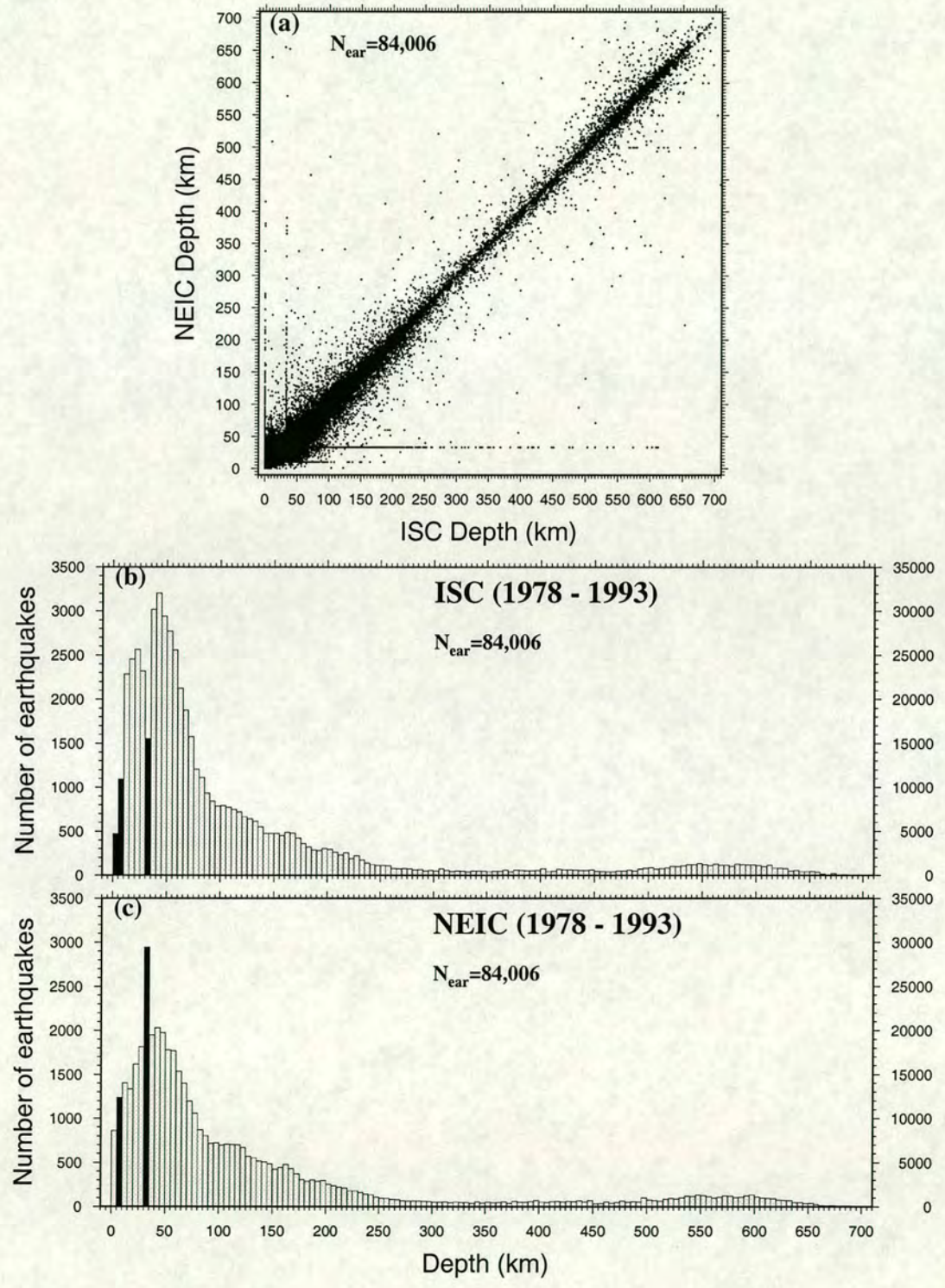

Figure 2.7. (a) Distribution of individual ISC depths against NEIC depths for 84,006 earthquakes which have been published by the ISC and NEIC from 1978 to 1993. (b) Histograms of ISC depths for the same dataset. (c) As (b) for NEIC depths. In (b) and (c) the scale of the black bars is ten times the scale of the grey histogram (right hand side). Black-shaded depths are artificial because they are used for fixing negative or otherwise unstable values. In (c) zero depth bar was not shaded black, because it seems in the NEIC Catalogue zero depth is not used for unstable cases.

2.12 Is the raw magnitude-frequency distribution symmetrical and Gaussian ?

Histograms of raw data used in Figures 2.6c and 2.6d binned in magnitude increments of 0.1 units are shown in Figure 2.8. These data take no account of the possible undersampling of the smaller magnitudes by either agency due to signal/noise ratios less than 1. Surprisingly, perhaps, the curves do show good agreement with a normal distribution. The data also show that the standard deviation of the mean body-wave magnitude $\overline{m_b}$ is less than that for the mean surface-wave magnitude $\overline{M_s}$ for both agencies. The distributions of m_b values appear to be smoother than those for M_s values, although this effect may result simply from the smaller numbers of M_s values in the datasets (by about a factor of ten— see difference in vertical scales in Fig. 2.8). Interestingly, although the distributions of M_s values show some asymmetry, with a longer tail towards larger values, those of m_b appear to be symmetrical. For comparison, a Gaussian curve with the same mean, standard deviation and normalised to the same maximum amplitude, has been superposed on each histogram. The distribution of the number of body-wave magnitudes is similar to a Gaussian distribution function.

Many authors (e.g., Aki, 1987; Rydelek and Sacks, 1989; Taylor *et al.*, 1990; Scholz *et al.*, 1991; Pacheco *et al.*, (1992); Frohlich and Davis, 1993) have pointed out that Gutenberg and Richter (1954) relationship (power law) for the observed earthquakes frequency is not a valid model across the full range of earthquake magnitudes and may not apply to restricted populations. For all four histograms in Figure 2.8 it is expected that the fall-off towards large magnitude would be governed by the b-value (a measure of the relative numbers of large and small earthquakes over time) and by the saturation of magnitude scales, whereas we expect the fall-off towards small magnitude to be governed by the network reporting threshold. In addition, various sources of error or bias may influence the shape of the histograms. Despite these expectations, it is observed that the body-wave histograms are Gaussian to a very close approximation.

Main (1987) showed that two classes of earthquakes (volcanic and tectonic) preceded the 18 May 1980 Mount St. Helens eruption, which population of second group (tectonic earthquakes) had a distribution similar to a normal distribution. Speidel and Mattson (1993) examined frequency-magnitude distribution in three datasets (m_b values of 4,660 deep worldwide earthquakes, M_s of 10,341 earthquakes in NEIC PDE (Preliminary Determination of Epicentres) between 1989 and 1991, and about 1,500 induced seismic events). They concluded that earthquake frequency-magnitude relations can be well described as a polymodal composite of normal distributions. Main (1987), and Speidel and Mattson (1993) do not mention the reason of normal distribution in earthquake population. This may either be a true feature or an artifact of incomplete reporting. Thus there would appear to be no obvious reason why the

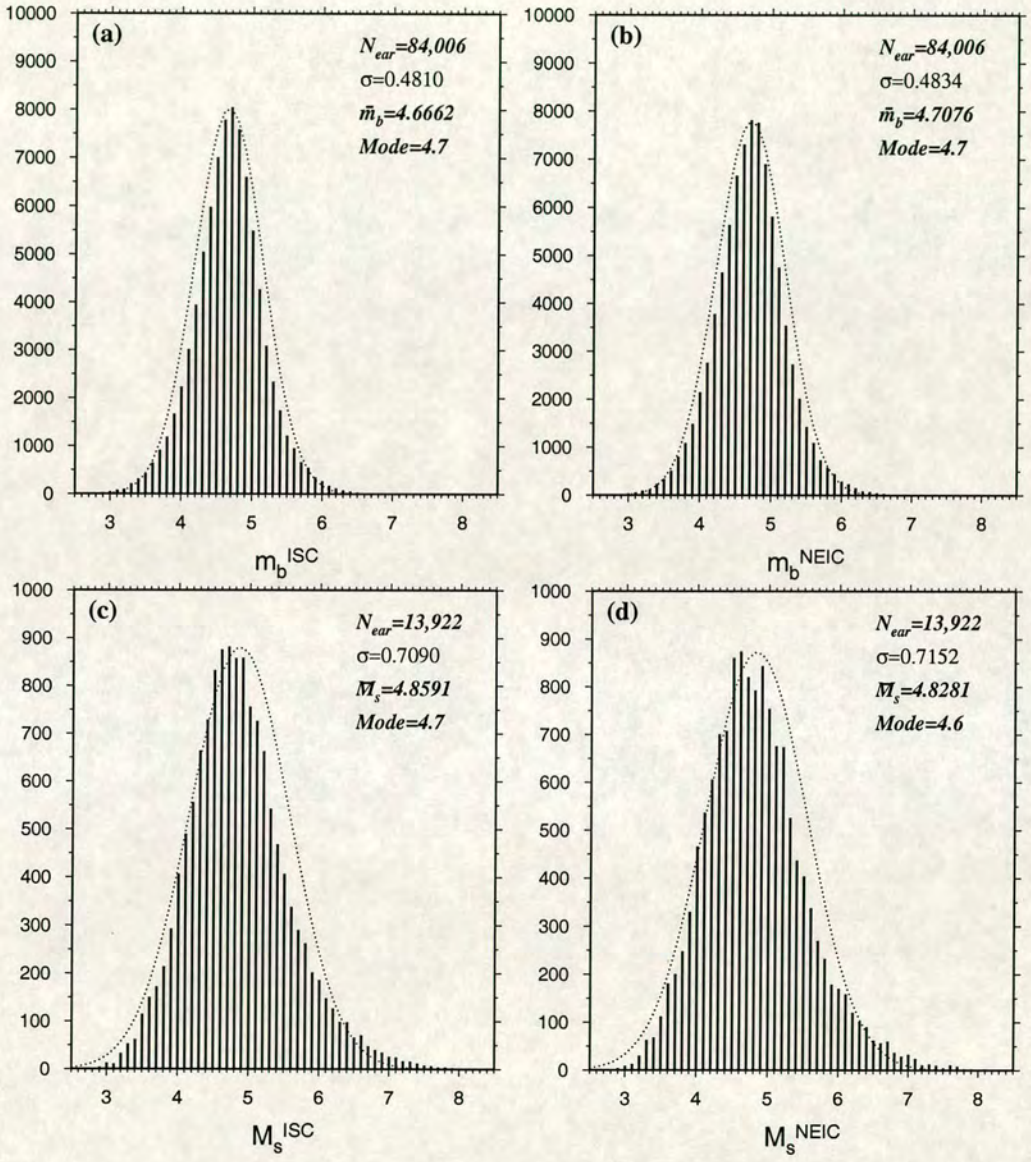

Figure 2.8. Distribution of body-wave and surface-wave magnitudes of the ISC and NEIC agencies, for the data used in Figures 2.6c and 2.6d. (a) and (b) for body-wave magnitude; (c) and (d) for surface-wave magnitude. In each case the dotted curve shows a Gaussian distribution function with the same mean and standard deviation. N_{ear} = number of earthquakes, σ=standard deviation of mean magnitude $\overline{M}$. Note the different vertical scales used for the m_b and M_s plots.

distributions should be either symmetrical or Gaussian.

Discrete and cumulative frequency of the data used in Figure 2.8 have been plotted on a logarithmic scale in Figure 2.9 for clarity. This confirms the conclusion from Figure 2.8, that the distribution of body-wave magnitudes is closer to a normal (Gaussian) distribution than the distribution of surface-wave magnitudes. In each case the cumulative number (which corresponds to a classical "b-value curve") shows how the data quantity falls off towards high and low magnitudes for the reasons given above, and shows the range of the apparently linear behaviour between these limits.

In Figure 2.10 the distribution of ISC magnitudes (m_b, and M_s) for the same earthquakes (i.e., 22,080 earthquakes with a calculated ISC depth of $h \leq$60 km) are compared. In Figures 2.10a′ and 2.10b′ magnitudes versus quantiles of standard normal are plotted for the data that are used in Figures 2.10a and 2.10b respectively. Any normally distributed curve will plot as a straight line on a probability graph, therefore on a probability graph, the degree to which all plotted points lie on a straight line determines the closeness of fit of the given distribution to a normal distribution. Deviations from a straight line indicate lack of normality across the whole range of samples. Figures 2.10a′ and 2.10b′ confirm that the departure from normality for M_s is more than for m_b.

Figure 2.11 shows the completeness of the dataset (all 110,225 earthquakes which occurred between 1978 and 1993) at small magnitudes and saturation of body-wave scale for large earthquakes. In this Figure the dataset is increased to include all ISC earthquakes for which body-wave magnitudes have been determined —not only those for which both the ISC and the NEIC have made determinations. In Figure 2.11a the successive values of discrete and cumulative frequency of the data are plotted. That part of the distribution where successive values (i.e., $\frac{\Delta \log N}{\Delta m_b}$) are approximately constant but not zero, are selected for obtaining b-value. This range of data is separated by two vertical dashed lines in Figure 2.11a. Figure 2.11b shows the distribution of discrete and cumulative frequency. The b-values obtained are shown on the graph. Also, in Figure 2.11b, the predicted saturation in the upper part of the data (magnitude of very large earthquakes) is clarified by horizontal solid arrows.

The similarity of the total globally distributed population of this dataset to a normal distribution is now examined. Figure 2.12 shows the frequency distribution on logarithmic and probability (cumulative percent) scales for these earthquakes. Comparison of Figure 2.12a with Figure 2.10a shows that the degree of asymmetry/normality in frequency-magnitude distribution is sensitive to the number of data. Since in the dataset used in Figure 2.12, the number of earthquakes which a few stations contributed in their event magnitudes, are more than those in dataset used in Figure 2.10a, the mean of distribution in Figure 2.12a decreases and its standard deviation increases in comparison with distribution of Figure 2.10a.

In Table 2.2 the statistical description for the distribution of m_b and M_s has been shown

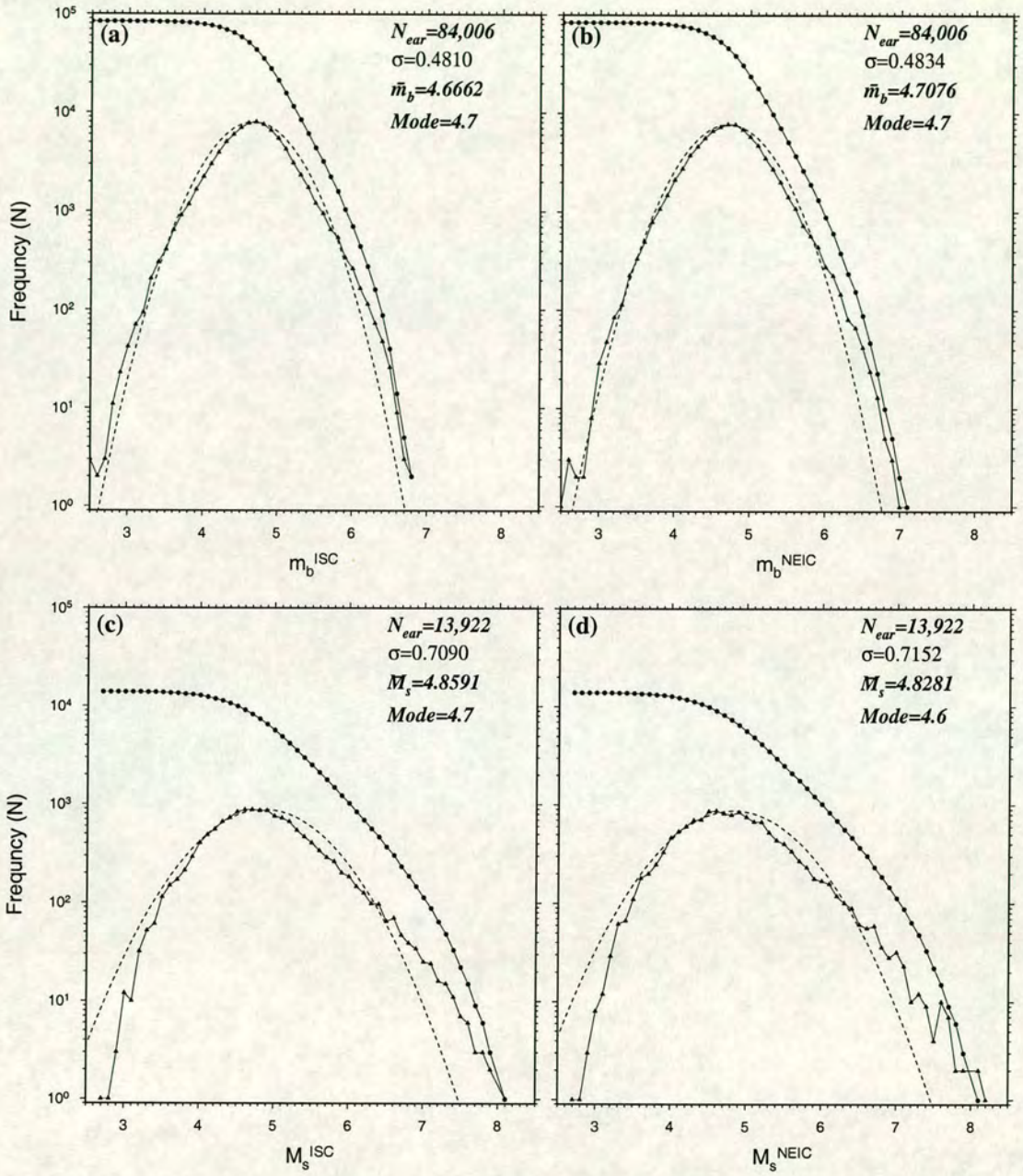

Figure 2.9. Distribution of body-wave and surface-wave magnitudes of ISC and NEIC agencies for the data used in Figure 2.8 on a logarithmic scale. In each case the filled triangles, and filled circles represent discrete and cumulative frequency of data respectively, and the dashed curve shows a Gaussian distribution function with the same mean and standard deviation (This appears as a log-normal distribution on these plots). N_{ear} = number of earthquakes, σ=standard deviation of mean magnitude $\overline{M}$.

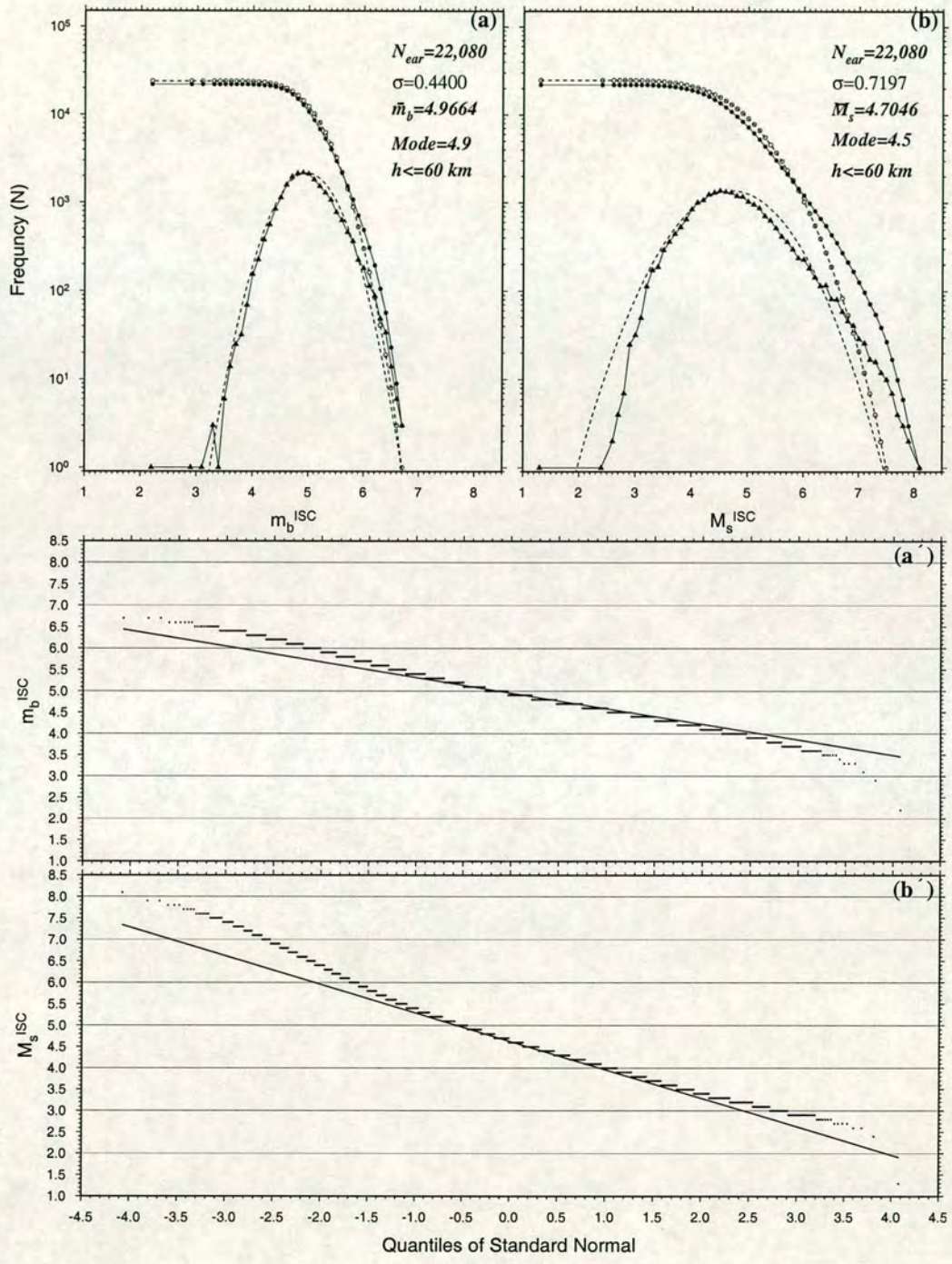

Figure 2.10. (a) Discrete and cumulative distribution of ISC body-wave magnitudes for 22,080 world-wide earthquakes with a calculated depth of $h \leq 60$ km in the ISC between 1978 and 1993. (b) as (a) but for ISC surface-wave magnitudes. (a′) Normal probability plot for m_b data used in (a). (b′) Normal probability plot for M_s data used in (b). In (a) and (b) the filled circles and filled triangles represent discrete and cumulative frequency of the data respectively. The dashed curve shows a Gaussian distribution function with the same mean and standard deviation, and the open circles represent cumulative frequency of Gaussian distribution functions. In (a′) and (b′) the solid lines show the fit to data between the first and third quantiles.

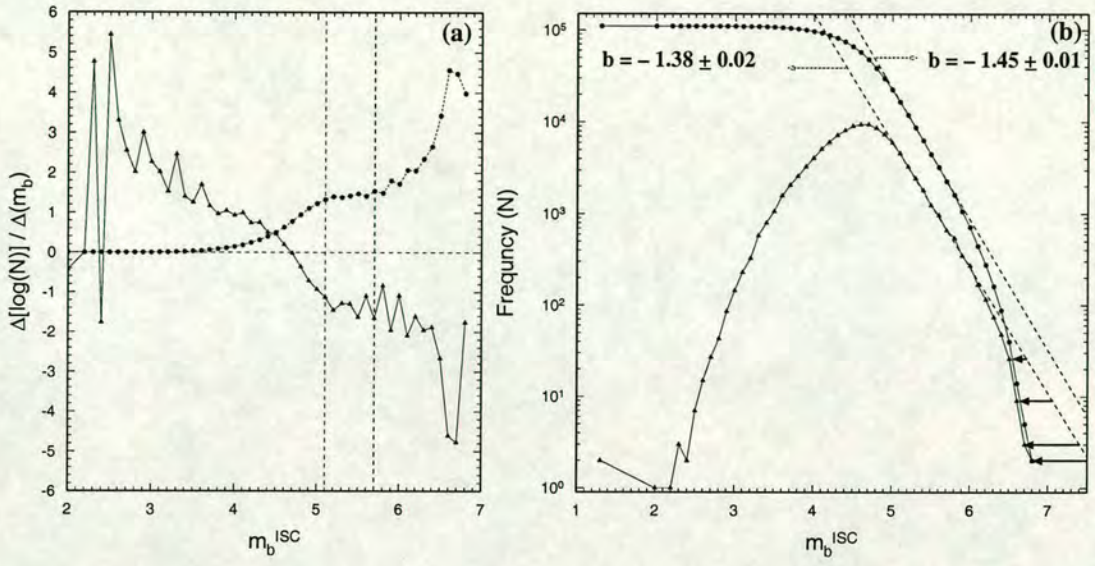

Figure 2.11. (a) Variation of successive values (i.e., $\frac{\Delta \log N}{\Delta m_b}$) on distributions of body-wave magnitude for 110,225 earthquakes. (b) Discrete and cumulative distribution of m_b values for a total of 110,225 worldwide earthquakes. In (a) the filled circles and filled triangles represent successive values of discrete and cumulative frequency of the data respectively; these symbols in (b) represent discrete and cumulative frequency respectively. The dashed lines (b) show the regression lines fitted to the data at range $5.1 \leq m_b \leq 5.8$ which is identified in Figure 2.11a by vertical dashed lines.

for data which were used in Figures 2.10 and 2.12. As this Table shows, when n is 22,080 (not the complete catalogue data) the skewness and kurtosis for both frequency-magnitude distributions are positive (i.e., skew gives a tail towards large magnitude) and these values for the m_b distribution are smaller than those for M_s distribution. This means that m_b curve is more symmetric than that of M_s, as can be seen visually.

The skewness and kurtosis should be used with caution or, preferably, not at all (Press *et al,* 1992). The significance in the deviation from normality is now tested by computing $t_s = \frac{\text{skew}-\gamma_1}{\sigma_{\text{skew}}}$, where γ_1 is the parametric value against which the sample statistic is to be tested. In the single tail test employing critical value of $t_{0.001}$ (t Distribution) with degrees of freedom $v = \infty$ i.e., $t_{0.001[\infty]} = 3.2905$, gives $t_s = \frac{0.28797-0}{0.026064} = 11.049$ (for m_b) and $t_s = \frac{0.534514-0}{0.026064} = 20.508$ (for M_s). Therefore, the observed skews are about three and six times $t_{0.001[\infty]}$. So, in spite of the apparent similarity to normality in Figure 2.10a, testing of significance shows that the probability ($P \lll 0.001$) is much less than one in a thousand the skew observed can be sampled from a population in which $\gamma_1 = 0$. Therefore, the hypothesis of $\gamma_1 \neq 0$ is accepted and it can be concluded that the distribution for both m_b and M_s is

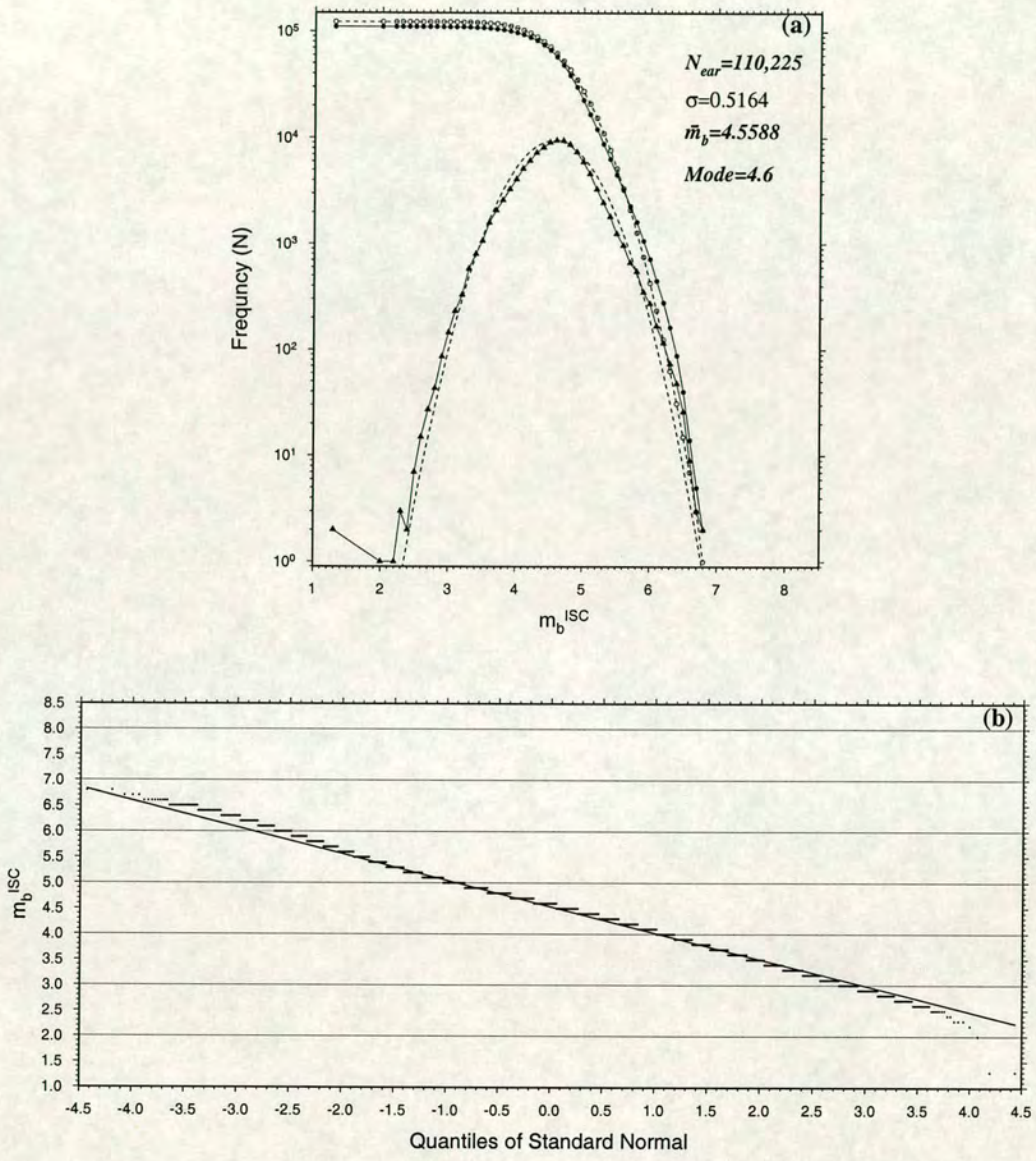

Figure 2.12. (a) Discrete and cumulative distribution of ISC body-wave magnitudes for the total 110,225 worldwide earthquakes which ISC have reported between 1978 and 1993. (b) Normal probability plot for m_b data used in (a). In (a) the filled circles and filled triangles represent discrete and cumulative frequency of the data respectively. The dashed curve shows a Gaussian distribution function with the same mean and standard deviation, and the open circles represent cumulative frequency of Gaussian distribution functions. In (b) the solid lines show the fit to data between the first and third quantiles.

asymmetrical (when n =22,080).

For the total dataset (n =110225) $t_s = \frac{|-0.049175|-0}{0.011665} = 4.216$ which, when ignoring the more anomalous data at small magnitudes (i.e., $m_b < 2.4$) the t_s reduces to 3.55. Therefore, again the probability ($P < 0.001$) is less than one in a thousand that the skew observed can be sampled from a population in which $\gamma_1 = 0$. So normality of the distribution is rejected because of asymmetry. In this case, testing the significance of kurt as $t_s = \frac{\text{kurt}-\gamma_2}{\sigma_{\text{kurt}}} = 17.653$ for employing a critical value of $t_{0.001}$ with degrees of freedom $v = \infty$, shows that the probability of $\gamma_2 = 0$ is very much less than 0.001. But, for distribution of m_b^{New} (see chapter 5) the probability of $\gamma_1 = 0$ is more than one in a ten (for $t_{0.25[\infty]} = 0.6745$ and $t_s = \frac{0.001801-0}{0.011665} = 0.1544$, so $P \gg 0.25$). However, the probability of $\gamma_2 = 0$ is very much less than 0.001. This suggests that the magnitude-frequency distribution for m_b^{New} is more symmetric.

As mentioned above, justifying the closeness/non-closeness of a distribution to asymmetry and normality based on skewness and kurtosis is difficult. As a result, in the more complete catalogue, the distribution of body-wave values appears deceptively close to normal (Gaussian), and symmetrical.

Table 2.2. Statistical description for distribution of the ISC magnitudes. m_b and M_s values of 22,080 earthquakes. m_b values of 110225 earthquakes.

n	mag-nitude	mean μ	deviation of mean (σ)	skewness skew[a]	kurtosis kurt[b]	σ_{skew} $\sqrt{15/n}$	σ_{kurt} $\sqrt{96/n}$
22080	m_b	4.966413	0.439990	0.287970	0.431289	0.026064	0.065938
22080	M_s	4.704592	0.719658	0.534514	0.707665	0.026064	0.065938
110225	m_b	4.558796	0.516367	−0.049175	0.520979	0.011665	0.029512
110225	$(m_b^{\text{New}})^c$	4.567677	0.504023	0.001801	0.639864	0.011665	0.029512

[a]The skewness characterises the degree of asymmetry of a distribution around its mean. skew$(x_1 \ldots x_n) = (1/n\sigma^3)\sum_{i=1}^{n}(x_i - \mu)^3$. Of course, any set of n measured values is likely to give a nonzero value for skew, even if the underlying distribution is in fact symmetrical. For the idealised case of a normal (Gaussian) distribution, the standard deviation of skew is approximately $\sqrt{15/n}$ (Press *et al*, 1992, page 606). The skew or statistic g_1 (the sample's symmetry measure) is the third central moment divided by the cube of the standard deviation, and its standard deviation for large $n(> 100)$ i.e., with degrees of freedom ∞, is approximately $\sqrt{6/n}$ (Sokal and Rohlf 1995).

[b]The kurtosis like skew is a nondimensional quantity, it measures the relative peakedness or flatness of a distribution. kurt$(x_1 \ldots x_n) = [(1/n\sigma^4)\sum_{i=1}^{n}(x_i - \mu)^4] - 3$. For the idealised case of a normal distribution, the standard deviation of kurt is approximately $\sqrt{96/n}$. (Press *et al*, 1992, page 606). The kurt or statistic g_2 is 3 less than the forth central moment divided by the forth power of the standard deviation, and its standard deviation for large $n(> 150)$ i.e., with degrees of freedom ∞, is approximately $\sqrt{24/n}$ (Sokal and Rohlf 1995).

[c]Body wave magnitude calculated using the new depth-distance terms obtained in this study and detailed in Chapter 5.

2.13 $M_s : m_b$ for ISC data

The relation $M_s : m_b$ is widely used as a discriminant to separate underground nuclear explosions from earthquakes. The $M_s : m_b$ discriminant is essentially empirical, with several effects contributing to its success — for example, the effect of source dimension on excitation of body and surface waves, the effect of radiation pattern on estimated m_b value, etc. As already discussed, the radiation pattern is an essential factor in explaining the observed magnitude scatter. The radiation patterns, dependence on fault parameters such as dip, slip angle of motion, rupture velocity, and focal depth, is clearly not relevant to explosions. However, in reality, radiation pattern effects are observed for explosions. Because of radiation effect, especially on the estimated m_b values for earthquakes, the scatter of points in M_s against m_b plots for earthquakes, are more than explosions points, when the source area and recording stations are the same.

To reduce the effect of radiation pattern at source, event magnitude (network-magnitude m_b) is determined by averaging station magnitudes. m_b is determined from P-waves alone, and is more strongly affected by the source mechanism (radiation pattern). In general, direct P-waves from a strike-slip event are nearly one magnitude unit smaller than those from a dip-slip event (Kanamori, 1983). Boore and Boatwright (1984) theoretically calculated averages of body-waves radiation pattern for various take off angles (corresponding to observation at near, regional, teleseismic distances) and whole focal sphere over all azimuths. Because m_b is determined at a distance range of $21° \leq \Delta \leq 100°$, the sampling of the focal sphere (radiation pattern) is limited to rays that take off to stations within this range. Boore and Boatwright (1984) assumed that at teleseismic distances take off angles are between 17° and 25° (correspond to only 2.5% coverage of the focal sphere by direct P-waves). Table 2.3 shows the averages of squared, absolute-value, and logarithmic radiation coefficients of direct P-waves over the whole focal sphere, and for different focal mechanisms teleseismic distances only. The values of $\langle \log |F| \rangle$ represent the scatter of network-averaged m_b for an earthquake, due to the direct P-wave radiation pattern relative to an explosion with the same M_0. It is clear that bias in estimated m_b may occur due to inadequate constraints on the radiation pattern and hence feed through to biases in the $M_s : m_b$ discriminant.

In order to examine the radiation effect on m_b, Bowers and Douglas (1998) calculated the far-field P-radiation coefficients for 38 aftershocks in the 1976 Gazli sequence. They calculated $\bar{m}_b^C$ values (corrected m_b for radiation pattern) after normalising the observed amplitudes by P-radiation coefficients. Bowers and Douglas (1998) confirmed the results of Boore and Boatwright (1984) and suggested that the most appropriate network average is $\bar{m}_m^C - 0.48$, where $\bar{m}_m^C$ is event magnitude corrected for the radiation effect by dividing by the radiation coefficient. Also, Nolet *et al.*, (1998) using the Harvard source solutions computed the

Table 2.3. Effective radiation coefficients of direct P calculated by Boore and Boatwright (1984) over whole focal sphere, and for different focal mechanisms with take-off angles between 17° and 25° (corresponding to teleseismic distances).

P average	$\sqrt{\langle F^2 \rangle}$	$\langle \lvert F \rvert \rangle$	$10^{\langle \log \lvert F \rvert \rangle}$	$\langle \log \lvert F \rvert \rangle$
Over whole focal sphere	0.52	0.44	0.33	−0.48
Vertical strike-slip	0.11	0.11	0.11	−0.96
30° dip-slip	0.74	0.70	0.64	−0.19
45° dip-slip	0.62	0.57	0.51	−0.29

radiation factors. They found an average of 0.48 for the radiation factor. (Theoretical average of the radiation factor is $4/3\pi = 0.42$ for a uniform coverage of the focal sphere). Their data contain 975 measurements from 53 deep earthquakes. Nolet *et al.*, (1998) suggested a correction factor for uncorrected network magnitude equal to 0.32 (i.e., $\log 0.48$), or $m_b^{unbiased} = m_b^{averaged} + 0.32$.

Here, following Frohlich and Apperson (1992), earthquakes are grouped according to dip angle values of their B, P, and T axes which were taken from Harvard source solutions. The mechanism is considered as strike-slip or normal faulting when dip angle of the B or P axes exceeds 60° respectively. When the T axis exceeds 50° the mechanism is proposed as thrust faulting. In Figure 2.13 focal mechanisms of 9,949 earthquakes (which are common to the ISC and the Harvard CMT Catalogues) are displayed on a ternary diagram. The m_b values for each group (strike-slip, normal, and thrust) averaged over 0.1-unit-wide intervals of $\log_{M_0}$ are plotted in Figure 2.14a. This shows that the estimated m_b values for earthquakes with strike-slip mechanisms are less than those for earthquakes with normal or thrust mechanisms. Frohlich and Apperson (1992) have proposed a way to express the non-double couple component of moment tensors as

$$\mathrm{f_{CLVD}} = \frac{\min(|\mathrm{m_T}|, |\mathrm{m_B}|, |\mathrm{m_P}|)}{\max(|\mathrm{m_T}|, |\mathrm{m_B}|, |\mathrm{m_P}|)} = \frac{|\mathrm{m_B}|}{\max(|\mathrm{m_T}|, |\mathrm{m_P}|)} \tag{2.30}$$

where $\mathrm{m_T}$, $\mathrm{m_B}$, and $\mathrm{m_P}$ are the largest, intermediate, and smallest principal moments, respectively. The $\mathrm{f_{CLVD}}$ i.e., compensated linear vector dipole ratio measures how different the source is from a pure double couple source. For a pure double couple source, $\mathrm{f_{CLVD}}$ is zero, while it is 0.5 for a pure Compensated Linear Vector Dipole (CLVD) source. In Figure 2.14b distributions of $\mathrm{f_{CLVD}}$ for different groups of mechanisms are compared.

Plotting m_b against $\log M_0$ for earthquakes classified according to source mechanism shows

that due to radiation effect, the m_b values for earthquakes with strike-slip mechanism are underestimated by 0.2–0.3 magnitude units in comparison with dip-slip and normal mechanisms. This affects the success of the $M_s : m_b$ criterion.

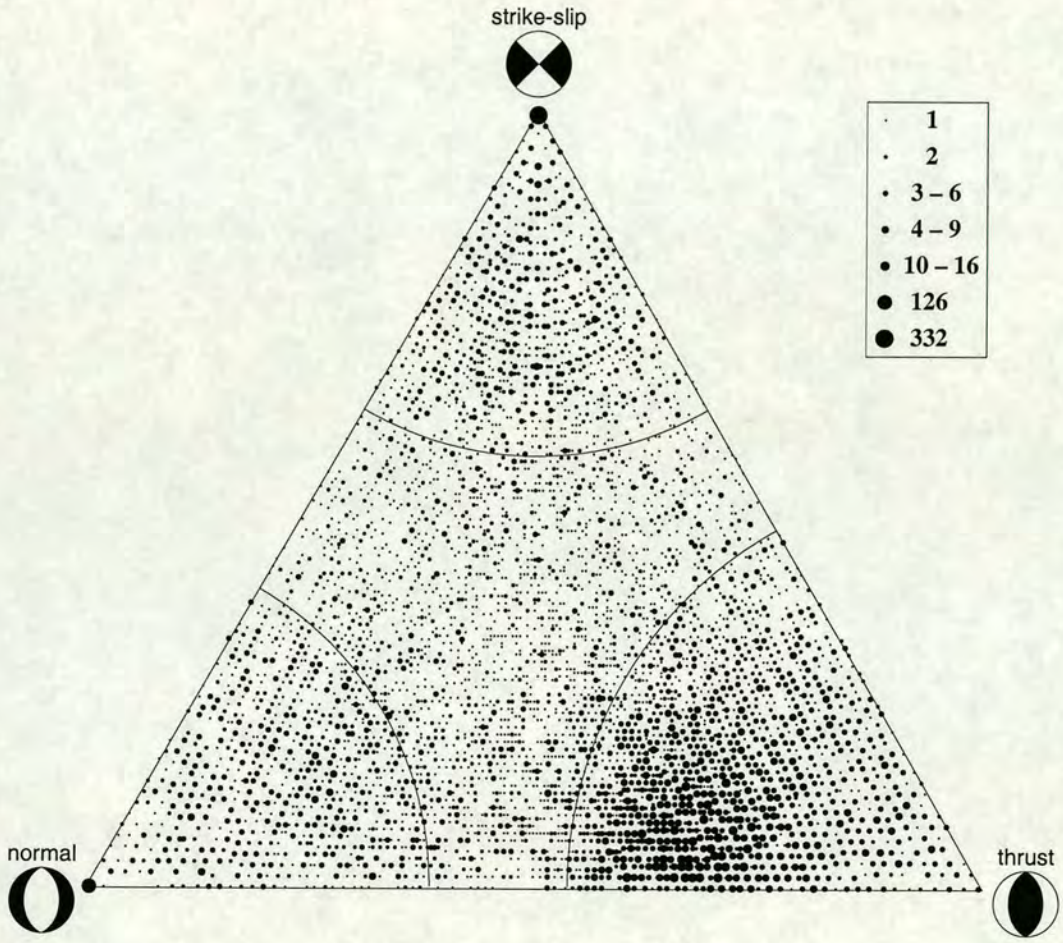

Figure 2.13. Display mechanisms of 9,949 earthquakes on a ternary diagram. The three vertices correspond to pure strike-slip, normal, and thrust fault mechanisms. Following Frohlich and Apperson (1992) the mechanisms of earthquakes are considered as strike-slip, normal, or thrust if the dip of the B or P axes exceeds 60°, or if the dip of the T axis exceeds 50°, respectively. The circles with different sizes represent the number of earthquakes with the same mechanism.

A number of studies have been carried out on the variation of M_s and m_b with geographical location. Marshall and Basham (1972) showed that the $M_s : m_b$ relationship varies between different underground nuclear explosion test sites, although they found no such variation for earthquakes in the same region. Many workers have confirmed the geographical variation of

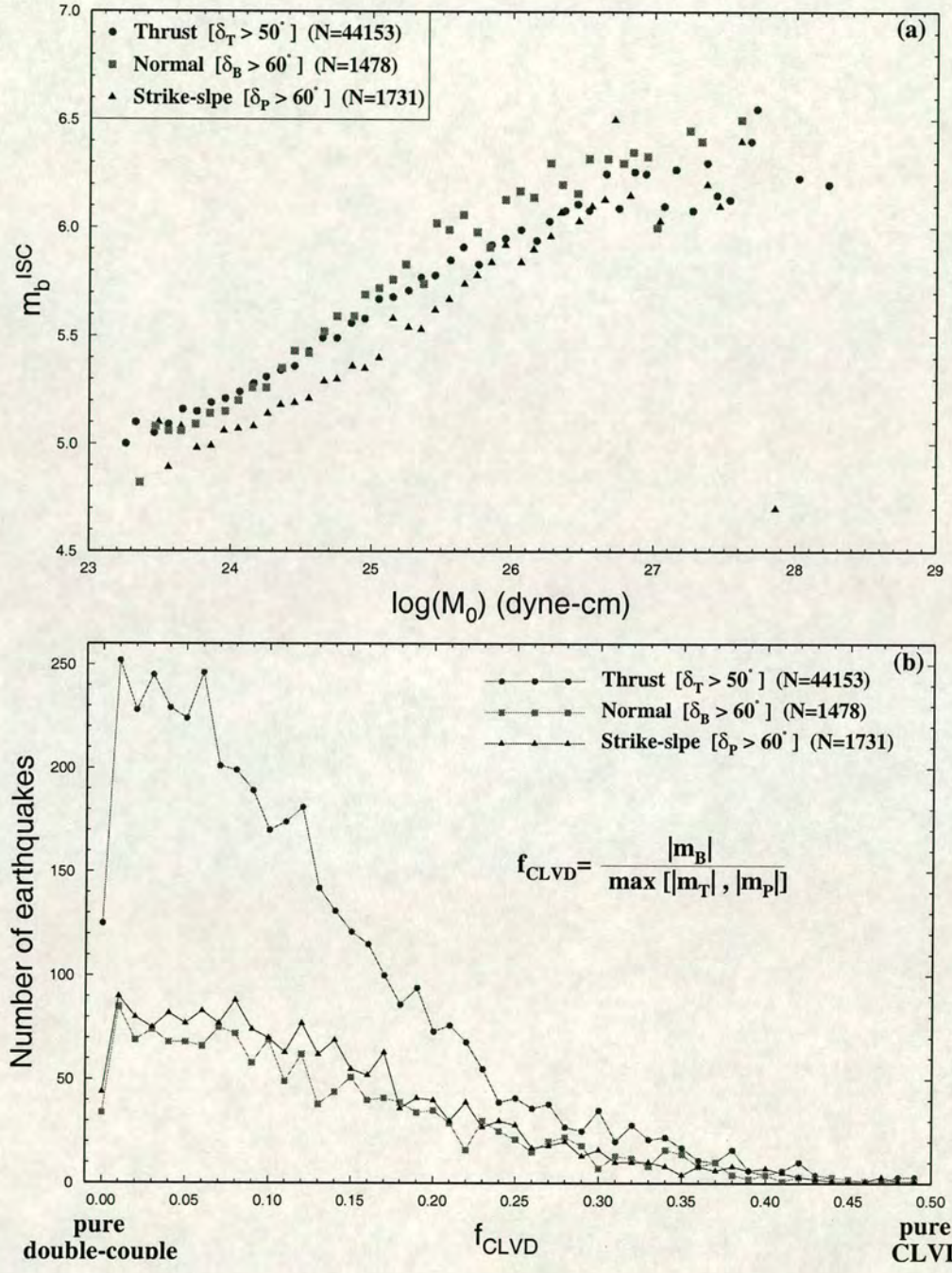

Figure 2.14. (a) Distribution of m_b^{ISC} averaged over 0.1-unit-wide intervals of $\log_{M_0}$ for earthquakes with different focal mechanisms. (b) Distribution of f_{CLVD}. δ_T, δ_B and δ_P are the dip angles of T, B, and P axis of focal mechanism respectively. Mechanisms of earthquakes were characterised as thrust, normal or strike-slip in terms of the dip angles with respect to horizontal of their T, B, and P axis. The compensated linear vector dipole ratio f_{CLVD} measures how different the source is from a "pure" double-couple source. m_T, m_B, and m_P are the largest, intermediate, and smallest principal moments, respectively.

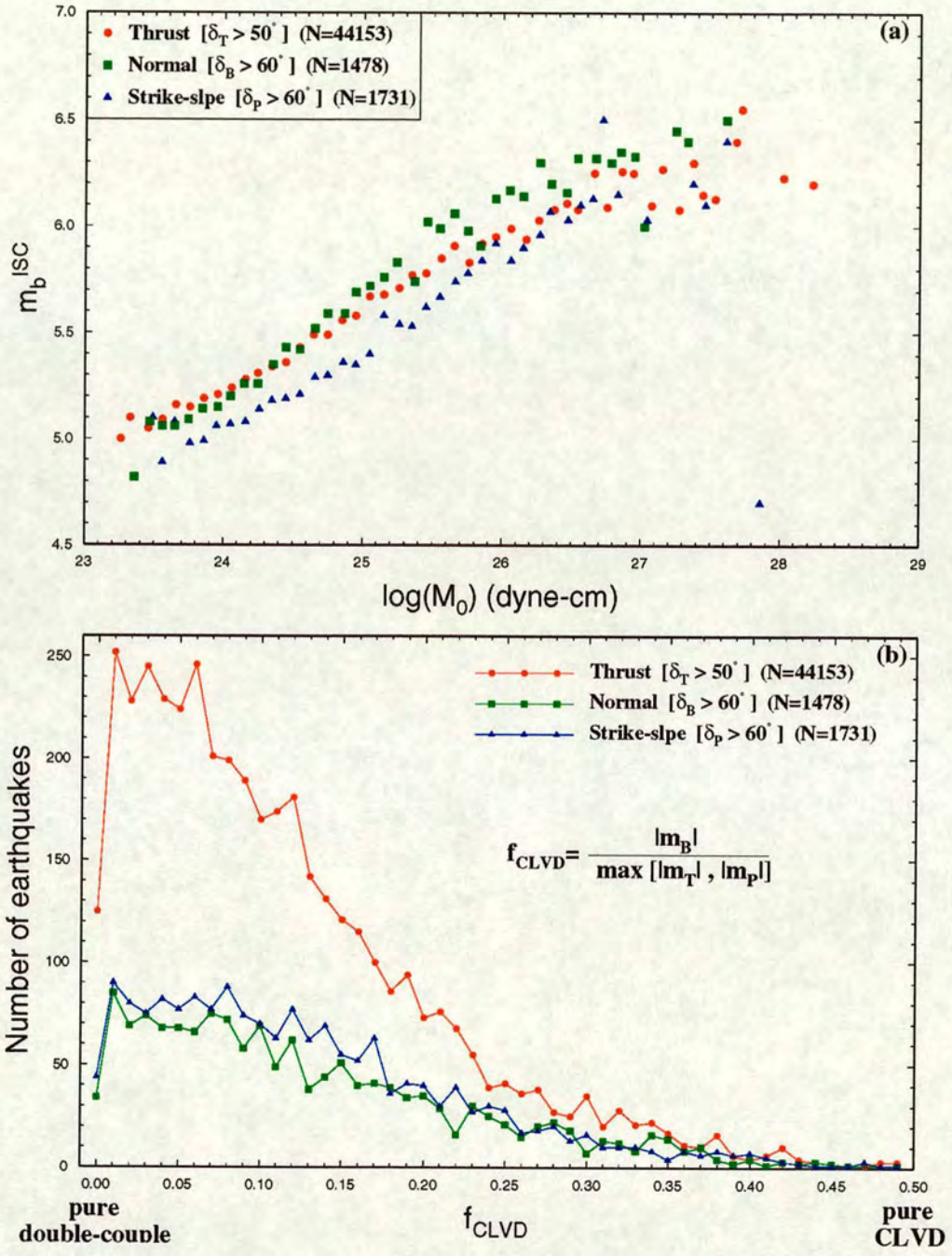

Figure 2.14. (a) Distribution of m_b^{ISC} averaged over 0.1-unit-wide intervals of $\log_{M_0}$ for earthquakes with different focal mechanisms. (b) Distribution of f_{CLVD}. δ_T, δ_B and δ_P are the dip angles of T, B, and P axis of focal mechanism respectively. Mechanisms of earthquakes were characterised as thrust, normal or strike-slip in terms of the dip angles with respect to horizontal of their T, B, and P axis. The compensated linear vector dipole ratio f_{CLVD} measures how different the source is from a "pure" double-couple source. m_T, m_B, and m_P are the largest, intermediate, and smallest principal moments, respectively.

$M_s : m_b$ due to attenuation, earth structure, the effect of tectonic strain release accompanying explosions. Many authors give a linear relationship between M_s and m_b. The coefficients of this relationship contain a large scatter because of structure variation near source, near receiver, and variation in analysis methods. For a different type of empirical relationship between M_s and m_b (earthquakes and explosions) see Båth (1981) and Nowroozi (1986).

Examination from the viewpoint of the discrimination of earthquakes and explosions in the ISC and NEIC Catalogues shows that respectively about 0.7% and 0.8% of reported earthquakes used in Figures 2.6a and 2.6b are located to the right of the discrimination line formulated by Nowroozi (1986):

$$m_b = 0.595M_s + 2.872 \tag{2.31}$$

This means that around 0.7% of the world earthquakes with $h < 50$km for which M_s values are available may be misidentified as explosions if other criteria were not used as a discriminant. The above discriminant line is marked in Figures 2.6a and 2.6b. Nowroozi (1986) derived the equation (2.31) as a discriminant line by analysing discriminant functions in population of 83 explosions and 72 earthquakes in Eurasia. Any point on this line has a 50% probability of being an earthquake or an explosion.

Figure 2.15a shows all the earthquakes that are identified as explosions using ISC magnitudes and Nowroozi's decision line. Because in this Figure ISC data are not compared with NEIC data, all earthquakes with a computed depth $h \leq 60$ km were included. There are 181 earthquakes (0.82%) in Figure 2.15a out of a total of 22,080 ISC determinations with $h \leq 60$ km. The worldwide distribution of these "anomalous" earthquakes is shown in Figure 2.15c; most are located in subduction zones. Most earthquakes ($\sim$ 80%) occur at or near subduction zones, and subduction-related events dominate the Catalogue even though trenches cover a relatively small fraction of the Earth's surface (Dziewonski and Anderson, 1983). A further clue to the problem of $M_s : m_b$ using ISC data is given by Figure 2.15b, which shows all events reported as explosions by the ISC (and as such have a zero depth constraint). For United States of America explosions, the "prime" determination is not that of the ISC, but these events nevertheless have been included in the Figure.

The question arises as to whether the absence of a depth correction in M_s is a major factor in these anomalous earthquake $M_s : m_b$ ratios; this cannot be the case for the explosions because their depths are all close to zero. Because Figure 2.15a includes earthquakes with an ISC computed depth of $\leq$ 60 km, the true depth of some of these events will be $>$ 60 km. This implies a failure to apply a depth correction to M_s for earthquakes with depths as great as (say) 80 km in some cases.

Figure 2.16a shows regression of M_s against depth for the anomalous earthquakes (without

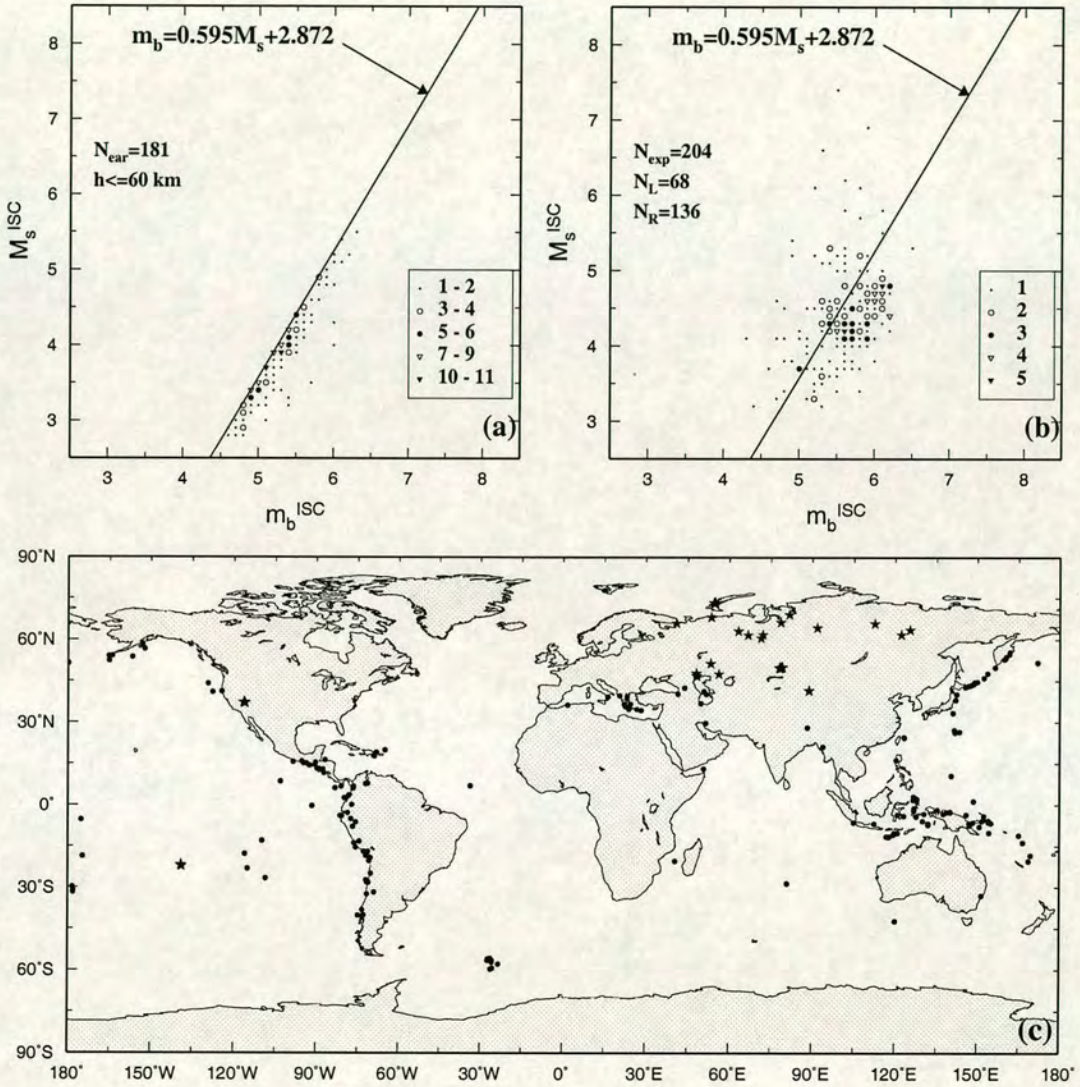

Figure 2.15. (a) Distribution of those events reported by the ISC as earthquakes which lie to the right of the discrimination line of Nowroozi (1986) in Figure 2.6a. (including only earthquakes with a reported depth $h \leq 60$ km.); (b) Distribution of all events reported as nuclear explosions in the ISC Catalogue for which M_s is available; and (c) location of these earthquakes and explosions. In (a) and (b) symbols indicate the number of data points as shown; in (c) circles and asterisks denote the events in (a) and (b) respectively. In (a) N_{ear} = number of earthquakes which lie to the right of the discrimination line. In (b) N_{exp} = total number of explosions; N_L = number of explosions which lie to the left of the discrimination line; N_R = number of explosions which lie to the right of the discrimination line.

attention to errors in either parameter). This gives a line of positive slope, but very close to zero, and with a high standard deviation. We would expect the calculated M_s to be lower towards greater depth in the absence of a depth correction (i.e., giving a negative slope in Figure 2.16a), this assumes that the true magnitude distribution is uniform over this depth range.

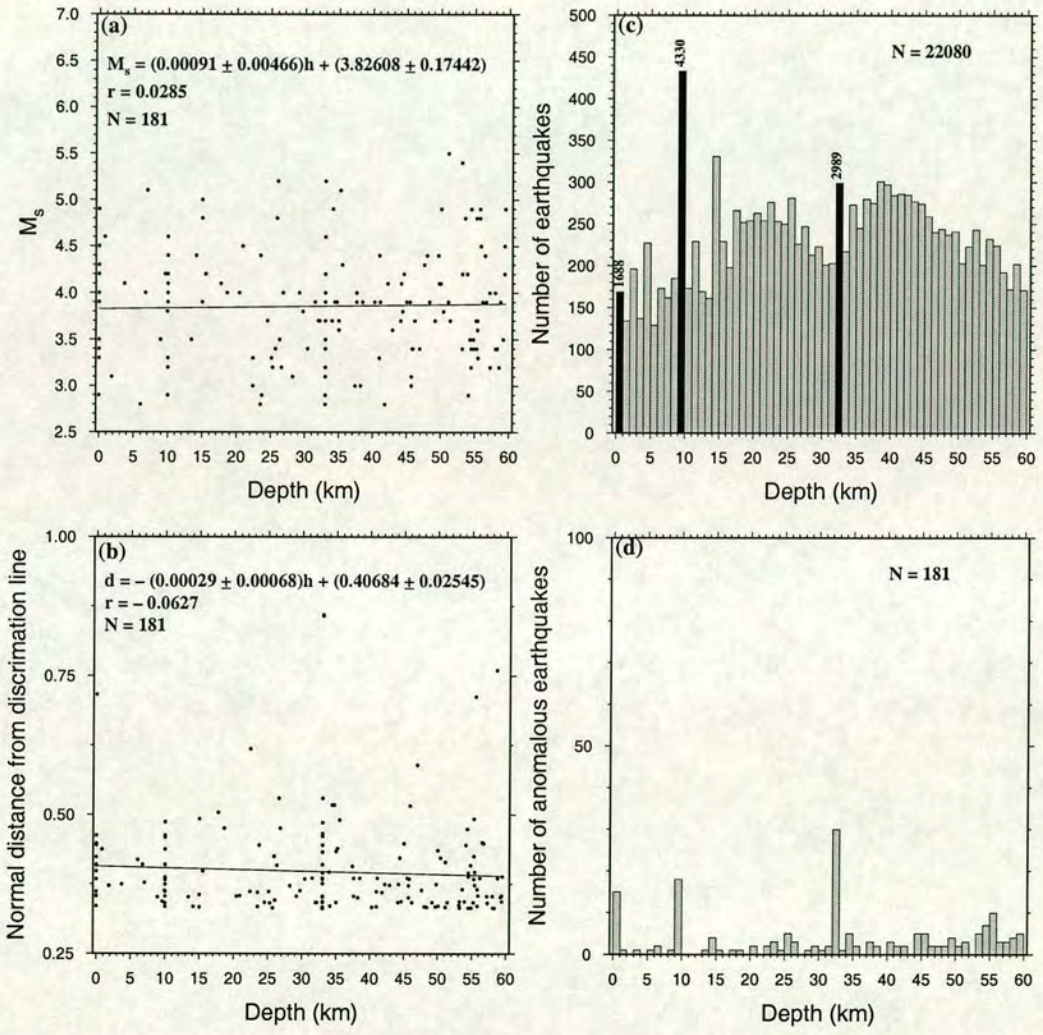

Figure 2.16. (a) M_s against depth for 181 anomalous earthquakes plotted in Figure 2.15a. (b) Normal distance from the discrimination line of Nowroozi ($m_b = 0.595M_s + 2.872$) versus depth, for these anomalous earthquakes. (c) and (d) show histograms for the total dataset and 181 anomalous earthquakes respectively. In (c) the scale of the black histograms is 10 times that of the gray histograms.

The regression of normal distance from the discrimination line against depth for these

anomalous earthquakes has a negative slope (Fig. 2.16b); however this value is not significantly different from zero. A histogram of these earthquakes against computed depth shows a steady increase in number with depth (Fig. 2.16d), whereas a histogram of all earthquakes for which M_s^{ISC} is available (Fig. 2.16c) differs in that the number decreases for depths greater than 40 km. This shows that there are more anomalous earthquakes for depths at which the correction would be larger. Therefore, it can be concluded that the absence of a depth correction is a contributory factor in making these earthquakes "anomalous" on the $M_s : m_b$ scale, but the main factor appears to be non-systematic.

The application of a depth correction to a given M_s value would always make events more earthquake-like, because observed surface wave amplitude always decreases with true focal depth. However, this would not assist discrimination by $M_s : m_b$, which must be achieved without a depth correction, because assignment of a non-zero depth itself implies prior identification of the source as an earthquake.

Since explosions tend to have a lower $M_s : m_b$ ratio than most earthquakes, the average distance of M_s observations will tend to be smaller for an explosion than for an earthquake with the same m_b. It follows that an inappropriate distance correction applied to surface wave amplitudes will introduce bias in $M_s : m_b$ ratios.

Kaverina *et al.*, (1996) showed that the global distribution of "creepex" (difference between M_s and the orthogonal regression of M_s on m_b) has an evident pattern of dominance of negative values in subduction zones, and positive ones in mid-ocean ridges. The name "creepex" was coined by combining two words: creep and explosion, which indicate the closeness of a seismic event by its spectral content either to an ultra-low-frequency (high, positive creepex) creep event or to a high-frequency (low, negative creepex) explosive one (Kaverina *et al.*, 1996).

2.14 Conclusions

Distributions of amplitude and period in the ISC Catalogue for surface-wave data show a predominance of "round number" values in A and T, which is evident from the peaks at multiples of 0.1 micron and 2 sec in amplitude and period respectively (due to precision of readings by analysts and speed of recording systems). The distribution of maximum azimuth gap for the same dataset and the total body-wave observations of 110,225 earthquakes showed that the majority of earthquakes have been recorded by seismic stations with a maximum azimuth gap of more than 120°.

A global comparison of magnitude determinations by the ISC and NEIC shows some small differences, but there are no systematic differences between the reported magnitudes of ISC and NEIC. Comparison of depth determinations by these two agencies shows that in the ISC

Catalogue, depths equal to 33, 10, and 0 km are poorly determined and dominated by artificial depth assignments, whereas in the NEIC Catalogue only depths equal to 33, and 10 km are dominated by artificial depth assignments. This will have an effect on the depth bias in m_b, slightly different in both cases.

Examination of frequency magnitude density for distribution of body-magnitude and surface-wave magnitudes showed that the standard deviation of $\overline{m_b}$ of all dataset is less than that for $\overline{M_s}$. The distribution of m_b values is smoother than those for M_s values in the ISC dataset (see Fig. 2.10). Also, frequency-magnitude density distribution for body-wave magnitudes is apparently symmetrical, but frequency-magnitude density of M_s values is asymmetrical. However, formal tests show that the m_b distribution is not symmetric.

Plotting m_b against $\log M_0$ for earthquakes with different source mechanisms shows that due to radiation pattern, the m_b values of earthquakes with strike-slip mechanism are underestimated by 0.2–0.3 magnitude units in comparison with those from normal and thrust mechanisms.

Examination of $M_s : m_b$ for ISC data has revealed some anomalous earthquakes which plot as explosions according to the $M_s : m_b$ discriminant when ISC magnitudes are used. However, the regression of M_s against depth for these anomalous earthquakes gives a line of positive slope (0.0091 ± 0.00466 error at 1 SD.), although it is expected that the average M_s would be lower at $h = 60$ km than at zero depth. The number of anomalous earthquakes according to the $M_s : m_b$ criterion increases towards increasing depth. It is therefore concluded that the absence of a depth correction is a contributory factor in causing these anomalous values, but the main factor appears to be non-systematic.

Chapter 3

Correction of distance calibration function for M_S determination

3.1 Introduction

Magnitude scales are logarithmic because the observed seismic-wave amplitudes from earthquakes varies enormously. A unit increase in magnitude corresponds to a 10-fold increase in amplitude of ground displacement equivalent to a 30-fold increase in radiated energy. Magnitudes are typically obtained by averaging observations from multiple stations to overcome amplitude biases caused by radiation pattern, directivity, and anomalous path properties, or other factors (see section 2.9). For determining magnitude from observations at non-standard distances, $\log(A/T)$ observations must ideally be calibrated to give the same value for earthquake size over all distances.

All empirical formulae for the M_s correction function $B(\Delta)$ include only the effects of geometrical spreading and anelastic attenuation. They commonly assume that the ratio of $\frac{A}{T}$ is independent of azimuth, and that there is a linear relation between $\log\left(\frac{A}{T}\right)$ and $\log \Delta$. However, the actual relationship between the two quantities $(\log(A/T), \log \Delta)$ is not linear, according to the theory of propagation of seismic waves, so equations (2.5) – (2.8) should be regarded as approximations leading to potential biases as a function of epicentral distance.

In this chapter the bias in M_s due to the use of the $B(\Delta)$ correction function is investigated, and some theoretical points are highlighted. The ISC global dataset is used to derive an optimum M_s distance-correction function, first assuming the empirical '$\log(\Delta)$' distance dependence of conventional magnitude scales, and secondly after allowing for those parts of the distance dependence that are known from theory. These approaches are compared, both with each other and with other published work. A new formula for M_s determination at distances $\Delta < 20°$ and $\Delta > 160°$ is examined. Also, the effect of the seismograph response on

M_s determination is discussed, and station corrections are determined using magnitude residuals. Then some remaining sources of scatter and bias, for example due to absence of depth correction, station correction, and effect of different paths in M_s are mentioned. The new M_s distance calibration function developed in this chapter has been published by Rezapour and Pearce (1998).

3.2 Bias in M_s due to inadequate distance calibration function

To investigate the effect of distance on M_s determination, the individual station magnitudes (M_s^{STA}) are determined from ISC Bulletin data using the Prague formula, for earthquakes with a published event magnitude (M_s^{ISC}) equal to 4, 4.5, 5, 5.5, 6, and 6.5 (M_s^{ISC} is essentially arithmetic mean of M_s^{STA} values over contributing stations). There are 851, 1383, 1039, 519, 229, and 82 earthquakes with estimated M_s of 4, 4.5, 5, 5.5, 6, and 6.5 respectively, and 89.5% of the measurements contributing to these data are from the vertical component. The difference ($M_s^{ISC} - M_s^{STA}$) is shown for these data in Figure 3.1. No attempt is made to reduce bias either by excluding poorly-recorded earthquakes or by further limiting the distance range, because I wish to illuminate, rather than obscure any factors that contribute to M_s values calculated by the ISC.

The differences in magnitude value established for waves of the same type at different stations are mainly due to different local conditions at the station, path effects, source effects, and instrumentation. In Figure 3.1 the slope of all regression lines is negative, which means that $M_s^{ISC} - M_s^{STA}$ decreases with increasing distance. In other words M_s^{STA} for larger distances is overestimated and for closer distances is underestimated. Confirming the results of Herak and Herak (1993), this result indicates that M_s values obtained by the Prague formula are significantly distance-dependent, and that the numerical value of the constant 1.66 in the Prague formula is too large.

The regression lines in Figure 3.1 also show a systematic increase in negative slope with increasing magnitude. There are several possible reasons for this. First, the change in slope could arise from the different distribution of observations with distance at different magnitudes. If the distance term were correct, then all "ideal" M_s^{STA} values for earthquakes of the same magnitude would lie on a horizontal line ($M_s^{ISC} - M_s^{STA} \approx 0$), so that their mean ($M_s^{ISC}$) for any earthquake of the same released energy, and hence all values of $M_s^{ISC} - M_s^{STA}$, would be equal. Any error in the distance term (whether linear or non-linear in $\log \Delta$) would cause M_s^{ISC} to depend on the distribution of M_s^{STA} with distance, causing a scatter in residuals $M_s^{ISC} - M_s^{STA}$. The systematic difference between station distance distributions at each magnitude would then cause a difference in the slope of the regression lines drawn through values of $M_s^{ISC} - M_s^{STA}$ at each magnitude. It follows that, when the correct value of the constant in

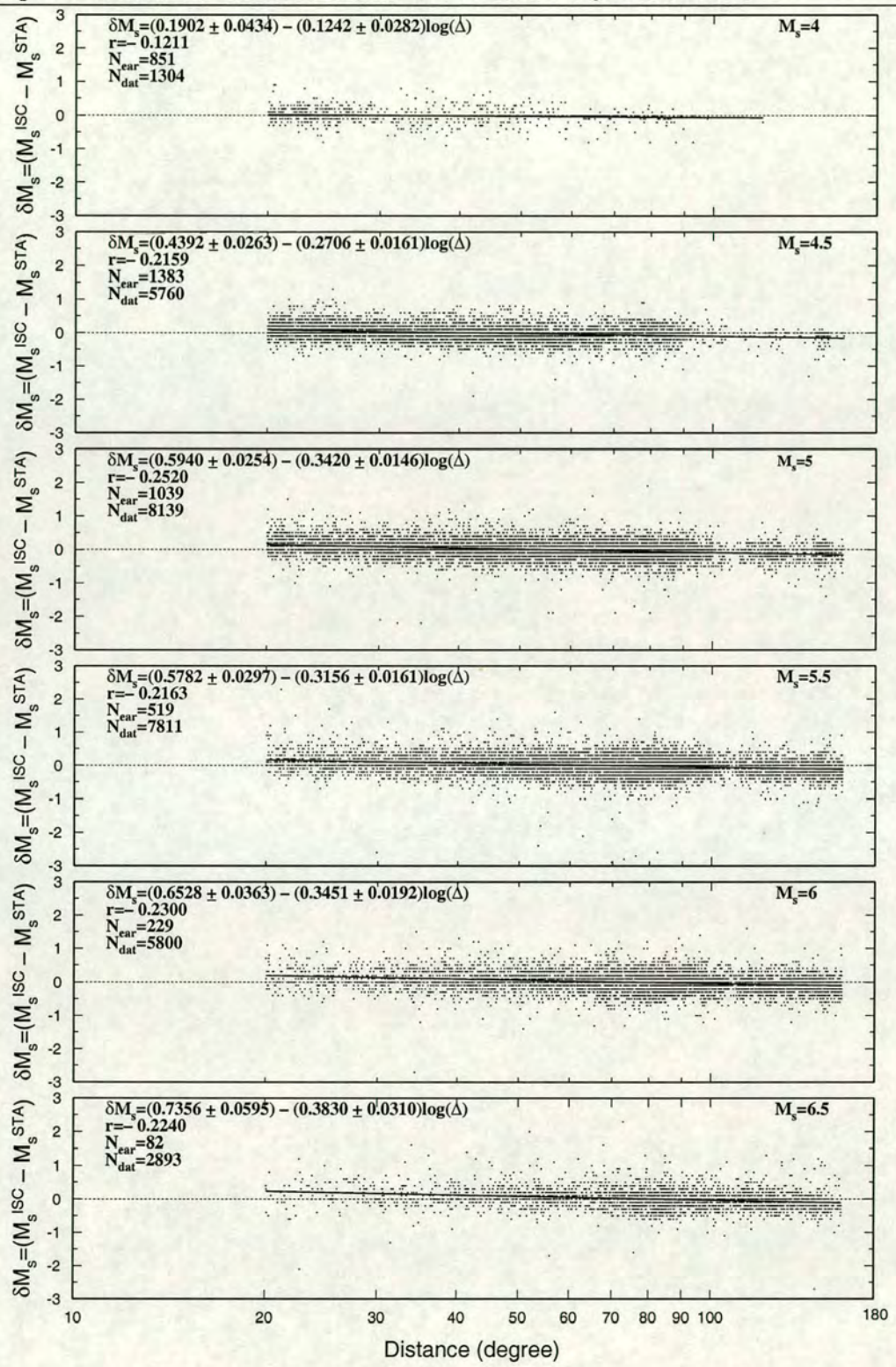

Figure 3.1. Deviation of individual station magnitudes from average magnitude, against distance for earthquakes with M_s^{ISC} equal to 4, 4.5, 5, 5.5, 6, and 6.5, plotted as reported by the ISC from 1978 to 1993 (only earthquakes with $h \leq 60$ km). N_{ear}=number of earthquakes, r=correlation coefficient, and N_{dat}=number of station records.

$\log \Delta$ is applied, any non-linear effect in $\log \Delta$ can be revealed, and once an adequate correction is applied, any true dependence of the distance correction on magnitude can be isolated.

Secondly, M_s^{STA} values close to the maximum detection distance may be biased in favour of sensitive stations ($M_s^{ISC} - M_s^{STA}$ low) while for large earthquakes, the closest observations of M_s^{STA} may be biased in favour of less-sensitive stations because of instrument saturation. These effects would cause similar slope changes to those observed in Figure 3.1. This is investigated by replotting Figure 3.1 using mean values of $M_s^{ISC} - M_s^{STA}$ for data averaged in equal increments (1-degree) of distance in Figure 3.2. At each magnitude any curving downwards or upwards of those points near to the maximum and minimum of the distance range was examined. There is some evidence of this curvature at the upper distance limit for M_s =4 and M_s =4.5, and possibly at the lower end for M_s =6.5. However, it can be concluded that the effect itself is insufficient to contribute significantly to the changes in slope observed in Figure 3.1.

Thirdly, it may be that the required distance correction term is truly magnitude-dependent, as a result of the dependence of the source spectrum on source size and duration, the variation with period T of different instrument responses, or a failure of the A/T term to compensate fully for these effects when determining M_s^{STA}. It is not possible to distinguish between this and the first possibility until the optimum value for the $\log \Delta$ correction has been determined.

In all the graphs of Figure 3.1 it is clear that, due to the P-wave shadow zone, the number of stations reporting to the ISC with epicentral distances between 100° and 120° is less than for other epicentral distances. The histogram of Figure 3.3 illustrates a limitation implicit in surface wave observations in the ISC and most other agencies. Although the ISC will accept unassociated surface wave observations, in practice a surface wave is usually reported only if a direct P-wave has already been identified. When the station is located in the shadow zone, the P-wave information is not usually reported; consequently neither is the surface wave. (The distribution of body wave observations is also shown in Fig. 3.3.) It follows that the form of the frequency-distance relation for single-station surface waves used in the determination of M_s is dominated by the structure of the body-wave amplitude-distance curve. The core shadow-zone, PKP amplitude peak and other features of the curve are closely reproduced, and this modulates the true surface-wave amplitude-distance effect, which tilts the distribution down towards increasing distance. A large proportion of data are located between Δ = 70° and 90°. This observed concentration is mainly due to the larger number of stations per unit distance at epicentral distances close to 90°, and to some extent on the non-random pattern of source-station distances over the Earth.

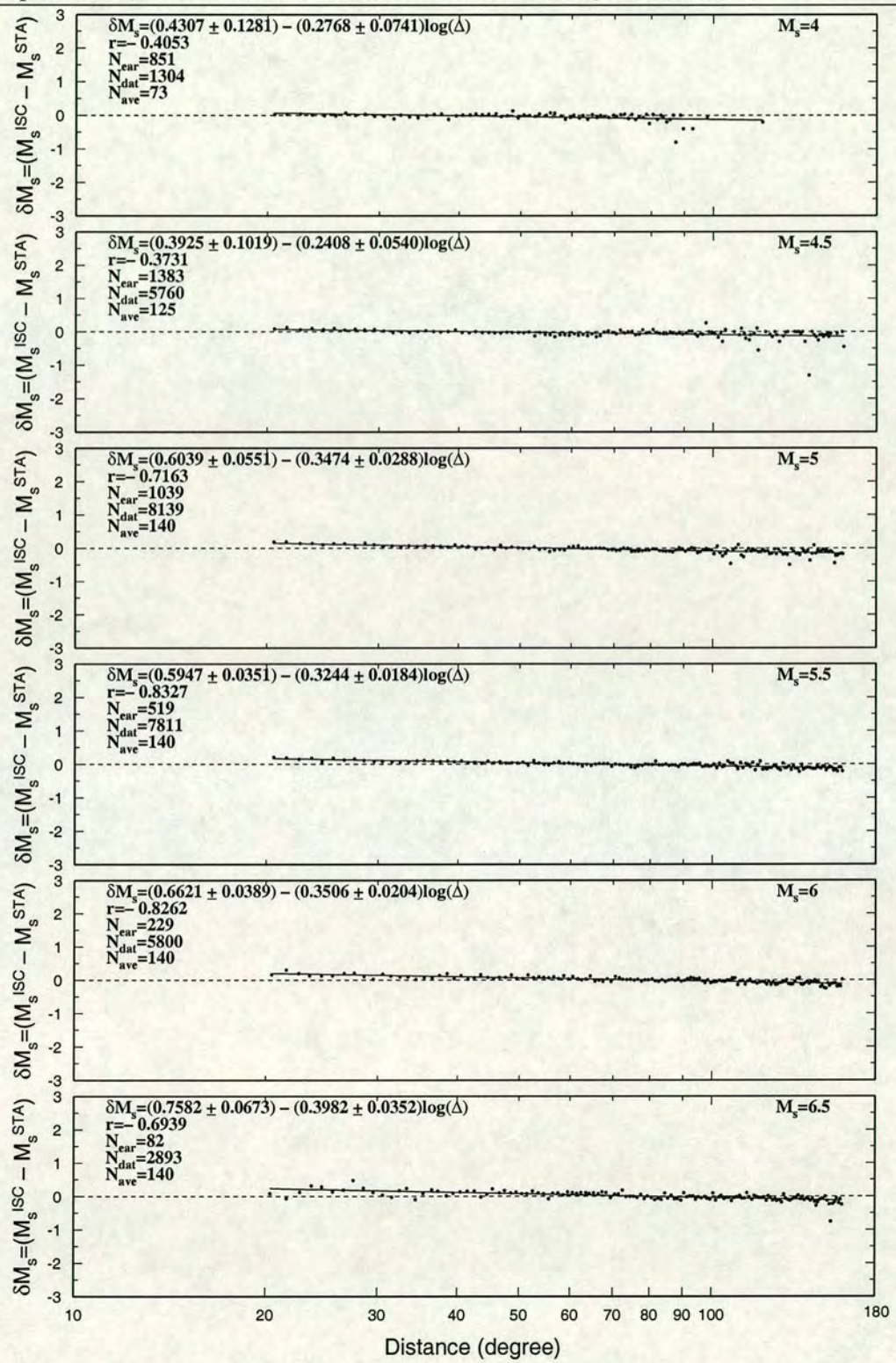

Figure 3.2. Distribution of averaged deviation ($\delta M_s = M_s^{ISC} - M_s^{STA}$) over 1-degree-wide intervals against distance for earthquakes with M_s^{ISC} equal to 4, 4.5, 5, 5.5, 6, and 6.5, as reported by the ISC from 1978 to 1993. N_{ear}=number of earthquakes, r=correlation coefficient, N_{dat}=number of individual station records and N_{ave}= number of data points after averaging over 1-degree intervals.

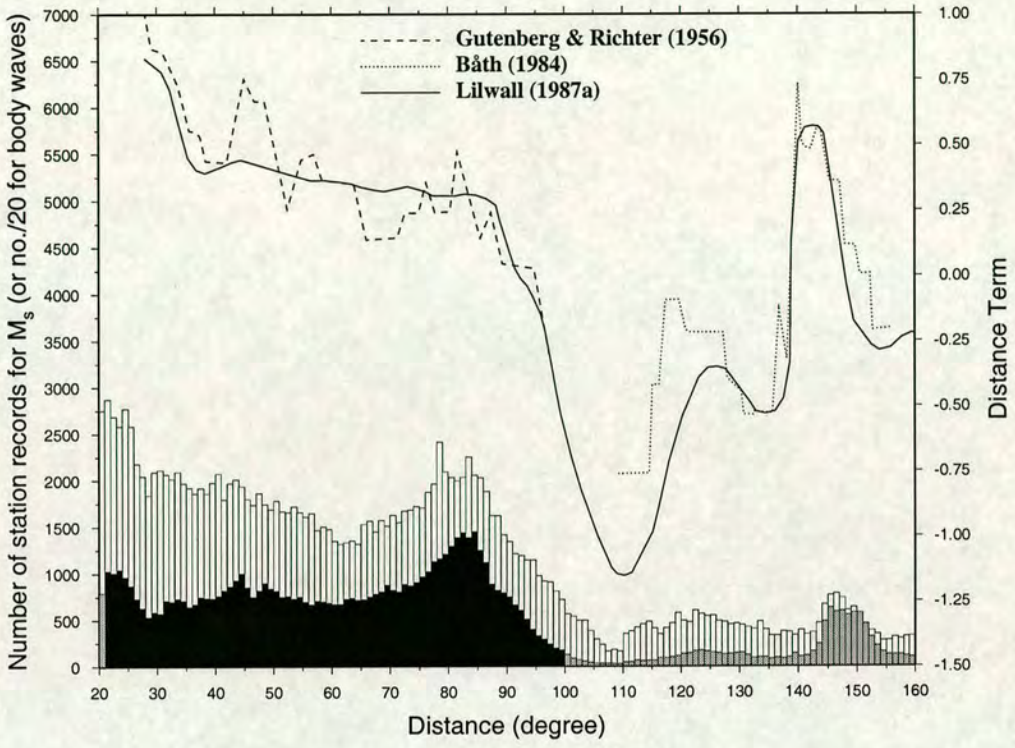

Figure 3.3. White histogram shows epicentral-distance distribution of 166,733 station records used in the M_s^{ISC} determination for 22,080 earthquakes with ISC depth $\leq$ 60 km, between 1978 and 1993 (left scale). This is overlain by a histogram showing the epicentral distance distribution of reported short period P-wave amplitudes during the same period. This is shown in black for the range $21° \leq \Delta \leq 100°$ which is used for m_b determination (1,267,548 station records for 110,225 earthquakes), and for other distances in grey (349,909 station records for 67,265 events). For this histogram multiply the left scale by 20. The white and black histograms both exclude records outside the period used for the respective magnitude determination. Smoothed and unsmoothed published body-wave amplitude-distance curves are shown for comparison (right scale).

3.3 Use of theoretical distance corrections

The second and subsequent terms on the right of equations (2.5) to (2.8) attempt to correct individual observations for effects other than the earthquake strength, to ensure that the magnitude database is internally consistent, and consistent with other magnitude scales. Okal (1989) considered theoretical issues of magnitude corrections in some detail. He compared a theoretical distance correction with that of the Prague formula, and found that the difference between

these corrections never exceeds ± 0.05 magnitude units for $20° < \Delta < 150°$. Okal found that, compared with the theoretical distance correction, the Prague distance correction overestimates M_s by between 0.02 and 0.04 magnitude units in the distance range 20° to 110°. Nevertheless, he concluded that the distance correction of the Prague formula was adequate except at very short distances.

None of the equations (2.5) to (2.8) incorporate corrections that are theoretically predicted, despite the fact that the main contributions to both distance and depth corrections are known from seismological theory, as pointed out by Nuttli (1973). Theoretically the distance correction term is not logarithmic with distance, so there is a limit in the distance range over which the conventional correction can be applicable. This explains, at least in part, the difficulties with previous M_s distance correction terms at short ($\Delta \leq 20°$) and very long ($\Delta \geq 140°$) distances. More importantly, in order to isolate those contributions to magnitude residuals which are unexplained, it is first necessary to remove correctly those components whose contribution is predictable from theory.

For a spherical earth, and assuming that the wavelength is small compared with the Earth's radius, the distance dependence of Rayleigh wave amplitude $A(\Delta, T)$ is given by (see e.g., Marshall and Carpenter 1966):

$$A(\Delta, T) \propto \Delta^{-\frac{1}{2}} (\sin \Delta)^{-\frac{1}{2}} \exp(-\pi^2 E \Delta / 180 QUT), \tag{3.1}$$

where Δ is the distance in degrees between source and receiver, U is the group velocity (which is assumed to increase monotonically with period T), E is the Earth's radius, and Q is the path-averaged apparent absorption coefficient for surface waves of period T. Here the three terms represent respectively the contributions of dispersion (Ewing *et al.*, 1957, p. 164), geometrical spreading on the surface of a sphere, and anelastic attenuation. For an observation at a known distance and period, this formula has only two unknowns—-the product QU and the constant of proportionality. Near a group velocity minimum (corresponding to an Airy-phase) the first term becomes $\Delta^{-1/3}$ (Ewing *et al.*, 1957, p. 165). Hence the correction for dispersion depends upon whether or not the measured amplitude is at a period close to a group velocity minimum.

Thomas *et al.* (1978) examined the fit of a distance correction function of this form, and found that the Airy-phase dependence better fitted observations, which suggested that most of their observations were made from the Airy-phase. However, their data are restricted to stations of the Long Range Seismic Measurement (LRSM) programme. Douglas *et al.* (1981b) studied this in more detail and were unable to discriminate between non-Airy-phase decay and Airy-phase decay from the statistics of their regression lines.

Herak and Herak (1993) also considered a theoretical correction similar to equation (3.1), but they assumed non-Airy-phase observation in their dispersion term. Also, the formula they

proposed did not include terms of a form corresponding to the theoretical corrections. Imposition of a distance dependence of the form of equation (3.1) does not increase the number of unknown constants to be determined by least-squares fitting of observations beyond two. In the next section a distance correction function based on this form is determined.

None of the established surface wave magnitude formulae include a depth-dependent correction, yet the effect of depth is known from theory to reduce Love-wave amplitude by about an order of magnitude between 0 and 60 km, (e.g., Panza *et al.*, 1989). This corresponds to the range of depths over which surface wave magnitudes are determined by the ISC. It appears that failure to include such a correction results in general from the poor accuracy of depth determinations; not that the effect of depth is insignificant.

3.4 Correction of calibration function

3.4.1 Empirical distance correction function

To re-examine the calibration function $B(\Delta)$ in equation (2.9) the method of Herak and Herak (1993) is used, but for the whole ISC Catalogue data and using different conditions to their study. In this study the parameters (α, β) of the regression line of station magnitude (M_s^{STA}) against epicentral distance as $M_s = \alpha + \beta \log \Delta$ are determined, for each earthquake with three or more stations contributing to the computation of M_s^{ISC} (event magnitude).

In the regression analysis for some earthquakes, the regression line of station magnitudes against epicentral distances have a steeper slope (β), also for some earthquakes the predicted Root Residual Mean Square Error (RRMSE) values are large. Therefore, to remove these type of data (as outliers) from procedure of the empirical distance correction function, the data are selected. To correct the calibration function $B(\Delta)$ those earthquakes for which the regression line of station magnitudes against distance has a slope of between -2.5 and $+3.5$, and with a RRMSE less than 0.5 magnitude units are selected. Figure 3.4 shows the distribution of regression-coefficient (β) and regression-constant (α) for 9,966 so selected earthquakes. As Figure 3.4a shows, about 76.8% of regression-coefficients (β^j) are positive; this means that calculated magnitude values increase towards increasing distance.

As Figure 3.3 shows, data are concentrated around $\Delta = 83°$, so the reference magnitude is defined as:

$$M_{83}^j = \alpha^j + \beta^j \log(83°), \tag{3.2}$$

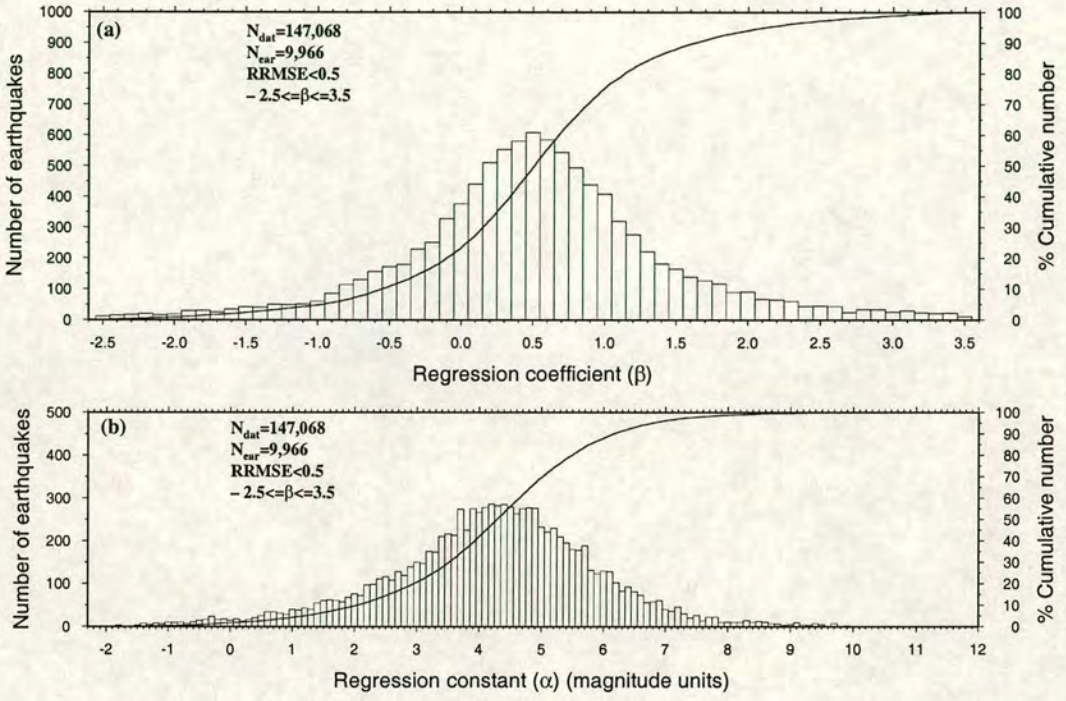

Figure 3.4. The distribution of regression parameters obtained from magnitude against distance, for 9,966 earthquakes with $-2.5 \leq \alpha \leq 3.5$, and Root Residual Mean Square Error (RRMSE) less than 0.5. (a) For regression-coefficients (β^j). (b) For regression-constants (α^j).

for the jth earthquake ($j = 1 \ldots$ 9,966). The difference between the individual station magnitude and the relevant computed M_{83}^j is given by

$$\delta M_i(\Delta) = M_i^j(\Delta) - M_{83}^j, \tag{3.3}$$

where, i is the ith reported M_s for the jth earthquake ($j = 1 \ldots 9{,}966, i = 1 \ldots N_j$). The results show that from 10,894 ($N_j \geq 3$) regression coefficients (β^j), only 2,728 are negative, so that 75% of the total dataset have a positive value. As Herak and Herak (1993) have pointed out, this indicates that M_s^{Prague} values are significantly distance-dependent; consequently the mean magnitude obtained by averaging all reported magnitude values is not an unbiased estimate of the earthquake's strength, but depends on the distance distribution of contributing stations.

Equation (3.2) (i.e., the difference between individual station magnitude and the reference magnitude at $\Delta = 83°$) is plotted against epicentral distance for all data in Figure 3.5a. The

regression line is:

$$\delta M_s = (0.5051 \pm 0.0037) \log \Delta - (0.9689 \pm 0.0066), \tag{3.4}$$

so the modified Prague formula M_s^e (empirically corrected) becomes:

$$M_s^e = \log (A/T)_{max} + 1.155 \log \Delta + 4.269. \tag{3.5}$$

Regression of averaged observations (δM_s) over 1-degree intervals against $\log \Delta$ had no significant effect on these regression parameters, and as expected the correlation coefficient increases to about 0.98 in this case (see Fig. 3.5b). Histogram of distances of constituent observation is plotted in Figure 3.5c.

For $\Delta = 83°$ the Prague formula M_s equation (2.6) and empirical formula M_s^e equation (3.5) are equivalent, but for $\Delta = 20°$ equation (2.6) underestimates M_s by 0.31 whereas for $\Delta = 160°$ M_s is overestimated by 0.14 magnitude units. This result is not surprising; similar results have already been obtained by other workers such as von Seggern (1977), Thomas *et al.*, (1978), and Herak and Herak (1993). This study, which uses a much larger number of ISC data (from 1978 to 1993 over the full range of M_s^{ISC}), further emphasises the need to revise the Prague formula, which most agencies, including the ISC and NEIC, use to determine surface-wave magnitude. The value of the constant in equation (3.5) is dependent solely upon the choice of reference magnitude. It is now clear from Figure 3.5, as well as from theory of surface-wave attenuation with distance, that the correction is not linear in $\log \Delta$.

3.4.2 Empirical distance correction function with theoretical constraints

In order to devise a magnitude M_s^t which incorporates theoretically predicted constraints in the distance-dependence terms in equation (3.1), each A/T observation is corrected according to:

$$(A/T)_{corrected} = (A/T)_{observed} (K \Delta^{-\alpha} \sin^{-\frac{1}{2}} \Delta e^{-k\Delta})^{-1}, \tag{3.6}$$

where, α is either $\frac{1}{2}$ (non-Airy-phase measurement) or $\frac{1}{3}$ (Airy-phase measurement), and K and k are constants to be determined. M_s^t is defined as:

$$M_s^t = \log(A/T) - \log K + \alpha \log \Delta + \frac{1}{2} \log (\sin \Delta) + k(\log_{10} e)\Delta, \tag{3.7}$$

Because the constant of proportionality in the $\log \Delta$ term is not a free parameter, there are still only two constants to be determined, as for previous formulae. Therefore, equation (3.7) has also the same number of degrees of freedom as the Prague formula, and the regression coefficients of the two equations can be compared directly.

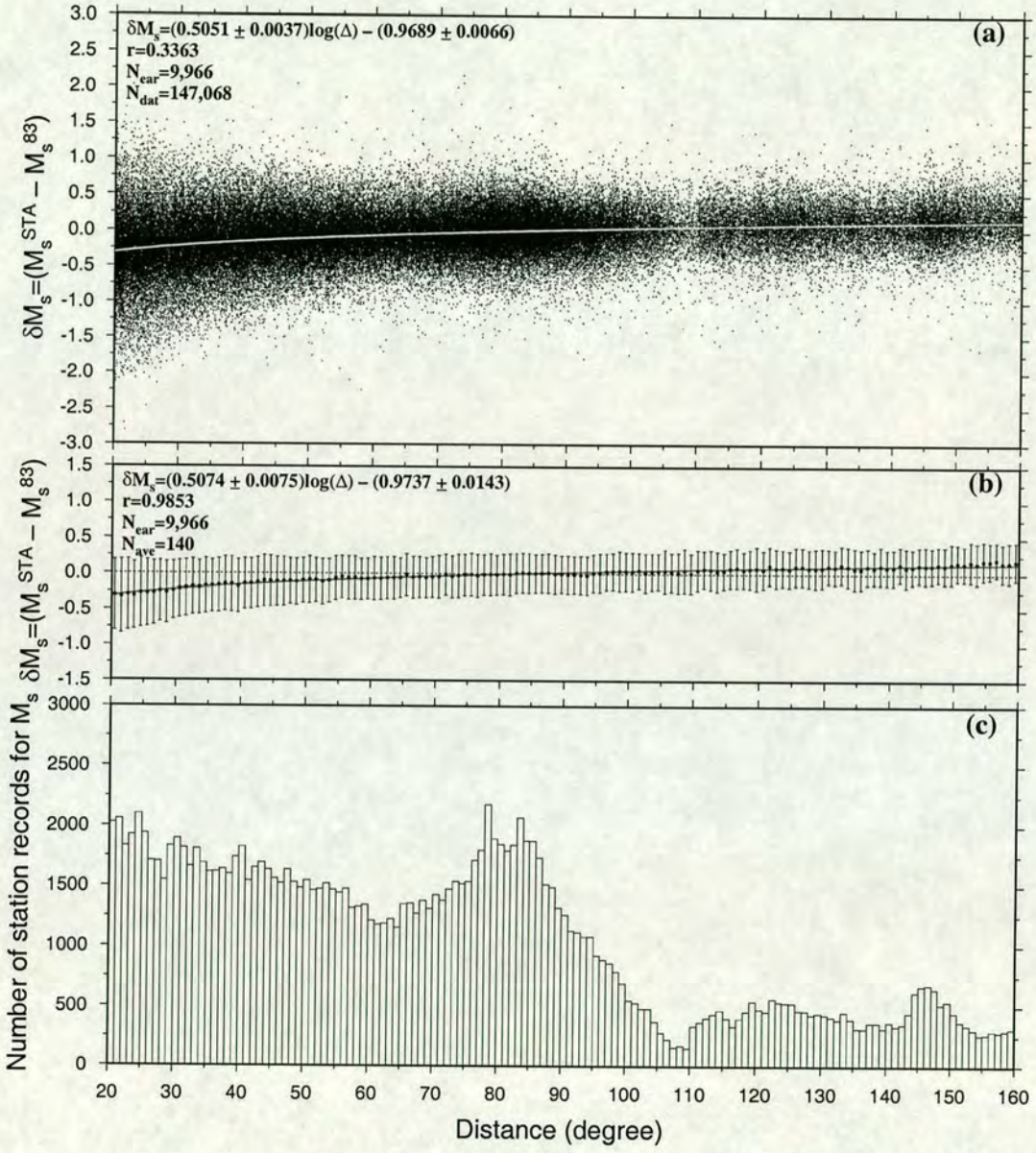

Figure 3.5. (a) Distribution of the differences between individual station magnitude and reference magnitude M_s^{83} against epicentral distance for 9,966 earthquakes. The plot includes those earthquakes for which at least three observations have been used, and for which the regression line of station magnitudes against distance has a slope of between -2.5 and $+3.5$, and with a Root Residual Mean Square Error (RRMSE) of less than 0.5 magnitude units. (b) Averaged δM_s in 1-degree bins with standard deviation against distance. (c) Histogram of distances of the constituent observations. In (a) and (b) r=correlation coefficient, N_{ear} =number of earthquakes, N_{dat}=number of station records, N_{ave} =number of data points after averaging over 1-degree intervals. In (a) the regression line (shown in white) is for δM_s against $\log \Delta$, and in (b) the regression line (solid line) is for averaged δM_s against $\log \Delta$, although the graphs are plotted linearly against Δ for clarity.

In order to estimate K and k I choose the total distance correction term for an individual observation as the difference between M_s^{ISC} for the corresponding earthquake, and $\log(A/T)_{station}$ for the individual observation. M_s^{ISC} is used because this is the best available estimate of M_s on the Prague scale. This distance correction was set to be the sum of the correction terms in equation (3.7), and rearrangement gives

$$M_s^{ISC} - \log(A/T)_{station} - \alpha \log \Delta - \frac{1}{2} \log (\sin \Delta) = k(\log_{10} e)\Delta - \log K. \qquad (3.8)$$

This should correspond to a straight line of slope $k(\log_{10} e)$ and intercept $\log K$ if the left hand side is plotted against Δ, and deviations from this straight line will represent additional effects not accounted for theoretically.

This procedure must be applied iteratively, replacing M_s^{ISC} by the average of the M_s^t values for each earthquake, $\overline{M_s^t}$, using equation (3.7) with K and k as determined. After three iterations no further reduction was seen in the mean deviation of data from the regression line. The iteration procedure was repeated using $\overline{M_s^e}$ values for each earthquake as the initial values, computed using equation (3.5). In this case no iteration was required to reach minimum deviation. Figures 3.6a and 3.6b show this relationship for all station data (152,539 records from 10,894 earthquakes in which more than two stations contributed in the network magnitude) with $\alpha = \frac{1}{3}$ and $\frac{1}{2}$ respectively. The regression lines are shown in white, and the regression parameters are also shown. This shows that there is an excellent linear trend of the form of equation (3.8) over all distances. The fit is equally good in Figures 3.6a and 3.6b, so it appears that it is not possible to resolve from the observed data whether Airy-phase or non-Airy-phase measurements predominate. A similar conclusion was drawn by Douglas *et al.*, (1981b). Okal (1989) suggested that the assumption of Airy-phase observations made by some authors is probably invalid at periods close to 20 sec. In reality, the mixture of continental, oceanic and mixed paths in global station magnitudes makes it difficult to make any prediction as to which, if either, type of observation will predominate within the period range of interest. However, the choice of α affects the value of k which is obtained, so the uncertainty in k must be increased to encompass the values which may be obtained with $\frac{1}{3} \leq \alpha \leq \frac{1}{2}$.

To examine the detail of the observed fit to the relationship represented in equation (3.8), Figures 3.6c and 3.6d, show the mean of data in Figures 3.6a and 3.6b respectively, averaged over each 1° increment in Δ. Although the deviations are small compared with the standard error of each point, it is clear that adjacent values are not independent, so that there are some details in the deviation which are systematic with distance. There is also a suggestion of an upward deviation for $\Delta < 30°$ in Figure 3.6d, which represents the only noticeable difference between Figures 3.6c and 3.6d. This suggests that at these close distances, Airy-phase measurements predominate (giving a straight line in Fig. 3.6c). Therefore $\alpha = \frac{1}{3}$ was chosen,

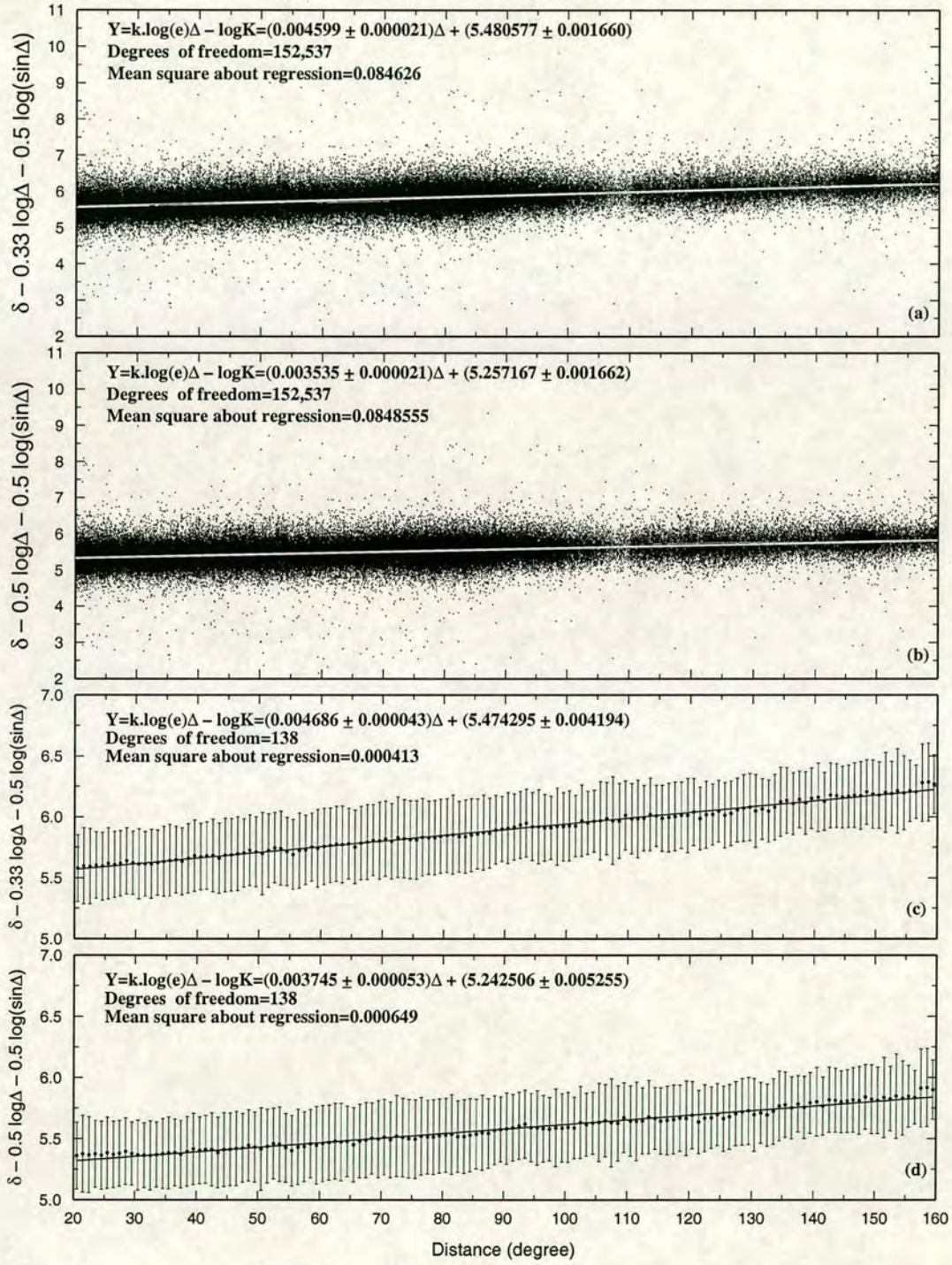

Figure 3.6. (a) The distance correction with the theoretically predicted parts removed assuming Airy-phase dispersion, plotted against epicentral distance. (b) as for (a) but assuming non-Airy-phase dispersion. (c) and (d), as for (a) and (b) respectively but showing amplitude averaged in 1-degree bins with standard deviation. On all four graphs $\delta = M_s^{ISC} - \log(A/T)_{station}$.

implying the overall predominance of observations close to an Airy phase. The random scatter in Figure 3.6a about the regression line is greater than ±0.3 magnitude units. The absence of a depth correction does not directly affect the scatter in Figure 3.6 since these are differences between event-average and station measurements for individual events with the same source depth.

The value of K in equation (3.8) determines only the relationship between this and other scales, and it may be chosen to maximise consistency with them. The most compelling condition to impose would be equality at $\Delta = 20°$, to maintain consistency with M_L as originally intended by Gutenberg. However, this is unhelpful in practice because it would result in large corrections to the established scale over a large range of distances beyond 20°, and hence a large correction to most existing magnitude determinations. An alternative condition is to leave the constant as it is; this corresponds to an agreement with the Prague formula at close to Δ=83°. Although this value was originally chosen because it represents the distance with greatest data density, a more appropriate condition for scale comparison is to set the constant so that the sum-squares correction needed to all ISC event magnitudes so far determined is minimised, i.e., set K to $K - \delta$, where δ is chosen to minimise $\sum[M_s^{ISC} - (\overline{M_s^t} + \delta)]^2$ where the sum is over all earthquakes. Figure 3.7 shows $\sum[M_s^{ISC} - (\overline{M_s^t} + \delta)]^2$ against δ for ISC dataset. $\delta = 0.111$ was found (see Fig. 3.7a), so that the initial K value of 5.481 becomes $K = 5.370$. Therefore the final form of M_s^t formula becomes:

$$M_s^t = \log(A/T)_{max} + \frac{1}{3}\log(\Delta) + \frac{1}{2}\log(\sin\Delta) + 0.0046\Delta + 5.370. \qquad (3.9)$$

According to the regression coefficient, $k \log_{10} e$ (see Fig. 3.6a), k is equal to 0.01050 ± 0.00005 degree^{-1}, and assuming 20 sec surface waves with group velocity of $U = 3.6$ km/sec the globally-averaged apparent Q^{-1} becomes 0.00218 ± 0.00001. Since it is unclear whether Airy-phase or non-Airy-phase measurements predominate (and in general a mixture may be expected), the best estimate and true error of Q^{-1} must include the uncertainty introduced by changing α from $\frac{1}{3}$ to $\frac{1}{2}$. Then $Q^{-1} = 0.00192 \pm 0.00026$ ($Q \approx 500$) was obtained, which is slightly higher than $Q = 405$ (with 95 percent confidence limits of 700 and 285) found by Marshall and Carpenter (1966) for the Northern Hemisphere. Von Seggern (1977), and, Herak and Herak (1993) obtained somewhat higher values of $Q = 605 \pm 20$, and $Q = 704$ respectively, assuming $U = 3.5$ km/ sec for 20 sec Rayleigh waves. The value of $Q = 297$ used by Okal (1989) is much lower because it was calculated assuming the Prague constant 1.66.

To re-examine the distance dependence of M_s^t formula, i.e., equation (3.9), the difference $(M_s^t - M_s^{STA})$ was plotted in Figure 3.8 as in Figure 3.1 but using equation 3.9. In this case there are 787, 1567, 1085, 463, 185, and 81 earthquakes with estimated M_s^t of 4, 4.5, 5, 5.5, 6, and 6.5 respectively. (These numbers can be compared with numbers in Figure 3.1 (N_{ear}) i.e.,

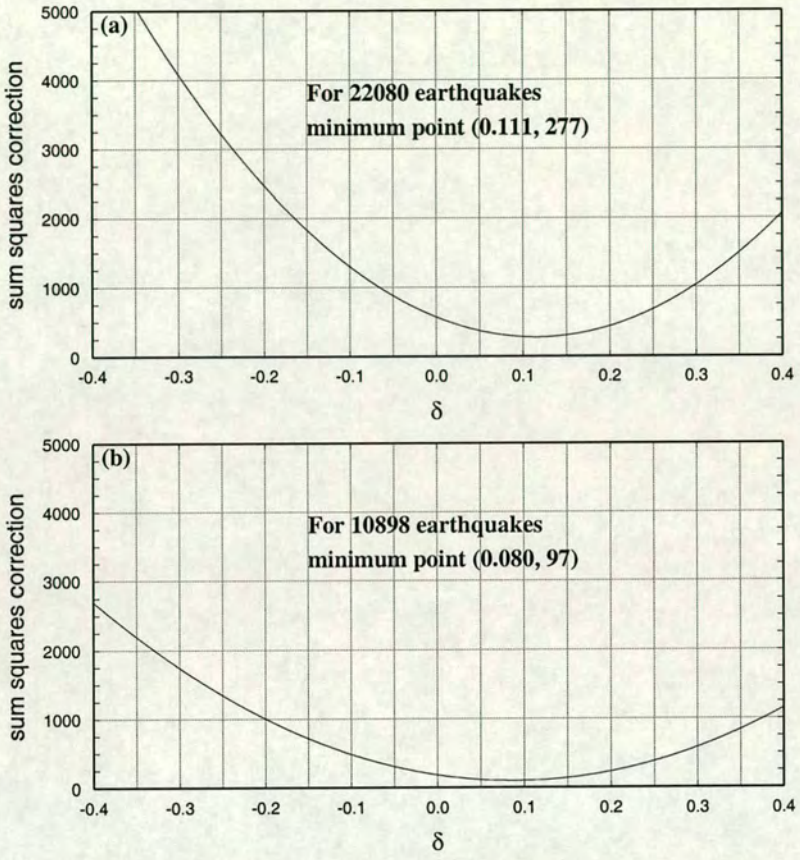

Figure 3.7. Distribution of $\sum[M_s^{ISC} - (\overline{M_s^t} + \delta)]^2$ against δ. (a) for all 22080 earthquakes. (b) for 10898 earthquakes in which more than three stations contributed in M_s^{ISC} or $\overline{M_s^t}$.

number of earthquakes with the same magnitude in the whole of the ISC Catalogue from 1978 to 1993).

The mean values of $M_s^t - M_s^{STA}$ were also plotted for data binned in equal increments of distance (1-degree-wide) in Figure 3.9. Both Figures 3.8 and 3.9 show that, when equation (3.9) is used, there is no longer any significant dependence of the regression line on magnitude—-it is horizontal at all magnitudes, which shows that there is not a true magnitude dependence in the theoretically-constrained distance correction (compare Figs. 3.8, and 3.9, with Figs. 3.1, and 3.2 respectively).

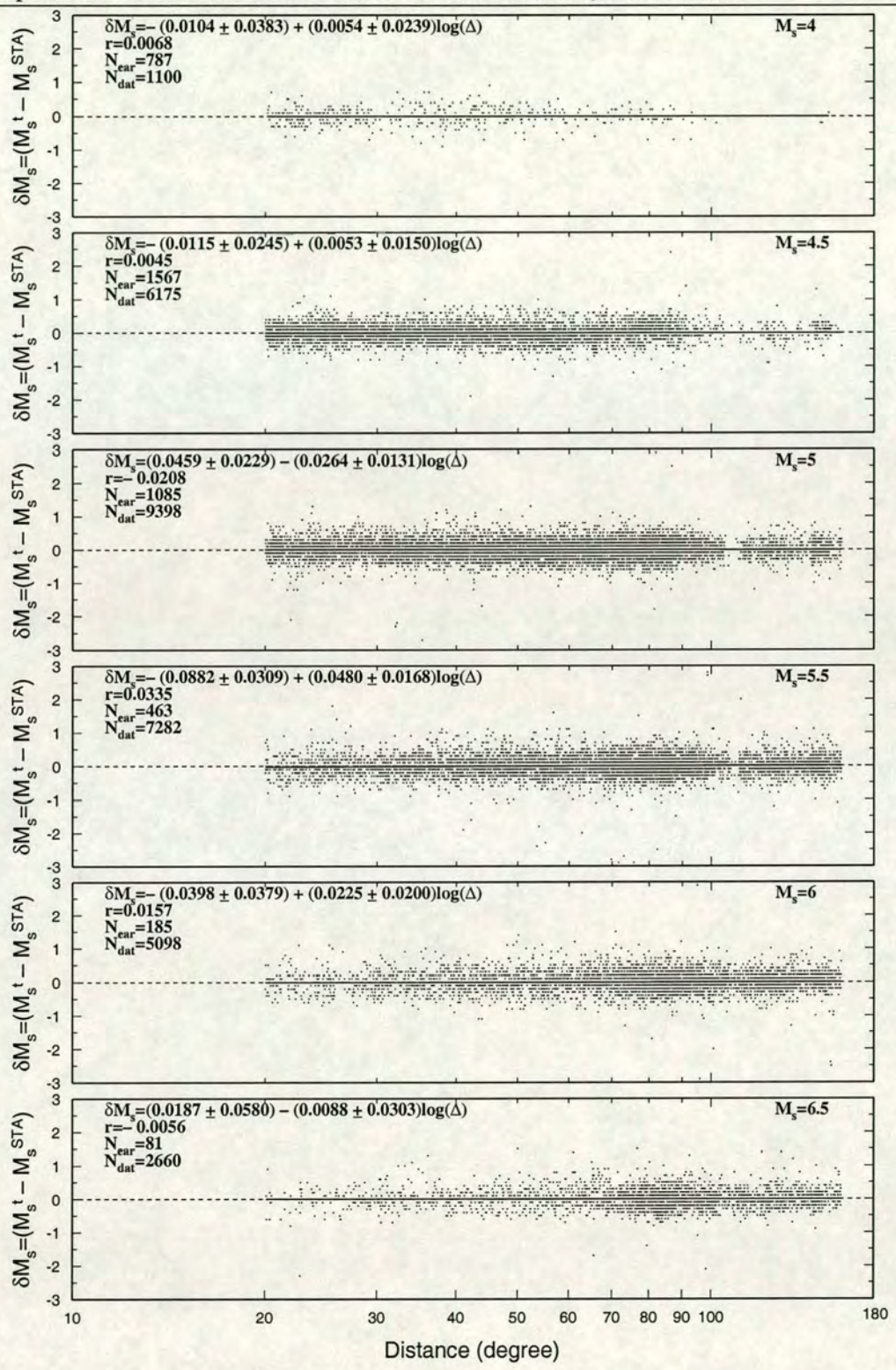

Figure 3.8. Deviation of individual station magnitudes from average magnitude, against distance for earthquakes with M_s^t equal to 4, 4.5, 5, 5.5, 6, and 6.5, which are estimated for the ISC from 1978 to 1993 by using equation 3.9. N_{ear}=number of earthquakes, r=correlation coefficient, and N_{dat}=number of station records.

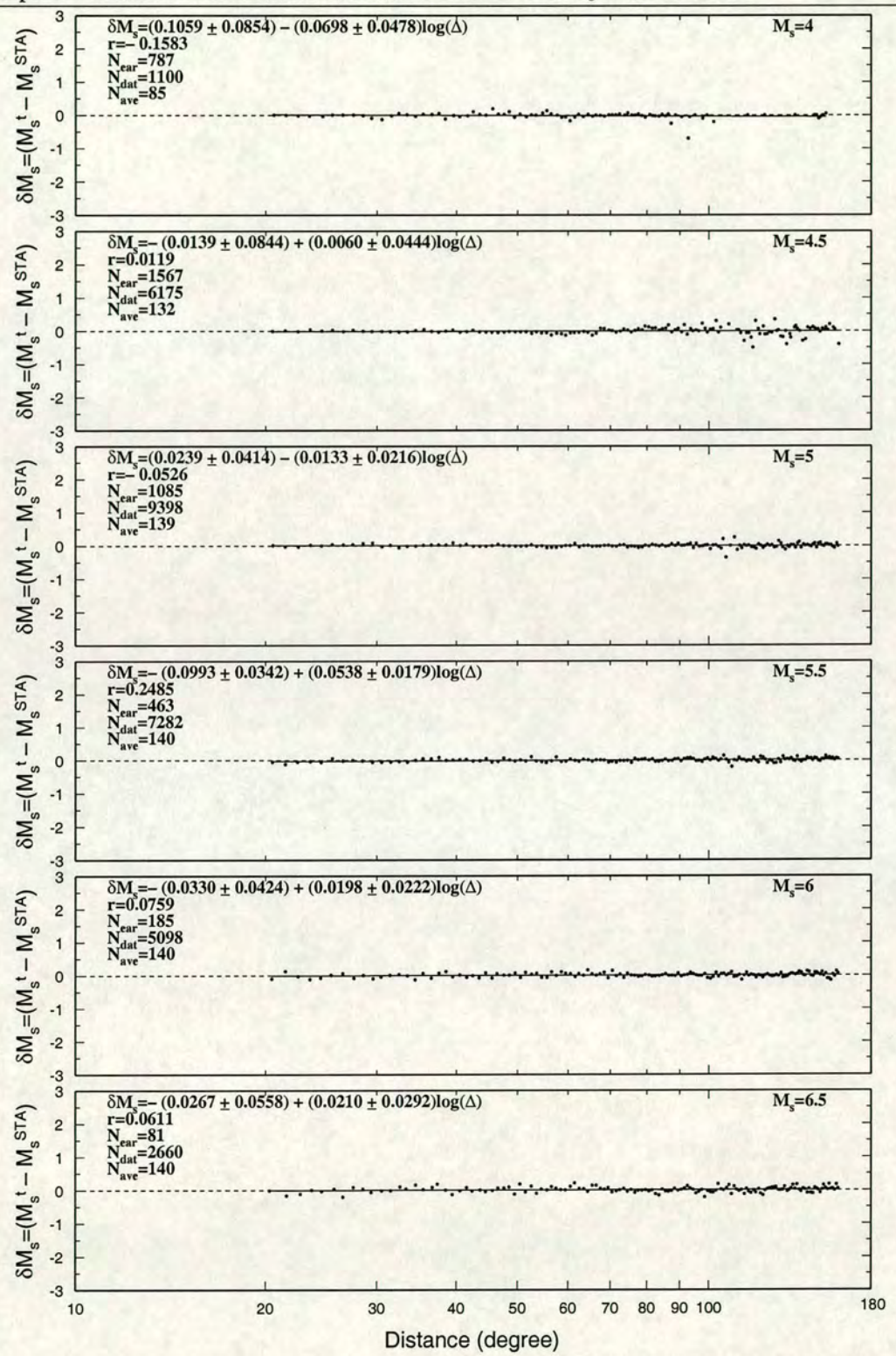

Figure 3.9. Distribution of averaged deviation ($\delta M_s = M_s^t - M_s^{STA}$) over 1-degree-wide intervals against distance for earthquakes with M_s^t equal to 4, 4.5, 5, 5.5, 6, and 6.5, which are estimated for the ISC from 1978 to 1993 by using equation 3.9. N_{ear}=number of earthquakes, r=correlation coefficient, N_{dat}=number of individual station records and N_{ave}=number of data points after averaging over 1-degree intervals.

3.5 Comparison of formulae for M_s determination

In Figures 3.10a and 3.10b the distance calibration $B(\Delta)$ of different empirical formulae for determining M_s at 20 sec period are compared, and in Figure 3.10c the differences between the distance corrections of M_s^e and M_s^t formulae (Eqs. (3.5) and (3.9) which were obtained in this study) and that of the Prague formula are shown. As, Figure 3.10c shows the calibration function $B(\Delta)$ of Prague formula through long range of distance i.e., 50° – 160° or $\Delta > 50°$ are greater than those for the M_s^t formula. This discrepancy is reversed for $\Delta < 50°$. In general large events are recorded at further distance, also the number of seismic stations per unit area can increase with increasing distance, in consequence the surface-wave observations at distance range 50° – 160° are more than observations at distance range 20° – 50°. Therefore, using the M_s^t formula for determination of surface-wave magnitude reduces the number of large magnitudes e.g., $M_s \geq 5.5$ in the dataset in comparison with using the Prague formula, although the number of small magnitudes e.g., $4.2 > M_s > 5.5$ increases. So, estimated b-value will be different.

The differences in the slope of the calibration functions of Gutenberg, Prague, Herak and Herak, and M_s^e must be due to differences in the type of data used to derive $B(\Delta)$. For example, Gutenberg (1945a) and Vaněk *et al.* (1962) used measurements made from horizontal components, whereas Herak and Herak (1993) used measurements from the vertical component. Here, both horizontal and vertical measurements are used, of which only a small fraction of data (11.8% and 10.8% for the first and second formulae respectively) are measured on the horizontal components. Horizontal component data may be either Love or Rayleigh wave amplitudes or a mixture of both. The specific quality factor for Love waves is less than for Rayleigh waves. So, if most of the data are Love wave amplitudes, a steeper slope is expected for the calibration function. Most importantly, to derive $B(\Delta)$ in M_s^e and M_s^t formulae a distribution of $\log(A/T)$ data used that ISC has used in its own magnitude determinations.

Some comment is required on the vertical position of each curve in Figures 3.10a and 3.10b, which is governed solely by the constant term in the respective formula. It was pointed out that this depends only on the condition used to establish a comparison between the scales. The Prague formula is related to the Gutenberg formula by putting $T = 20$ sec, then using a different constant. The Marshall and Basham formula has the form $1.66\log\Delta$ + constant for $\Delta > 40°$ and is approximately $0.8\log\Delta$ + constant for $\Delta < 25°$. The Herak and Herak formula is set equal to the Prague formula at $\Delta = 100°$ by definition. The M_s^e formula (equation (3.5)) is equivalent to the Prague formula at $\Delta = 83°$ because of different choice of reference magnitude (M_s^{83}). The M_s^t formula (equation (3.9)) has been chosen to require minimum change in a least-squares sense to existing ISC magnitudes as explained in the previous section. (from Figure 3.10 it is seen to equal M_s^{Prague} at $\Delta \approx 50°$, and to equal $M_s^{Gutenberg}$ at $\Delta \approx 130°$.)

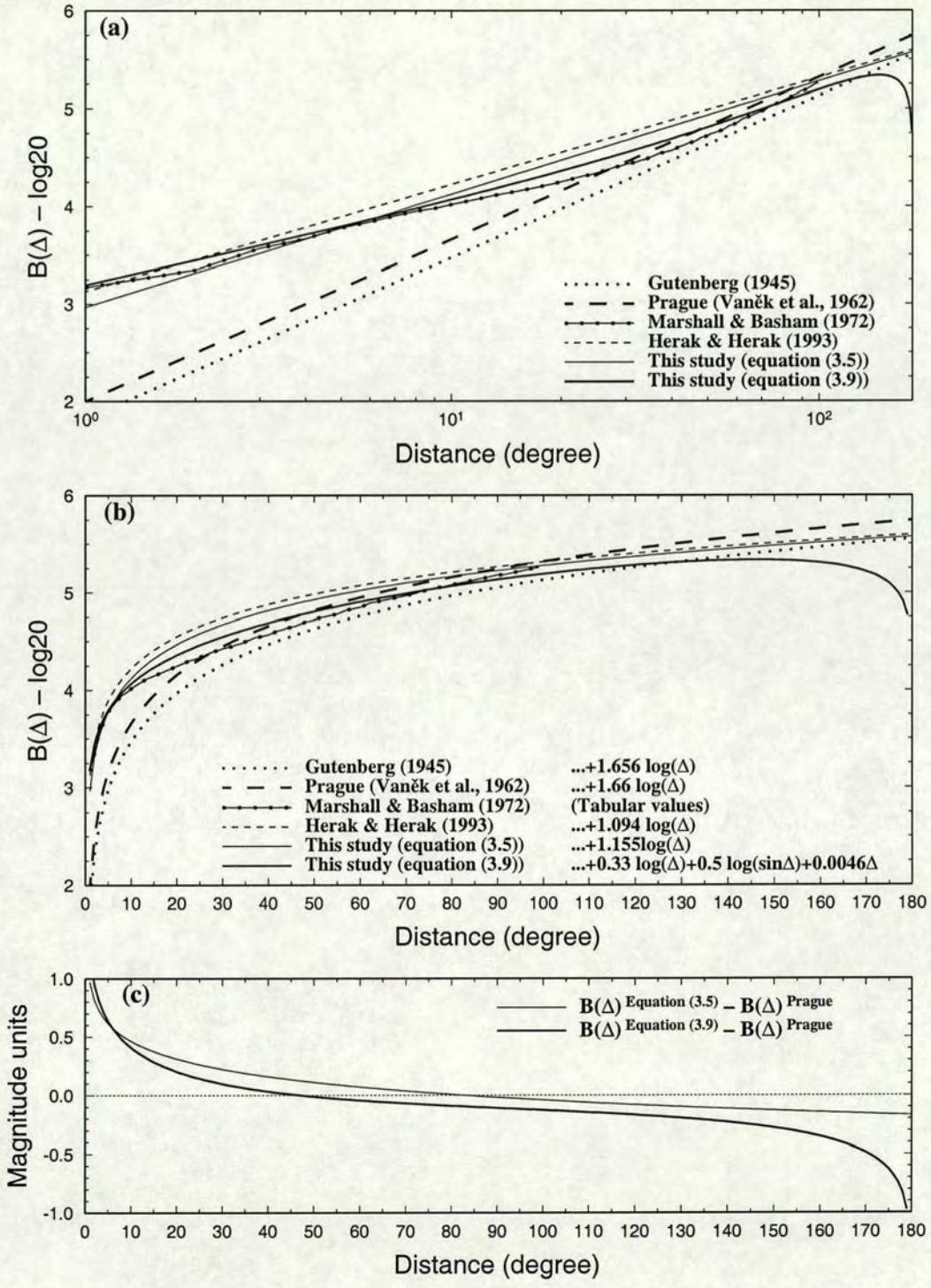

Figure 3.10. Distance-calibration functions $B(\Delta)$ for the determination of surface-wave magnitude using observations of 20 sec period for calibration functions of: Gutenberg without station correction; Prague; Marshall and Basham without path correction; Herak and Herak; equation (3.5) (M_s^e); and equation (3.9) (M_s^t). (a) On a log scale. (b) The same distance-calibration functions on a linear scale for more clarity. (c) Residual of distance corrections for M_s^e and M_s^t compared with that of M_s^{Prague}.

To examine the accuracy of the formulae obtained in this study and other empirical formulae for the determination of M_s, 166,733 individual surface-wave magnitudes of 22,080 earthquakes recorded by 343 seismic stations were calculated. The deviation of individual station magnitudes from the average magnitude of the relevant earthquake computed using the same formula, averaged in 1-degree-wide bins in distance, is shown in Figure 3.11. As is observed in Figures 3.11c, 3.11d, and 3.11e, values of M_s determined by the Herak and Herak

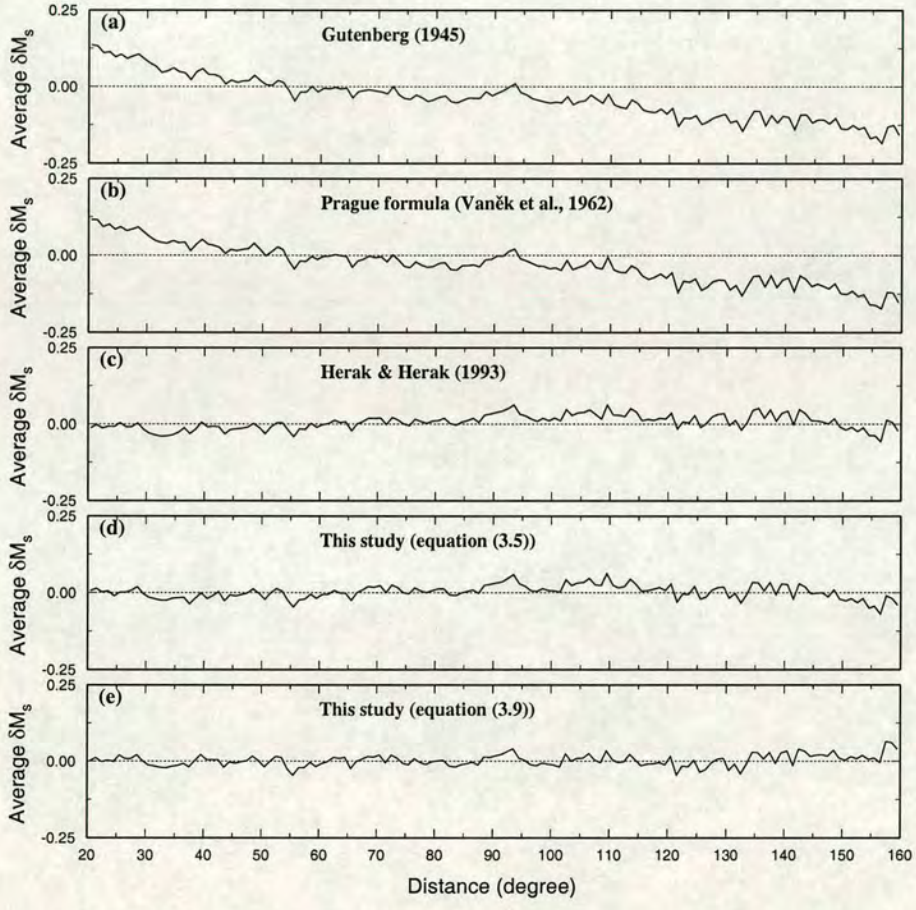

Figure 3.11. Observations of average magnitude residual for all earthquakes, binned at one degree distance intervals with individual magnitude calculated using: (a) Gutenberg formula; (b) Prague formula; (c) Herak and Herak formula; (d) This study according to equation (3.5); and (e) This study according to equation (3.9). In all five cases 166,733 station records were used from 22,080 earthquakes between 1978 to 1993. In all cases the standard error of each point is approximately 0.25.

(1993) formula and formulae obtained in this study are almost independent of distance within the range $20° \leq \Delta \leq 145°$. The M_s^t formula (Figure 3.11e) is independent of distance at least

throughout the range $20° \leq \Delta \leq 160°$; this indicates an absence of distance bias when this formula is used.

For comparison of the Prague formula with equation (3.9), the discrete and cumulative magnitude-frequency distribution of the dataset (22,080 earthquakes) are plotted in Figure 3.12. As Figure 3.12 shows, the b-values obtained from the Prague formula and equation (3.9) which

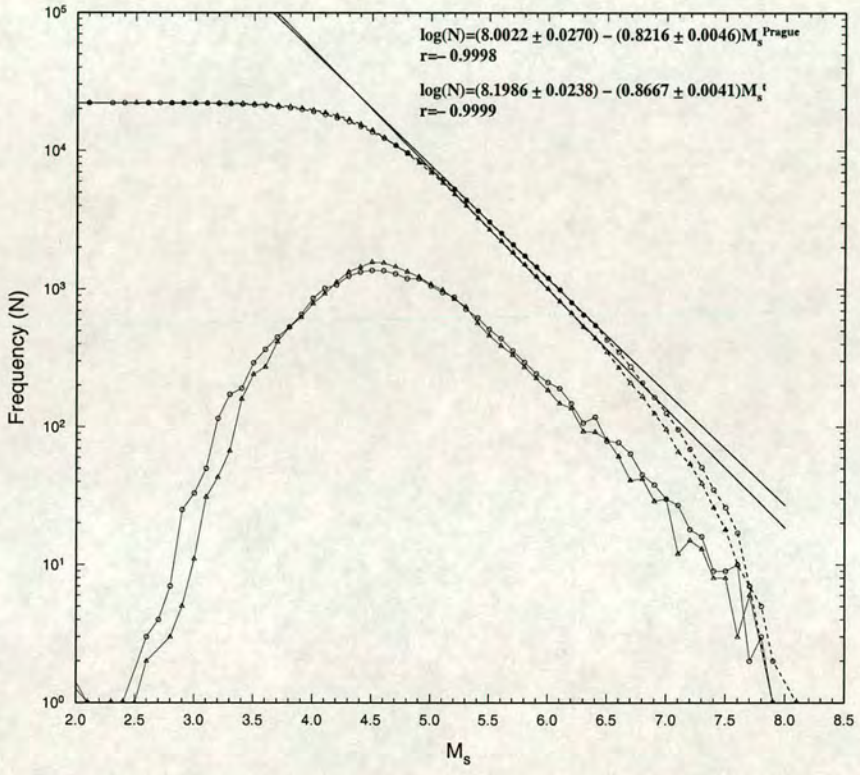

Figure 3.12. Discrete and cumulative magnitude-frequency distribution of 22,080 earthquakes in ISC Catalogue between 1978 and 1993. Solid and dashed curves show discrete and cumulative distribution respectively. Circles indicate data obtained using the Prague formula, and triangles indicate data obtained using equation (3.9). The solid lines are the fit for b-value calculated for the cumulative curves between magnitudes 5.2 and 6.4 (filled circles and triangles).

have been shown on Figure 3.12 are systematically different. The b-value obtained from the dataset based on the Prague formula and equation (3.9) are 0.8216 ± 0.0046 and 0.8667 ± 0.0041 respectively. However, the difference between the two b-values i.e., 0.0451 is small but significant compared to the error (± 0.004) in determination b-value in Figure 3.12.

Also, in Figure 3.13 the standard deviation of the mean magnitude using the Prague formula

for 13,905 earthquakes with a calculated ISC depth $\leq$60 km, is compared with the standard deviation of the mean magnitude when equation (3.9) is used. This shows that the standard deviations for $\overline{M_s^{Prague}}$ values are on average systematically larger than those for $\overline{M_s^t}$ values.

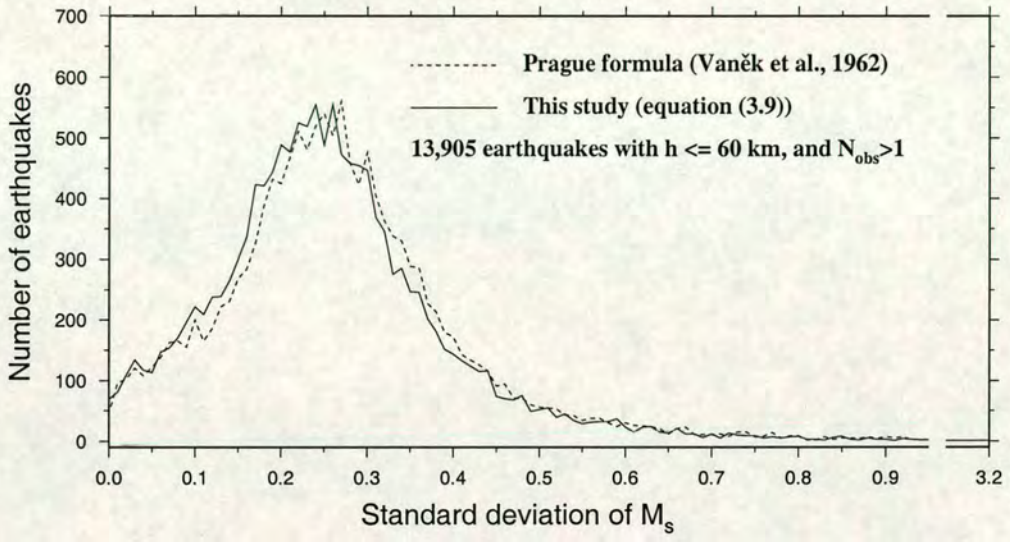

Figure 3.13. Comparison of standard deviation of mean magnitude for 13,905 earthquakes in which more than one station contributed in mean magnitudes, and with a calculated ISC depth $\leq$ 60 km, when the Prague formula and equation (3.9) are used for the determination of M_s.

Figure 3.14a shows those 149 out of the 22,080 earthquakes with $h \leq 60$ km that are identified as explosions using the discrimination line of Nowroozi (1986) and surface-wave magnitudes which have been determined using equation (3.9). Figure 3.14b shows the distribution of 204 nuclear explosions around Nowroozi's decision line. Figure 3.14 shows that, by comparison with Figure 2.15a, the application of the M_s^t formula (equation (3.9)) results in 149 earthquakes plotting in the explosion region, compared with 181 for the ISC Catalogue (Prague formula). For the explosion population, 63 explosions plot in the earthquake region, compared with 68 in Figure 2.15b. Because of the method that was used here for determining K, it was expected that the discrimination line of Nowroozi (1986) would behave similarly. Therefore, it can be concluded that $M_s^t : m_b$ may provide a small improvement in earthquake/explosion discrimination compared with $M_s^{ISC} : m_b$.

In summary, the application of the theoretically-modified distance correction leads to a magnitude M_s which is less biased with distance; gives a systematically-higher seismic b-value; a lower standard deviation in the determination of M_s, and reduces the overlap in the $m_b : M_s$ criterion for explosions and earthquakes.

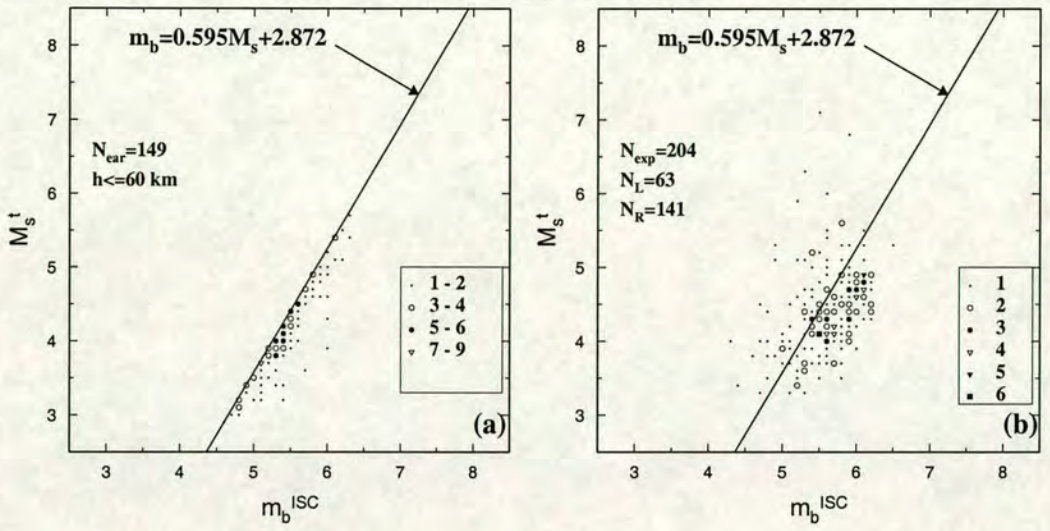

Figure 3.14. (a) Distribution of 149 out of 22,080 earthquakes which lie to the right of the discrimination line of Nowroozi (1986) when M_s^t formula is used in the determination of surface-wave magnitude (compare with the case in which the Prague formula has been used i.e., Fig. 2.15a)). (b) Distribution of 204 events reported as nuclear explosions (compare with Fig. 2.15b). In (a) N_{ear} = number of earthquakes which lie to the right of the discrimination line. In (b) N_{exp} = total number of explosions; N_L = number of explosions which lie to the left of the discrimination line; N_R = number of explosions which lie to the right of the discrimination line.

3.6 Application of M_s^t for $\Delta < 20°$ and $\Delta > 160°$

The sufficiency of equation (3.9) for determination of M_s at distances $\Delta < 20°$ and $\Delta > 160°$ is examined using the same dataset as before. First, a set of data for which ISC have published station magnitudes M_s^{STA} is used. There are 184,257 station records from 22,080 earthquakes with $h \leq 60$ km. Therefore, all stations (with published M_s^{STA}) in the distance range $5° \leq \Delta < 160°$ are included in the computation of $\overline{M_s}$. The period and depth restriction still remain i.e., $10 \leq T \leq 60$ sec, $h \leq 60$ km. The deviations of individual station magnitudes are averaged over 1-degree-wide intervals, and are plotted against distance in Figure 3.15. As is observed in Figure 3.11, the values of M_s which are determined using the Herak and Herak (1993) formula and equation (3.5) are almost independent of distance. This result for equation (3.9) is better than for Herak and Herak (1993), and this shows that equation (3.9) is nearly independent of distance over the whole distance range.

Secondly, all data that ISC have reported (without distance limitation) are used, and where amplitudes and periods are given for surface waves in the distance range of $0° < \Delta < 180°$, station magnitude and mean magnitude ($\overline{M_s}$) are determined using the different formulae. The number of earthquakes is the same i.e., 22,080, but the number of station records increases to 197,553; for 13,296 of these the ISC has not given M_s^{STA}. Here, 7,767 out of 13,296

observations have been recorded on horizontal components. For these, the amplitude of one component is multiplied by $\sqrt{2}$ instead of using the vector sum of the horizontals. (Where surface-waves are recorded on horizontal components and the ISC has given M_s^{STA}, $\log(A/T)$ was first calculated using the Prague formula, then station magnitudes were determined em-

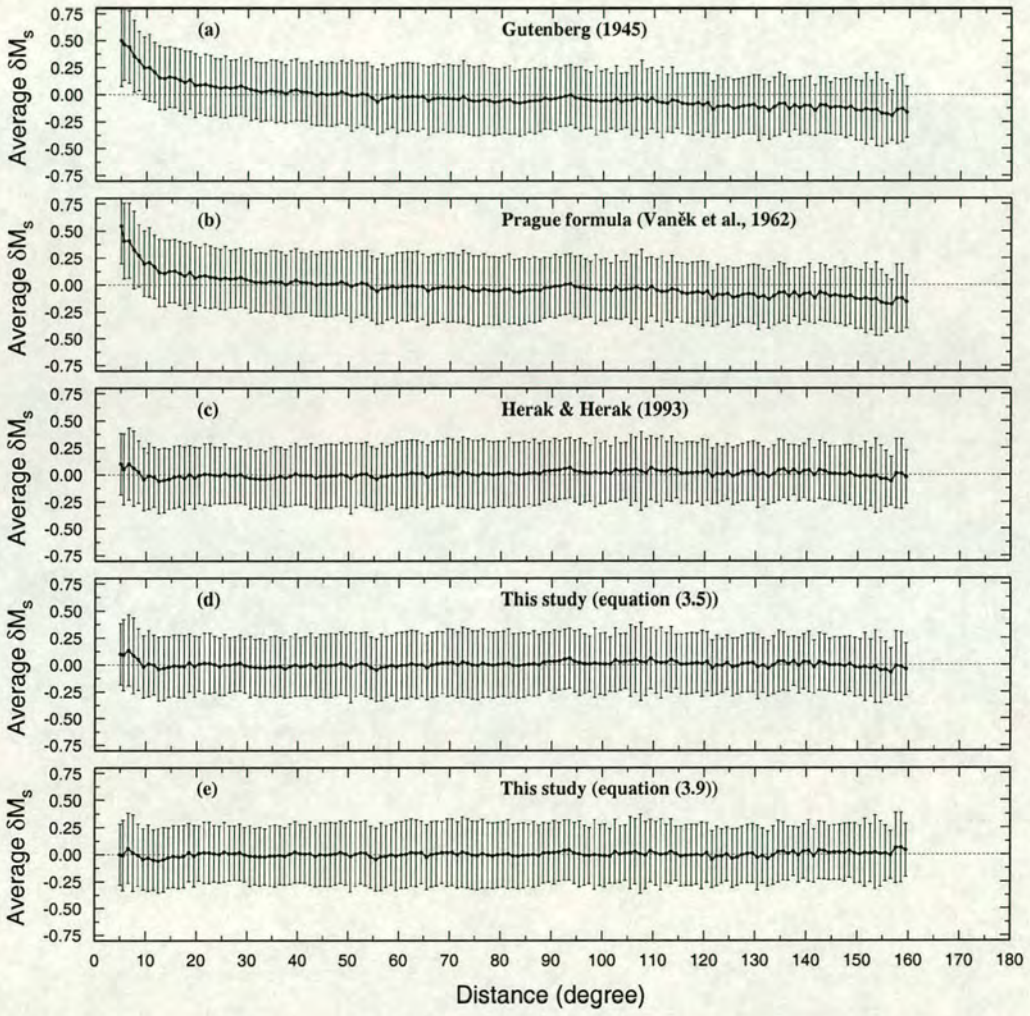

Figure 3.15. Observations of average magnitude residual for all earthquakes, binned at one degree distance intervals with individual magnitudes calculated in the distance range of $5° \leq \Delta < 160°$ using: (a) Gutenberg formula; (b) Prague formula; (c) Herak and Herak formula; (d) this study using equation (3.5); and (e) this study using equation (3.9). In all five cases 184,257 station records are used from 22,080 earthquakes between 1978 to 1993. In all cases the standard error of each point is plotted.

ploying alternative formulae). The deviations of 197,553 individual station magnitudes from

the mean magnitude are averaged over 1-degree intervals and are plotted against distance in Figure 3.16. However, Figure 3.16e shows that surface-wave magnitude is underestimated for distances greater than 160° when equation (3.9) is used, but still the result of estimating M_s for M_s^t (Eq. (3.9)) is better than other formulae for distances less than 160°.

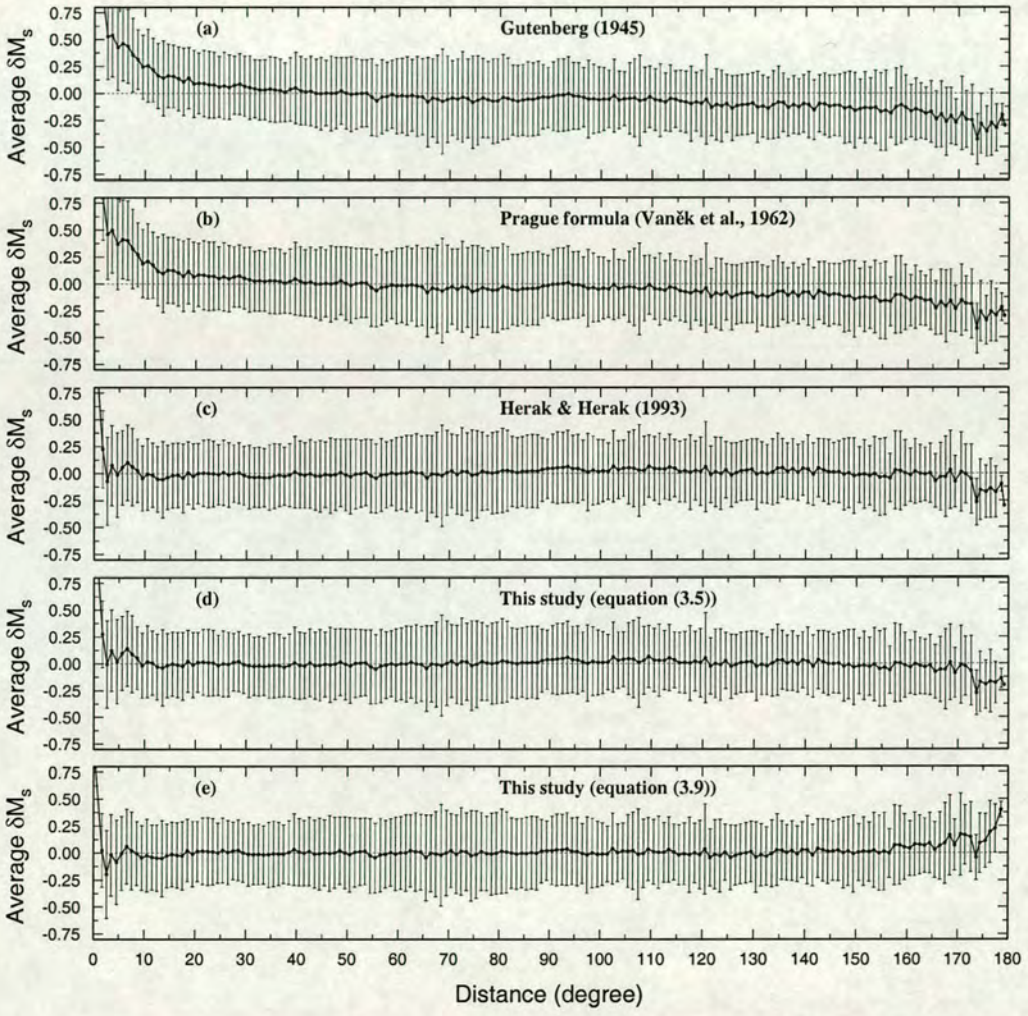

Figure 3.16. Observations of average magnitude residual for all earthquakes, binned at one degree distance intervals with individual magnitudes calculated in the distance range of $0° < \Delta < 180°$ using: (a) Gutenberg formula; (b) Prague formula; (c) Herak and Herak formula; (d) this study using equation (3.5); and (e) this study using equation (3.9). In all five cases 197,553 station records are used from 22,080 earthquakes between 1978 to 1993. In all cases the standard error of each point is plotted.

3.7 Effect of station instruments on M_s determination

Båth (1977) pointed out that short period Benioff- and Grenet-seismometer systems operated on the same pier gave magnitudes differing consistently by 0.47 units. It is clear that this difference is mainly due to the difference in the bandwidths of the respective systems. The range of seismographs that are used for recording of ground motion is increasing from day to day and their amplitude-frequency responses are all different, so the recorded dominant period for events with different sizes are not the same on different seismographs. Moreover, generally the peak frequency of the radiated signal, which depends on source physics, decreases with earthquake size. All instruments for recording seismic signals from earthquakes have response characteristics which correctly sample only a limited range of the seismic energy spectrum about their natural frequency, or equivalent period. In this section the effect of this filtering on the determination of A_{max} and T, and hence on the determination of M_s is quantitatively examined. The relative magnification of some seismographs are shown in Figure 3.17. For

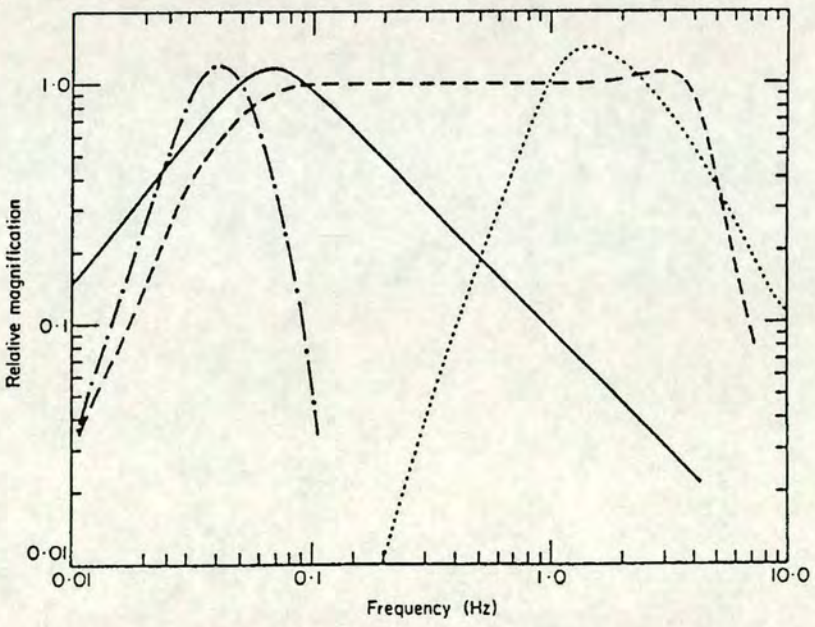

Figure 3.17. Relative magnification of seismographs. Solid line for World-Wide Standard Station Long Period seismograph, dashed line for Broadband seismograph, dot-dashed line for Narrow Band Long Period seismograph, dotted line for World-Wide Standard Station Short Period seismograph.(After Douglas *et al.* 1981a)

digital systems with high dynamic range this problem can be avoided by converting recordings to a common instrument response.

To examine the effect of the instrument on surface-wave amplitude measurement, Long Range Seismic Measurement Long Period (LRSM LP), World-Wide Standard Station Long Period seismograph (WWSSN LP), Seismic Research Observatory Long Period (SRO LP), and broad band Red Kirnos seismographs were selected; these represent a range of responses in common use.

Here some examples are given to examine the instrument effect on the recorded seismogram, by generating synthetic seismograms using the method of Douglas *et al.*, (1972). The model used to generate synthetic fundamental mode Rayleigh wave seismograms is shown in Table 3.1. Two different shapes of fault i.e., circular and elliptical shape are considered. The synthetic seismograms at $\Delta = 30°$ from a vertical dip slip circular fault (with radii of 5 km and 25 km corresponding to magnitude of $m_b \sim 5$ and $m_b \sim 6.5$ respectively) are shown in Figure 3.18. Also, the synthetic seismograms at $\Delta = 90°$ from a vertical strike slip elliptical fault are shown in Figure 3.19. In models which are used for generating the seismograms of Figures 3.18 and 3.19, variables such as source structure and other source parameters (i.e., stress drop, focal depth, etc.) were held constant. In each Figure, two different source sizes have been used. Measured maximum peak to peak amplitude $(2A)$, period of signals (T), and corresponding M_s plus a constant value are shown on each graph.

Table 3.1. Structure models and source parameters used for generating synthetic seismograms (without using Q^{-1}).

Source structures	P-wave velocity km/s	S-wave velocity km/s	Density g cm^{-3}	Thickness km
Layer 1	4.80	$v_\alpha/\sqrt{3}$	2.7	2.0
Layer 2	6.15	//	2.8	31.0
Layer 3	8.20	//	3.0	∞

Source parameters	value used in models
Focal depth	22 km
Stress drop across fault	100 bar
Displacement	constant over fault plane
Fracture velocity	$0.6v_\beta$ (v_β =S-wave velocity in source layer)
Dip of fault plane δ	90°
Direction of slip in fault plane ψ	90°, 0°
Strike of fault plane σ	90°, 0°

Figures 3.18 and 3.19 show that the difference in estimated magnitude from different seismograms is small but this difference for some seismometers such as WWSSN LP is systematic. As a result, estimated surface-wave magnitude from seismograms recorded by a WWSSN LP seismometer is larger by about 0.1 magnitude compared with other seismometers.

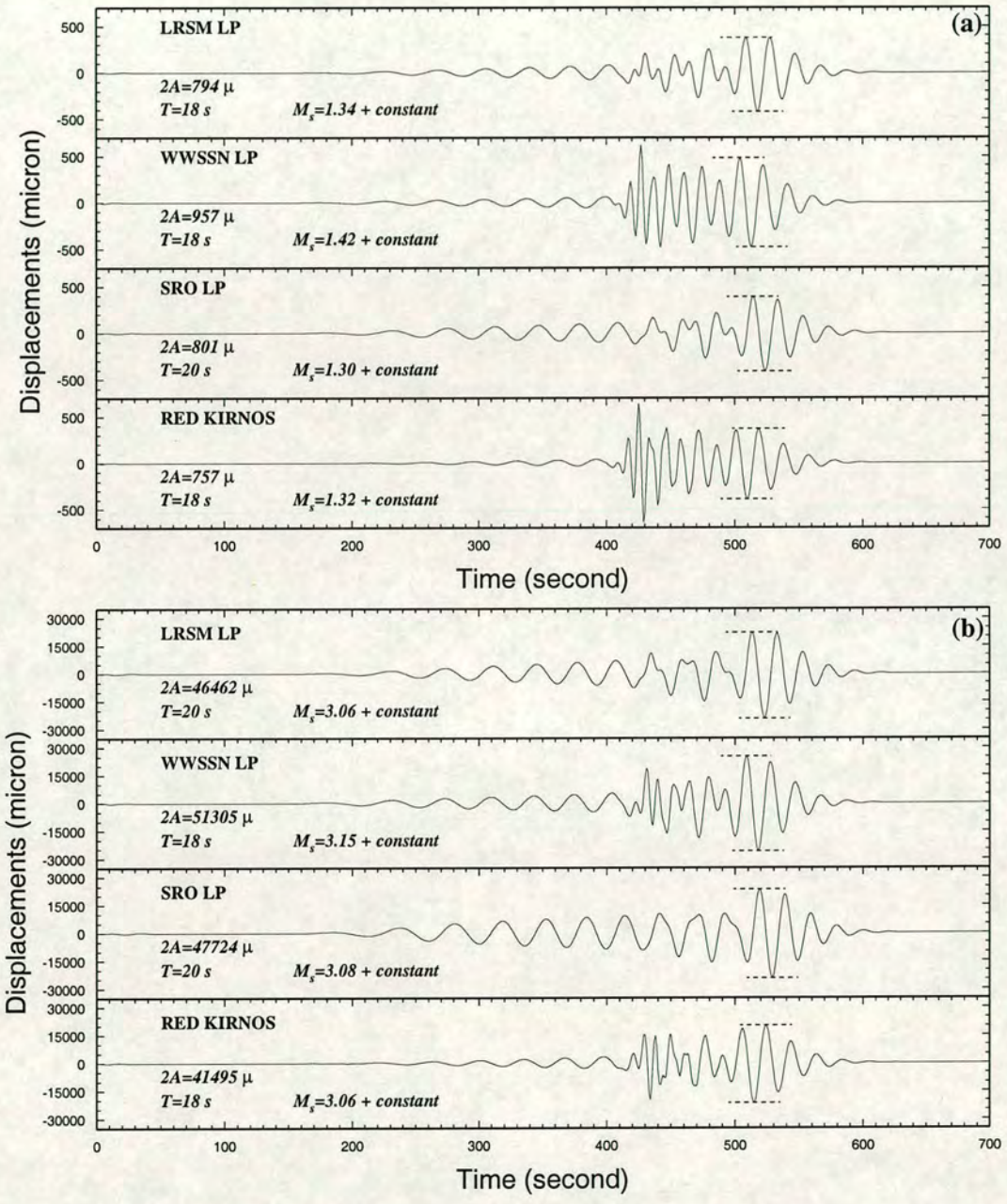

Figure 3.18. Synthetic fundamental mode Rayleigh wave seismograms on vertical component of different instruments from a vertical dip slip fault ($\delta = 90°, \psi = 90°, \sigma = 90°$). Distance and azimuth of recording station are 30° and 45° respectively. (a) For circular fault with radius of 5 km. (b) For circular fault with radius of 25 km. On each seismogram the measured peak to peak amplitude has been clarified by dashed lines.

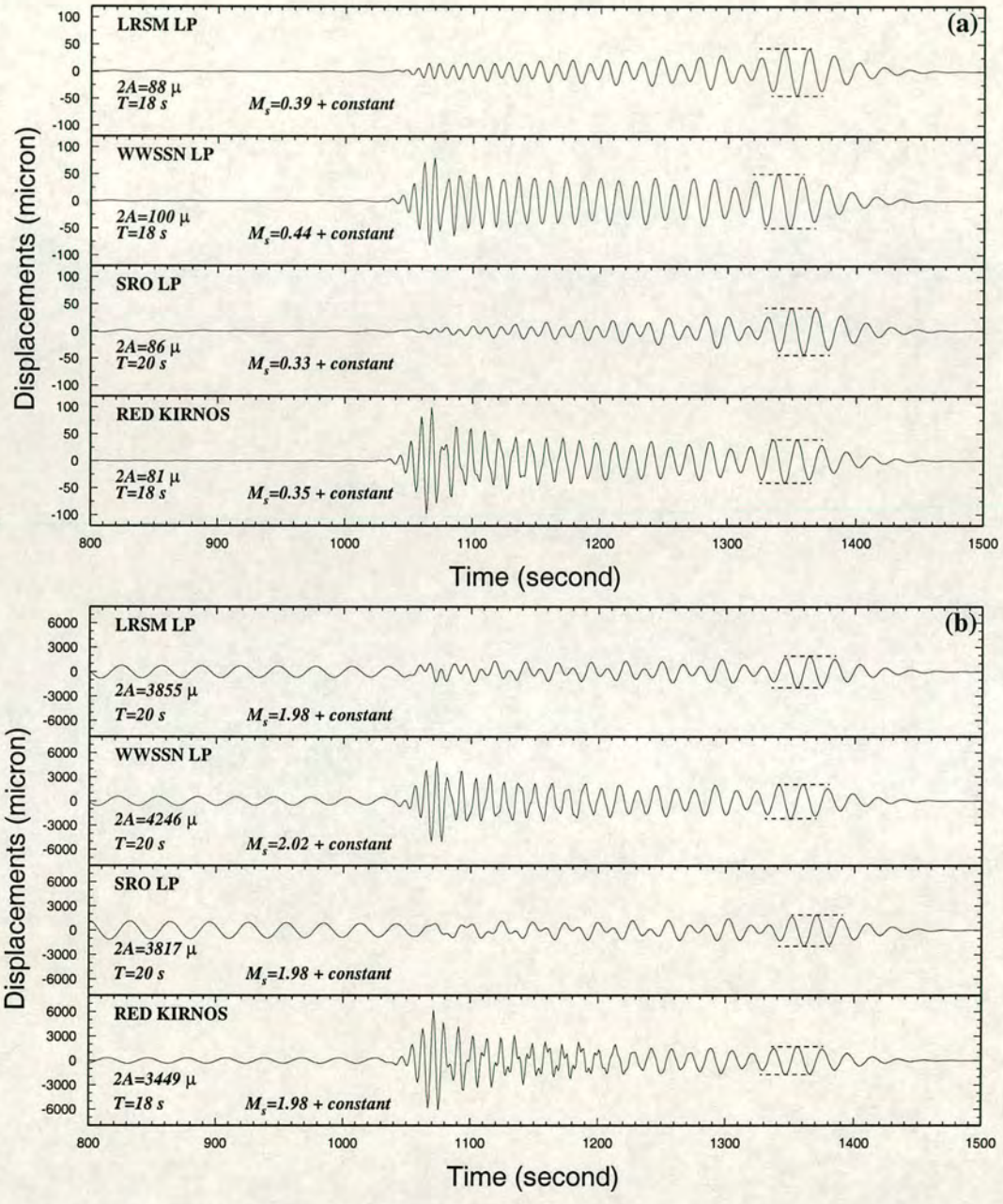

Figure 3.19. Synthetic fundamental mode Rayleigh wave seismograms on vertical component of different instruments from a vertical strike slip fault ($\delta = 90°, \psi = 0°, \sigma = 0°$). Distance and azimuth of recording station are 90° and 45° respectively. (a) For elliptical fault with semi-axis of 5 and 3 km. (b) For elliptical fault with semi-axis of 30 and 20 km. On each seismogram the measured peak to peak amplitude has been clarified by dashed lines.

3.8 Magnitude residuals for individual stations

In addition to the effects described above, systematic magnitude residuals remain due to station effects. Here this is explicitly examined. From 1978 to 1993 the ISC has determined M_s for 22,080 earthquakes with $h \leq 60$ km, using measurements from 343 seismic stations. There are 10,894 earthquakes for which three or more observations have been used in the calculation of M_s^{ISC}. For all 343 stations, the value of $\overline{M_s} - M_s^{STA}$ averaged over all earthquakes was computed using the Prague formula (M_s^{Prague}) and equation (3.9) (M_s^t). Values for those 231 seismic stations which have contributed M_s observations for more than 25 earthquakes are listed in Table 3.2. The absolute values of the average deviation for most (84%) of the stations is less than 0.2 magnitude units, but at some stations this value is very high (see Table 3.2).

Station BRS, with the largest negative average ($\overline{\delta M_s}$), has been measured on vertical component amplitudes and for all its 52 readings, δM_s is negative. For station ALM, where measurements have all been made on horizontal components, the reverse is true. These biases at stations BRS, and ALM can be generated by measuring amplitudes on different components, because according to theory the amplitude of Rayleigh waves (in plane-layered structures) measured on the vertical component is greater than that measured on the horizontal components (Bullen and Bolt, 1985). Also, errors in station calibration can be a significant source for this type of bias. However, other sources of bias such as subsurface conditions near the station, and type of seismometer, affect the scatter of individual magnitude estimates. Since vertical component systems came into general use, most amplitude measurements have been restricted mostly to the vertical component Rayleigh waves. This is convenient, partly because only one record needs to be measured instead of two, and there is no interference from Love waves on the vertical seismograms.

As mentioned before, ISC uses observations on both vertical and horizontal components. In a homogeneous structure, the maximum displacement parallel to the direction of transmission of Rayleigh waves is about two-thirds of that in the vertical direction (Bullen and Bolt, 1985, p. 113), which suggests a reduction of the constant term by 0.18 in the M_s scale when horizontal Rayleigh-wave measurements are used. Due to the layering in the station area, this constant will vary somewhat from station to station and it has to be determined empirically (Båth, 1977; Noguchi, 1979).

Figure 3.20 shows separately the averaged magnitude residuals for ISC data when equation (3.9) is used for M_s^{STA} determination for using observations of both vertical and horizontal components, and only vertical component, and only horizontal components. As Figure 3.20b shows when both horizontal and vertical observations are used, residuals of M_s^{STA} values for horizontal observations are negative specially at closer distances. This means the horizontal

Table 3.2. Mean deviation $\overline{\delta M_s}$ of all values of $\delta M_s = \overline{M_s} - M_s^{STA}$ for those 231 seismic stations at which the ISC has used more than 25 measurements between 1978 and 1993.

1[a]	2[b]	3[c]	4[d]	1	2	3	4	1	2	3	4
AAA	-0.05 ± 0.20	-0.06 ± 0.20	42	HAU	0.11 ± 0.27	0.16 ± 0.26	1276	PPT	0.18 ± 0.56	0.08 ± 0.53	164
AAS	-0.20 ± 0.31	-0.26 ± 0.30	87	HFS	0.03 ± 0.31	0.07 ± 0.31	2677	PRA	-0.11 ± 0.26	-0.06 ± 0.23	750
ADK	0.12 ± 0.31	0.07 ± 0.27	49	HHC	-0.03 ± 0.20	-0.07 ± 0.20	2378	PRE	-0.11 ± 0.31	-0.07 ± 0.33	120
AKU	-0.05 ± 0.25	-0.05 ± 0.23	160	HLW	0.23 ± 0.42	0.22 ± 0.40	65	PRU	-0.11 ± 0.23	-0.06 ± 0.21	3684
ALM	1.10 ± 0.41	1.10 ± 0.42	35	HOF	-0.13 ± 0.23	-0.11 ± 0.21	229	PRZ	-0.17 ± 0.25	-0.20 ± 0.25	211
ALQ	0.01 ± 0.28	0.04 ± 0.28	3510	HON	0.17 ± 0.32	0.15 ± 0.30	893	PUL	-0.06 ± 0.26	-0.04 ± 0.25	536
ANMO	0.01 ± 0.31	0.03 ± 0.28	174	HRV	0.00 ± 0.25	0.04 ± 0.24	618	PYA	-0.11 ± 0.25	-0.08 ± 0.22	284
ANN	0.10 ± 0.21	0.12 ± 0.19	139	ILT	0.10 ± 0.33	0.08 ± 0.30	541	QIZ	0.09 ± 0.21	0.01 ± 0.21	583
ANR	-0.11 ± 0.27	-0.11 ± 0.25	378	IRK	0.05 ± 0.25	0.01 ± 0.25	1112	QZH	0.18 ± 0.21	0.10 ± 0.21	735
ANTO	0.18 ± 0.46	0.21 ± 0.47	35	ISA	0.01 ± 0.23	0.03 ± 0.23	448	RAC	-0.12 ± 0.28	-0.08 ± 0.28	213
APA	-0.13 ± 0.24	-0.11 ± 0.25	300	JCT	-0.04 ± 0.27	-0.02 ± 0.25	1219	RIV	0.38 ± 0.45	0.21 ± 0.47	95
APP	0.01 ± 0.30	0.07 ± 0.30	47	JFWS	-0.02 ± 0.23	0.00 ± 0.22	151	RJF	0.08 ± 0.30	0.14 ± 0.29	1100
ARC	0.10 ± 0.29	0.07 ± 0.29	46	KAT	-0.12 ± 0.34	-0.09 ± 0.32	242	RSCP	0.01 ± 0.36	0.01 ± 0.33	168
ARU	-0.12 ± 0.25	-0.10 ± 0.24	1082	KBS	-0.28 ± 0.84	-0.31 ± 0.81	58	RSNT	0.07 ± 0.24	0.05 ± 0.24	71
ASH	-0.15 ± 0.28	-0.15 ± 0.27	149	KEV	-0.07 ± 0.27	-0.06 ± 0.27	795	RSNY	0.04 ± 0.28	0.06 ± 0.28	908
ASPA	0.08 ± 0.35	0.00 ± 0.39	1672	KHC	-0.03 ± 0.27	0.02 ± 0.24	2335	RSON	0.03 ± 0.34	0.05 ± 0.33	369
BAK	-0.35 ± 0.38	-0.36 ± 0.36	103	KHE	-0.11 ± 0.29	-0.09 ± 0.28	432	RSSD	0.10 ± 0.31	0.12 ± 0.30	645
BCAO	0.10 ± 0.33	0.18 ± 0.31	76	KHO	0.05 ± 0.27	0.05 ± 0.26	54	SAM	-0.05 ± 0.27	-0.04 ± 0.26	259
BER	0.01 ± 0.71	0.02 ± 0.71	73	KIS	-0.10 ± 0.31	-0.05 ± 0.28	464	SAO	0.00 ± 0.27	0.00 ± 0.27	233
BINY	-0.07 ± 0.22	-0.01 ± 0.20	88	KIV	0.08 ± 0.27	0.14 ± 0.26	216	SBA	0.10 ± 0.26	0.04 ± 0.24	44
BJI	0.10 ± 0.23	0.07 ± 0.22	3402	KJF	-0.19 ± 0.22	-0.18 ± 0.22	867	SCO	-0.26 ± 0.41	-0.25 ± 0.39	46
BKR	-0.12 ± 0.31	-0.10 ± 0.30	42	KMI	-0.01 ± 0.25	-0.04 ± 0.24	1727	SDN	-0.01 ± 0.43	-0.02 ± 0.40	362
BKS	0.02 ± 0.33	-0.01 ± 0.33	1431	KOD	0.06 ± 0.22	0.00 ± 0.22	34	SEM	-0.08 ± 0.21	-0.08 ± 0.20	37
BLA	0.03 ± 0.29	-0.02 ± 0.28	211	KON	-0.24 ± 0.58	-0.26 ± 0.57	31	SEY	0.05 ± 0.31	0.00 ± 0.26	199
BNS	-0.23 ± 0.29	-0.20 ± 0.27	360	KRA	-0.18 ± 0.26	-0.15 ± 0.24	2385	SHE	-0.05 ± 0.32	-0.04 ± 0.31	148
BOCO	0.17 ± 0.26	0.22 ± 0.25	40	KRV	0.14 ± 0.30	0.13 ± 0.29	82	SIM	0.03 ± 0.29	0.06 ± 0.27	355
BRG	-0.11 ± 0.22	-0.06 ± 0.21	1146	KSH	-0.26 ± 0.26	-0.25 ± 0.25	924	SIT	0.04 ± 0.35	0.03 ± 0.33	642
BRK	0.00 ± 0.31	-0.03 ± 0.30	151	KTG	-0.13 ± 0.26	-0.11 ± 0.27	77	SJG	0.06 ± 0.29	0.06 ± 0.27	433
BRS	-0.73 ± 0.29	-0.84 ± 0.33	52	KUL	-0.19 ± 0.26	-0.19 ± 0.27	49	SKO	-0.11 ± 0.38	-0.06 ± 0.37	1264
BRVK	0.00 ± 0.23	0.03 ± 0.22	72	KUR	0.10 ± 0.32	0.03 ± 0.29	262	SKR	0.18 ± 0.39	0.10 ± 0.37	84
BTO	-0.06 ± 0.21	-0.10 ± 0.21	2270	LBNH	-0.11 ± 0.21	-0.05 ± 0.22	102	SLL	-0.08 ± 0.37	-0.02 ± 0.36	102
BUL	-0.16 ± 0.33	-0.14 ± 0.34	230	LEN	0.21 ± 0.31	0.20 ± 0.29	59	SLM	0.02 ± 0.31	0.05 ± 0.30	367
CAR	0.05 ± 0.38	0.06 ± 0.39	182	LIC	0.11 ± 0.39	0.17 ± 0.38	700	SLR	-0.30 ± 0.36	-0.26 ± 0.35	1072
CBM	-0.05 ± 0.23	0.00 ± 0.21	348	LOR	0.06 ± 0.37	0.12 ± 0.36	1633	SMY	-0.01 ± 0.36	-0.05 ± 0.33	666
CCM	0.23 ± 0.33	0.25 ± 0.32	97	LPA	-0.02 ± 0.27	-0.02 ± 0.27	638	SNG	0.23 ± 0.40	0.10 ± 0.40	47
CD2	0.01 ± 0.21	-0.02 ± 0.21	1512	LPB	-0.10 ± 0.27	-0.07 ± 0.29	1647	SNY	0.02 ± 0.20	-0.02 ± 0.19	1792
CEH	0.08 ± 0.25	0.11 ± 0.24	565	LRG	0.05 ± 0.30	0.11 ± 0.29	491	SOC	-0.01 ± 0.30	0.01 ± 0.28	313
CHG	0.26 ± 0.38	0.22 ± 0.36	65	LSA	0.05 ± 0.30	0.01 ± 0.29	422	SPA	-0.03 ± 0.36	-0.05 ± 0.35	1757
CHTO	0.46 ± 0.49	0.45 ± 0.45	104	LSCT	-0.14 ± 0.21	-0.07 ± 0.22	86	SPC	-0.30 ± 0.39	-0.29 ± 0.38	122
CIT	-0.04 ± 0.27	-0.13 ± 0.28	126	LTX	0.05 ± 0.51	0.07 ± 0.50	193	SRO	-0.14 ± 0.31	-0.12 ± 0.30	563
CLL	-0.02 ± 0.22	0.02 ± 0.20	926	LVV	-0.20 ± 0.31	-0.16 ± 0.29	306	SSE	0.12 ± 0.26	0.07 ± 0.25	3226
CMB	0.04 ± 0.25	0.05 ± 0.25	425	LZH	-0.02 ± 0.24	-0.04 ± 0.24	3873	SSPA	0.21 ± 0.48	0.25 ± 0.47	35
CN2	0.01 ± 0.23	-0.01 ± 0.22	2292	MAK	-0.04 ± 0.32	-0.04 ± 0.30	248	STAN	0.10 ± 0.25	0.05 ± 0.25	34
COL	0.00 ± 0.29	-0.02 ± 0.27	668	MAT	0.22 ± 0.27	0.17 ± 0.25	2741	STU	0.04 ± 0.24	0.06 ± 0.22	269
COP	-0.06 ± 0.27	-0.03 ± 0.26	776	MAW	-0.08 ± 0.33	-0.10 ± 0.35	263	SUR	-0.32 ± 0.32	-0.31 ± 0.31	232
CTA	-0.02 ± 0.37	-0.17 ± 0.37	280	MCWV	-0.10 ± 0.27	-0.07 ± 0.24	333	SVE	-0.10 ± 0.29	-0.08 ± 0.29	974
CTAO	0.15 ± 0.43	0.07 ± 0.44	26	MDJ	0.01 ± 0.23	-0.03 ± 0.23	1053	TAS	-0.08 ± 0.27	-0.07 ± 0.26	523
DAG	-0.05 ± 0.30	-0.04 ± 0.30	308	MGD	0.17 ± 0.34	0.13 ± 0.29	472	TIA	0.07 ± 0.21	0.02 ± 0.21	1514
DBN	0.09 ± 0.29	0.11 ± 0.28	1133	MHC	0.09 ± 0.44	0.06 ± 0.42	163	TIK	-0.02 ± 0.27	-0.03 ± 0.26	842
DL2	0.16 ± 0.27	0.11 ± 0.26	976	MIAR	0.13 ± 0.25	0.17 ± 0.22	362	TIY	-0.08 ± 0.22	-0.09 ± 0.20	2963
DOU	-0.04 ± 0.22	-0.01 ± 0.21	458	MIN	0.16 ± 0.51	0.13 ± 0.52	40	TLG	0.12 ± 0.31	0.10 ± 0.31	331
DSH	-0.05 ± 0.29	-0.05 ± 0.29	62	MIR	0.04 ± 0.26	0.00 ± 0.28	133	TPNV	-0.18 ± 0.30	-0.18 ± 0.29	191
DUG	0.10 ± 0.23	0.13 ± 0.23	230	MNK	-0.24 ± 0.22	-0.20 ± 0.20	179	TUC	0.06 ± 0.26	0.08 ± 0.26	404
ELT	-0.15 ± 0.31	-0.16 ± 0.31	254	MOS	-0.17 ± 0.28	-0.16 ± 0.26	512	TUL	0.09 ± 0.37	0.11 ± 0.35	2828
ERE	0.11 ± 0.28	0.12 ± 0.28	96	MOX	-0.04 ± 0.24	0.00 ± 0.24	2764	UER	0.02 ± 0.33	-0.03 ± 0.34	72
FLN	0.05 ± 0.28	0.10 ± 0.28	1089	MSO	0.00 ± 0.48	0.00 ± 0.48	119	UKR	0.02 ± 0.20	-0.01 ± 0.18	29
FRU	-0.06 ± 0.24	-0.06 ± 0.23	677	MTA	0.32 ± 0.36	0.35 ± 0.36	140	UPA	0.12 ± 0.32	0.13 ± 0.29	496
FUR	-0.06 ± 0.29	-0.03 ± 0.28	582	MUN	-0.01 ± 0.32	-0.12 ± 0.34	363	UZH	-0.21 ± 0.30	-0.16 ± 0.27	435
FVM	-0.14 ± 0.33	-0.11 ± 0.30	479	NAI	0.23 ± 0.37	0.25 ± 0.37	180	VKA	0.07 ± 0.22	0.10 ± 0.21	713
GAC	-0.15 ± 0.75	-0.16 ± 0.76	27	NDI	0.11 ± 0.33	0.07 ± 0.32	373	VLA	0.37 ± 0.47	0.29 ± 0.46	77
GAM	-0.43 ± 0.99	-0.45 ± 1.01	28	NEW	-0.11 ± 0.35	-0.11 ± 0.34	663	WAR	-0.23 ± 0.24	-0.21 ± 0.23	447
GAR	0.06 ± 0.37	0.05 ± 0.36	56	NJ2	0.16 ± 0.25	0.11 ± 0.24	1332	WDC	0.05 ± 0.28	0.07 ± 0.28	402
GDH	-0.04 ± 0.25	-0.03 ± 0.25	269	NNA	0.26 ± 0.42	0.26 ± 0.42	419	WEL	-0.09 ± 0.29	-0.21 ± 0.27	170
GLD	-0.04 ± 0.31	-0.03 ± 0.29	1249	NRI	-0.21 ± 0.31	-0.22 ± 0.29	505	WET	-0.12 ± 0.24	-0.09 ± 0.22	337
GOGA	0.04 ± 0.22	0.08 ± 0.20	81	NRN	-0.29 ± 0.36	-0.31 ± 0.36	36	WHN	0.04 ± 0.22	-0.01 ± 0.22	1554
GOL	0.06 ± 0.28	0.08 ± 0.27	1817	NUR	-0.03 ± 0.27	0.00 ± 0.27	2696	WIN	-0.29 ± 0.34	-0.26 ± 0.34	367
GRA1	-0.09 ± 0.63	-0.08 ± 0.62	26	NVL	-0.06 ± 0.30	-0.06 ± 0.30	360	WMOK	-0.05 ± 0.24	-0.01 ± 0.22	251
GRB1	0.10 ± 0.51	0.14 ± 0.50	70	NVS	-0.14 ± 0.26	-0.16 ± 0.26	357	WMQ	-0.12 ± 0.24	-0.10 ± 0.23	2684
GRF	0.10 ± 0.28	0.15 ± 0.27	3938	NWAO	0.22 ± 0.38	0.17 ± 0.40	629	WOL	-0.10 ± 0.83	-0.05 ± 0.82	81
GRM	0.02 ± 0.40	0.04 ± 0.40	179	OBN	-0.13 ± 0.26	-0.08 ± 0.25	1695	XAN	-0.02 ± 0.23	-0.05 ± 0.22	1358
GRO	-0.28 ± 0.32	-0.26 ± 0.33	306	OJC	-0.12 ± 0.30	-0.07 ± 0.28	105	YAK	0.05 ± 0.26	0.00 ± 0.24	595
GRS	0.16 ± 0.29	0.17 ± 0.28	272	ORV	0.19 ± 0.25	0.19 ± 0.24	53	YBH	0.09 ± 0.21	0.08 ± 0.22	50
GTA	-0.12 ± 0.22	-0.12 ± 0.22	3216	PAS	0.12 ± 0.27	0.10 ± 0.25	300	YSNY	-0.06 ± 0.22	-0.01 ± 0.21	101
GUA	0.32 ± 0.27	0.17 ± 0.28	457	PET	0.19 ± 0.29	0.14 ± 0.25	431	YSS	0.16 ± 0.29	0.12 ± 0.26	721
GUMO	0.48 ± 0.34	0.39 ± 0.34	526	PME	0.07 ± 0.40	0.04 ± 0.38	201	ZAK	-0.04 ± 0.23	-0.08 ± 0.23	1188
GYA	0.02 ± 0.21	-0.02 ± 0.22	1599	PMG	0.02 ± 0.40	-0.08 ± 0.41	127	ZOBO	0.12 ± 0.28	0.20 ± 0.29	1475
GZH	0.09 ± 0.22	0.02 ± 0.23	756	PMR	0.10 ± 0.32	0.10 ± 0.30	1849	ZST	-0.27 ± 0.40	-0.23 ± 0.39	173

[a] Station code

[b] Mean deviation with standard error ($\overline{\delta M_s} \pm \sigma_{mean}$) according to the Prague formula

[c] Mean deviation with standard error ($\overline{\delta M_s} \pm \sigma_{mean}$) according to equation (3.9)

[d] Number of readings

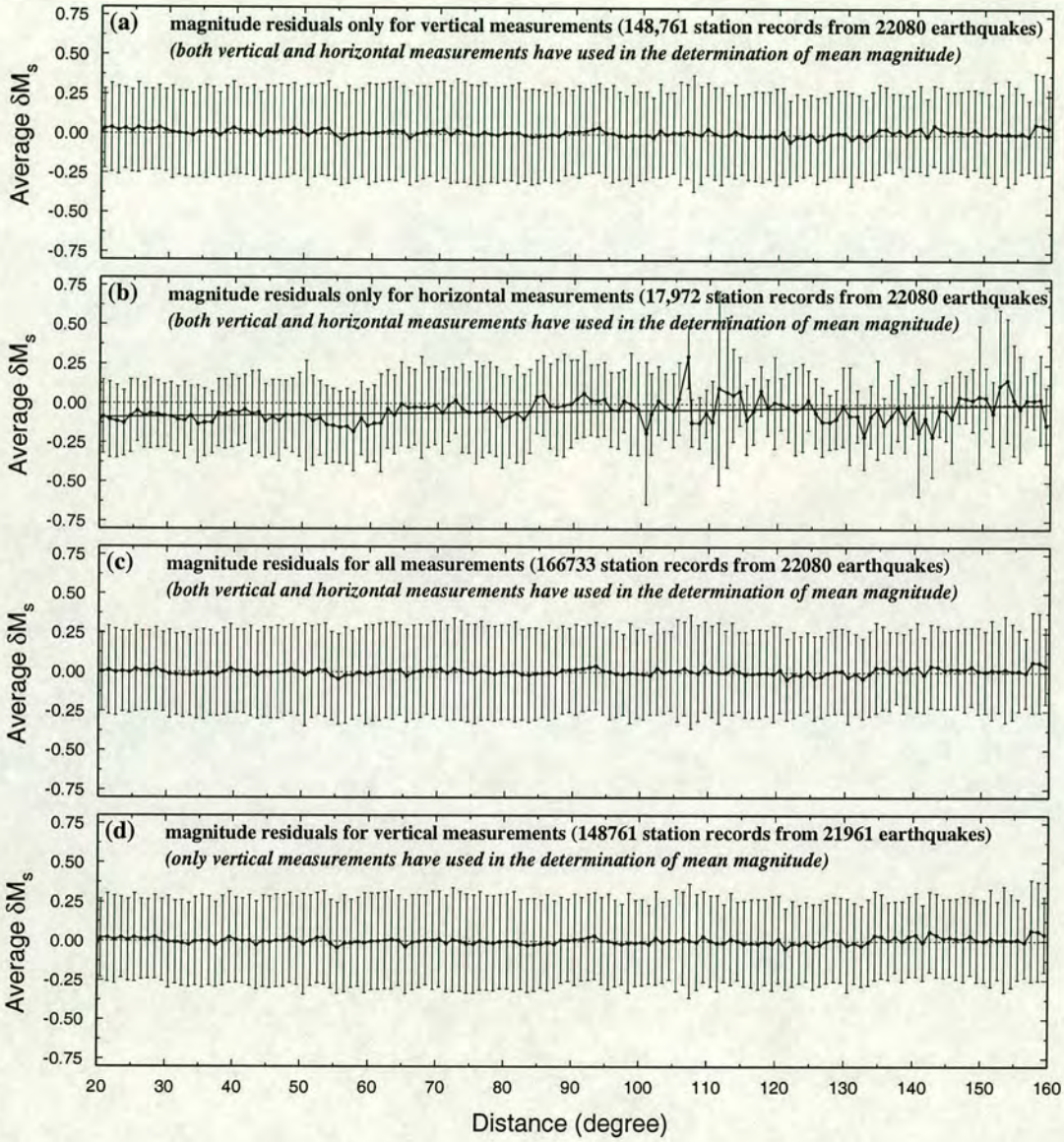

Figure 3.20. Observations of average magnitude residual ($\overline{M_s^t} - M_s^{STA}$) for all earthquakes, binned at one degree distance intervals with individual magnitude calculated using equation (3.9). (a) For measurements on vertical component. (b) For measurements on horizontal components. (c) For all measurements (vertical and horizontal). In (a), (b) and, (c) both measurements (vertical and horizontal) contribute to the mean M_s. In (b) the solid line shows the regression line. (d) For measurements on vertical component. In (d) only vertical component measurements have been used to estimate earthquake magnitude (mean magnitude). In all cases the standard error of each point is shown on the graphs.

observations give a value larger than vertical observations for M_s^{STA}, thus Love-waves predominate amplitude measurements on horizontal components.

In Figure 3.21 the distribution of the deviation obtained using the M_s^t formula for 231 stations (mentioned before) is plotted on a world map. Stations in southern Africa, the eastern part of Europe, and in the former Soviet Union have negative deviations i.e., $\overline{M_s^t} < M_s^{STA}$ (Fig. 3.21b filled circles). The path effect is one of the sources of bias in the determination of magnitude specially surface-wave magnitude (see Ekström and Dziewonski, 1988; Abercrombie, 1994). To examine the path effect on station terms in other words azimuthal dependency, station terms are calculated over 45-degree-wide intervals of azimuth (azimuth from station to epicenter i.e., backbearing) of arrival signals to receivers. The calculated station terms for stations with absolute azimuthal terms greater than 0.1 magnitude units, and in each azimuthal interval (45-degree-wide) more than 25 times contributed in $\overline{M_s^t}$, are plotted in Figure 3.21c. Figure 3.21c includes those stations which have contributed more than 200 earthquakes. As this Figure shows there is no significant correlation between values of station terms and oceanic/continental paths when station terms of stations near continental-oceanic boundaries are compared with those in continent or ocean. However, in some stations the station terms are large in some direction, but generally these terms are controlled by concentration of data with azimuth according to the location of stations relative to the active seismic belts. As a result the azimuthal station terms do not show a clear effect of different path in M_s^{STA} values of each individual station.

Station corrections are essential to improve the measure of earthquake size obtained from M_s. This is well known, and station magnitude residuals have long been used as an indicator of regional seismic attenuation. However, the station term obtained here by averaging station residuals contains the effect of radiation pattern, path effect, effect of seismometer type, and subsurface effect near-station. Here I would have liked to differentiate between true near-station effects caused by subsurface conditions, and any purely instrumental effect which may result from biases due to the prevalence of different recording instruments in different regions of the world. Unfortunately, comprehensive information on the type of instrument used is not easily available for most stations. Future studies using digital data transformed to a common instrument response, should be able to isolate any contribution of instrumentation.

3.9 Remaining sources of scatter and bias in M_s

Now the scatter remaining in M_s^t values is considered. First, the question posed by Figure 3.1, in which the distance dependence changes with magnitude, is reconsidered. All the graphs in Figure 3.1 have been recomputed using equation (3.9), so that the ordinate becomes $\overline{M_s^t} - M_s^t$. As Figures 3.8 and 3.9 show in all cases the gradient of the regression line is $\lesssim \pm 0.03$, with

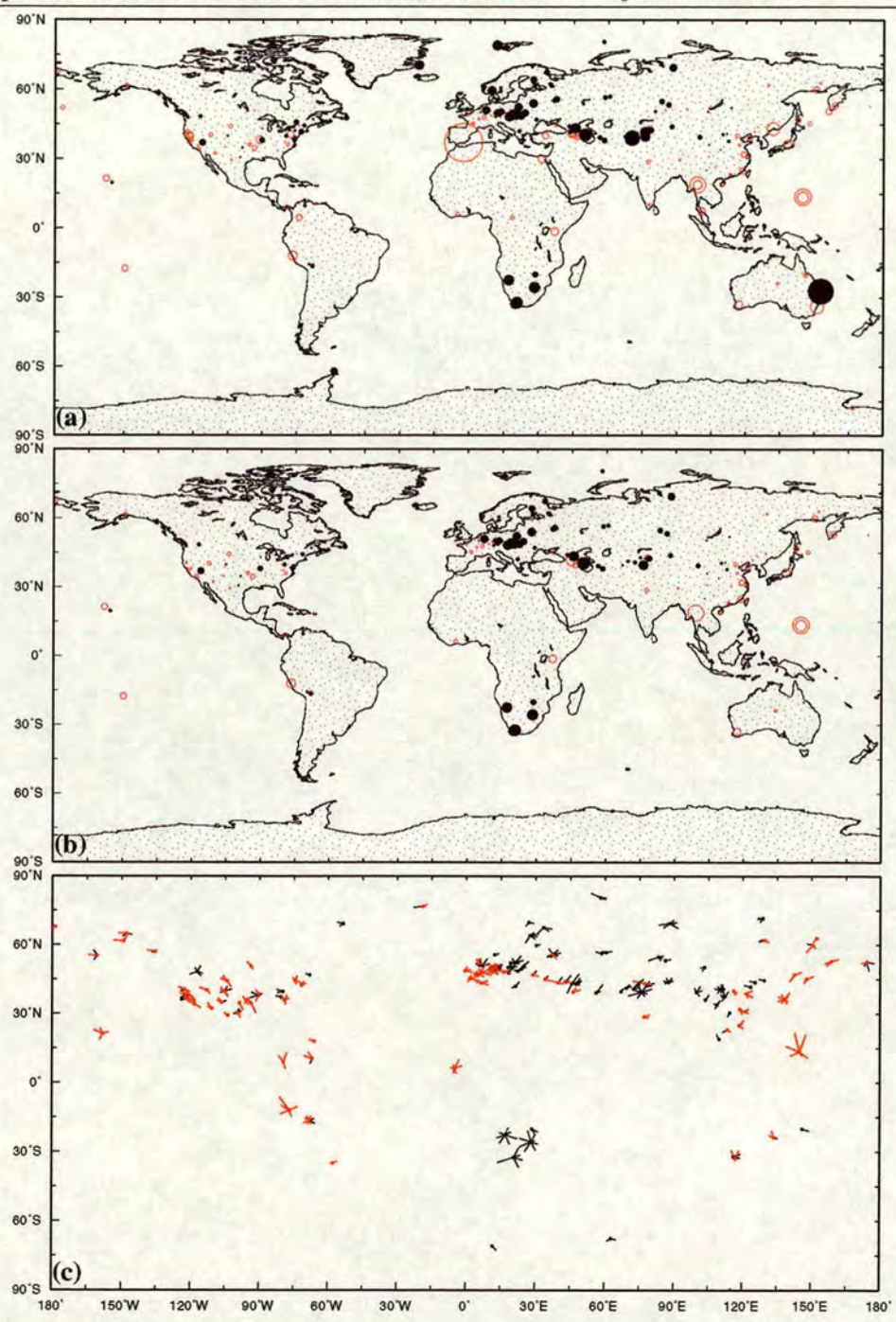

Figure 3.21. Global maps showing the average value of $\overline{M_s^t} - M_s^{STA}$ for all earthquakes (in which more than two stations contributed in $\overline{M_s^t}$) recorded at individual stations. (a) Includes those stations which have contributed more than 25 earthquakes. (b) Stations which have contributed more than 100 earthquakes. (c) Station which have contributed more than 200 earthquakes, and absolute deviations in direction of averaged azimuth greater than 0.1 magnitude units for stations which in each azimuth interval (45-degree-wide) each station more than 25 times contributed in $\overline{M_s^t}$. In (a) and (b) open circles (red) show positive deviations ($\overline{M_s^t} > M_s^{STA}$), and filled circles (black) show the negative deviations. In (c) the solid and red lines represent the negative and positive deviations respectively. The size of circles and the length of lines are proportional to the absolute value of the mean deviation; the largest circle and line correspond to a deviation of 1.1 and 0.55 magnitude units respectively.

no systematic difference. Therefore it can be concluded that there is no significant magnitude dependence in the distance correction term of equation (3.9), over the whole distance range $20° \leq \Delta \leq 160°$.

Secondly, there is possibility that there is a systematic effect arising from the absence of a depth correction to M_s. Romanelli and Panza (1995) conclude that this effect is significant. One way to examine this is to use the CMT depth as a reference. The effect of depth on M_s determination will be discussed separately in chapter 4.

Thirdly, the Prague formula has no station correction. The station correction may be influenced by the seismograph type as well as local geological conditions. Historically there has been a tendency for specific instrument types to be concentrated in specific regions—e.g., in the former Soviet Union; these regional differences are disappearing with digital broad band instrumentation becoming widespread and the tendency towards more global mixing of seismograph types. The regional differences in station magnitude residuals observed in Figure 3.21 may be the result of regional clustering of common instrumentation.

Fourthly, the Prague formula has no path correction, although the substantial effect on M_s^{STA} of surface wave propagation path has long been well-known. From equation (3.9) it follows that the appropriate way to introduce a path correction into the M_s^t scale would be to determine a path-specific value of K, since this constant reflects both the average anelastic attenuation along the path, and the average velocity structure. This implies that the path correction would be linear in distance Δ.

Fifthly, it is well known that radiation pattern (azimuthal variation of surface-wave) contributes significantly to scatter of M_s^{STA}. Therefore, the source radiation effects are expected to remain as a contributory factor in M_s scatter.

Sixthly, there is a scatter implicit in the observatory practice of measuring surface wave amplitude and period (see Fig. 2.4 and section 2.6) which can create variations as much as 0.5 magnitude units for small earthquakes.

Finally, due to regional variation of α in equation (3.7) and dependencies on path, equation (3.9) could be regionalised (Stevens and McLaughlin, 1997). So, using a different value for α hence a different value for k may be more appropriate in some regions, and to make M_s^t period-dependent.

3.10 Conclusions

The frequency-distance plot for reported surface wave amplitude observations was shown to exhibit detailed structure of the body-wave amplitude-distance curve at all distances. The number of reported surface wave amplitude observations at epicentral distances Δ corresponding

to the P-wave shadow zone ($100° \leq \Delta \leq 120°$) is low, because most seismic stations measure surface waves after recognising the first arrival P-wave. Indeed, the frequency-distance relation for surface wave amplitude measurements is dominated by the body-wave amplitude-distance curve. It follows that many potentially useful observations of surface wave amplitude are missing from the datasets.

Investigation of the distance calibration function has shown that in the Herak and Herak (1993) formula, and, the best fitting empirical M_s^e and theoretical M_s^t formulae (obtained in this study), the residuals of individual station magnitudes from the mean magnitudes are less than for other formulae in common use. M_s^e (Eq. (3.5)) was obtained using the whole ISC data from 1978 to 1993 and over the whole range of M_s. Here, I derive and determine a formula containing theoretical distance-dependence terms (M_s^t (Eq. 3.9)), to reduce systematic errors in the distance correction over the full range of distances ($20° \leq \Delta \leq 160°$). There is some evidence that Airy-phase, rather than non-Airy-phase distance dependence dominates measurements for $\Delta < 35°$. A globally-averaged Q^{-1} of 0.00192 ± 0.00026 is obtained for Rayleigh-waves with 20-second period and group velocity of 3.6 km/s.

Deviations in M_s determinations made using the M_s^t formula isolate those remaining sources of scatter that are unexplained. It appears that the absence of a depth correction, and of station and path corrections, contribute to this remaining scatter, but that there is no discernible magnitude dependence remaining in the M_s^t distance correction. It is possible that regional variations in instrumentation are distorting the perceived regional differences in M_s station residuals, but further investigation of this must await more seismic data from the global digital networks.

The type of study reported here is important in the removal of bias in M_s. I have demonstrated that it is also important in the correct determination of seismic b-values; the correct application of the $M_s : m_b$ discriminant; and in confirming the need to modify the formula for M_s calculation. In particular, the importance of applying a suitable distance correction term which is theoretically valid has been clearly demonstrated.

Chapter 4

Relations between seismic moment and magnitude (M_S) for global dataset

4.1 Introduction

In this chapter the observed relationships between moment and surface wave magnitude (M_s^t) is studied for large global dataset, with attention to sources of bias and observational error. The result is compared with theoretical relationships between moment and magnitude in order to explore improvements which can be made in the quantification of earthquake size. The linearity or non-linearity in relationship between moment and magnitude is investigated and global empirical relation is given in this chapter, which estimate sizes of events over a wide range of magnitudes.

Aki (1966) showed that the physical characterisation of most earthquake sources is a double couple, quantified by its seismic moment M_0 which has the same dimensions as energy. Because of the linearity of all the physical laws involved, the excitation of all seismic waves by a point source double-couple is proportional to M_0. So the relationship between the logarithm of seismic moment and magnitude would be expected to be linear, and the slope of the relationship should be unity assuming no other effects. However, earthquakes are not point sources, and the distribution of moment release over space and time reduces the observed maximum amplitude for large earthquakes below that for a point source of the same moment. This saturation of the magnitude scale is one effect which creates nonlinearity between moment and magnitude. The moment at which this effect becomes significant is governed by the frequency at which magnitude is measured. In Geller's (1976) model, nonlinearity between $\log M_0$ and M_s starts at about $M_0 = 4\times10^{25}$ dyne-cm and he gives a slope of $\frac{2}{3}$ between $\log M_0$ and M_s for seismic moment ranges of $4\times10^{25} - 5\times10^{27}$ dyne-cm. Beyond $M_0 = 1.5\times10^{28}$ dyne-cm full saturation is predicted. Many workers (e.g, Purcaru and Berckhemer, 1978, 1982; Hanks and Kanamori, 1979; Caputo and Consol, 1980; Hyndman and Weichert, 1983) have given global and regional linear

relations between $\log M_0$ and M_s, and the slopes are ≈ 1.5. Some researchers (e.g., Johnston, 1996; Ambraseys and Adams, 1996) give a nonlinear relation between these two quantities. Purcaru and Berckhemer, (1978) found that for very large earthquakes M_0 may differ by two orders of magnitude for a given value of M_s, depending on the space-time distribution of moment release. Here the linear and nonlinear relation between $\log M_0$ and magnitude M_s^t (for which distance bias has been minimised in chapter 3) are studied for a large dataset.

While the pioneering studies to determine the seismic moment occurred in the late 1960s and in the early 1970s, the Harvard CMT method of Dziewonski *et al.* (1981) became a common systematic determination of earthquake moment tensors. The Harvard group have utilised long-period (45–200 sec) body and surface waves (for very large earthquakes) to determine scalar moments and moment tensors. The seismic moments of most earthquakes above $m_b \approx 5.0$ are available in the CMT Catalogue from 1977.

Seismicity studies require homogeneous earthquake catalogues, that is, catalogues in which earthquake magnitudes are calculated using the same scale over time, and preferably using the seismic moment magnitude scale. Seismic moment magnitudes are available only for a limited number of earthquakes, so regarding the targets of seismicity studies, the catalogue used has been extended to cover a longer time and a larger range of earthquake sizes by using other global or regional empirical relationships between magnitude and seismic moment.

During the development of the Harvard CMT method, Sipkin (1982, 1986) developed the method of United States Geological Survey (USGS) to determine the moment tensor from body waves. This method is also applied systematically for all appropriate events (a similar magnitude cut-off to the Harvard method). The Harvard group use entire seismograms, but USGS use just long period P-waves. More recently, the Earthquake Research Institute (ERI) in Japan began to systematically determine the CMT using long period body-waves. This method is quite similar to the Harvard method, and they broadcast the results of the automatic inversion with no human intervention (Kawakatsu, 1995). Here the Harvard CMT Catalogue is used, because it is more complete and more globally representative than other CMT Catalogues. Also, in the final section the seismic moment and depths from the Harvard CMT Catalogue is compared with those in the USGS CMT Catalogue for earthquakes with both seismic moments available.

4.2 Relation of seismic moment with magnitude

The magnitude was the first quantitative measure of the strength of an earthquake. It is still a widely used earthquake parameter although its shortcomings are well known. As mentioned before, magnitude is calculated from seismic-wave amplitudes at a given period while the seismic energy release involves integration over the whole spectrum. The seismic moment

is ideally determined from the long-period level which may be quite removed, in period or frequency, from the period at which the magnitude is measured.

The relationship between M_0 and magnitude may be understood by considering the radiation spectra of earthquakes. The far-field displacement spectrum for the ω^{-2} model has been expressed by Aki and Richards (1980) as

$$U(\omega) = \frac{U(0)}{[1 + (\omega/\omega_0)]^2} \tag{4.1}$$

where $U(\omega)$ is the spectral amplitude at angular frequency (ω) and U is the square root of the spectral power per unit frequency interval. U has a constant value $U(0)$ at $\omega \ll \omega_0$, but $U(\omega) \propto \omega^{-2}$ at $\omega \gg \omega_0$, where $f_0 = \omega_0/2\pi$ is the corner-frequency.

Aki (1966) assumed that large earthquakes are similar in this respect to small earthquakes. From equation (4.1) we have

$$U(0) = \text{constant} \times \omega_0^{-2} \tag{4.2}$$

Once the above constant is fixed, a family of spectral curves is determined that describes the scaling law of seismic spectra. These curves are shown in Figure 4.1.

It is well known that an observed spectrum is a function of source, path, and receiver. Similarity between earthquakes is a dynamic as well as a static concept. Spectral similarity can best be demonstrated by comparing two earthquakes with identical location and focal mechanism, but with different magnitude. Such a comparison ensures that seismograms from both earthquakes will be affected equally by the medium response, so that all differences between the records will be due to source effects. Berckhemer (1962), whose results were interpreted by Aki to support Aki's ω^{-2} model, collected six pairs of earthquakes from Stuttgart records for the period 1931–1951, with the same epicentre but of different magnitudes (4.5 – 8). He found a strong frequency dependence of amplitude ratio in each case between two earthquakes.

By comparing the ratio of trace amplitudes of Love-waves at a given period for two earthquakes with the ratio of amplitude spectral densities at that period, Aki (1967) showed that both ratios agree well. Thus one can assume that the trace amplitude of surface waves with 20 seconds period are equal to the amplitude spectral density of waves with that period, except for a factor that is independent of the source size. Therefore, the dependence of amplitude spectral density, $|U(\omega)|$, on the magnitude M_s, will be such that $\log|U(\omega)|$ at a period of 20 seconds is equal to M_s plus a constant (Aki, 1967). So that, on a logarithmic scale, the spectra of two earthquakes differing by $\delta M_s = 1.0$ will be separated by 1.0 along the ordinate at a period of 20 seconds.

Thus in Figure 4.1 neighbouring curves are separated by a constant factor at frequency 0.05 Hz, so that the curves are designed by a uniform scale of M_s defined. Therefore one can then

find the amplitude ratio between two earthquakes of any magnitude as a function of frequency. By trial and error, Aki (1967) found the family of spectral curves shown in Figure 4.1, which best fits Berckhemer's observed amplitude ratio. As mentioned, Aki (1966) calculated M_s by adding a constant to the logarithm of spectral amplitudes at 20 seconds. The constant was

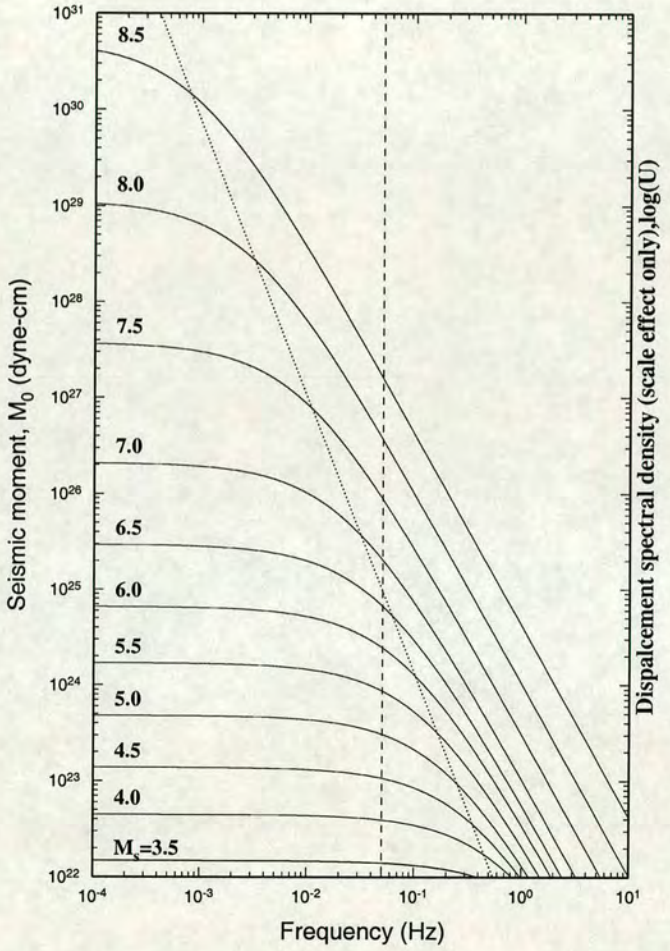

Figure 4.1. Schematic spectra of far-field body-wave displacement observed at a fixed distance from earthquakes with different M_s. The curves follow equation (4.1), giving spectral amplitude $U(\omega)$, and similarity between large and small earthquakes is assumed. The dotted line is the locus of corner-frequency ω_0, the dashed line shows 20 second period used to defined M_s. Recalculated from Aki, 1967, according to ω-square model of Aki. (Note that the predicted magnitude saturation limits implied by these spectra are not numerically correct.)

chosen to give the best agreement between theoretical and observational spectral ratios of pairs of similar earthquakes studied by Berckhemer (1962). Figure 4.1 illustrates several conclusions of spectral studies:

1. The spectra are flat (white) and proportional to M_0 at long period, so the flat part of the spectrum can be used to determine seismic moment.

2. The spectrum falls off as ω^{-2} above the corner-frequency. This is the observed general form or envelope, as the high frequency spectra of earthquakes are generally irregular.

3. The corner-frequency ω_0, which marks the boundary between low and high frequency regimes, increases systematically with decreasing seismic moment or magnitude. For large earthquakes the corner-frequency falls below 0.05 Hz, and for very small earthquakes it appears to have a higher limit, that is, corresponding to $M_s \approx 3$.

4. The 20 second intersection with the spectral curves has equal intervals for about $M_s \leq 5.5$, so in this part M_s is directly proportional to 20 second period, but, for about $M_s > 5.5$, the 20 second period measurement is an unsatisfactory measure of earthquake size. For onset of magnitude saturation in the different scales see Figure 2.2.

5. The corner-frequency is inversely proportional to duration time of rupture ($t_r = \frac{L}{v_r}$, L=fault length, v_r =the average rupture velocity), and, consequently to the linear dimension of the fault.

Considering the far-field spectrum (displacement against frequency) of earthquakes, it has been observed that earthquakes concentrate their seismic energy at frequencies below a limit called the *corner frequency*, generally denoted by ω_0, which decreases as the size of the earthquakes increases. If we look at seismic waves in a band of frequencies that are lower than $(t_r)^{-1}$ (corresponding to frequency of fault movement), the fault displacement appears as a step function, consequently the elastic pulse that it transmits appears as a delta function. So the spectrum of the particle displacement in the waves is white, and its amplitude is approximately a direct measure of the fault displacement.

4.3 Data

Instrumental recording of seismic body and surface waves from earthquakes is essentially limited to the twentieth century, which may be divided into an early instrumental period (before 1964) and a modern instrumental period (after 1964). An important sub-era is the period 1977-present, for which the catalogue of CMT solution is available for most earthquakes having body-wave magnitude of about 5 and greater. This data set provides uniform global coverage for most earthquakes exceeding $M_0 \sim 10^{24}$ dyne-cm.

In the CMT Catalogue the "prime" location information is that of the NEIC PDE, or in 23.5% of cases from its Monthly Listing. Where NEIC determinations are included in the ISC Catalogue, they are always from the Monthly Listing. The NEIC epicentral location and origin

time (in the ISC Bulletin) were compared with those in the CMT Catalogue. Those epicentral estimates whose positions are the same within 0.2 degree in both latitude and longitude and whose times of origin are the same within 5 seconds are considered to be the same earthquake. 9,949 earthquakes with available m_b were matched in this way, of which 6,553 with $h \leq 60$ have an M_s determined by the ISC. This is of course a small number compared with the 22,080 and 110,225 which were used in previous chapters.

For most events in the ISC, NEIC, and CMT catalogues M_s is determined by both the ISC and NEIC. However, minor differences between ISC and NEIC exist in the application of the Prague formula in terms of acceptable ranges of wave period, hypocentral depth, averaging technique, and number of stations contributed to averaged M_s. These differences contribute to scatter in $\log M_0 : M_s$ data.

4.4 Relation between seismic moment M_0 and magnitudes M_s^{Prague} and M_s^t

Ekström and Dziewonski (1988) studied bias in M_s by comparison with seismic moment M_0, and showed evidence of systematic deviations in M_s dependent upon tectonic setting. On the basis that the CMT values of M_0 give a true measure of earthquake size, they concluded that M_s tends to overestimate the strength of most continental earthquakes, and to underestimate the strength from mid-ocean ridges earthquakes. Ekström and Dziewonski (1988) also concluded that estimates of seismic versus aseismic strain release may suffer because seismic moments determined from magnitudes (M_w) can be wrong by as much as a factor of four.

Here the relationship between seismic moment M_0 and two M_s scales, M_s^{Prague} (ISC) and M_s^t (Eq. 3.9)) are compared, using M_0 values obtained from CMT Catalogue, and the conclusions of Ekström and Dziewonski are reexamined.

If the moment release in the earthquake occurred instantaneously and at a single point in space, M_s would be proportional to $\log M_0$ with a proportionality factor of one, because the amplitudes of seismic waves at any period would be linearly proportional to M_0 (assuming that the Green function's are same globally). Due to the finite duration and extent of the earthquake source, the excitation of seismic waves falls off with increasing frequency above some corner frequency; this make the proportionality factor between M_s and $\log M_0$ less than one for large sources because magnitude is normally measured at the same frequency irrespective of earthquake size.

To consider the difference in scatter of M_s about given values of M_0 when applying the Prague formula and the M_s^t formula, I now compare the data based on the new magnitudes M_s^t together with an equivalent dataset based on the Prague formula, which for clarity is referred as M_s^{Prague}. (M_s^{Prague} differs from M_s^{ISC} only in some minor details of computation.) Values

of $\log M_0$ are derived from M_0 values in the CMT Catalogue and are expressed to two decimal places, as for the magnitude values.

Figures 4.2a and 4.2b show the distribution of individual values of M_s^{Prague} and M_s^t for 6,553 earthquakes respectively. As Ekström and Dziewonski (1988) point out, for the smallest earthquakes there is some scatter and the data set is biased towards large values of M_s because of the incomplete reporting of low-magnitude earthquakes and the selection of events to analyse with the CMT method. There is also some scatter for very large earthquakes due to the saturation problem. M_s^{Prague} and M_s^t are each plotted against $\log M_0$, averaged in increments of 0.1 for these 6,553 earthquakes; these plots are shown in Figures 4.2c and 4.2e respectively. Factors contributing to the relationship between M_s^{Prague} and M_0 (see Fig. 4.2c) have been discussed by Hanks and Kanamori (1979), and by Ekström and Dziewonski (1988). To show the range of M_0 values contributing to a given M_s value, Figures 4.2d and 4.2f present averaged surface wave magnitude, again in intervals of 0.1, against $\log M_0$ using the same two M_s formulae respectively. It is well known that M_s for small events is in general determined from significantly fewer stations than is the case for larger events. Therefore, uncertainty of single M_s value probably increases with decreasing magnitude, and also towards earlier time.

An early attempt at a relation between magnitude and seismic moment resulted in the "moment magnitude" scale, M_w (Kanamori, 1977; Hanks and Kanamori, 1979). Ekström and Dziewonski (1988) introduced an empirical global relation between surface wave magnitude and seismic moment. They used reported M_s values from the PDE published by NEIC, and corresponding M_0 values of the CMT Catalogue from 2,341 earthquakes between 1977 and 1987 for which both NEIC and CMT depths are less than 50 km. To remove the dominance of the small earthquakes Ekström and Dziewonski (1988) averaged observations over 0.1 units of $\log M_0$. They then attempted a fit of the data to a hypothesised M_s—M_0 relation. In their (analytical) relation between M_s (as the dependent variable) and $\log M_0$ (as independent variable) they imposed a slope of unity for small events, gradually changing to $\frac{2}{3}$ for moderate to large events. Hence they proposed a global average relationship between M_s and $\log M_0$ as:

$$\bar{M}_s = \begin{cases} k - \frac{(a+b)}{6} + \log M_0 & \log M_0 < a \\ k - \frac{(a+b)}{6} + \log M_0 - \frac{(\log M_0 - a)^2}{6(b-a)} & a \leq \log M_0 \leq b \\ k + \frac{2}{3} \log M_0 & \log M_0 > b \end{cases} \tag{4.3}$$

where k, a, and b were constants to be determined in the fit.

To determine the three unknowns in equation (4.3), Ekström and Dziewonski used only the data with moments in the range 2×10^{24} to 1×10^{28} dyne-cm (i.e., the range between the lower threshold of incompleteness, and the onset of M_s saturation and possible high-end incompleteness). Accordingly they set $k = -10.76$, a =24.5, and b =26.4, obtaining the following global

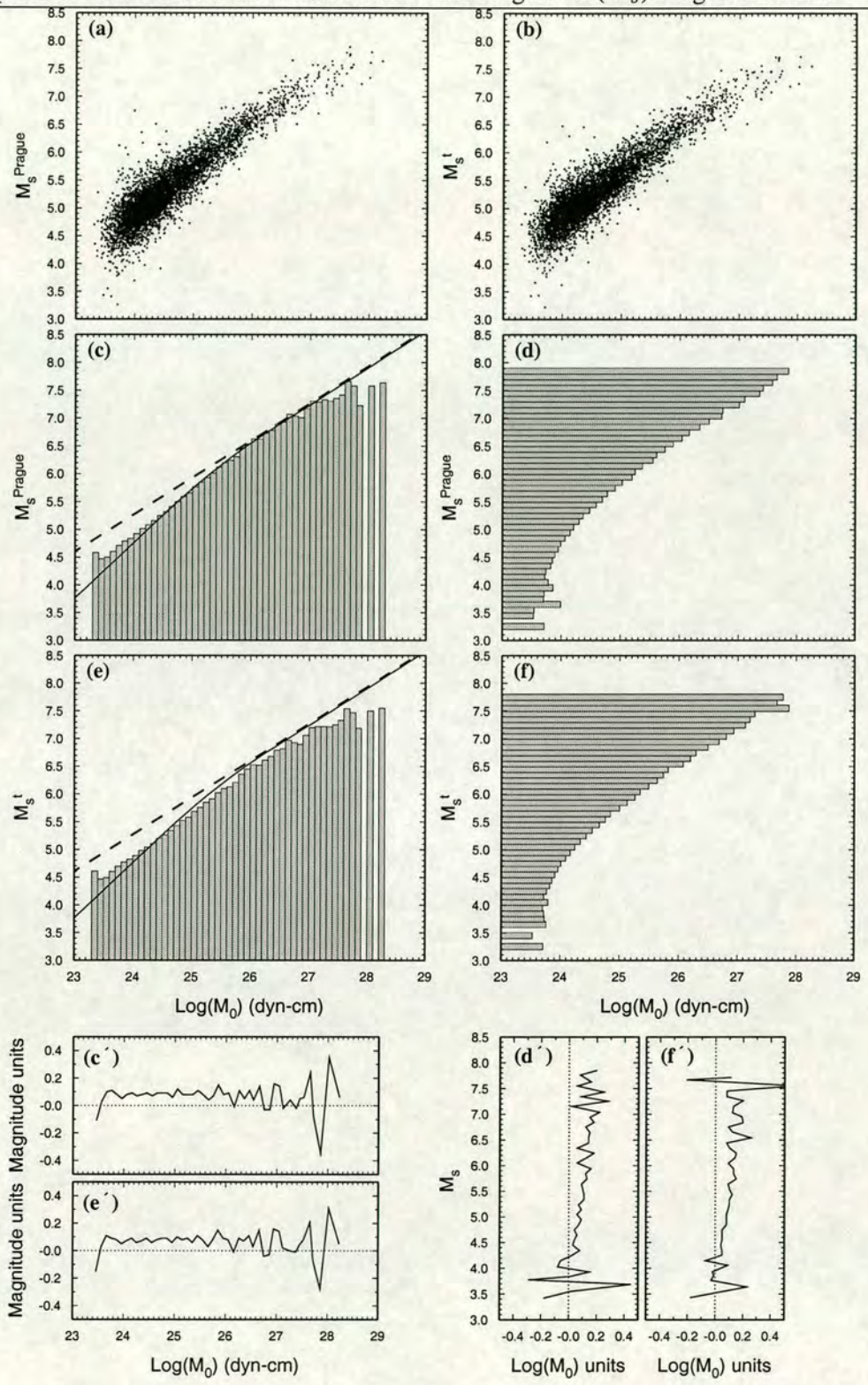

Figure 4.2. (a) Distribution of individual M_s^{Prague} values for 6,553 earthquakes in the CMT Catalogue used in this study. (b) Shows the same using M_s^t values. (c) Distribution of M_s^{Prague} averaged in 0.1-unit-wide ranges of log M_0. (d) Distribution of log M_0 averaged over 0.1-wide intervals of magnitude. (e) and (f) as (c) and (d) but using M_s^t. In (c) and (e) the dashed line shows the relationship obtained by Hanks and Kanamori (1979) under the assumption that the relationship is linear with a slope 2/3, and the solid line shows the analytical relationship developed by Ekström and Dziewonski (1988). (c′)–(f′) Difference between successive values in the averaged data (histograms) of (c)–(f) respectively.

average relationship:

$$\log M_0 = \begin{cases} 19.24 + M_s & M_s < 5.3 \\ 30.20 - \sqrt{92.45 - 11.40 M_s} & 5.3 \leq M_s \leq 6.8 \\ 16.14 + \frac{3}{2} M_s & M_s > 6.8 \end{cases} \quad (4.4)$$

This analytical relationship is included as a solid line in both Figures 4.2c and 4.2e, and that of Hanks and Kanamori (1979) is shown by a dashed line.

The differences between the relationship observed using M_s^{Prague} and using M_s^t formula are now examined. First, the differences between Figures 4.2d and 4.2f at the largest M_s values are not significant as they result from small differences between M_s values for a small number of very large earthquakes. Secondly, M_s values are generally lower in Figure 4.2e than 4.2c. This is because the Figure includes only the larger earthquakes in the ISC Catalogue, whereas the M_s^t scale has been normalised to minimise differences over the whole ISC dataset. Thirdly, in Figure 4.2e the slope does not tend to 1.0 towards smaller magnitudes (even disregarding the region below $M_0 = 2 \times 10^{24}$ dyne-cm which is contaminated by the effect of incompleteness of the CMT Catalogue). Fourthly, it is apparent from the difference in slope of the averaged data in Figures 4.2c and 4.2e that the b-value obtained using the Prague formula on a large dataset will be different from that obtained using M_s^t. Finally, there is significantly less scatter in $\log M_0$ for a given M_s when M_s^t is used. This can be seen from Figures 4.2c′–4.2f′, which show differences between successive values in the averaged data (histograms) of 4.2c–4.2f respectively. This is particularly noticeable in the magnitude range 4.3 to 6.3 (compare Figs. 4.2d′ and 4.2f′), and reflects the reduction in variance resulting from the improved distance term in the M_s^t formula.

The process of fitting the analytical function proposed by Ekström and Dziewonski (1988) (Eq. 4.3) is now applied to the dataset of 6,553 earthquakes between 1978 and 1993. Magnitudes have been recomputed from amplitude and period measurements in the ISC Catalogue, and corresponding M_0 values are taken from the CMT Catalogue. There are some minor differences between this dataset and that of Ekström and Dziewonski (1988) resulting from their use of NEIC rather than ISC data. They used M_s^{NEIC} values from events for which both h^{NEIC} and h^{CMT} are less than 50 km, whereas here data from events with $h^{ISC} \leq 60$ km is used. Also, their data window was 1977–1987 whereas here 1978–1993 is used (Consistent ISC M_s determination began in 1978). Although here the same lower M_0 limit of 2×10^{24} dyne-cm is used for fitting, a more restrictive upper limit of $M_0 = 1.26 \times 10^{27}$ dyne-cm is imposed because saturation and incompleteness in this dataset appear at this lower value.

The result of this analysis is shown in Table 4.1. The first two rows show the resulting fit when the Residual Sum Square Error (RSSE) is minimised in k, a and b using the specified

Table 4.1. Fitting parameters obtained applying the analytical relation of equation (4.3) to the M_s^{Prague} and M_s^t datasets. Details are given in the text.

	M_s formula	Parameters			Residual Sum Square Error (RSSE)[a]				No. of data points[b]			
		k	a	b	r1	r2	r3	R	n1	n2	n3	N
1	M_s^{Prague}	−10.78	24.31	26.41	0.0000	0.0158	0.0243	0.0401	0	21	7	28
2	M_s^t	−10.89	24.31	26.16	0.0000	0.0239	0.0275	0.0514	0	18	10	28
3	M_s^{Prague}	−10.78	24.46	26.32	0.0047	0.0134	0.0245	0.0426	2	18	8	28
4	M_s^t	−10.89	24.46	26.11	0.0108	0.0179	0.0275	0.0563	2	16	10	28

$M_s = \alpha \log M_0 + \beta$

	M_s	α	β	RSSE	Correlation coefficient	N
5	M_s^{Prague}	0.783727±0.012359	−13.875954±0.317816	0.072714	0.996783	28
6	M_s^t	0.763518±0.011680	−13.448340±0.300357	0.064944	0.996971	28

[a] r1, r2, and r3, and respectively the Residual Sum Square Error of the three sections of the relationship in equation (4.3), and R is that for the total relation.

[b] n1, n2, n3, and N are the number of data points used to compute the four RSSE values respectively.

range of M_0. For the case of M_s^t the full relation is given by

$$\log M_0 = \begin{cases} 19.30 + M_s^t & M_s^t < 5.01 \\ 29.86 - \sqrt{86.41 - 11.10 M_s^t} & 5.01 \leq M_s^t \leq 6.55 \\ 16.34 + \frac{3}{2} M_s^t & M_s^t > 6.55 \end{cases} \tag{4.5}$$

It is seen that for both M_s^{Prague} and M_s^t a is equal to 24.31, which corresponds to $M_0 = 2 \times 10^{24}$ dyne-cm; i.e., the left extremity of the data range. This suggests that the observed data do not provide strong evidence of a slope of unity for small events. (In other words, there are no data to support the first line of the relation in equation (4.3)).

The values of k, a and b obtained for M_s^{Prague} are somewhat different from those obtained by Ekström and Dziewonski (1988) (Eq. 4.3)); this is not unexpected on account of small differences between the datasets, though it is also unclear what process was used by Ekström and Dziewonski (1988) to optimise their fit. If a minimum of two points are required to lie in the first linear range of equation (4.3), then for M_s^{Prague} the values of k, a, and b are then almost identical to those given by Ekström and Dziewonski (1988). However, it is less good for M_s^t (see the second two rows of Table 4.1).

When M_s^{Prague} values are used the RSSE is smaller than when M_s^t values are used. Equations (4.4) and (4.5) are plotted in Figures 4.3a and 4.3b respectively; dark histogram bars are used to highlight the range of data used to compute the fit. This shows that the evidence in support of the analytical relation proposed by Ekström and Dziewonski is weaker when the improved M_s^t scale is used.

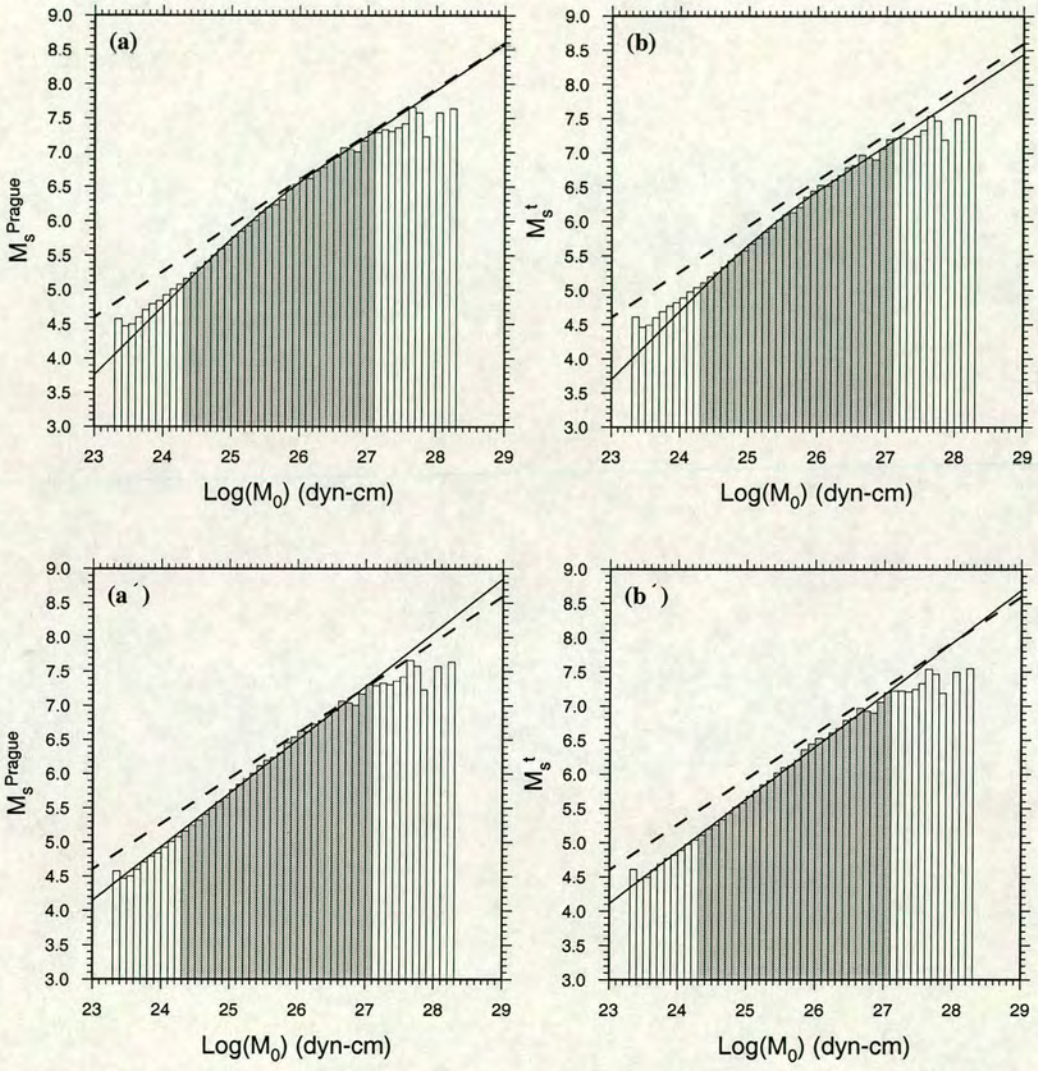

Figure 4.3. Distribution of average M_s values over 0.1-unit-wide intervals of log M_0 for 6,553 earthquakes in the CMT Catalogue. (a) and (a′) show data for M_s^{Prague} values. (b) and (b′) are as for (a) and (a′) but for M_s^t values. In each case the dashed line shows the relationship of Hanks and Kanamori (1979). In (a) and (b) the solid curves represents the analytical relation of equations (4.4) and (4.5) respectively. In (a′) and (a′) the solid lines show the linear regression fit to the same data. In all cases the range of data used in the fits is highlighted in grey.

It is important to compare the success of testing different hypotheses. The decreased quality of fit observed in Figure 4.3b is now compared with the quality of fit obtained using a standard linear regression (see rows five and six of Table 4.1). A better fit is obtained for M_s^t than for M_s^{Prague}. Moreover, it is apparent from both Figures 4.3a′ and 4.3b′, that the good fit extends to smaller moments which were discarded because of data incompleteness. (It is apparent, however, that the goodness of linear fit strongly depends on the selected point of high-end saturation.)

Ekström and Dziewonski's main reason for imposing a lower limit of 2×10^{24} dyne-cm when fitting their relation was the well-known upward biasing of M_s values caused by station threshold effects. However, this specific source of bias is governed by magnitude rather than moment. Figures 4.2a and 4.2b show a large scatter in the M_0:M_s relation for individual events, particularly at smaller magnitude. If data points below, say, $M_s = 4.5$ are affected by station threshold bias (see Figs. 4.2d and 4.2f), then this would have only a marginal effect on Figure 4.3 because moment bins (averaged magnitude over intervals) are predominantly occupied by higher magnitude events down to $M_0 = 1 \times 10^{23}$ dyne-cm. It is therefore concluded that these data are more consistent with a linear fit than with the more complicated analytic relation of equation (4.3) and this is so over the wider moment range from 2.5×10^{23} to 1.26×10^{27} dyne-cm. This conclusion implies that $\log M_0$ is proportional to $1.3M_s$ over a wider magnitude range. The use of maximum-likelihood M_s values (e.g. as used by Stevens and McLaughlin, 1997) may reduce the source of bias described above, because in the maximum-likelihood M_s value the station threshold is taken into account).

Ekström and Dziewonski (1988) stated that the regional variation of M_s in subduction zones does not show a simple pattern, e.g., the Aleutian and New Hebrides regions show predominantly low M_s, while M_s is overestimated for the Tonga-Kermadec region. They suggested possible contributing factors to this anomaly, such as focal depth, faulting geometry, Earth structure near the source, attenuation along the path, radiation pattern, and non-uniform station coverage. Both Abercrombie (1994) and Ekström and Dziewonski (1988) rejected path effects because two of the contrasting areas (New Hebrides and Tonga-Kermadec) are close, so that M_s measurements are made at the same range of stations and along similar paths. Also, Abercrombie (1994) stated that the Tonga-Kermadec earthquakes have a deeper mean depth (41.7 km) than those of the New Hebrides, and this should reduce M_s values in the Tonga-Kermadec area. Abercrombie (1994) assumed that the majority of earthquakes in both areas have thrust mechanisms with strikes parallel to the strike of the subduction zone (New Hebrides 160°, Tonga-Kermadec 195°). On the predominance of observations along the azimuth range 270° to 350°, Abercrombie (1994) concluded that such Rayleigh-wave observations from Tonga-Kermadec earthquakes sample the maximum of the radiation pattern, while those from

earthquakes in the New Hebrides area sample near to a minimum. Abercrombie (1994) therefore concluded that the radiation pattern is the most important factor in the observed anomaly of M_s values in these regions.

Figure 4.4 shows the comparison of M_s versus $\log M_0$ plots for the above subduction zones using the M_s^{Prague} and M_s^t formulae. This Figure shows that for some large earthquakes in all three regions M_s^t is smaller than M_s^{Prague}. However, this is not significant in the Aleutian Arc or the New Hebrides region. In the Tonga-Kermadec region estimated M_s^t values are reduced for most large earthquakes compared with M_s^{Prague} values (see Figs. 4.4c and 4.4c′).

Of course, the dataset used here is different from that used by Ekström and Dziewonski (1988), and Abercrombie (1994). The histograms of distance observations, calculated depth by ISC, and azimuthal observations for data used in Figure 4.4, are shown in Figure 4.5. The mean magnitude residuals (M_s^t(event) $-$ M_s^t(station)) in 1° azimuth increments are plotted as red radial bars in Figures 4.5a″, 4.5b″ and 4.5c″ for each region. Figures 4.5b and 4.5c show that some observations have been measured at greater distances especially in the Tonga-Kermadec area, and confirm the resulting differences between estimated M_s^{Prague} and M_s^t values which were observed in Figures 4.4c and 4.4c′. This is expected because at greater distances e.g., Δ>50° the Prague formula overestimates M_s in comparison with the M_s^t formula (see Fig. 3.10c).

Comparison of depth observations in Figures 4.5a′, 4.5b′ and 4.5c′ shows that the depths calculated by ISC for earthquakes in the New Hebrides area have apparently not been much affected by artificial effects (fixing 0, 10, or 33 km in the case of a negative depth or otherwise unstable value), while for the Aleutian and the Tonga-Kermadec areas a depth of 0, or 33 km has been set for many earthquakes. If these earthquakes (i.e., h^{ISC} =0, and 33 km) are excluded from the dataset of the Tonga-Kermadec area, then the mean depths for the New Hebrides and the Tonga-Kermadec are approximately the same. However, if earthquakes with a calculated depth of 0 and 33 km are excluded from the Tonga-Kermadec data, the scatter of M_s is reduced, but it still shows that estimated M_s values for most earthquakes in this area are larger than those in the New Hebrides area for earthquakes with the same $\log M_0$ values. So, as Abercrombie (1994) stated, the depth effect is not the major factor for observed differences in M_s values between the New Hebrides and Tonga-Kermadec.

Also, comparison of the mean magnitude residuals with azimuth in Figures 4.5b″ and 4.5c″ shows that, contrary to Abercrombie's conclusion, the estimated individual station magnitudes are smaller than event magnitudes in the azimuth range 270° to 350° i.e., M_s^t(event) $-$ M_s^t(station) > 0 (red radial bars plotted to the outside of circle). In both New Hebrides and Tonga-Kermadec regions the magnitude residuals in the azimuth range 270° to 350° are almost the same. As is observed in Figures 4.5b″ and 4.5c″, it seems that the path effect is an important

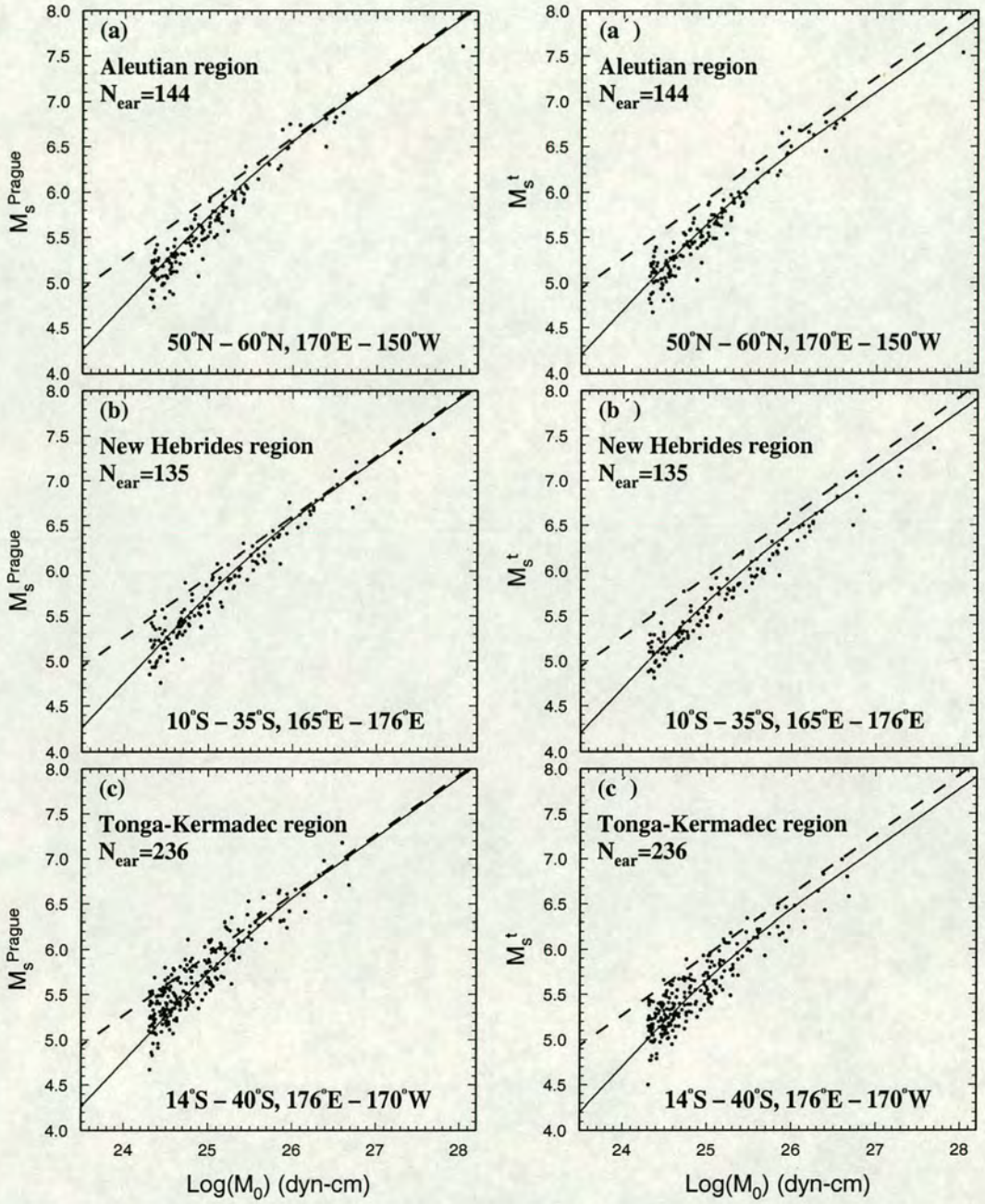

Figure 4.4. Comparison of M_s versus $\log M_0$ plots in three subduction zones, using the M_s^{Prague} and M_s^t formulae. In each case the data include earthquakes with thrust mechanism (i.e., when the dip of the T axis exceeds 50°) for earthquakes which are common to the ISC and the CMT Catalogues, between 1978 and 1993 (values of δ_T are taken from the CMT). The limits of each area (latitude and longitude) have been shown on each graph. In the case of (a), (b), and (c) the solid line represents equation (4.4) while in (a′), (b′), and (c′) it represents equation (4.5). In each case the dashed line shows the relationship of Hanks and Kanamori (1979). N_{ear} indicates the number of earthquakes.

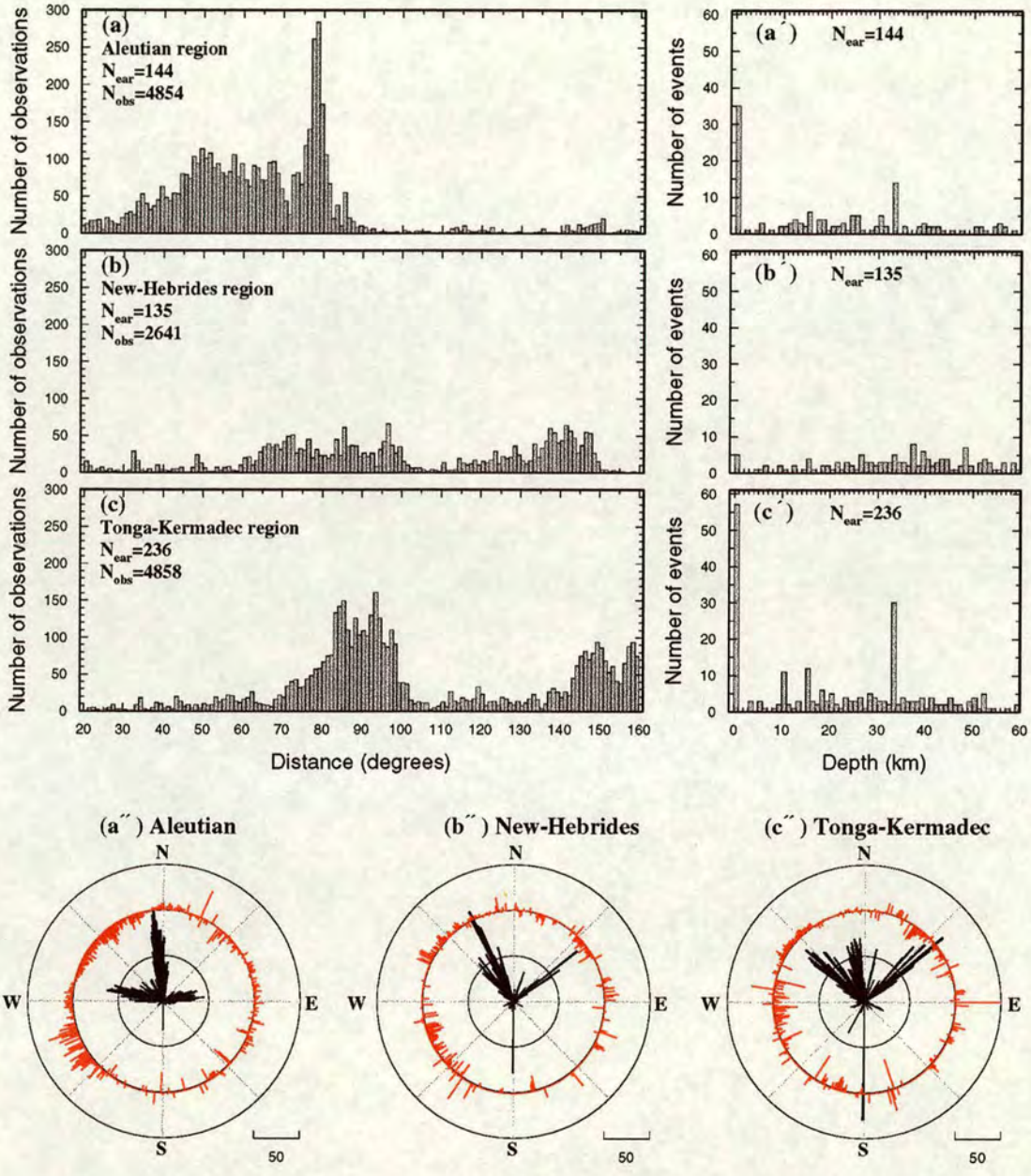

Figure 4.5. Distributions of distance observations, calculated depths, azimuthal observations, and magnitude residuals in three subduction zones. In (a″), (b″) and (c″) the black radial bars show the number of observations for each azimuth, and their linear scale is shown. The red radial bars represent the magnitude residuals, plotted to the outside of the circle for positive deviations (M_s^t(event) > M_s^t(station)) and to the inside of the circle for negative deviations. The length of the red bars is proportional to the absolute value of the mean deviation, where the largest red bar corresponds to a deviation of 1.36 magnitude units. N_{ear} and N_{obs} indicate the number of earthquakes and the number of observations respectively.

factor for the difference of observed surface waves in these regions, and this suggests that observations approximately along NE-SW directions give a large value for station magnitude i.e, $M_s^t(\text{event}) < M_s^t(\text{station})$. The azimuthal observations (black radial histograms) in these Figures show that there are more observations in the azimuth range 30° to 60° in Tonga-Kermadec than in the New Hebrides.

As mentioned before, Ekström and Dziewonski (1988) and Abercrombie (1994) have pointed out that the average M_s over 0.1-wide intervals of $\log M_0$ for observation in the New Hebrides region are smaller than those M_s values obtained from the analytical relationship of equation (4.4) for given $\log M_0$ values, while for observation in the Tonga-Kermadec region the reverse is true. As a result, most of the anomaly observed by Ekström and Dziewonski and Abercrombie between M_s values in the New Hebrides region and those in Tonga-Kermadec region is due to the inadequate distance calibration term in the Prague formula. For the M_s^t formula this anomaly is substantially reduced. For the remainder of the anomaly I conclude that the path effect is more likely to be responsible than the other possible contributing factors (e.g., radiation pattern, non-uniform station coverage, attenuation in path, etc.) addressed by Ekström and Dziewonski.

To compare average M_s at different tectonic settings defined as "oceanic ridges and fracture zones", "continental", and "subduction zones"; the data were classified using seismic region number, and M_s values were averaged over 0.1-wide intervals of $\log M_0$. In Figure 4.6 average M_s versus $\log M_0$ are compared for different tectonic regions. As this Figure shows, the continental earthquakes have a larger M_s than earthquakes along Mid-oceanic ridges and subduction zones with the same seismic moment. However, the largest earthquakes occurred in subduction zones. Mid-oceanic ridge earthquake zones have a smaller M_s than earthquakes of other regions. The difference between these regions is not constant and it increases with increasing seismic moment. Also, the number of individual data points controls the scatter of averaged data.

Comparison of M_s^t with M_s^{Prague} for different regions in Figure 4.6 shows that the scatter for M_s^t is less than that for M_s^{Prague}, and in all regions the standard deviation of data points is less than those for M_s^{Prague}. Also, the regional differences in M_s are probably separated when M_s^t is used rather than M_s^{Prague}.

4.5 Depth effect on the determination of M_s

The M_s scale, as defined by the Prague formula, is strictly valid only for crustal events. Also, the M_s^t formula does not include a depth effect. Remarkably few attempts can be found in the literature to include a depth correction for M_s. The theoretical relationship between amplitude and depth for Rayleigh waves in homogeneous media (see Bullen and Bolt 1985, p. 113),

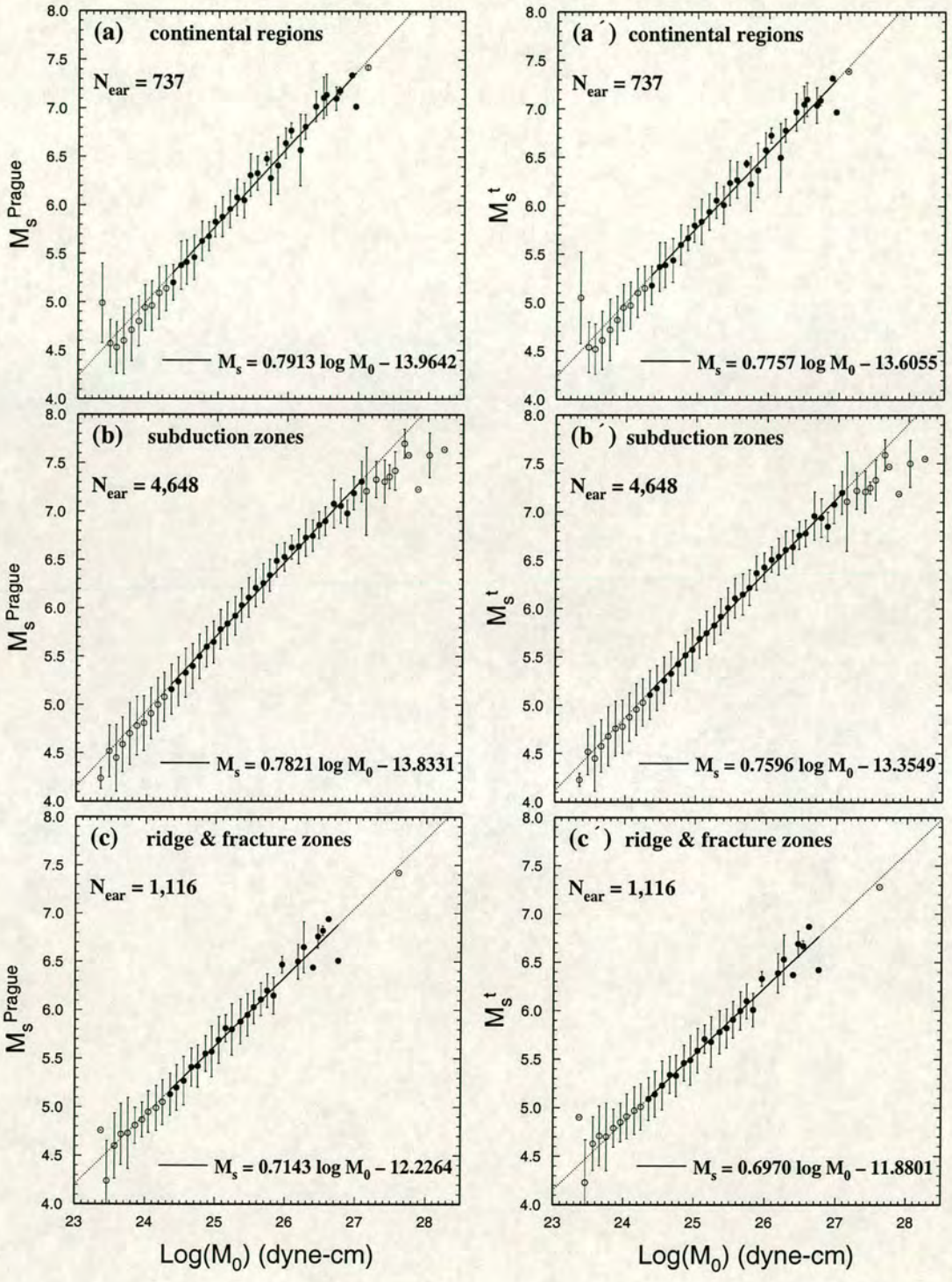

Figure 4.6. Average M_s over 0.1-wide intervals of $\log M_0$ against $\log M_0$ with standard deviations in different tectonic regions. (a) Continental regions. (b) Subduction zones. (c) Mid-oceanic ridge including fracture zones. (a′)–(c′) are as (a)–(c) but for M_s^t formula. In each case the solid line represents a linear regression line to the data points in the seismic moment range 2.5×10^{23} to 1.26×10^{27} dyne-cm. The data points in this range are shown by filled symbols. N_{ear} shows the number of earthquakes in each region which have been classified using seismic region number.

shows that the depth dependence of amplitude would be more purely exponential for larger depth. Båth, (1977) concluded that the magnitudes could be expected to vary linearly with h for $h > 50$ km. He extended his earlier result (Båth, 1952) and a depth correction δM_s for M_s defined as the difference between calculated $(M_s)_c$ and observed $(M_s)_o$:

$$\delta M_s = (M_s)_c - (M_s)_o = c(h - 50), \tag{4.6}$$

where h is focal depth in kilometres. For a given m_b value Båth (1977) calculated $(M_s)_c$ values using twelve regional regressions between M_s and m_b which were already determined according to epicentre location for data with $50 \leq h$. His data included the published $(M_s)_o$ and m_b in the Uppsala bulletin (containing observations from seismic stations at Uppsala and Kiruna) from January 1970 to April 1975. Båth found c =0.0088 for $50 < h < 100$, but for $h > 100$, contrary to theory, $c(h - 50)$ was constant $= 0.38 \pm 0.03$. In 1984 Båth calculated $(M_s)_c$, using a global empirical relation of $M_s = 1.83m_b - 5.45$ based on shallow earthquakes (for details see Båth, 1984), instead of different regional relations, and obtained:

$$\delta M_s = (0.0095h - 0.41) \pm 0.03 \qquad \text{for} \qquad 50 \text{ km} \leq h \leq 100 \text{ km}, \tag{4.7a}$$

$$\delta M_s = (0.0003h + 0.46) \pm 0.10 \qquad \text{for} \qquad 100 \text{ km} < h. \tag{4.7b}$$

In equation (4.7b), as in his early results (Båth, 1952, 1977), δM_s steadily increases with increasing depth.

Therefore, in order to use M_s as a measure of a size that is valid for events at all depths, a depth correction for sub-crustal earthquakes is required. However, some studies have shown that, to estimate unbiased M_s, a depth correction is necessary even in the crust. Panza *et al*, (1989), obtained a depth correction term as

$$\delta M_s(h) = 0.0174h - 0.52, \tag{4.8}$$

where h is depth in km. Equation (4.8) is based on a theoretical M_s calibrating function for Love waves. This shows that the depth effect is more than one magnitude unit comparing surface-focus with a depth of about 60 km.

ISC determines M_s for earthquakes with a calculated depth of $h \leq 60$ km, although for some earthquakes with $h > 60$ km M_s values are available in the ISC Catalogue. However, these represent only a small number (1,050 out of 23,130 i.e., 4.5%) of all earthquakes with available M_s. In Figure 4.7a M_s^t values averaged over 0.1-wide intervals of sorted $\log M_0$ are plotted against averaged $\log M_0$ values. Also, values of $\log M_0$ averaged over 0.1-wide intervals of sorted M_s^t values are plotted in Figure 4.7b. The data are sorted in three groups

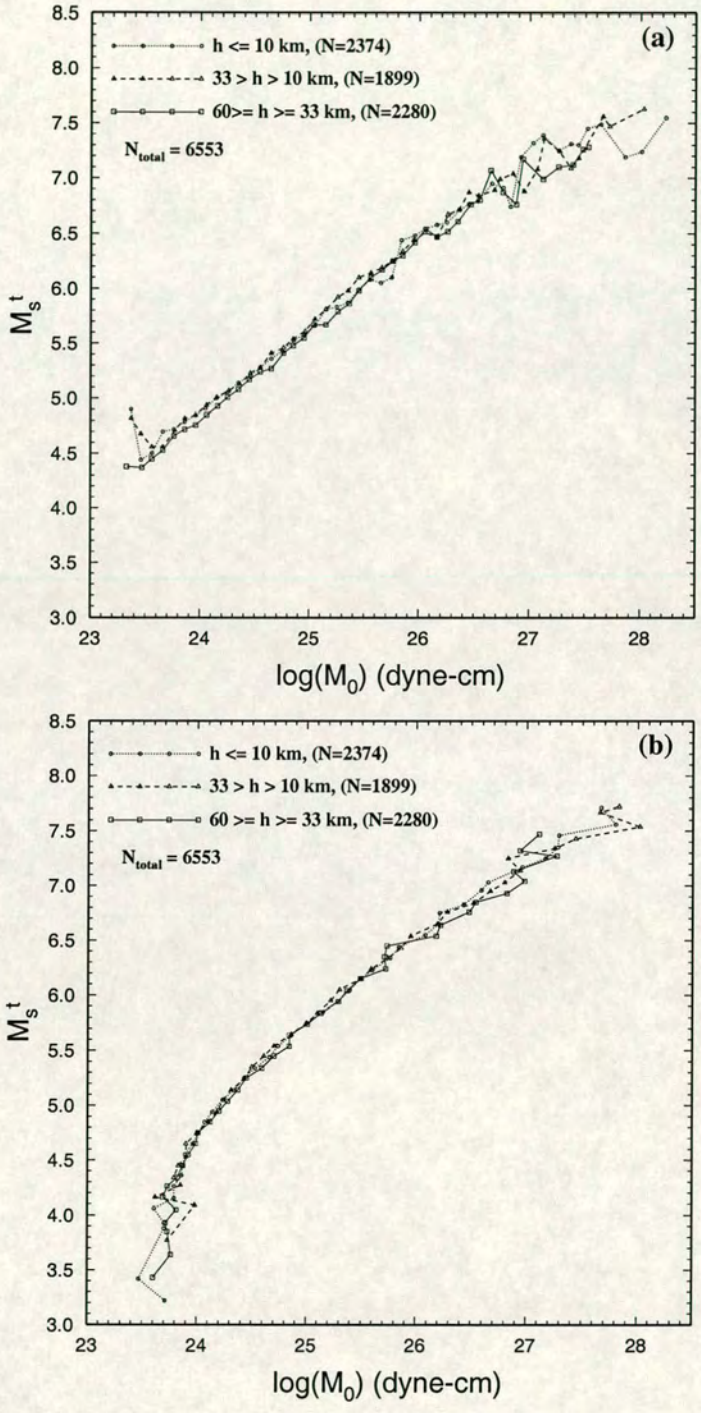

Figure 4.7. Plot of M_s^t against $\log M_0$ for 6553 earthquakes with $h^{ISC} \leq 60$ km. (a) Averaged M_s^t values over 0.1-wide intervals of $\log M_0$. (b) Averaged $\log M_0$ values over 0.1-wide intervals of M_s^t. The data were grouped according to ISC depth, and show no significant separation.

of; $h \leq 10$, $10 < h < 33$, and $33 \leq h \leq 60$ km according to the ISC depths. Figure 4.7 shows that M_s values of earthquakes with a depth of between 33 and 60 km, are underestimated by approximately 0.1 magnitude units in comparison with earthquakes which occurred at depths of $h < 33$ km. If Figure 4.7 is replotted with the exclusion of artificial depths (0, 10, and 33 km), the above discrepancy increases to 0.15 magnitude units. As Figure 4.7 shows, the observations of M_s do not support the results of Panza *et al*, (1989) who include their theoretical correction for the effect of depth (Eq. (4.8)). However, the observations do show that M_s determinations are biased due to a depth effect.

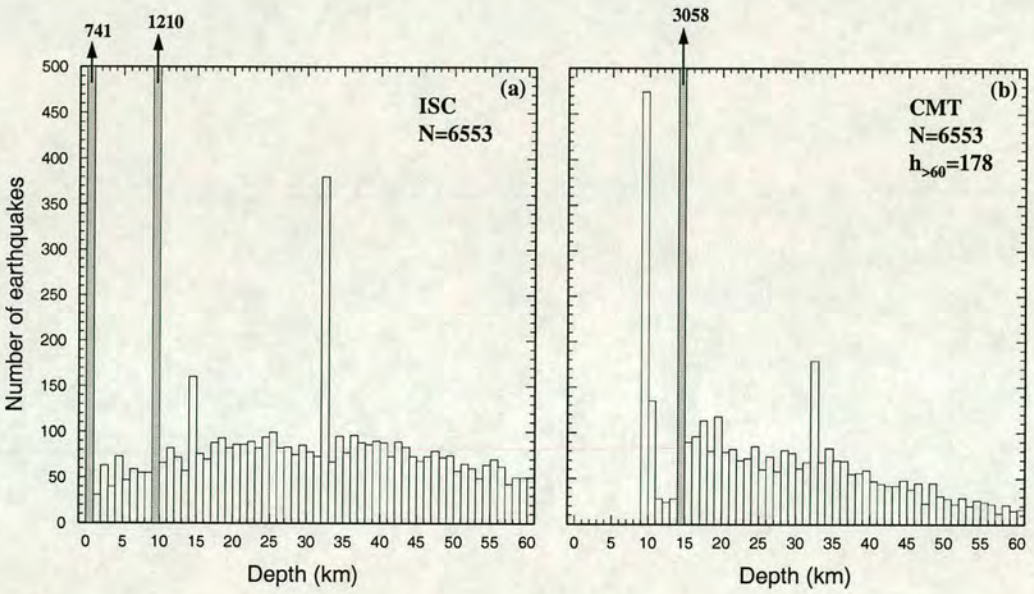

Figure 4.8. Comparison of ISC depth with CMT depth for 6,553 shallow earthquakes with $h^{ISC} \leq 60$ km.

The uncertainty of depth determination is the main problem in applying a depth correction to the estimation of M_s. Figure 4.8 shows a comparison of depths from the ISC Catalogue with those from the CMT Catalogue for 6,553 earthquakes. It is clear that depth values of 0, 10, 15, and 33 km are artificial, since these represent characteristic depths in the inversion algorithm. The CMT technique (long-period body-waves with a period of about $\geq$ 45 sec) results in poor centroid depth resolution for shallow sources. The process of spatial parameter determination will depend on λ (wave length) used in observation. Interference with the surface will degrade depth determination. If depth $\ll \lambda$ the earthquake will not be resolved. In the CMT technique, because of the instability of the solution for $M_{r\theta}$ and $M_{r\phi}$ (two components of the centroid moment tensor associated with vertical dip slip) for shallow depths compared

with a wavelength, the depth is not allowed to be less than 10 km, and in cases for which the centroid depth becomes less than 10 km it is usually fixed at 10.0 km or 15.0 km (Dziewonski and Woodhouse, 1983). So the CMT technique gives a depth for any earthquake of at least 10 km, and locates the majority of earthquakes in the mid to lower crust (10–20 km). This distorts the true distribution of seismicity, and M_s values, with depth.

To show the possible depth effect on estimated M_s values, individual values of M_s^t, $\log M_0$, $M_s^t - \log M_0$ and $M_s^t - M_w$ are plotted against ISC depth in Figures 4.9a–4.9e. These quantities after averaging over 1-kilometer intervals of depth, are plotted in Figures 4.9a′–4.9e′. Also, individual and averaged values of $\log M_0$, $M_s^t - \log M_0$ and $M_s^t - M_w$ are plotted against CMT depth in Figure 4.10 as well as in Figure 4.9. The equation of regression line for averaged data in the depth range 10 km $< h <$ 60 km is shown on each graph. In Figure 4.9 average M_s^t, $\log M_0$, $M_s^t - \log M_0$, and $M_s^t - M_w$ increase from the surface to 10 km, then they steadily decrease with depth. All graphs in Figures 4.9 and 4.10 show an approximately linear decrease in the mean of these quantities with increasing depth from 10 to 60 km. Remember that in reality there is significant error in depth which is masked by averaging in depth.

Assuming that the Harvard CMT value (M_0) gives an unbiased estimate of the released energy with depth, Figures 4.9c′and 4.10a′ show that CMT seismic moment also systematically decreases with depth for $h > 10$ km. Possible reason for $\log M_0$ and M_s decreasing with depth could relate to either source or path effects. Alternatively, there could be a real decrease in the energy of the average earthquake with increasing depth, in which case we expect a decrease with depth even for unbiased M_s. Although we do see this, the slope of the regression line for M_s^t against depth in Figure 4.9b′ is greater than that for $\log M_0$ against depth in Figure 4.9c′. Therefore, there is a small but systematic bias due to depth effect on estimated M_s. The difference between the slopes of the regression lines in Figures 4.9b′ and 4.9c′ suggest a correction of $\delta M_s = 0.0026h$ for estimated M_s values of earthquakes with a calculated depth of between 10 km and 60 km. This depth-correction term for $h = 60$ gives a correction value of $\delta M_s = 0.156$ which is very close to the correction values of 0.12 and 0.23 which are obtained plotting $M_s^t - \log M_0$ and $M_s^t - M_w$ residuals respectively against depth (see Figs. 4.9d′ and 4.9e′). However, uncertainty in estimated depths for some earthquakes are large, and applying a depth correction in the determination of M_s for these earthquakes itself may introduce bias.

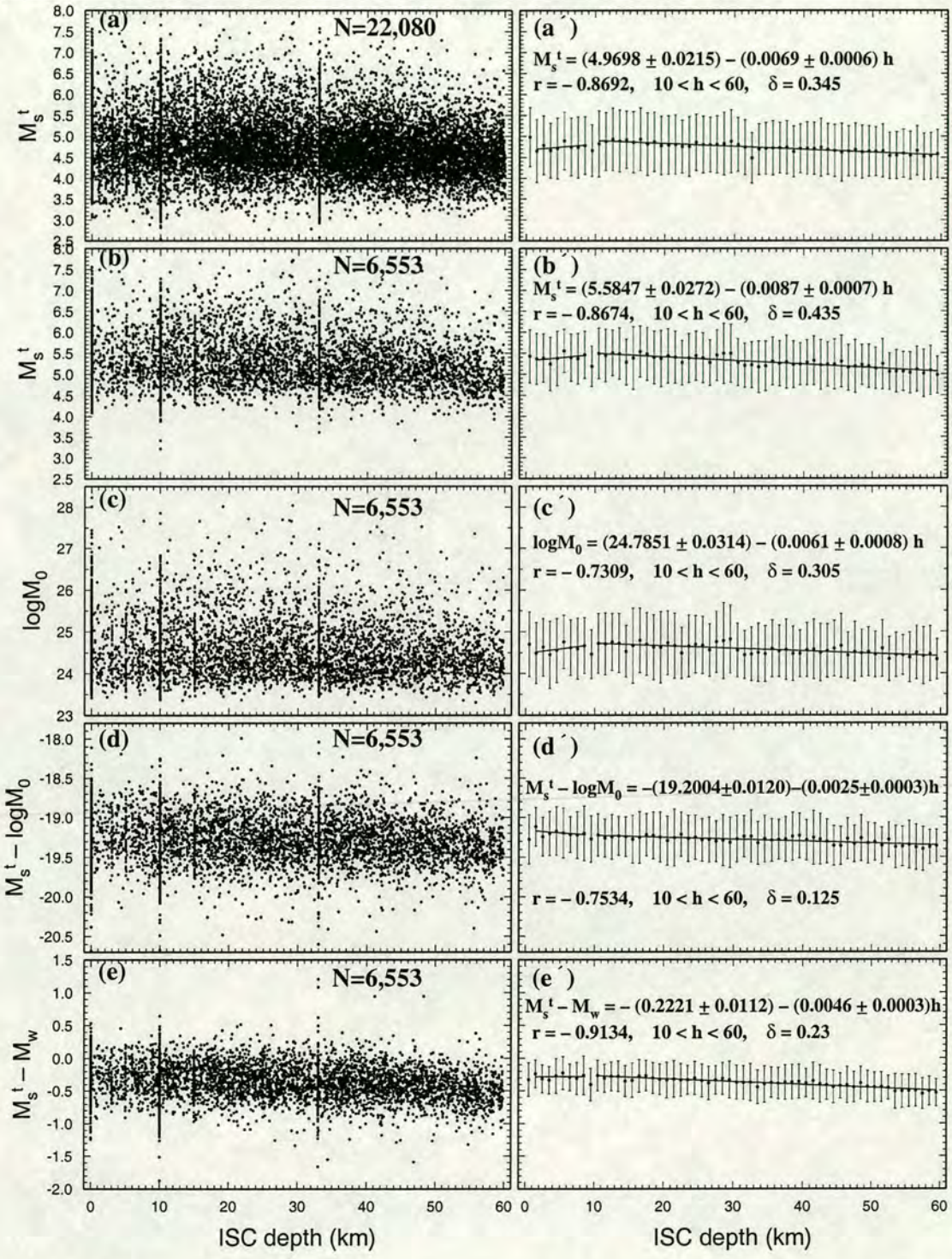

Figure 4.9. M_s^t, $\log M_0$, $M_s^t - \log M_0$ and $M_s^t - M_w$ against ISC focal depths for shallow earthquakes. (a)–(e) for individual data points. (a′)–(d′) for the data averaged over 1-kilometre intervals, then plotted together with standard deviations. N=22,080 for all earthquakes with available M_s and with a calculated depth $h \leq 60$ km in the ISC Catalogue between 1978 and 1993. N=6,553 for earthquakes which matched between ISC and CMT Catalogues in that period. In each case of (a′)–(e′) the solid lines represent the regression lines for data group of $0 < h < 10$ and $10 < h < 60$. For the later case ($10 < h < 60$) equation of regression line is shown on each graph. r= correlation coefficient. δ = difference of relevant quantity between a depth of 10 km and 60 km according to the regression line.

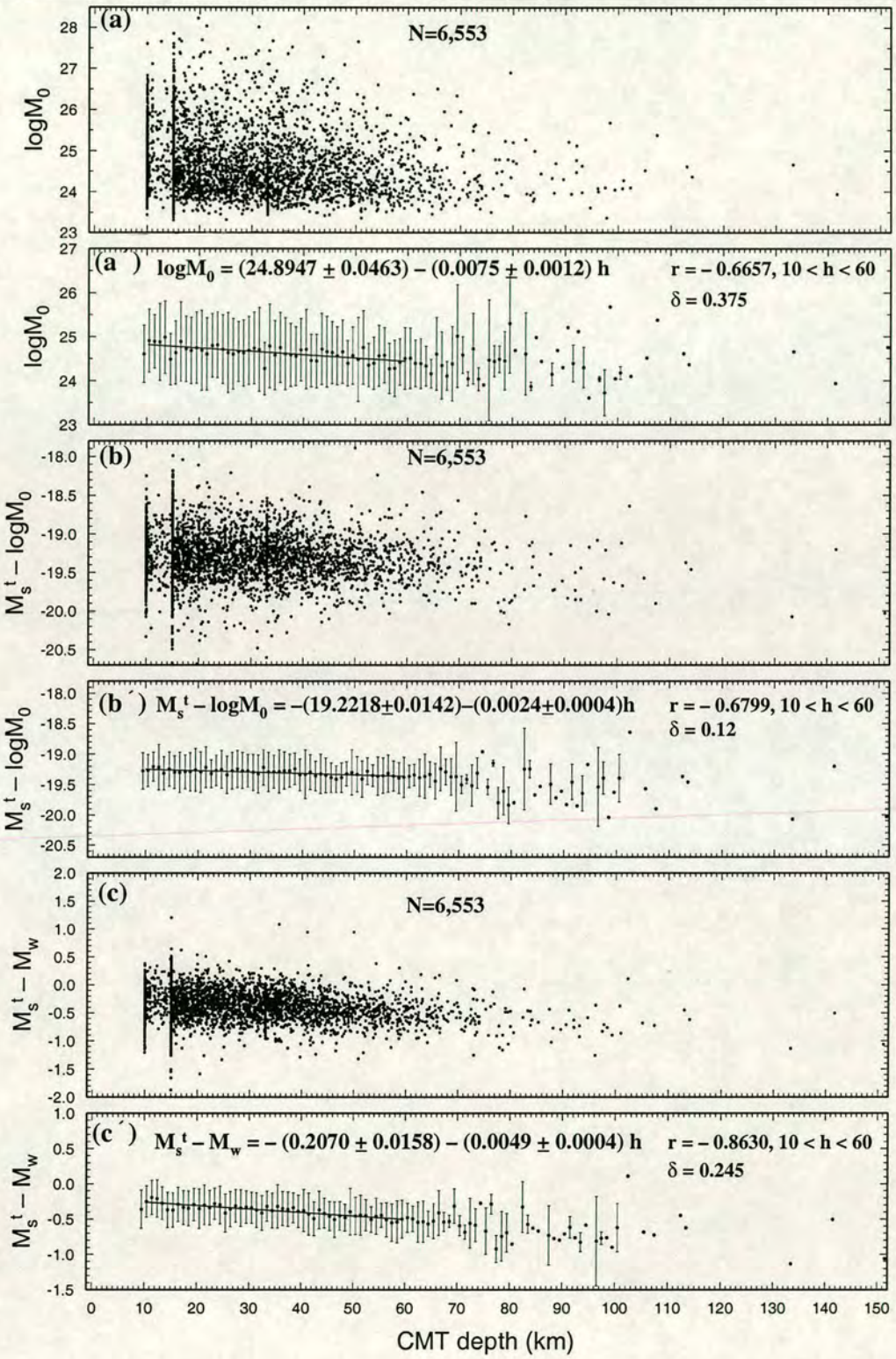

Figure 4.10. $\log M_0$, $M_s^t - \log M_0$ and $M_s^t - M_w$ against CMT focal depths for 6,553 earthquakes with $h^{ISC} \leq 60$ km. (a), (b) and (c) for individual data points. (a′), (b′) and (c′) for the data averaged over 1-kilometre intervals, then plotted together with standard deviations. In each case of (a′), (b′) and (c′) the solid line represents the regression line for data in depth range $10 < h < 60$. r=correlation coefficient. δ = difference of relevant quantity between a depth of 10 km and 60 km according to the regression line.

4.6 Seismic moment versus surface wave magnitude

As Figure 2.2 shows, the relationship between seismic moment and surface-wave magnitude is not linear over the whole range of magnitudes. Observations (Fig. 4.2) show that a linear relation will only provide an acceptable fit to a limited range of seismic moments. Most earlier studies have assumed linear relation between surface-wave magnitude and seismic moment. Under the hypothesis of constant stress drop, theoretical models predict that $\log M_0$ and M_s are related by a linear law as

$$\log M_0 = A + BM_s. \tag{4.9}$$

The slope (B) commonly found in the literature (e.g., Kanamori and Anderson, 1975; Purcaru and Berckhemer, 1978; Hanks and Kanamori, 1979; Dziewonski and Woodhouse (1983)) is around 1.5. However, that data and the range of magnitude they used were slightly different. Moreover, the slope of equation (4.9) found 1.5 for local magnitude M_L e.g., Aki, 1969; Thatcher and Hanks, 1973; etc. Also, as was discussed in section 4.4, there is evidence that the slope in equation (4.9) departs from 1.5 (Ekström and Dziewonski, 1988, Caputo, 1983). So according to the Kanamori and Anderson (1975) model (constant stress drop), if the theoretical correlation coefficient in equation (4.9) is large, then the data set contains events with almost constant stress drop, and in the case of low correlation the reverse is true (Romanelli and Panza, 1995). Romanelli and Panza (1995) have shown that the application of equation (4.8) to M_s values of large events in different tectonic settings give a high correlation coefficient in equation (4.9), and that the slope moves towards 1.0 in global data, whereas for regional data it can vary from about 1.0 to 2.0.

4.6.1 Regression analysis of $\log M_0$ versus M_s

The appearance of the graphs in Figures 4.2d and 4.2f show that relations of $\log M_0$ with M_s over the whole range of magnitudes in general are non-linear. In this study, by considering M_s as the independent variable and $\log M_0$ as the dependent variable, using the same procedure that Johnston (1996) used for small number of earthquakes from Stable Continental Regions (SCR), an attempt is made to fit the best regression to a large global dataset, and this is compared with the other results. First the regression models are fitted to the data (Fig. 4.11) and residuals (observed minus calculated values) are obtained. The fit is repeated after removing outlier points determined from the residual (for calculation outlier see Appendix A). As was observed in Figures 4.2b and 4.2f, due to incompleteness of the catalogue the scatter of data at small magnitudes is large. For this reason only the data of $M_s > 3.7$ is used in the regression analysis. Table 4.2 provides brief statistical results of the regression models. The statistic software of S-PLUS (1992) was used in the regression analysis.

Table 4.2. Regression parameters of linear fitting and different types of non-linear fitting such as quadratic, cubic, and exponential with statistical comparison. Regression models: $\log M_0 = \sum_{j=1}^{p} \beta_j M^{j-1}$, $\log M_0 = \beta_1 + \beta_2 e^{\frac{-\beta_3}{M}}$.

M (M_s)	type of data	type of fit	β_1	β_2	β_3	β_4	ν^a	outliers removed	$\sigma_{res}{}^b$	R^c	F-value^d	z^e
First fit (with outliers)	Individual	linear	18.9000	1.0703	–	–	6546	–	0.2877	0.8221	30260	3.913
		quadratic	25.1133	-1.2003	0.2048	–	6545	–	0.2692	0.8443	17750	3.913
		cubic	33.3167	-5.6578	1.0027	-0.0470	6544	–	0.2682	0.8454	11930	3.913
		exponential	23.302	90.5106	22.9094	–	6545	–	0.268852	–	–	3.913
	Averaged	linear	18.9524	1.0989	–	–	39	–	0.2701	0.9604	945	2.508
		quadratic	25.3589	-1.2276	0.2023	–	38	–	0.08195	0.9964	5228	2.508
		cubic	32.5798	-5.2014	0.9114	-0.0411	37	–	0.06207	0.998	6202	2.508
		exponential	23.4208	95.1137	23.5875	–	38	–	0.0759973	–	–	2.508
Second fit (removing outliers)	Individual	linear	18.8996	1.0705	–	–	6534	12	0.2815	0.8273	31310	3.905
		quadratic^f	25.1079	-1.2015	0.2052	–	6534	11	0.2634	0.8506	18590	3.906
		cubic	33.9557	-6.0107	1.0664	-0.0508	6532	12	0.262	0.8522	12550	3.905
		exponential	23.2965	90.4049	22.8737	–	6534	11	0.263041	–	–	3.906
	Averaged	linear	18.9513	1.0996	–	–	39	–	0.2675	0.9612	966	2.508
		quadratic	25.2871	-1.2012	0.2001	–	38	–	0.08213	0.9964	5307	2.508
		cubic	32.7349	-5.2998	0.9315	-0.0424	37	–	0.06074	0.9981	6480	2.508
		exponential	23.4133	93.1541	23.4177	–	38	–	0.0757128	–	–	2.508

[a] $\nu = N - p$ where ν is degrees of freedom, N is number of data points, and p is number of regression parameters.

[b] σ_{res} is standard deviation of the residuals in $\log M_0$ units according to fitting model.

[c] R is *squared multiple-correlation coefficient* (Multiple R-Squared).

[d] F-value is variance ratio of two populations with sizes of N_1 and N_2 i.e., $F = \frac{s_1^2/\sigma_1^2}{s_2^2/\sigma_2^2}$ where s_1 and s_2 are the variance of populations.

[e] z is a dimensionless deviation $z = |x - \mu|/\sigma$ i.e., the numerical multiplier of σ_{res}, such that $C = \pm z\sigma_{res}$ that is outliers limit. Value of z is taken from standard tables which contain the probability function $P_G(x; \mu, \sigma)$ (which is calculated using $P(z, \sigma) = 1 - \frac{0.5}{N}$) versus z for the Gaussian or normal error distribution (see Appendix A).

[f] selected as the best regression.

In any type of least-squares fit, the distribution of repeated data points affects the result of the fit, so to remove the dominance of smaller earthquakes which occur more frequently, the observations were reduced by the average of the observed $\log M_0$ values over ranges of 0.1 units of M_s. Here both data sets (individual and averaged data) in the regression analysis are used. Figure 4.11 shows the regression fit of $\log M_0$ against M_s for global data.

The statistical results of the regression models which are listed in Table 4.2, show that in the linear model the standard deviation of residuals (σ_{res}) is greater than those in the non-linear models, and the *squared multiple-correlation coefficient* of linear fit is smaller than those for non-linear fits. Also, the F-value in the linear fit for individuals data points, is much greater than those for non-linear fits. For the averaged data the reverse is true. Therefore, the linear fit is significantly worse than in all of the non-linear models.

The appearance of Figure 4.11 shows that the difference between the non-linear fits, for

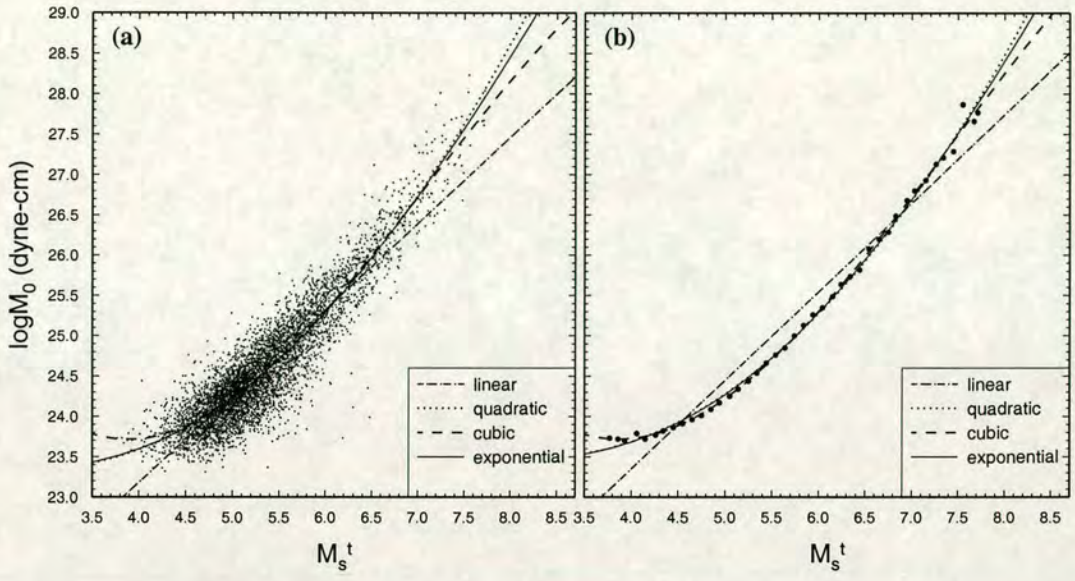

Figure 4.11. Linear, quadratic, cubic, and exponential regression of $\log M_0$ against M_s on global data. (a) For individual data points. (b) For observation averaged in 0.1-unit-wide ranges of M_s. In both cases dash-dotted, dotted, dashed, and solid lines represent respectively, linear, quadratic, cubic, and exponential regressions.

small earthquakes (about $M_s < 4.5$) and for very large earthquakes (about $M_s > 7.8$) is significant, but for intermediate events it is relatively insignificant. The cubic fit gives smaller residuals but offers only a slight improvement at the expanse of an extra parameter. It underestimates $\log M_0$ for very large earthquakes ($M_s \gtrsim 7.7$) and overestimates $\log M_0$ for small earthquakes ($M_s \lesssim 4.5$). Figure 4.12 shows the regression fits made to the data after eliminating the outlier points (according to the regression parameters obtained in the first fit). Table 4.2 gives the regression parameters and statistical comparison of linear, quadratic, cubic, and exponential fits. Table 4.2 shows that the difference of regression parameters for data before and after rejecting outliers is not significant, because the correlation coefficient, the standard deviation of residuals, and F-value do not change much for the case of removing outliers in comparison with those in the first fit (with outliers).

I conclude from the above that using a cubic model for an empirical relation between $\log M_0$ and M_s is not preferred. The quadratic fit has a minimum point at small magnitude and this model is not applicable for very small events, because a quadratic model is a symmetric function and predicts larger $\log M_0$ for any given M_s value which is less than minimum point. The exponential model does not pass through a certain minimum at small magnitude and may be applicable for very small events, but for very large earthquakes it underestimates $\log M_0$ by

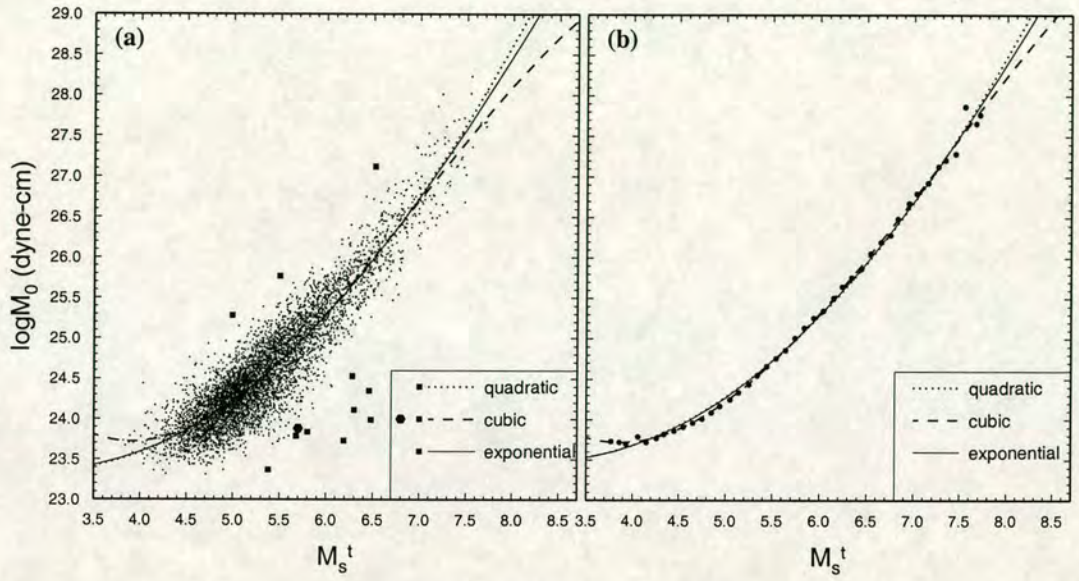

Figure 4.12. Quadratic, cubic, and exponential regression of $\log M_0$ against M_s on global data, which is used in Figure 4.11, but with eliminating outlier points in fitting. (a) For individual data points. (b) For observation averaged in 0.1-unit-wide ranges of M_s. In both cases dotted, dashed, and solid lines represent respectively, quadratic, cubic, and exponential regressions. Closed squares, and hexagon represent data points which were outliers in the regressions.

about 0.1 to 0.2 unit in comparison with quadratic model (see 4.12). The standard deviation of residuals in quadratic model is slightly smaller than that in the exponential model. Also, using a quadratic fit is more common and it is convenient. Therefore, between two second-order models the quadratic model is preferred. A quadratic polynomial fit to averaged data (Fig. 4.12b) gives a regression as:

$$\log M_0 = (25.1079 \pm 0.2014) - (1.2015 \pm 0.0730)M_s + (0.2052 \pm 0.0066)(M_s)^2. \quad (4.10)$$

Errors in the parameters in equation (4.10) are quoted within 68% confidence limits. Equation (4.10) passes through an inflection point at small M_s and predicts larger $\log M_0$ with decreasing M_s for $M_s \leq 3$. Therefore this equation (quadratic regression of Figure 4.12a) should not be applied below $M_s \approx 3$. However, this is below the range of most teleseismic M_s reports. Some researchers e.g., Johnston (1996), Ambraseys and Adams (1996) have considered a quadratic polynomial model with $\log M_0$ as the dependent variable between M_s and $\log M_0$ in global or regional scales.

By using an error matrix (see appendix A) as Johnston (1996) used, the residuals of $\log M_0$ (observed values minus those computed from the regression equation) for quadratic fitting are shown in Figure 4.13. Closed squares represent outlier point according to the regression

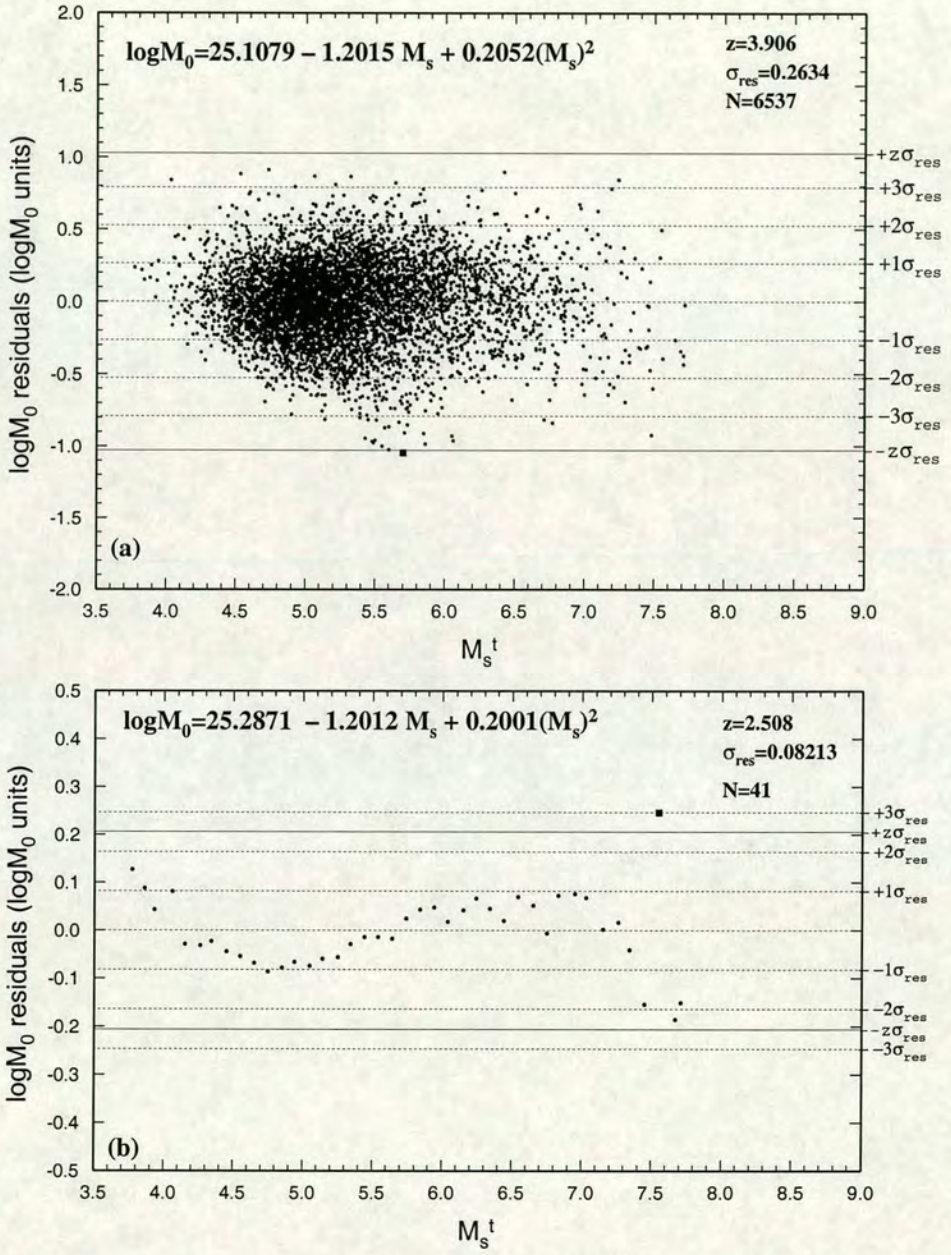

Figure 4.13. $\log M_0$ residuals (observed minus computed) for quadratic fitting. (a) For individual data points. (b) For observations averaged in 0.1-unit-wide ranges of M_s. Closed square represents outlier points according to the regression parameters in the second fit (for fit in which outliers based on the standard deviation of residuals (σ_{res}) obtained in the first fit, are removed). The dashed lines show the $\pm 1\sigma_{res}$, $\pm 2\sigma_{res}$, and $\pm 3\sigma_{res}$ and the solid lines are the outlier threshold $C = \pm z\sigma_{res}$.

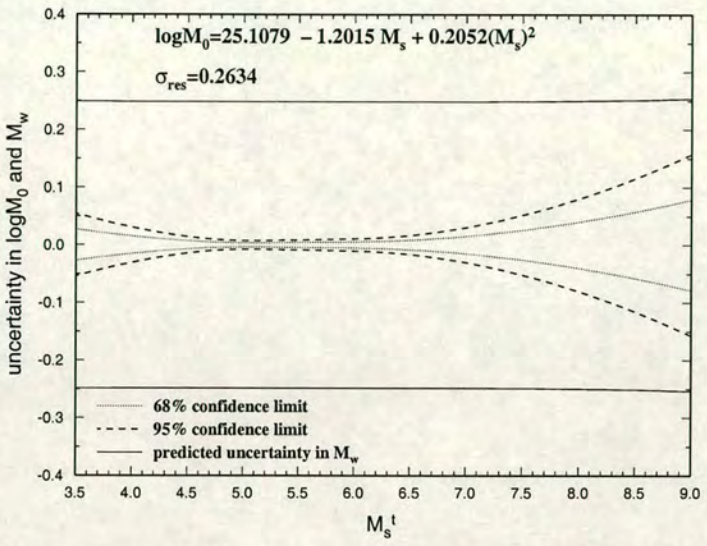

Figure 4.14. Graphical display of 68% ($\pm\sigma^R_{\log M_0}$) and 95% ($\pm 2\sigma^R_{\log M_0}$) confidence limits on the regression relation, also Johnston's (1996) "prediction" uncertainties ($\pm\sigma^P_{M_w}$) in M_w.

parameter in the second fit. For the relation of (4.10) the 68% confidence limit ($\pm\sigma^R_{\log M_0}$), and the 95% confidence limit ($\pm 2\sigma^R_{\log M_0}$) are computed from the regression using an error matrix (equation (A.2)) and are displayed in Figure 4.14. Johnston's (1996) "prediction" uncertainty in M_w for a given observation of M_s is plotted, computed from equation (A.7) (see appendix A). The increase in $\sigma^R_{\log M_0}$ at small- and large-M_s levels is characteristic of least-squares curve fits, and expresses the greater uncertainty of the regression where data are sparse.

4.6.2 Comparison of empirical relation of $\log M_0$ and M_s

Many workers introduced regional and global relations between M_s and M_0. Hanks and Kanamori (1979) defined the moment magnitude M_w, as $M_w = \frac{2}{3}\log M_0 - 10.7$. According to Hanks and Kanamori (1979), the relationship for M_s should be the same as that for M_w for magnitudes between approximately 5 and 7.5 which have been plotted in Figure 4.15. Dziewonski and Woodhouse (1983) used CMT data of 201 moderate and large earthquakes that occurred during 1981, and regressed M_s on $\log M_0$ as:

$$M_s = 0.668 \log M_0 - 10.86, \tag{4.11}$$

which differ only by 0.1 from the value of M_w defined by Hanks and Kanamori (1979), and it is virtually identical to the theoretical values for M_w for magnitudes ranging between approximately 5 and 8.

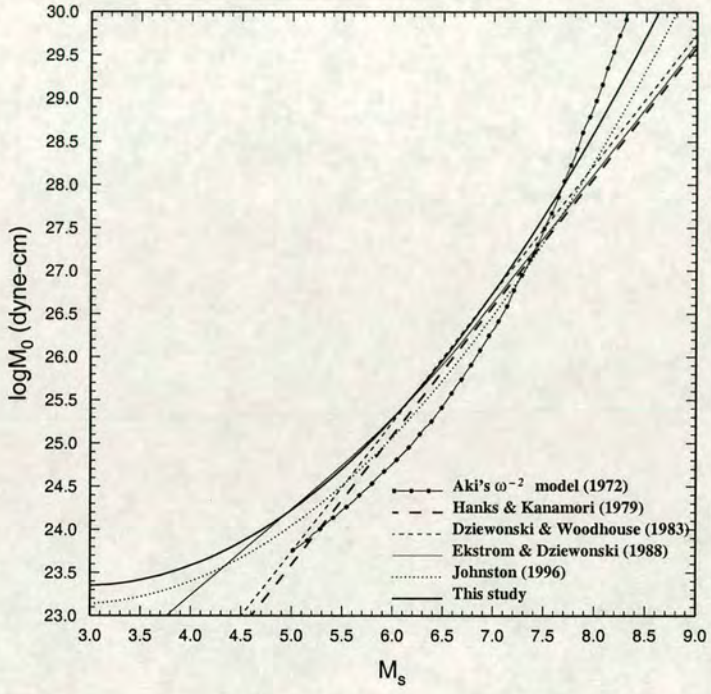

Figure 4.15. Comparison of quadratic $\log M_0 : M_s$ polynomial (heavy solid line) with other global relations between $\log M_0$ and M_s. Dotted solid line is Aki's ω^{-2} model. Light and heavy dashed lines represent Hanks and Kanamori, and Dziewonski and Woodhouse linear functions respectively. Dotted line represents quadratic regression of $\log M_0$ made on SCR teleseismic M_s by Johnston (1996). Thin solid line represents the Ekström and Dziewonski expressions (equation 4.4).

Figure 4.15 compares this study's quadratic regression (Eq. (4.10) with global relations such as Hanks and Kanamori (1979), Dziewonski and Woodhouse (1983), Ekström and Dziewonski (1988), Johnston (1996), and the theoretical model of Aki (1967). Equations (4.4) and (4.11) actually regress M_s on $\log M_0$, with $\log M_0$ as the independent variable. As Ekström and Dziewonski (1988) pointed out, it seems that the data used here do not support the tacit assumption that M_s is similar to the moment magnitude M_w over the whole range of magnitudes. In Figure 4.15 the dotted solid line is the ω^{-2} model proposed by Aki (1972), and was drawn by plotting the height of the flat portion of the spectrum for a given M_s shown in Figure 4.1. Aki (1972) fixed the absolute value in such a way that the curve passes through the observed

point for the Niigata earthquake ($M_s = 7.5$, $\log M_0 = 3 \times 10^{27}$ dyne-cm), for which the first accurate determination of seismic moment was made by Aki (1967).

There is no theoretical reason that $\log M_0 : M_s$ dependence should be of a quadratic functional form. Ekström and Dziewonski (1988) found it necessary to use a non-linear regression (linear segments separated by a gradual transition) to fit the global M_s versus $\log M_0$ data. More recently Johnston (1996) used 104 observations of $\log M_0$ and M_s from stable continental regions (SCR) and regressed a quadratic relation on $\log M_0$ against M_s. His relation is:

$$\log M_0 = 24.66 - 1.083 M_s + 0.192 (M_s)^2. \tag{4.12}$$

Also, Ambraseys and Adams (1996) have given a quadratic polynomial relation for 51 Central American earthquakes with magnitudes M_s greater than 7.0.

Moment rates calculated from the global relation (4.10) would be systematically larger than those obtained from the global relation of Hanks and Kanamori (1979). Predicted values of $\log M_0$ from Equation (4.10) are slightly different in the magnitude range 4.5 to 8, but for $M_s > 8$ and $M_s < 4.5$ the difference is significant. Equation (4.10) predicts larger values of $\log M_0$, by about 0.15 $\log M_0$ units, for a given M_s, in comparison with equation (4.12), although this relation is applicable only for events in stable continental region.

4.7 Comparison of depth and scalar moments in the CMT and USGS Catalogues

Sipkin (1986) compared the seismic moments and depths determined by the USGS for 260 large earthquakes occurring during 1981 to 1983 with those determined by CMT. He concluded that for all except the largest earthquakes ($M_0 > 10^{27}$dyne-cm), the scalar moments determined by USGS are close, but somewhat larger than the CMT moments. Also, the CMT depths tend to be slightly greater than USGS depths. USGS (NEIC) in the moment tensor inversion processing uses the 1066B model of Gilbert and Dziewonski (1975) for computing the Green's function (Sipkin, 1982), and CMT uses the PREM model (Preliminary Reference Earth Model) (Dziewonski and Anderson, 1981). To estimate seismic moment USGS uses just the P-waves, but, CMT in addition to P-waves uses the entire seismogram in the inversion of waveform data.

In Figure 4.16 scalar seismic moment and focal depth estimates of USGS for 1,444 earthquakes are compared with those estimations by the CMT. As this Figure shows, the CMT seismic moments are larger than those determined by the USGS for high scalar moments, but for the rest there is a tendency for USGS moments to be larger than CMT moments, although the size of the discrepancy is much smaller. The systematic difference between CMT depth

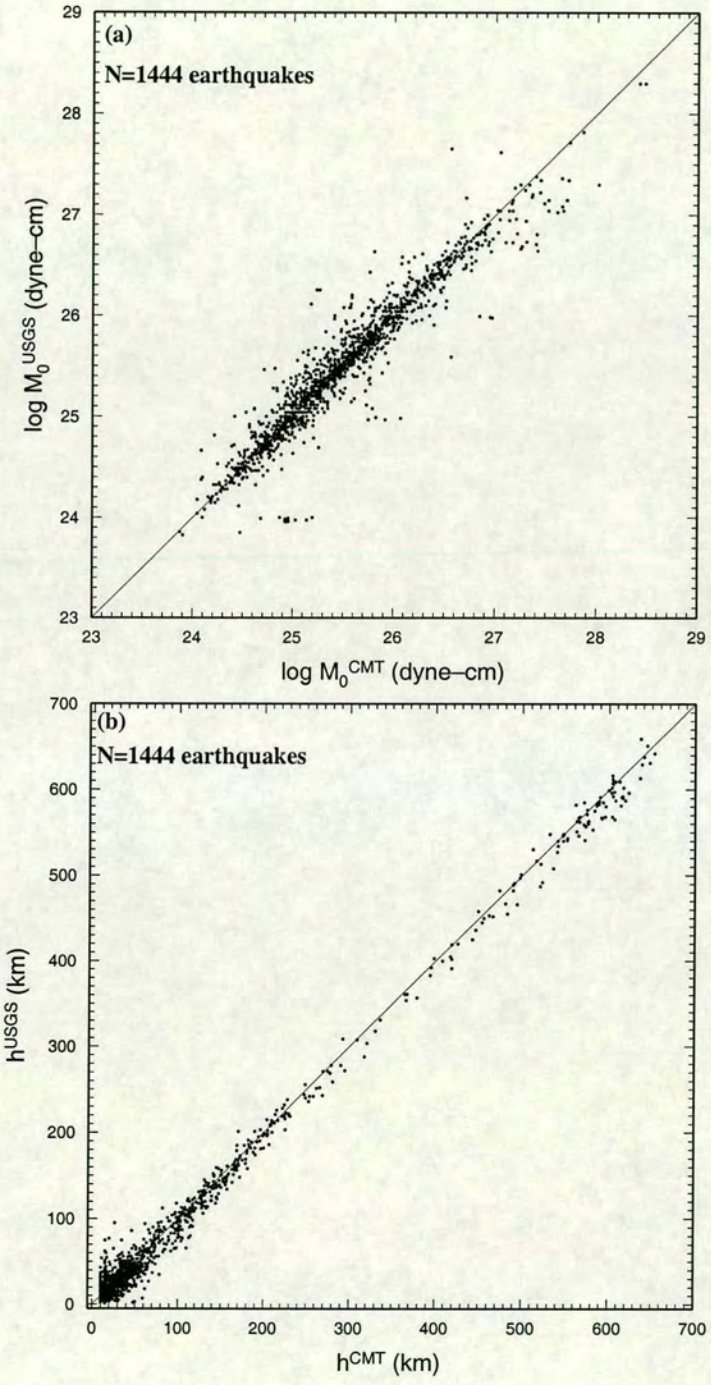

Figure 4.16. Comparison of seismic moment and depth of 1,444 earthquakes in the USGS and CMT Catalogues between January 1980 and November 1994. (a) Comparison of seismic moment. (b) Comparison of depths. In both of (a) and (b) solid lines show the locus of equality.

and USGS depth is statistically significant, with CMT estimating a larger value than the USGS for source depths. These confirm the early result of Sipkin. As Sipkin (1986) stated, the main reason for these discrepancies may be related to the difference between the 1066B and PREM models which USGS and CMT use respectively.

4.8 Conclusions

Comparison of the relationship between M_s and M_0 for M_s^{Prague} and M_s^t has shown that there is significantly less scatter in $\log M_0$ for a given M_s when M_s^t is used. This is particularly noticeable in the magnitude range 4.3 to 6.3 (compare Figs. 4.2d′ and 4.2f′). In the relation of M_s^t with $\log M_0$ the observed data do not provide strong evidence of a theoretical slope of unity towards smaller events. A linear regression analysis gives a better fit for M_s^t than M_s^{Prague} over a wider moment range from 2.5×10^{23} to 1.26×10^{27} dyne-cm (Figs. 4.3a′ and 4.3b′). It is therefore concluded that a linear fit is preferable to the analytical relation of equation (4.3). A linear fit with $\log M_0$ proportional to $1.3M_s$ is obtained over this wider magnitude range.

Reexamination of the conclusions of Ekström and Dziewonski (1988), and Abercrombie (1994) about the observed differences in M_s values between New Hebrides and Tonga-Kermadec subduction zones for earthquakes with the same seismic moment, show that these differences for M_s^t values are smaller than those for M_s^{Prague} values. Also, the path effect has an important effect in creating the observed anomaly between estimated surface-wave magnitudes for earthquakes with the same seismic moment in these regions.

The depth bias in the M_s formula was considered, and a correction of $\delta M_s = 0.0025h$ was found for earthquakes in a depth range 60 km $\geq h \geq$ 10 km. However, this was shown not to be very significant, but it is systematic for earthquakes with a calculated depth less than or equal to 60 km.

The principal results of this study in regression analysis consists of the global relation of seismic moment and surface-wave magnitude based on the data compared for the ISC and CMT Catalogues. The quadratic regression on teleseismic magnitude is

$$\log M_0 = (25.1079 \pm 0.2014) - (1.2015 \pm 0.0730)M_s + (0.2052 \pm 0.0066)(M_s)^2$$

.

Comparison of depths and scalar moments for 1,444 earthquakes in the CMT and USGS Catalogues confirms the early result of Sipkin (1986), and shows that CMT depths are larger than those for USGS, but the discrepancy in the two scalar moments is very small, and for $M_0 > 10^{26.7}$ the CMT scalar moments are larger than those for USGS scalar moments.

Chapter 5

Calibration functions for m_b determination

5.1 Introduction

Magnitude has played a particular role in the realistic description of global seismicity and in the study of dynamic parameters of seismic waves. The main advantage of this quantity appears to be in its close relation to seismic wave energy generated by an earthquake, and in the simple method of its estimation. However, there are some shortcomings such as the saturation in the magnitude scale toward very large earthquakes. Therefore, the problem of magnitude has always been a focus of interest in seismological research. As mentioned in previous chapters the calibration function which is used for magnitude determination is one of the sources of magnitude bias.

Much research has been done in the analysis of P-wave amplitudes, and several amplitude-distance curves containing a correction term for determining body-wave magnitude have been published, e.g., Carpenter *et al.* (1967), Cleary (1967), Veith and Clawson (1972), Booth *et al.* (1974), Christoskov *et al.* (1979, 1985, 1991), Vaněk *et al.* (1982), Nortmann and Duda (1882, 1983), Marshall *et al.* (1986), Lilwall (1987a, 1987b), Duda (1989) and Duda *et al.* (1989) etc. Most of these curves have the same general form as those of Gutenberg-Richter, but are much smoother.

Comparison of established global distance or depth-distance correction terms reveals significant differences. Moreover, comparison of calculated values of m_b differences reveals inadequacies in the various correction schemes, especially in that of Gutenberg-Richter (1956) which in still being used by global agencies such as the ISC and the NEIC. Here, new depth-distance

correction terms for m_b are determined using seismic moment for normalising amplitude-distance curves of P-waves from events with different sizes; moments from the Harvard Centroid Moment Tensor (CMT) Catalogue are used. By comparing body-wave magnitudes determined using different calibration functions applied to the ISC dataset, it is shown that existing distance or distance-depth calibration functions including those of Gutenberg and Richter (1956), Veith and Clawson (1972), Marshall *et al.* (1986), and Lilwall (1987b) are inadequate, and that the new function developed here is superior. The relationship of m_b to $\log M_0$ is compared using different depth-distance calibration functions and M_0 values from the CMT Catalogue. Finally the application of station corrections in the determination of m_b is examined.

5.2 Review of some calibration terms for m_b determination

5.2.1 Gutenberg and Richter (1956)

Gutenberg in 1945 used the following expression for calculating the ground displacement during a single body-wave phase (P, PP, and S) as a function of Δ

$$u = KTU\sqrt{E_1} = KTb\sqrt{E_1 f e^{-kD} \frac{\sin i_h}{\cos i_0 \sin \Delta} \frac{di_h}{d\Delta}} \tag{5.1}$$

Here u is the ground displacement produced by the vertical component of a seismic wave at its point of emergence. K is a constant equal to the fraction of the energy E_1 passing into the relevant wave and is different for P, SH, and SV waves. T is the period of the wave which is centred around 5 sec for the P-wave. E_1=$qTE/t = qT_0E/t_0$ is the portion of total energy (E) which is propagated as P-waves assuming that the duration t of a given phase increases with epicentral distance Δ. q is the fraction of the energy going into the phase considered and assumed to be constant. t_0 and T_0 are the duration and period of wave at the source respectively, and t_0/T_0 should not depend appreciably on the magnitude. b is the ratio of ground displacement to incident amplitude, and has different values for the horizontal and vertical component of total ground displacement (Gutenberg 1944). b is a function only of i_0 and of Poisson's ratio just below the surface of the earth. f is given by $\sqrt{f_1 f_2 f_3 \ldots}$, the values of $\sqrt{f_1}$, $\sqrt{f_1}$, etc., representing the square root of the fraction of energy remaining after a reflection or refraction at the surface of the Earth (for PP only). k is the anelastic attenuation factor which Gutenberg assumed to be constant along the ray path length, D. Gutenberg used $k = 0.00012$ in his calculation of u. i_0 is the angle of incidence of the ray at the Earth's surface, which Gutenberg calculated from the travel times of Gutenberg and Richter (1939), assuming a velocity of $V_0 = 5.6$ km/sec for the longitudinal waves near the surface, and using $\sin i_0 = \frac{V_0}{V_\Delta}$ where V_0 is the true velocity of longitudinal waves at the surface of the Earth,

and $\overline{V_\Delta}$ is the apparent velocity ($\frac{d\Delta}{dt}$) of that wave of a particular Δ. Gutenberg evaluated the slope of the curve obtained from t_0 versus Δ, as the differential $\frac{di_0}{d\Delta}$. Gutenberg considered that the scatter of residuals may be increased by assuming the same angle of incidence at a given distance for waves with different periods, and for reducing this effect he added a correction term for a calculated value of U (see table 1 of Gutenberg 1945b).

Gutenberg, using the empirical relation

$$\log E = 11.3 + 1.8M_s \quad (E \text{ is released energy in ergs}) \tag{5.2}$$

for shallow earthquakes, and combining with equation (5.1) obtained

$$L = 0.9M_s - \log u + \log T + \log U \tag{5.3}$$

where he assumed that $L \equiv -\log K - 5.6$ should have a nearly constant value for all waves starting as P-waves, another constant value for all waves starting as SV, and a third for those starting as SH. Gutenberg adjusted M_s and m_B to coincide near $M = 7$ and obtained

$$C = m_B - \log u + \log U - 0.1(m_B - 7) + \log T \tag{5.4}$$

and

$$A \equiv C - \log U = m_B - \log u - 0.1(m_B - 7) + \log T \tag{5.5}$$

where the constant (C) is independent of earthquake size. Equations (5.5) and (2.3) are the same, and the constant A in equation (5.5) is equivalent to Gutenberg's distance correction term $Q(\Delta)$. Gutenberg, using 221 observed values of u and T from 10 stations, and applying equation (5.5), obtained a value of 6.51 ± 0.03 for the average C for the vertical component of P, 6.34 ± 0.03 for horizontal P, etc., and he tabulated the values of $A = 6.3 - \log U$ for use in equation (5.5) as a function of distance. He determined the magnitude of shallow earthquakes using correction terms calculated from a comparison between the average value of C for a given station and the general average of 6.3 (Gutenberg 1945b, table 1), in equation (5.5), with a tentative additional correction of $+0.1(m_B - 7)$ for all longitudinal waves, to be applied only to very large shocks, and to shocks of magnitude less than 6.5.

Gutenberg extended the above method for deep shocks and calculated the values of A using equation (5.5). Equation (5.1) includes the focal depth h. However, equation (5.2) connects the magnitude with the energy of shallow shocks, and for deep shocks for which surface-wave magnitudes are not calculated. He assumed that the average magnitude found from the theory, assuming $C = 6.3$ and using data from various distances, is basically correct. Gutenberg calculated A for focal depths of 200, 400, and 600 km in the same way as for shallow shocks,

including the previous value $C = 6.3$ for all phases. He used the resulting values of A, and drew theoretical curves for A, (Gutenberg, 1945b figures 2 to 4), so for the calculation of magnitude of a given deep-focus earthquake in each individual observation, corresponding values of A were interpolated from those curves. Due to lack of data, Gutenberg expected systematic errors such as spurious "highs" or "lows" to occur in some parts of the curve.

As mentioned in the chapter 1, the Gutenberg-Richter calibration function for body-waves was based on medium-period instruments. Duda and Nortmann (1983) stated that the Gutenberg-Richter calibration terms are an unspecified average of calibration function for waves with different periods. The period dependent attenuation increases with decreasing period. Thus the calibration function of Gutenberg-Richter will introduce systematic discrepancies into magnitude values (Nortmann and Duda 1983) when using different types of seismograph.

Gutenberg and Richter, (1956) revised their formula for m_B determination as

$$m_B = log(A/T) + Q(\Delta, h) + S_c \tag{5.6}$$

where $Q(\Delta, h)$ is the A mentioned previously, and values of A (Gutenberg, 1945b, 1945c) were revised and published as $Q(\Delta, h)$ (Gutenberg and Richter, 1956).

5.2.2 Veith and Clawson (1972)

Veith and Clawson (1972) used approximately 2400 normalised log (A/T) values for P-waves of magnitude 5.0, from 43 large explosions recorded at 19 different sites. They obtained a preliminary amplitude-distance curve by computing weighted average amplitudes at the midpoint of a ten-degree-wide sliding windows where amplitudes within the window were weighted with a cosine taper. After deleting amplitudes which deviated by more than three standard deviations from the expected value, they calculated event magnitude by using the preliminary amplitude-distance curve for the distance range 25° to 90°. Again they renormalised log (A/T) according to the new magnitudes, and obtained a modified amplitude-distance curve using the above process. They repeated the process until both the amplitude-distance curve and the recomputed magnitudes became stable. Veith and Clawson (1972) plotted a smooth curve adopted beyond 30° as the final empirical amplitude-distance curve for surface focus.

Veith and Clawson used Gutenberg's formulation of equation (5.1), and evaluated the relative amplitudes of ground displacements as a geometric spreading curve, without attenuation, for the Herrin (1968) P-wave, surface travel-time curve and earth model. They used the following expression for anelastic attenuation along a ray path.

$$A = A_0 \exp\left(-\pi f \int^{\text{ray path}} \frac{dS}{Qv}\right) \tag{5.7}$$

where f is the frequency of signal, dS is the differential path length, and v is the velocity (This corresponds to a Q independent of frequency.) Veith and Clawson assumed that the Q is constant over the interval between the bottom of the ith ray path, and the bottom of the jth ray path which is relatively close. They assumed a Q value for the crust based on values given by Steinhart and Meyer (1961). They inverted the differential amplitudes (relative differences in the $\log(A)$ between epicentral distances Δ_i and Δ_j) to Q in the mantle using the formula

$$\bar{Q}_{ij} = 2\pi f c \int_{r_j}^{r_i} \frac{dS}{Qv} \Bigg/ \left[dA_i - dA_j + \pi f c \left(\int \frac{dS}{Qv} - 2 \int_{r_j}^{r_s} \frac{dS}{Qv} \right) \right] \tag{5.8}$$

where c is the conversion factor from natural to common logarithms, $r_{i,j}$ are the radii at the bottom of the ith and jth ray paths respectively, and r_s is the radius of the Earth (using $f = 1$, and Herrin's (1968) velocity structure). Veith and Clawson (1972) corrected the amplitudes of geometric spreading curves obtained from the travel-time curves and Earth model of Herrin (1968), for attenuation corresponding to $\bar{Q}$ structure by evaluation of equation (5.7), then tabulated as correction terms for the determination of m_b for use with peak-to-peak, short-period, vertical P-wave amplitude in mμ/sec.

5.2.3 Christoskov *et al.*, (1979)

Christoskov *et al.*, (1979) published empirical amplitude-distance curves as a calibration function for body-waves recorded by broadband Class-C, and short-period Class-A seismographs (for classification of instruments see Willmore and Karnik 1970). They used the Homogenised Magnitude System (HMS) which is a method of improving magnitude estimation using well-calibrated networks of reference stations in the USSR and Eastern Europe.

Christoskov *et al.* (1979) selected a set of 286 shallow earthquakes from 1966 to 1970 observed in the distance range 20° – 100° recorded at 32 seismic stations, to determine the station correction system and to optimise the calibration functions; their final results for P-wave were based on a total 3,526 observations ($\log(A/T)_{max}$ from the ISC Bulletin) recorded on short-period Class-A seismographs at 23 HMS stations.

Christoskov *et al.* (1979) recommended application of their calibration function for estimating the network magnitudes on an experimental basis, but they recommended postponing it for seismological practice until the problem of unifying the magnitude level for wave types (long- and short- period body-waves, and surface-waves magnitudes) was solved. Christoskov *et al.* (1991) published the numerical values of the final calibration functions after unification of different wave types. The differences of these numerical values for short period P-waves is only 0.03 magnitude units. Although the calibration function of Christoskov *et al.* derived from observations of Eurasian seismic stations, they recommended testing it for global usage.

5.2.4 Nortmann and Duda (1982)

Nortmann and Duda (1982) pointed out that body-wave magnitude obtained using the Gutenberg-Richter calibration function depends upon the period of measured amplitude at the seismic station, and postulated that m_b increases with increasing T. Nortmann and Duda also concluded that the variation of body-wave amplitudes with distance was period-dependent; they obtained a synthetic (theoretical) calibration function based on employing Herrin's (1968) P-wave velocity model with Q-models of Anderson and Hart (1978a, 1978b), under the assumption that amplitudes of teleseismically recorded body waves are affected by velocity heterogeneity and the imperfect elasticity in the earth's crust and mantle. Nortmann and Duda (1982) presented a new calibration function $B(\Delta, h, T) = g(\Delta, h) + a(\Delta, h)/T$ considering geometrical spreading and period-dependent anelastic dissipation $Q(\Delta, h, T)$ of the waves.

Nortmann and Duda applied their new calibration functions to a set of data and the calculated m_b showed a negative trend i.e., the strength of high-frequency spectral components exceeds the strength of low-frequency components of body-waves radiated from an earthquake-focus. Nortmann and Duda (1983) improved their synthetic calibration function by adjusting the period T for the absorption band model using relaxation time $\tau_H = 0.2\,\text{sec}$ (see fig. 6 of Nortmann and Duda (1983)). Nortmann and Duda used the new synthetic calibration function on about 20,500 amplitude-period ratios reported for 300 earthquakes by NEIC, and they found a smaller variation of magnitudes with epicentral distance in comparison with Gutenberg-Richter's calibration function.

5.2.5 Marshall *et al.*, (1986)

Marshall *et al.* (1986) used 15,691 amplitude and period data from 1,621 shallow earthquakes in the magnitude range 4.5–7, occurring globally and recorded at 26 seismic stations in the former Soviet Union (USSR). They extracted these data from the *USSR 10 DAY Earthquake Bulletin* for 1978. Marshall *et al.* (1986) used the amplitude of the first arrival P-wave with an extra restriction on period in order to construct a short-period ($T \sim 1$ sec) data based on Class-A instruments. Marshall *et al.* (1986) used the method described by Carpenter *et al.* (1967) and estimated the P-wave amplitude-distance curve for Soviet stations in the distance range $0° - 180°$, assuming that all the earthquakes have about the same depth. They then smoothed by eye, in the distance range $0° - 100°$. Marshall *et al.* (1986) also normalised their correction terms to the Gutenberg-Richter values.

5.2.6 Lilwall (1987)

Lilwall (1987a, 1987b) determined the calibration terms for m_b determination in the distance range $20° - 180°$ using a joint maximum-likelihood estimation technique. He supposed that a

measured amplitude/period $\log(A/T)$ from jth source, at kth station and lth distance is

$$a_{jkl} = b_j + s_k + d_l + \epsilon_{jkl}, \tag{5.9}$$

where b_j is a measure of source size, s_k a station effect, d_l a distance term and ϵ_{jkl} is a random variable which approximately normally distributed. Therefore, the likelihood function for the N observed values of a_{jkl} becomes

$$L(b_j, s_k, d_l, \sigma) = \prod_{i=1}^{N} p_i \tag{5.10}$$

where $p_i \equiv p(a_i; b_j, s_k, d_l, \sigma) = \frac{1}{\sqrt{2\pi}\sigma} \exp\left[-0.5\left(\frac{a_{jkl}-b_j-s_k-d_l}{\sigma}\right)^2\right]$ is the probability density function (PDF), and σ is the standard deviation of a_{jkl}. To reduce biases in the estimation of the PDF, Lilwall took account of the station thresholds G_k. He maximised equation (5.10) by maximising the variables b_j, s_k, d_l, and σ numerically in a piecewise iteration scheme, then used the Newton-Raphson method. To achieve a more uniform data coverage, he selected seismic events in the magnitude range 5 to 6, and a maximum of 3, 5, 5, 10, 10 seismic events per region ($\approx 10^\circ$ square) with assigned depth intervals of 0–50, 50–150, 150–250, 300-500, and 500–700 km respectively. From the ISC Bulletins from 1964 to 1981 he selected 500, 245, 152, 111, and 132 events in those depths intervals respectively. Lilwall computed station terms using only shallow focus data. These were then applied to all input data (even deeper focus) in the determination of distance terms. Also, Lilwall used a running 5° window with weighted cosine taper over most of the distance range.

5.3 New calibration terms for m_b using M_0 values of the CMT Catalogue

To determine depth-distance correction terms for the determination of body-wave magnitude, the CMT Catalogue is used assuming that M_0 is unbiased. This is available for 9,949 earthquakes for which the ISC "prime" location information are almost identical with those in the CMT Catalogue for time period 1978 to 1993 (see section 4.3). Figure 5.1 shows $m_b^{\text{G-R}}$ (m_b which has been determined using the Gutenberg-Richter (1956) correction terms) against $\log M_0$ for the these earthquakes. Figure 5.1a shows the individual events, and $m_b^{\text{G-R}}$ values averaged over 0.1-wide intervals of $\log M_0$ are plotted in Figure 5.1b with standard deviations. A linear regression for these averaged data in the seismic moment range 5.8×10^{23} to 1.0×10^{27} dyne-cm gives

$$m_b^{\text{G-R}} = 0.389 \log M_0 - 4.1374. \tag{5.11}$$

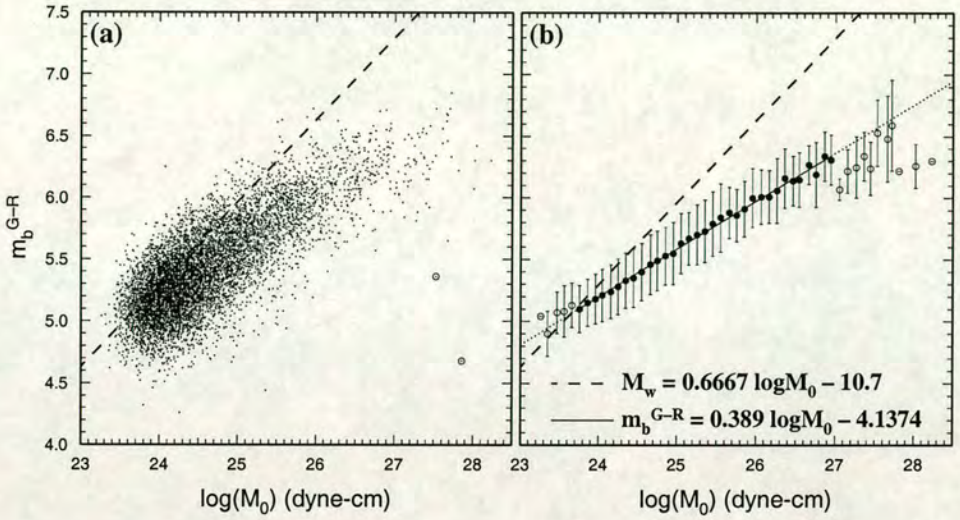

Figure 5.1. $m_b^{\text{G-R}}$ against $\log M_0$ for 9,949 earthquakes. (a) Individual data. (b) Averaged $m_b^{\text{G-R}}$ values over 0.1-wide intervals of $\log M_0$. The two circled earthquakes in (a) were thought to be in error and were not used in averaging process. In (b) the solid line represents a linear regression to the data in the seismic moment range 5.8×10^{23} to 1.0×10^{27} dyne-cm. The data points in this range are shown by filled circles. In both (a) and (b) the dashed line shows the M_w relationship of Hanks and Kanamori (1979) assuming $m_b^{\text{G-R}} = M_w$.

5.3.1 Depth-distance correction curves $B(\Delta, h)$

Assuming the published M_0 values in the CMT Catalogue give a true estimate of source size i.e., released energy, the P-wave amplitude-distance curves from sources with different sizes could be normalised to a unit P-wave amplitude-distance curve. Then, to obtain new calibration terms for determination of m_b, using M_0 values, $\log(A/T)$ measurements in a large global dataset can be normalised.

Body-wave magnitude is determined using an empirical relation such as

$$m_b = \log(A/T) + B(\Delta, h), \tag{5.12}$$

where Δ is epicentral distance in degrees, and h is focal depth in kilometres. By assuming a linear relation between m_b and $\log M_0$ such as equation (5.11) as shown in Figure 5.1b, substituting equation (5.12) in (5.11) gives

$$B(\Delta, h) = 0.389 \log M_0 - 4.1374 - \log(A/T). \tag{5.13}$$

The values of $B(\Delta, h)$ according to equation (5.13) were calculated for 478,122 amplitude/period

measurements from 9,949 earthquakes and were selected in the depth intervals of 0–35, 35–70, 70–150, 150–300, 300–500, and 500-650 km. Table 5.1 shows the data which were selected. The $B(\Delta, h)$ values in each depth interval were averaged over 1-degree-wide intervals in distance as a depth-distance correction curve at the mean of each depth interval. These curves were then smoothed using the *kernel smoother* of S-PLUS function (1992), with a 3-degree bandwidth, and are plotted in Figure 5.2.

Table 5.1. The grouped data which were used to obtain depth-distance correction curves $B(\Delta, h)$.

Depth range km	$\approx$ mean depth km	Number of earthquakes	Number of readings $(\log(A/T))$
$0 \leq h < 35$	15	4997	236748
$35 \leq h < 70$	50	2289	107648
$70 \leq h < 150$	100	1338	64233
$150 \leq h < 300$	200	631	33053
$300 \leq h < 500$	400	229	14130
$500 \leq h < 650$	550	454	21983

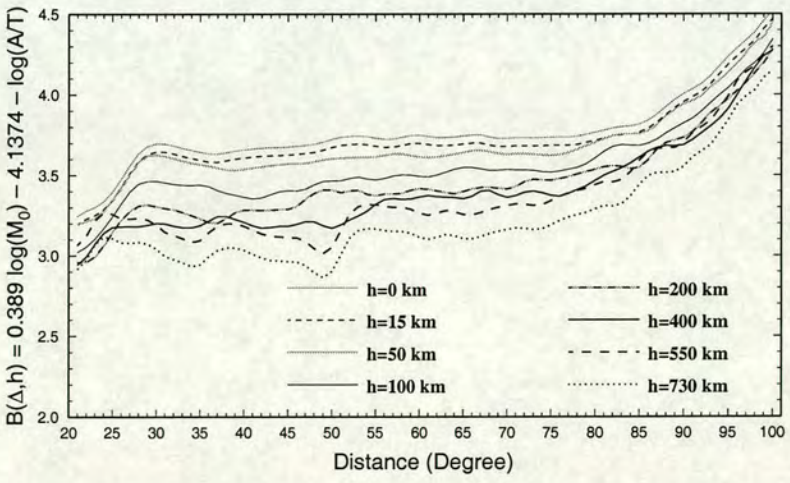

Figure 5.2. New depth-distance correction curves $B(\Delta, h)$ using equation (5.13) and M_0 values from CMT Catalogue. The depth-distance correction curve for zero depth was plotted by adding 0.05 to depth-distance correction curve at 15 km, and the depth-distance correction curve at 730 km depth was plotted by subtracting 0.15 from the depth-distance correction curve at 550 km.

The above procedure was repeated using $M_w - \log(A/T)$ residuals assuming $M_w = m_b$.

It is known that M_w theoretically related to released energy from source. Combining equation (5.12) with the relationship of Hanks and Kanamori (1979) (i.e. with $M_w = \frac{2}{3}\log M_0 - 10.7$) gives

$$B(\Delta, h) = 0.6667 \log M_0 - 10.7 - \log(A/T). \tag{5.14}$$

The difference in $B(\Delta, h)$ curves obtained using equation (5.14) with those obtained using equation (5.13) are small. Actually, using these two equations, the amplitude-distance curves of the P-waves from earthquakes of different sizes are normalised. Suppose seismic moments of two events with the same focal depth are 1.0×10^{24} and 1.0×10^{27} dyne-cm. Applying the equations (5.13) and (5.14) for normalising P-wave amplitude-distance curves, assume that the vertical difference between P-wave amplitude-distance curves for these two events are 1.176 and 2.0 magnitude units respectively. Therefore, small value for the coefficient of $\log M_0$ gives a little smoother $B(\Delta, h)$ curves than a large value. Increasing the coefficient of $\log M_0$ in equations (5.13) and (5.14) affects the slope of $B(\Delta, h)$, the curves increase at Δ>85°, and this gives a negative station residual i.e., m_b(event) < m_b(station) at distance range of Δ>85°, in other words large calibration terms at Δ>85°. The reverse of this discrepancy becomes true as the coefficient of $\log M_0$ is decreased. The sensitivity of $B(\Delta, h)$ at distance range of Δ>85°, is due to the core shadow transition or PKP zones which P-wave amplitude is quickly reduced with distance. Also, in the distance range of $85° < \Delta < 100°$ the observations are less. By decreasing or increasing the coefficient of $\log M_0$, the $B(\Delta, h)$ curves obtained do not change much at distance range of $21° \leq \Delta \leq 85°$. In general the $B(\Delta, h)$ curves obtained using equation (5.13) give slightly better results in comparison with those obtained using equation (5.14).

To eliminate saturation effect, and the effect of sensitive station on determined magnitude from small events, the procedure of obtaining $B(\Delta, h)$ curves using equations (5.13) and (5.14) was repeated for excluding earthquakes with seismic moment of $M_0 < 5.8 \times 10^{23}$ and $M_0 > 1.0 \times 10^{27}$ dyne-cm from dataset, and the $B(\Delta, h)$ curves obtained did not change.

It is then appropriate to calibrate the scale so that the sum-squares correction needed to all ISC event magnitudes so far determined is minimised i.e., to minimise $\sum[\overline{m_b^{\text{G-R}}} - (\overline{m_b^{\text{New}}} + \delta)]^2$ where the sum is over all events. The same criterion was used for M_s^t in chapter 3. $\delta = -0.037$ was found for m_b. The numerical values of $B(\Delta, h)$ include the value of $\delta = 0.037$ and are tabulated in Table 5.2.

In Figure 5.3 the new and the Gutenberg-Richter correction terms are compared at specific depths. Figure 5.3 shows that the Gutenberg-Richter correction curve for shallow events is lower than the new curve in the distance range $20° - 30°$ whereas in the range $45° - 90°$ it is higher. These discrepancies are reversed at greater depths.

Table 5.2. Global depth-distance correction $B(\Delta, h)$ for determination of body-wave magnitude. Δ is epicentral distance in degrees and h is focal depth in kilometers.

$h \rightarrow$ $\Delta \downarrow$	15	50	100	200	400	550	$h \rightarrow$ $\Delta \downarrow$	15	50	100	200	400	550
21	3.233	3.232	3.059	2.995	2.980	3.104	61	3.728	3.647	3.527	3.449	3.410	3.288
22	3.266	3.251	3.092	2.998	3.032	3.160	62	3.722	3.651	3.538	3.440	3.404	3.302
23	3.289	3.268	3.143	3.032	3.110	3.256	63	3.722	3.659	3.556	3.428	3.401	3.318
24	3.324	3.313	3.206	3.099	3.177	3.304	64	3.725	3.667	3.574	3.422	3.398	3.310
25	3.383	3.379	3.279	3.180	3.213	3.295	65	3.731	3.679	3.585	3.435	3.391	3.293
26	3.463	3.456	3.361	3.260	3.218	3.267	66	3.737	3.690	3.586	3.452	3.407	3.291
27	3.549	3.542	3.436	3.314	3.219	3.266	67	3.737	3.693	3.577	3.460	3.438	3.305
28	3.623	3.618	3.484	3.347	3.219	3.271	68	3.725	3.684	3.567	3.462	3.442	3.324
29	3.668	3.659	3.500	3.353	3.227	3.260	69	3.715	3.672	3.569	3.456	3.416	3.339
30	3.683	3.663	3.501	3.343	3.238	3.229	70	3.716	3.668	3.573	3.451	3.400	3.350
31	3.681	3.655	3.491	3.332	3.235	3.183	71	3.720	3.670	3.571	3.467	3.410	3.359
32	3.671	3.641	3.482	3.323	3.222	3.164	72	3.720	3.671	3.571	3.497	3.432	3.357
33	3.655	3.626	3.476	3.307	3.212	3.144	73	3.719	3.668	3.568	3.512	3.438	3.349
34	3.642	3.613	3.475	3.287	3.212	3.120	74	3.720	3.663	3.559	3.508	3.429	3.353
35	3.631	3.604	3.477	3.267	3.224	3.132	75	3.723	3.661	3.556	3.506	3.412	3.378
36	3.621	3.595	3.467	3.244	3.254	3.182	76	3.725	3.665	3.564	3.516	3.406	3.407
37	3.619	3.583	3.443	3.240	3.282	3.220	77	3.725	3.679	3.575	3.529	3.425	3.427
38	3.629	3.571	3.425	3.271	3.282	3.237	78	3.729	3.700	3.585	3.545	3.448	3.442
39	3.639	3.568	3.414	3.305	3.264	3.236	79	3.741	3.721	3.608	3.559	3.470	3.455
40	3.645	3.575	3.401	3.321	3.245	3.221	80	3.753	3.742	3.645	3.574	3.505	3.479
41	3.651	3.583	3.391	3.321	3.223	3.196	81	3.766	3.763	3.685	3.590	3.537	3.498
42	3.656	3.590	3.397	3.319	3.209	3.173	82	3.780	3.783	3.716	3.595	3.561	3.495
43	3.659	3.598	3.417	3.321	3.214	3.158	83	3.788	3.792	3.727	3.591	3.583	3.509
44	3.661	3.604	3.435	3.324	3.220	3.155	84	3.792	3.792	3.723	3.577	3.614	3.559
45	3.664	3.608	3.441	3.326	3.220	3.150	85	3.803	3.796	3.722	3.585	3.649	3.630
46	3.668	3.609	3.440	3.344	3.233	3.148	86	3.828	3.814	3.735	3.633	3.685	3.684
47	3.673	3.612	3.451	3.388	3.250	3.126	87	3.866	3.850	3.760	3.700	3.709	3.704
48	3.680	3.622	3.478	3.424	3.248	3.081	88	3.914	3.903	3.799	3.740	3.720	3.703
49	3.694	3.633	3.499	3.446	3.223	3.051	89	3.958	3.948	3.832	3.755	3.719	3.709
50	3.711	3.640	3.502	3.445	3.208	3.090	90	3.993	3.978	3.860	3.772	3.726	3.741
51	3.723	3.644	3.504	3.428	3.229	3.193	91	4.023	3.999	3.890	3.806	3.758	3.800
52	3.729	3.647	3.518	3.440	3.259	3.296	92	4.057	4.032	3.935	3.863	3.801	3.838
53	3.731	3.648	3.526	3.444	3.284	3.343	93	4.103	4.080	3.986	3.923	3.841	3.875
54	3.727	3.648	3.515	3.419	3.314	3.355	94	4.163	4.128	4.034	3.967	3.887	3.949
55	3.718	3.651	3.508	3.409	3.357	3.354	95	4.226	4.178	4.081	4.012	3.951	4.032
56	3.710	3.660	3.518	3.420	3.385	3.342	96	4.277	4.234	4.136	4.063	4.038	4.126
57	3.712	3.671	3.533	3.421	3.393	3.338	97	4.325	4.296	4.195	4.112	4.126	4.179
58	3.723	3.669	3.540	3.424	3.387	3.337	98	4.375	4.362	4.235	4.173	4.207	4.216
59	3.734	3.659	3.539	3.444	3.390	3.326	99	4.445	4.394	4.296	4.233	4.277	4.292
60	3.736	3.651	3.530	3.453	3.402	3.301	100	4.506	4.482	4.380	4.317	4.312	4.337

A comparison of different correction terms versus distance for different focal depths are shown in Figure 5.4. Most of these curves show considerable similarity over the distance range 30° to 90°, within which the calibration varies little. The correction curves obtained in this study, the Veith-Clawson correction curves and the Lilwall's curves are similar with increasing distance and depth. However, the deeper curves of Lilwall, and those of this study cross at different places as for the Gutenberg-Richter curves. Figure 5.4a shows that variation of Gutenberg-Richter terms along distance and with depth is much more complicated. Nortmann and Duda (1982) stated that the strong variation with distance which the Gutenberg-Richter calibration function displayed, is simply due to scatter of the underlying observations made prior to 1955, which they used for the determination of their calibration terms.

Figure 5.4 shows that, in the cases of Gutenberg-Richter, Veith-Clawson, Lilwall and this study, the difference between the average corrections over distances 20° – 100° for 0 – 700 km depth events are 0.56, 1.06, 0.58, and 0.52 magnitude units respectively. Also, this Figure shows that the $B(\Delta, h)$ curves are approximately parallel at shallow and intermediate depths.

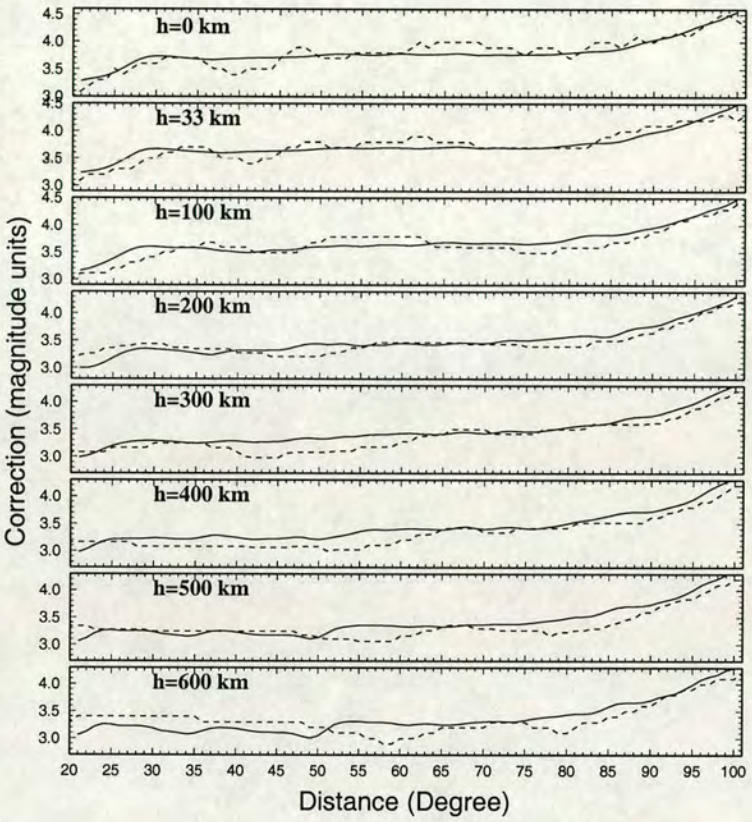

Figure 5.3. Comparison of depth-distance correction terms of the Gutenberg-Richter with the new correction terms. In each graph the solid and the dashed lines represent the new and the Gutenberg-Richter correction curves respectively.

But for deeper earthquakes $B(\Delta, h)$ curves show more structures. Some parts of this structure and unsmoothness are due to lack of data. In general any empirical $B(\Delta, h)$ curve based on observations, is obtained using data over a depth range. For example, in this study $B(\Delta, h)$ at 200 km depth was obtained by averaging normalised P-wave amplitude-distance curves over the depth range 150 km $\leq h <$ 300 km (see Table 5.1). Therefore, nonuniformity in distribution of events with depth, and error of determined depths, affects the uniformity of $B(\Delta, h)$ curves. The appearance of these curves in Figure 5.4 suggests that one can assume that $B(\Delta, h)$ curves are parallel. Also, a small percent of the dataset contains earthquakes that have occurred at greater depths. Therefore, in the next section a distance correction curve $B(\Delta)$ is obtained using the same procedure. Then a depth correction term $B(h)$ is separately obtained.

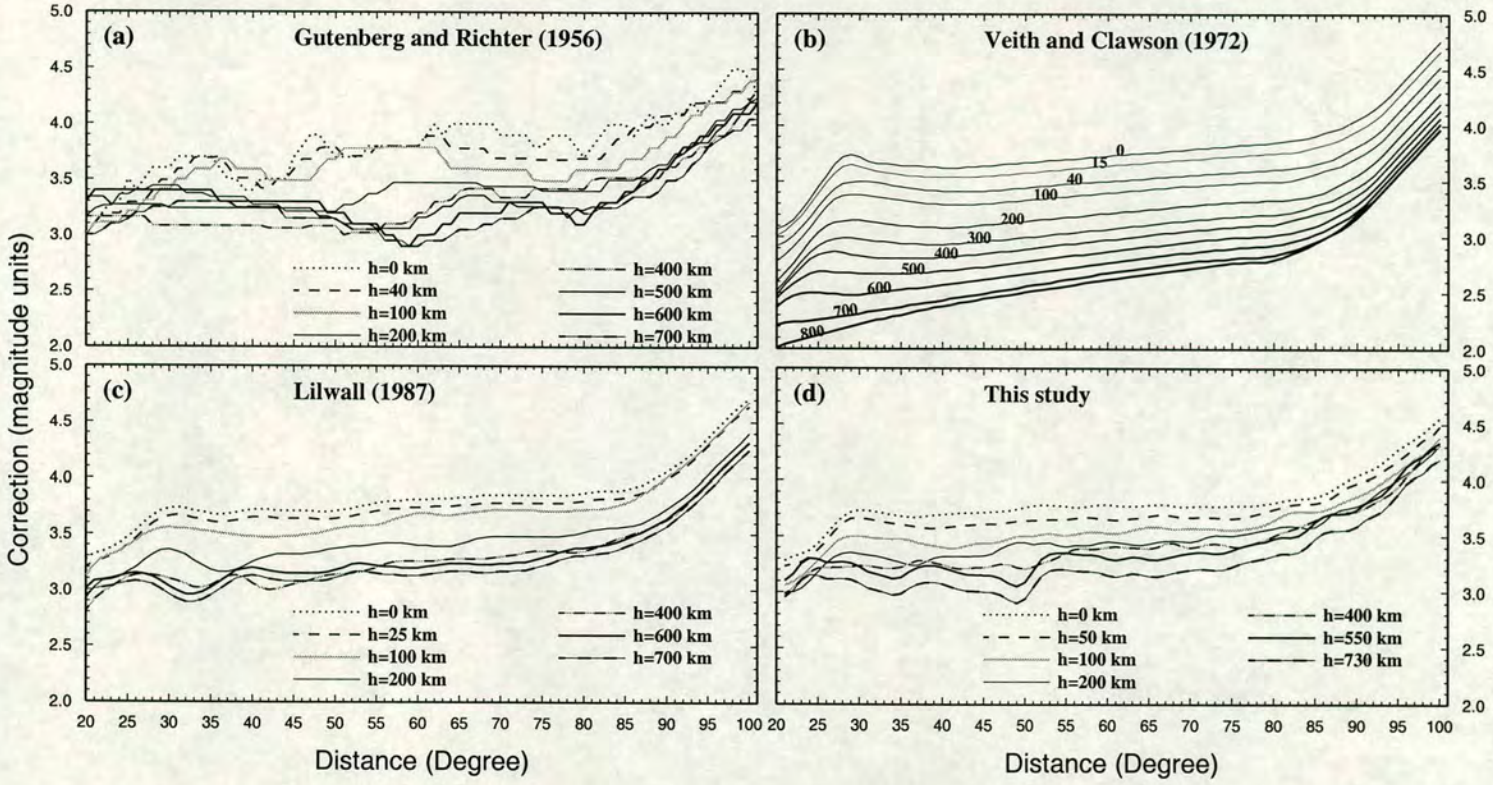

Figure 5.4. A comparison of different depth-distance correction curves $B(\Delta, h)$ against distance. (a) Gutenberg and Richter (1956). (b) Veith and Clawson (1972); line thickness increases with depth as annotated. (c) Lilwall (1987b). (d) This study.

5.3.2 Distance correction curve $B(\Delta)$, and depth correction term $B(h)$

Distance correction curve $B(\Delta)$— Putting $B(\Delta, h)$ as $B(\Delta)+B(h)$ in equation (5.12) (where $B(\Delta)$ is the correction for surface focus) and assuming $B(h) = 0$, the calculated $B(\Delta, h)$ values for 478,122 amplitude/period measurements from 9,949 earthquakes using equation (5.13) are averaged over 1-degree-wide intervals and are then plotted in Figure 5.5a as a preliminary distance correction curve with standard deviations.

Now, to determine m_b, for the time being ignoring the depth effect i.e., $B(h) = 0$, the preliminary distance correction is applied to all of the 110,720 events in the dataset; the magnitude residuals are calculated and are averaged in 1-degree-wide intervals. The preliminary correction curve is then revised by adding these residuals. The distance correction is then smoothed using the *kernel smoother* of S-PLUS function (1992), with a 4-degree bandwidth. In Figure 5.5a′ the preliminary correction, the revised correction, and the smoothed correction are compared. As this Figure shows there is no large deviation between these curves against distances.

The above procedure was repeated using equation (5.14) and the resulting curves are shown in Figures 5.5b and 5.5b′. Comparison of Figure 5.5b′ with 5.5a′ shows that there is no significant difference between using the empirical relation of equation (5.11) and the relationship of Hanks and Kanamori (1979); the distance corrections are almost identical (after a baseline shift). However, in the case of using equation (5.14) the preliminary correction is very close to the final correction at distances $\Delta > 85°$ (compare dotted and solid curves in Fig. 5.5b′) but as expected the standard deviation of the preliminary correction is greater than when equation (5.13) is used (compare Fig. 5.5a with Fig. 5.5b). Therefore, as in the previous section the distance correction curve $B(\Delta)$ obtained using equation (5.13) is preferred to that obtained using equation (5.14).

Depth correction term $B(h)$— The distance correction obtained using equation (5.13) is now applied to the ISC dataset to redetermine m_b taking into account the depth effect. From equations (5.12) and (5.13) giving $B(\Delta, h) = B(\Delta) + B(h)$ (where $B(\Delta)$ is the correction for surface focus) we have, $B(h) = 0.389 \log M_0 - 4.1374 - m_b$. (Above, m_b has been determined assuming $B(h)$ equal to zero). Values of $B(h)$ are averaged over 9,949 earthquakes in 10-kilometre-wide intervals, and plotted against depth in Figure 5.6. (In an attempt to reduce depth error, the ISC and NEIC depths were averaged.) A depth dependence in estimated m_b is expected, so variation of $B(h) = 0.389 \log M_0 - 4.1374 - m_b$ with depth should show the effect of depth on recorded displacement ($\log(A/T)$), corresponding to estimated magnitude. The best non-linear regression model fitting these data points, weighted by the inverse square

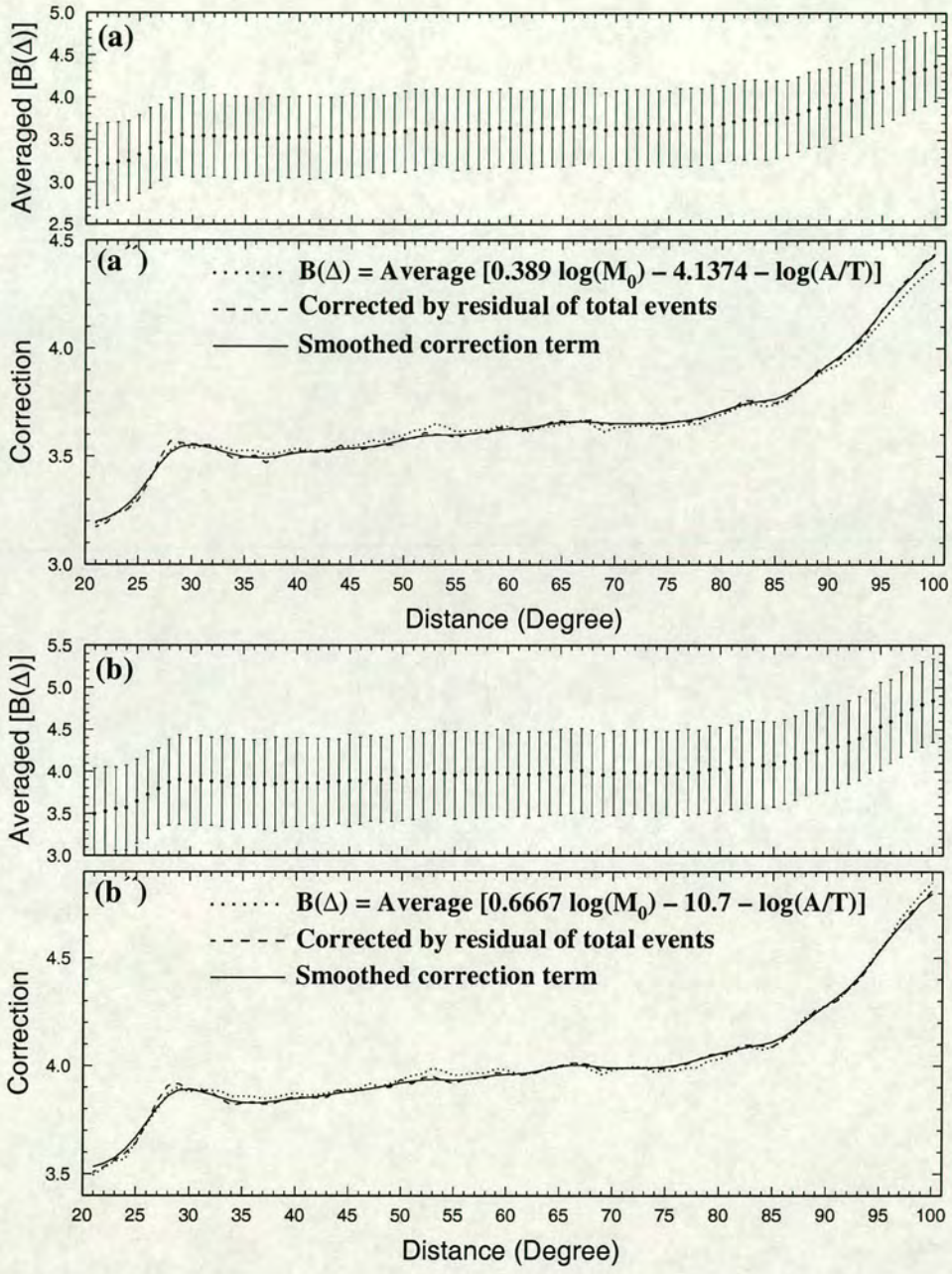

Figure 5.5. (a) Average of $B(\Delta)$ over 1-degree-wide intervals versus distance with standard deviations. (a′) Global distance correction curve for surface focus events; dotted, dashed, and solid curves show preliminary correction, corrected for residual, and smoothed distance correction curve respectively. (b) and (b′) as (a) and (a′) but using equation (5.14) instead of equation (5.13).

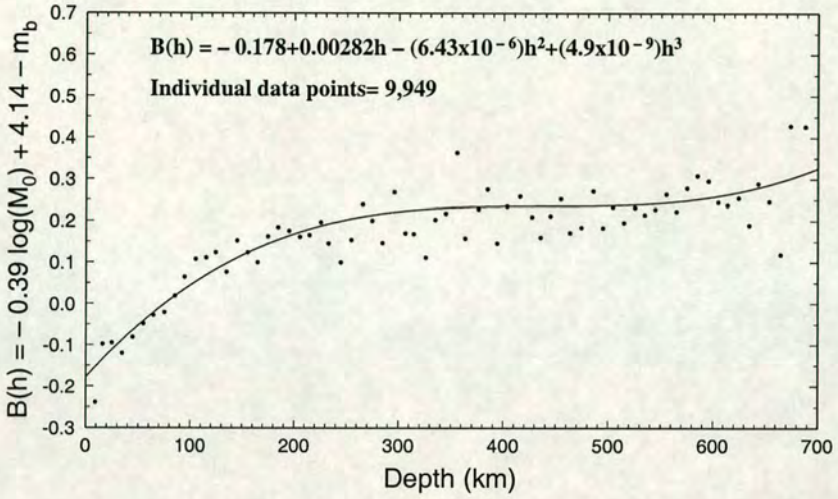

Figure 5.6. Depth correction function $B(h)$ for body-wave magnitude obtained by fitting a cubic regression model to averaged $B(h) = 0.389 \log M_0 - 4.1374 - m_b$ in 10-kilometre-wide intervals versus depth ($[h^{ISC} + h^{NEIC}]/2$). m_b has been calculated only using distance correction terms, and without depth correction.

of the standard deviation (σ^{-2}) is cubic, and is given by

$$B(h) = -0.178 + 0.00282h - 6.43 \times 10^{-6}h^2 + 4.9 \times 10^{-9}h^3 \tag{5.15}$$

where h is depth in kilometres, and $B(h)$ is the depth correction term in magnitude units. Therefore, if a distance correction curve $B(\Delta)$ and a separate depth correction term $B(h)$ are used, the formula for determining body-wave magnitude becomes

$$\begin{aligned} m_b^{\text{New}} &= \log(A/T) + B(\Delta, h) = \log(A/T) + B(\Delta) - B(h) \\ B(h) &= 0.00282h - 5.43 \times 10^{-6}h^2 + 4.9 \times 10^{-9}h^3 \end{aligned} \tag{5.16}$$

To calibrate the scale by minimising $\sum[\overline{m_b^{\text{G-R}}} - (\overline{m_b^{\text{New}}} + \delta)]^2$ (where the sum is over all events) $\delta = -0.025$ was found. The numerical values of $B(\Delta)$ include the value of -0.178 from equation (5.15), and value of $\delta = -0.025$ are tabulated in Table 5.3.

Calibration terms of Christoskov *et al.* (1979) and Marshal *et al.* (1986) have been published only for crustal events. In Figure 5.7 these two distance correction curves are compared with the depth-distance correction curves $B(\Delta, h)$ of Gutenberg-Richter, Veith-Clawson, Lilwall and this study at h=15 km. As this Figure shows, the new correction curve obtained in this study at a depth of 15 km is very close to Lilwall's curve up to $\Delta = 55°$, and its difference with other curves is significant.

Table 5.3. Global distance correction terms $B(\Delta)$ for determination of body-wave magnitude at distance range of $21° \leq \Delta \leq 100°$ for surface-focus events.

$\Delta°$	$B(\Delta)$	$\Delta°$	$B(\Delta)$	$\Delta°$	$B(\Delta)$	$\Delta°$	$B(\Delta)$	$\Delta°$	$B(\Delta)$	$\Delta°$	$B(\Delta)$	$\Delta°$	$B(\Delta)$	$\Delta°$	$B(\Delta)$
21	3.351	31	3.701	41	3.674	51	3.742	61	3.782	71	3.806	81	3.880	91	4.115
22	3.367	32	3.689	42	3.678	52	3.749	62	3.787	72	3.806	82	3.894	92	4.157
23	3.392	33	3.674	43	3.682	53	3.752	63	3.795	73	3.806	83	3.904	93	4.206
24	3.429	34	3.660	44	3.687	54	3.752	64	3.804	74	3.807	84	3.910	94	4.264
25	3.481	35	3.651	45	3.691	55	3.752	65	3.810	75	3.809	85	3.919	95	4.325
26	3.548	36	3.647	46	3.694	56	3.755	66	3.814	76	3.814	86	3.938	96	4.386
27	3.617	37	3.647	47	3.698	57	3.762	67	3.814	77	3.822	87	3.968	97	4.443
28	3.670	38	3.652	48	3.707	58	3.769	68	3.812	78	3.832	88	4.004	98	4.491
29	3.698	39	3.662	49	3.718	59	3.776	69	3.808	79	3.846	89	4.042	99	4.548
30	3.706	40	3.670	50	3.730	60	3.780	70	3.806	80	3.863	90	4.079	100	4.583

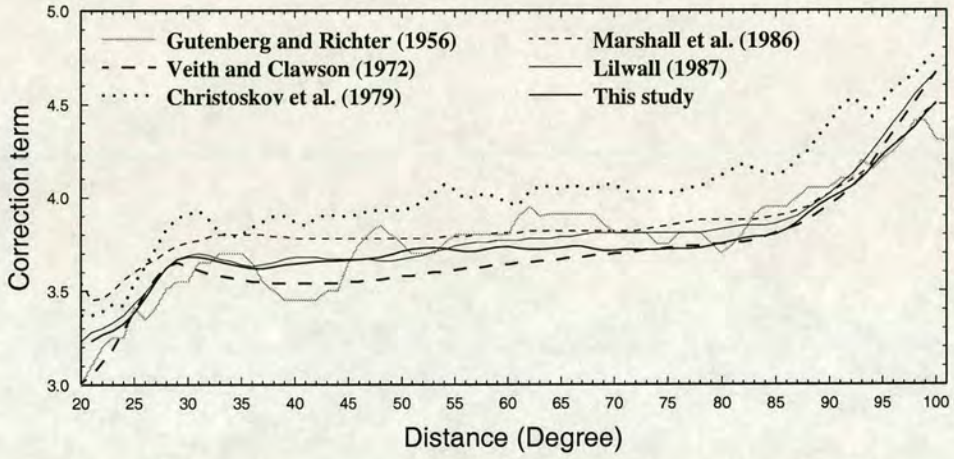

Figure 5.7. A comparison of different depth-distance correction curves at 15 km depth, together with calibration terms of Christoskov *et al.* (1979) and Marshal *et al.* (1986).

5.4 Comparison of different correction terms applied to ISC data

The correction terms of Gutenberg-Richter (1956), Veith-Clawson (1972), Christoskov *et al.* (1979), Marshall *et al.* (1986), Lilwall (1987b), and the new correction terms obtained in this study are applied to the ISC dataset between 1978 and 1993. As mentioned above, correction terms of Christoskov *et al.* (1979) and Marshall *et al.* (1986) are applicable only for shallow events. Most of the dataset (70%) considered here has a calculated depth of less than 70 km (shallow depth). ISC has extracted distance calibration values from Gutenberg-Richter's chart (fig. 5 Gutenberg-Richter, 1956) for depths of 0.0, 33, 96.38, 159.76, 223.14, 286.52, 349.9, 413.28, 540.04, 603.42, 666.8, and 730 km, and in the determination of m_b uses the calibration terms according to the closest depth which is calculated. Here the same ISC extracted values are used with interpolation for determination of $m_b^{\text{G-R}}$, and there is no significant difference

from the ISC calculated m_b. Also, here other depth-distance correction terms $B(\Delta, h)$ are used with interpolation for determination of m_b.

The calibration terms considered above were applied to 16 years of data in the ISC Bulletin between 1978 and 1993. The residuals of station magnitude from event magnitude are averaged in 1-degree-wide intervals and are plotted against distance in Figure 5.8. As this Figure shows, in all seven cases the variation of δm_b is small in the distance range 30° – 85°, but it is high for regional distances and distances of $\Delta > 90°$. The variety of δm_b in the case of Gutenberg-Richter which is presently used by ISC and NEIC, has more spurious variation than other ones with epicentral distance.

Therefore, comparison of the curves in Figure 5.8 apparently shows that bias in the cases of Veith-Clawson, Lilwall and this study are less than Gutenberg-Richter, but in the case of Veith-Clawson and Lilwall there is a systematic bias for distances beyond about 88°. Also, in the case of Veith-Clawson and Lilwall, as for the Gutenberg-Richter there is a systematic underestimation of m_b for deeper earthquakes (see next section). Figures 5.8c and 5.8d show that in the case of applying the correction terms of Christoskov *et al.* (1979) and Marshall *et al.* (1986), the calculated m_b values have a systematic bias. For example, at distances less than 28° and greater than 85° m_b is underestimated when using Christoskov *et al.* (1979) and Marshall *et al.* (1986) correction terms respectively.

Application of depth-distance correction terms $B(\Delta, h)$ obtained in this study give the best estimate of m_b along epicentral distances (see Fig. 5.8f). Also, application of distance correction terms $B(\Delta)$ at surface focus with a separate depth correction term $B(h)$ gives a better m_b estimation with distance, especially for shallow and intermediate events which contain 93.6% of total events which have been reported to the ISC between 1978 and 1993 (see Fig. 5.8g). However, in this case bias of m_b with distance for deep earthquakes is more than that when the new depth-distance correction terms $B(\Delta, h)$ and Lilwall (1987b) correction terms are used.

Therefore, using the depth-distance correction curves $B(\Delta, h)$ is preferred to a distance correction curve $B(\Delta)$ at surface focus with a separate depth correction term $B(h)$. *In the rest of this thesis the new depth-distance correction terms or the new calibration terms is referred to $B(\Delta, h)$ which has been obtained in this study (see Table 5.2 and Fig. 5.2) and m_b^{New} is referred to m_b which is estimated using the above depth-distance correction terms $B(\Delta, h)$.*

In comparison with the surface-wave magnitude, the scatter of body-wave magnitude at all epicentral distances using any calibration function, is large. One of the possible sources of this scatter can be the period range which is used for determination of body-wave magnitude. For surface-wave magnitude NEIC uses period from 17 to 23 sec, and ISC uses 10 – 60 sec. A variation of 0 – 0.13 and 0 – 0.78 magnitude units exists in the values of M_s respectively. But for body-wave magnitude which both agencies use, the period is less than 3 sec (0.1 – 3), and this is associated with a variation of 0 – 1.48 magnitude units in m_b. It is difficult to separate

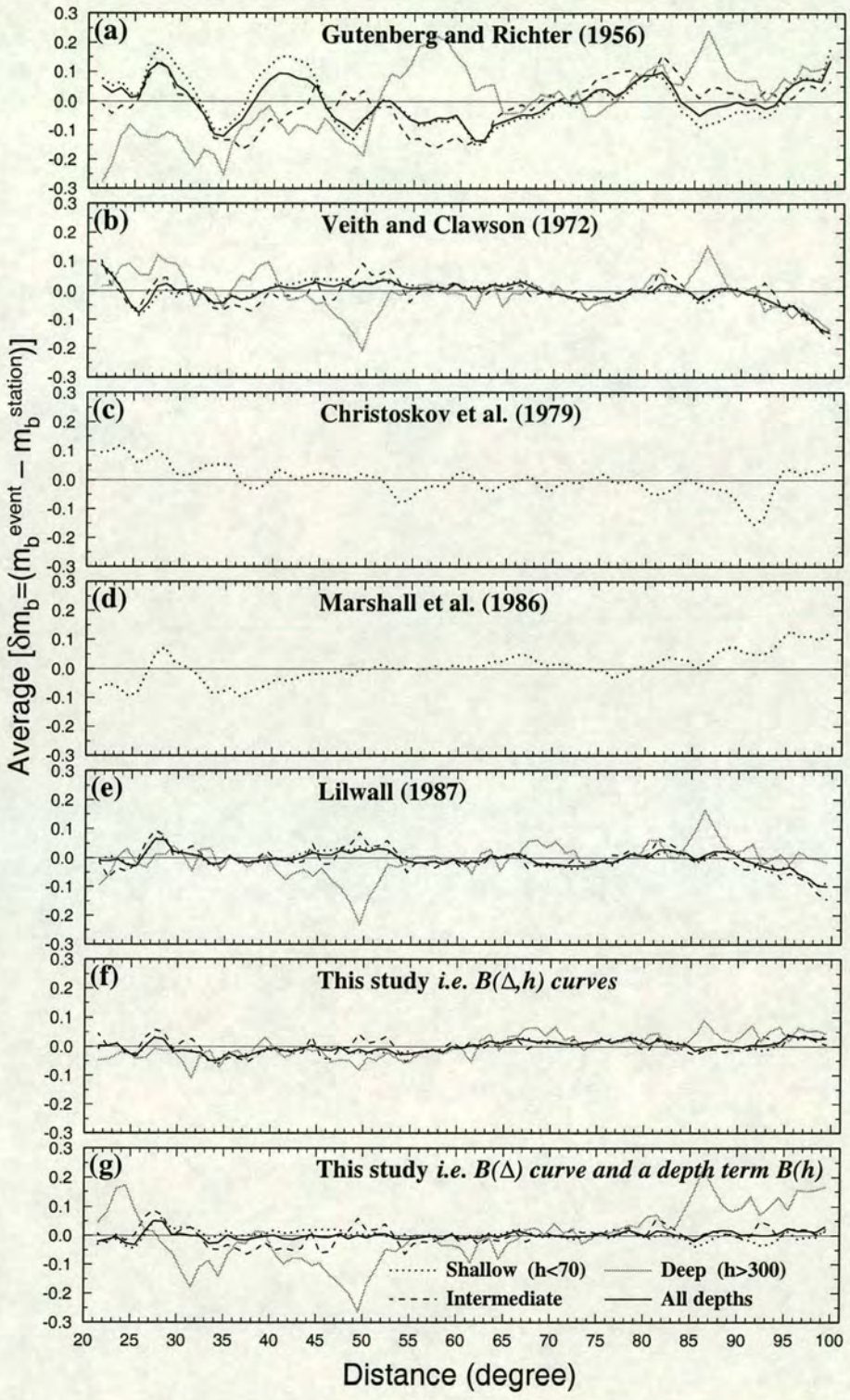

Figure 5.8. Comparison of averaged residual of station magnitude from the mean magnitude with 1-degree-wide interval against distance for Gutenberg-Richter (1956), Veith-Clawson (1972), Christoskov *et al.* (1979), Marshall *et al.* (1986), Lilwall (1987b), and new correction terms. In each case the dotted-line indicates 905,785 observations from 60,631 shallow events ($h < 70$ km), the dashed-line 269,269 observations from 20,095 intermediate earthquakes (70 km $\leq h \leq$ 300 km), the gray-line 94,141 observations from 6,222 deep earthquakes (300 km $\leq h$), and the thick solid-line 1,269,195 observations from 86948 events with all depths. The residual calculation excludes 23,772 events with only one observation.

this effect from other ones along the ray paths. But, scatter due to this effect is very small, because more period measurements are in the range of 1–3 seconds.

Duda *et al.* (1989), using the Preliminary Reference Earth Model (PREM) (Dziewonski and Anderson, 1981) model of velocity and anelasticity of the Earth, theoretically computed the amplitude of refracted P-waves along the Earth's surface, and showed that the amplitude increases with increasing period of the wave. For observations in the ISC dataset it is difficult to verify this result because a variety of instruments have been used. However, the result of regressing m_b on T or $\log T$ (with m_b as the dependent variable) for 68,318 events for which more than two period observations are available, supports the result of Duda *et al.* (1989). This shows that the estimated m_b values (using four different depth-distance terms) are period-dependent, and increasing of m_b with increasing period dominates about 13% more than the reverse case (i.e., when m_b is decreased with increasing period).

To compare easily the irregularities at the teleseismic distance and terminal curves in relation to the concentration and scattering of data points, histograms of observations for shallow, intermediate, and deep events are plotted in Figure 5.9a. Ignoring the concentration of observations at particular distances, it is assumed that each event is recorded only at one station over 1-degree-wide intervals of distance, then histograms of binned events in 1-degree intervals are plotted in Figure 5.9b (in each bin any event is counted only once). Figure 5.9b shows that the frequency-distance plot for reported events exhibits the structure of P-wave amplitude decay (i.e. the inverse of calibration curves) with distance. In Figures 5.9a and 5.9b, high concentration of observation at distance about 85° is due to the large number of stations per unit distance. In Figure 5.9c the histograms of events with 5-kilometre-wide bins are shown. In the ISC Catalogue the data dominate at depths of 0, 33 km (ISC conventional depths, Adams *et al.*, 1982), and 10 km. Figure 5.9c shows that the frequency-depth distribution follows an exponential function up to 500 km depth and at depth range of about 500–650 km the shape of distribution has a *platykurtic* form.

The histograms of estimated m_b values using Gutenberg-Richter calibration terms and new calibration terms are shown in Figure 5.10. As observed in Figure 5.3, the Gutenberg-Richter calibration terms in the distance range $45° - 90°$ are greater than those of the new calibration terms, for shallow depths. This discrepancy is the reverse at greater depths. From other side the majority of events have a shallow depth, and concentration of observations are high in this distance range (see Fig. 5.9). Also, most of the large events occurred at shallow depths and hence are observed at greater distances ($45° - 90°$). Events with small size are generally observed at closer distances where the Gutenberg-Richter calibration terms are less than those of the new calibration terms. For these reasons using the new correction terms for some large events in which $m_b^{\text{G-R}}$ are large gives small m_b^{New}, and for some small events the reverse is true.

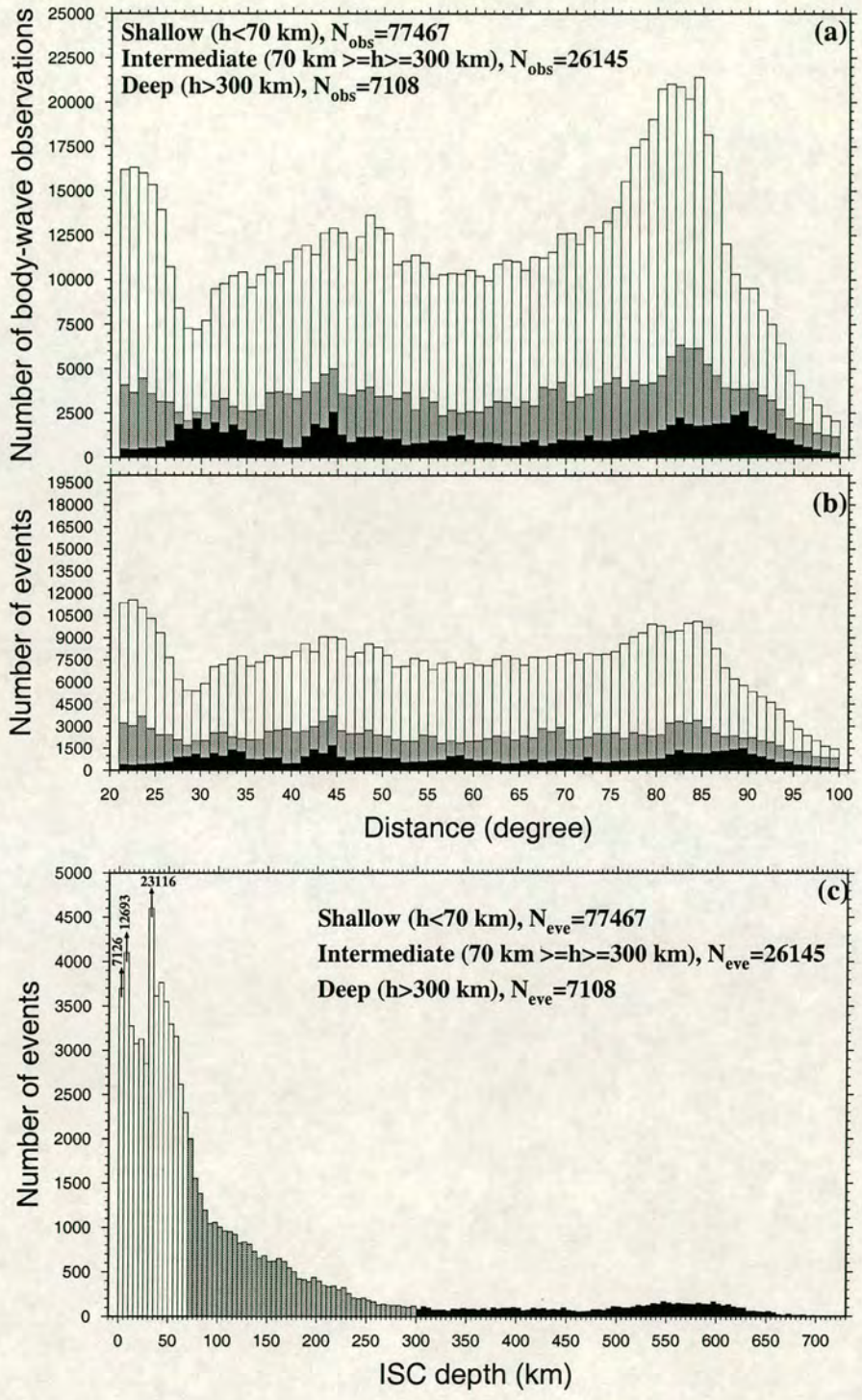

Figure 5.9. (a) Histogram of observations (N_{obs}) versus distance with 1-degree-wide interval. (b) Histogram of number of events binned in 1-degree interval (each event counted only once in each 1-degree bin). (c) Distribution of events (N_{eve}) versus ISC depth with 5-kilometre-wide interval. In all cases white, gray, and black histograms show shallow, intermediate, and deep events respectively. Note that the bins with 7126, 12693, and 23116 events are dominated by artificial depth assignments.

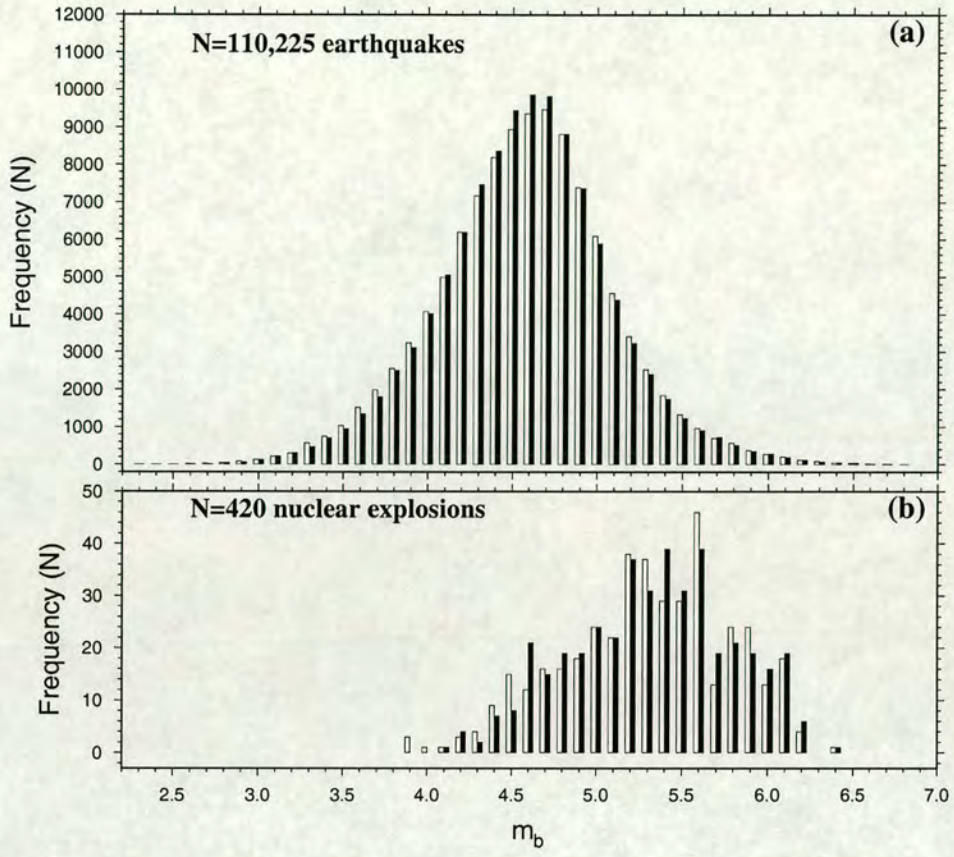

Figure 5.10. Histogram of m_b for 110,225 earthquakes and 420 nuclear explosions, in the ISC dataset between 1978 and 1993. (a) For earthquakes. (b) For nuclear explosions. In each case the white histograms present the frequency of $m_b^{\text{G-R}}$ (using Gutenberg-Richter calibration terms), and black histograms present the frequency of m_b^{New} (using calibration terms obtained in this study).

Therefore, the frequency of magnitude values in the range of about $4.3 - 4.8$ in magnitude-frequency distribution for m_b^{New} are higher than that for $m_b^{\text{R-G}}$, and for about $m_b > 4.8$ and $m_b < 4.3$ the reverse is true. Therefore, for a dataset in seismicity studies, the b-value based on m_b^{New} values will be systematically higher than that for $m_b^{\text{G-R}}$ values. So, b-value will be different in seismicity studies for a set of data based on these two calibration terms.

In general the m_b^{New} values obtained using the new calibration terms are larger than those obtained using the Gutenberg-Richter calibration terms. Figure 5.11 shows this difference for 60,544 out of 110,225 earthquakes, and for 180 out of 420 nuclear explosions. Values of $m_b^{\text{G-R}} - m_b^{\text{New}}$ are averaged and are plotted against $m_b^{\text{G-R}}$ in this Figure for earthquakes and nuclear explosions, for which calculated $m_b^{\text{G-R}}$ and m_b^{New} are different. Therefore, each point on the graphs presents the average difference of two m_b values for events for which the calculated

$m_b^{\text{G-R}}$ are not equal to m_b^{New} (i.e., events with the same $m_b^{\text{G-R}}$ value and different m_b^{New} values).

In summary, the application of the new depth-distance calibration terms to the ISC dataset show that estimated m_b is then approximately independent of distance and provides unbiased estimates of m_b in comparison with other correction terms. Comparison of event magnitude m_b calculated using the Gutenberg-Richter calibration, and that of this study, shows that the new calibration terms increase small magnitudes and decrease large magnitudes, hence the new depth-distance terms give a higher b-value.

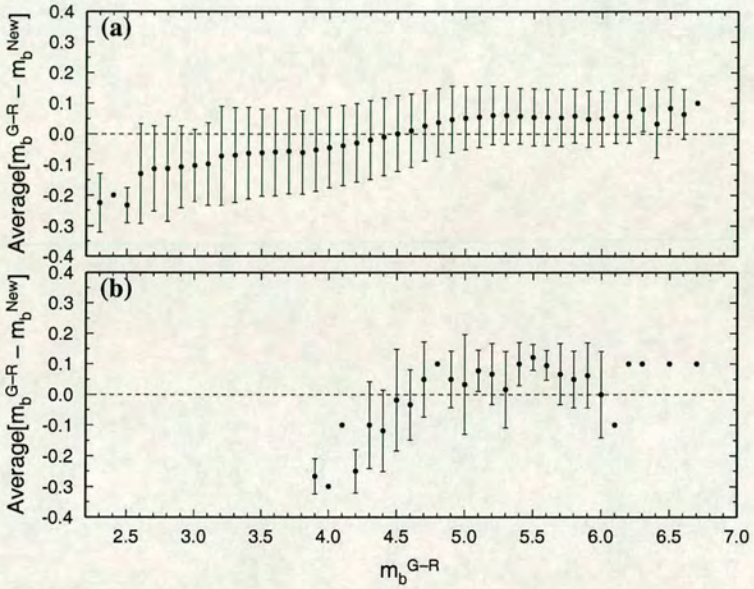

Figure 5.11. Average values of $m_b^{\text{G-R}} - m_b^{\text{New}}$ against $m_b^{\text{G-R}}$ with standard deviations. (a) For 60,544 out of 110,225 earthquakes. (b) For 180 out of 420 nuclear explosions.

5.5 Comparison of m_b against $\log M_0$ for different correction terms

Figure 5.12 shows a comparison of four different determinations of m_b versus $\log M_0$ for the ISC dataset of magnitudes and depths and the CMT Catalogue of seismic moment, with m_b averaged in 0.1-wide intervals in $\log M_0$. In m_b against $\log M_0$ plots of this section, both

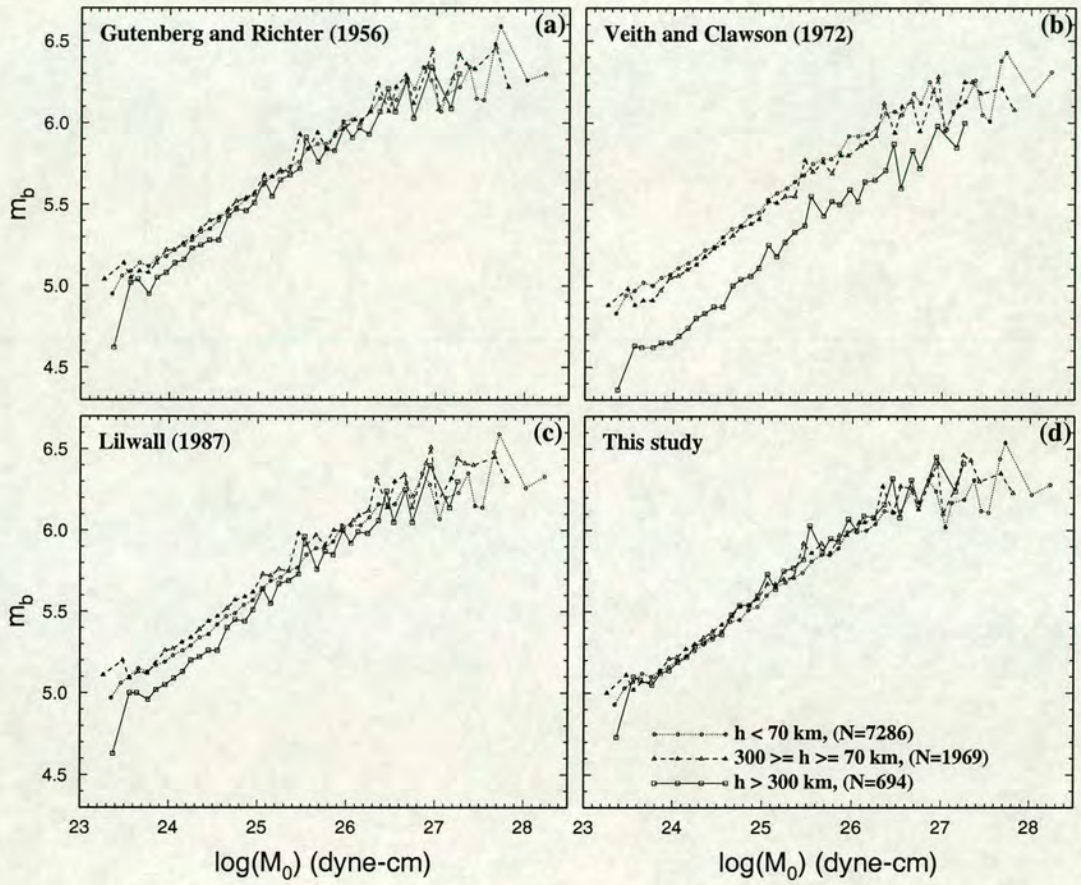

Figure 5.12. m_b, averaged over 0.1-wide intervals of $\log M_0$, versus $\log M_0$, using ISC focal depths. (a) Using Gutenberg-Richter (1956) depth-distance terms in determining body-wave magnitude. (b) Using Veith-Clawson (1972) depth-distance terms. (c) Using Lilwall (1987b) depth-distance terms. (d) Using new depth-distance terms.

m_b and $\log M_0$ values are expressed to two decimal places, so each data point on the graph indicates the position of magnitude values for earthquakes with the same $\log M_0$, but with different magnitude when averaged. In the case of the Gutenberg-Richter and Lilwall corrections (Figs. 5.12a and 5.12c), the m_b of deep earthquakes is underestimated by about $0.1 - 0.2$ and by about $0.1 - 0.3$ magnitude units respectively, but when the Veith-Clawson depth-distance

terms are used, m_b is underestimated by about 0.3 – 0.4 magnitude units for deep earthquakes (Fig. 5.12b). This discrepancy is even larger when the CMT focal depth is used instead of ISC focal depth (Fig. 5.13).

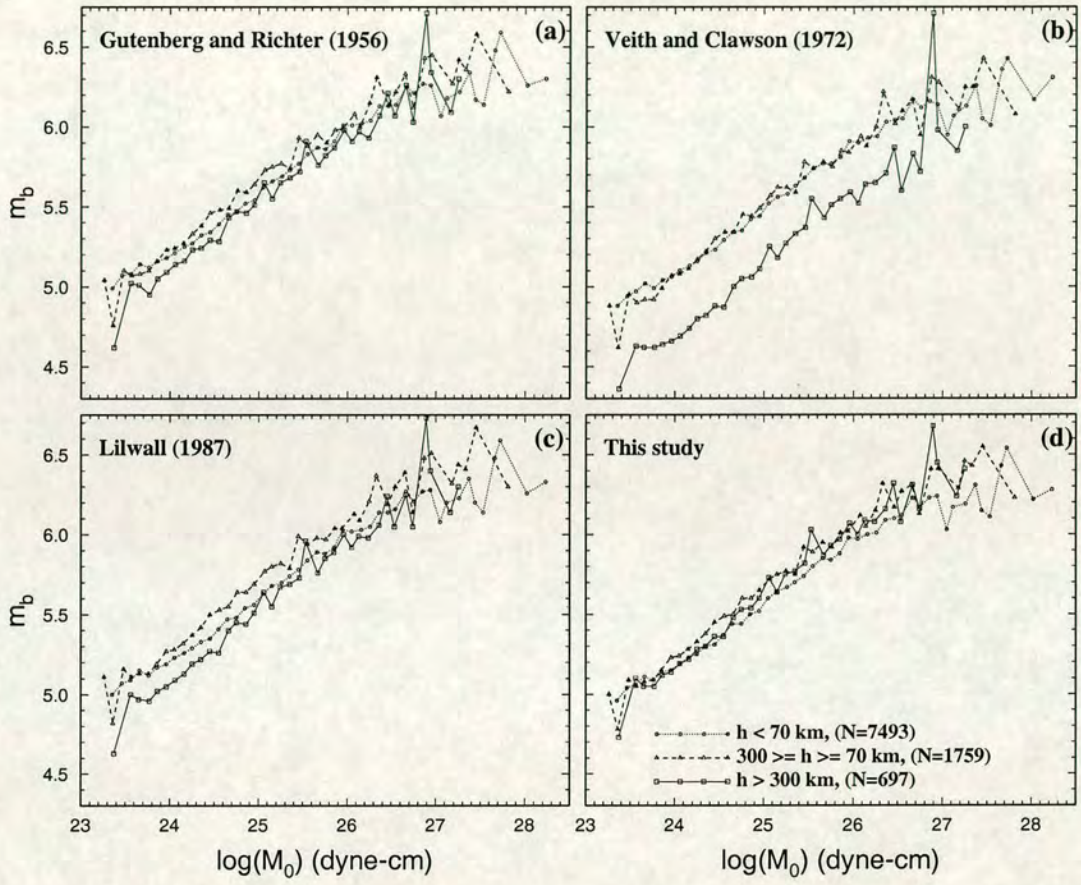

Figure 5.13. As Figure 5.12 except CMT focal depths.

Application of the new depth-distance correction terms for the determination of m_b approximately does not give bias with depth using ISC depths (Fig. 5.12d), but for CMT depth there is a bias of about 0.15 magnitude units for earthquakes at different depths. As Figure 5.14a shows, for some earthquakes ISC has given a zero depth, while those earthquakes in the CMT Catalogue have depths in the range of about 10 km to 300 km. Therefore for those earthquakes with small ISC depth, the large values of depth-distance correction terms have been used in the determination of m_b. When considering CMT depth, those earthquakes move systematically to the deeper range, which should have small values of depth-distance correction terms. It is well known that heterogeneity within the Earth, and in some cases the acceptable solution

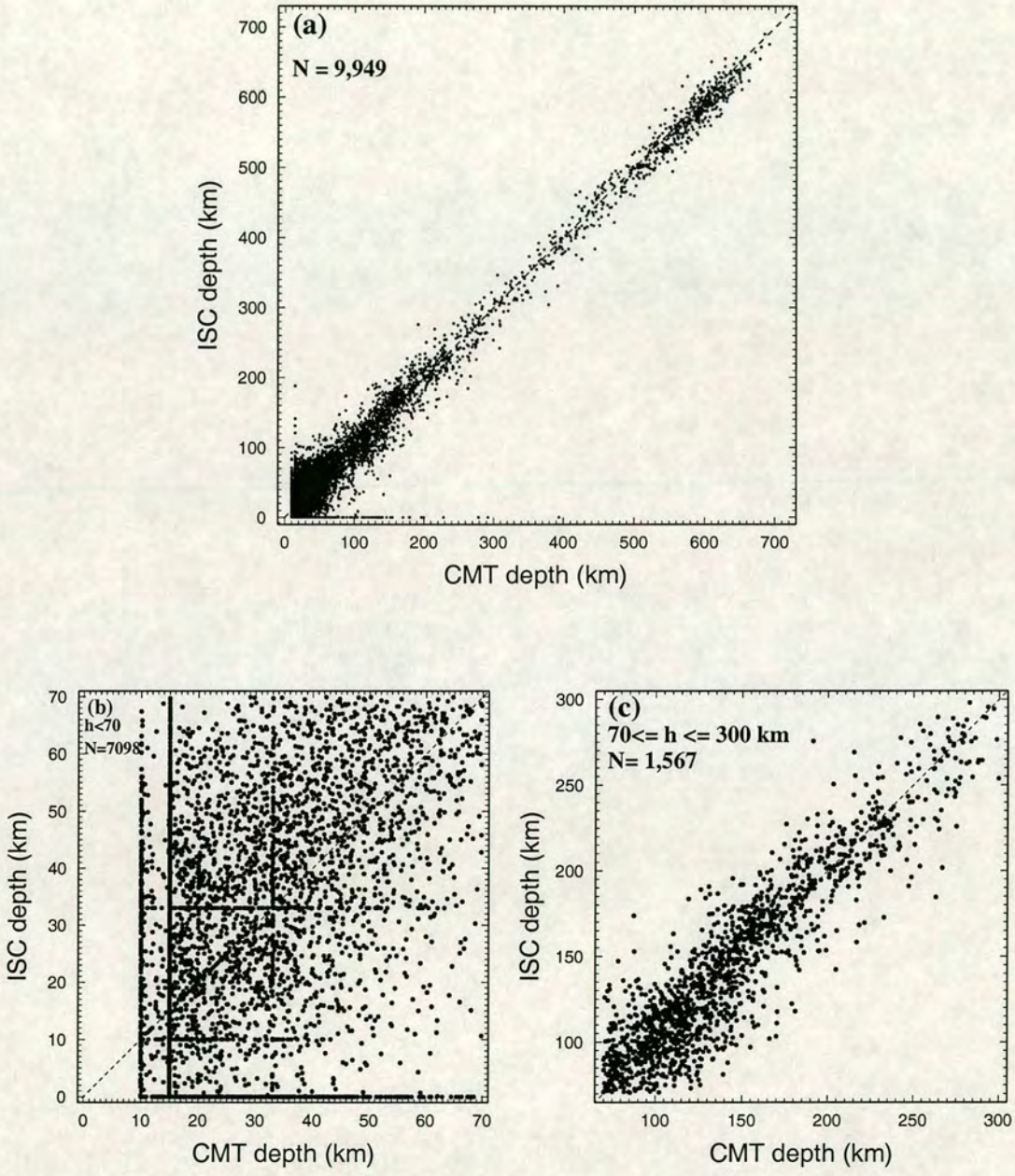

Figure 5.14. Comparison of ISC depth with CMT depth. (a) 9,949 individual data points of all earthquakes. (b) For 7,098 shallow depth ($h < 70$ km) earthquakes. (c) For 1,567 intermediate depth (70 km $\leq h \leq$ 300 km) earthquakes. In each case the dashed line shows the locus of equality.

of the standard least-squares analysis, affects the accuracy of the determination of earthquake locations specially on focal depth (see Adams, 1992, and Adams *et al.*, 1982). As mentioned before, depths values of 0, 10, and 33 km in the ISC Catalogue and depths values of 10, 15, and 33 km in the CMT Catalogue are dominated by artificial effects such as fixing for negative or unstable values and probably as starting depth in inversion routine. Figure 5.14 shows that, for shallow earthquakes, the ISC depth tends to be larger than the CMT depth; for intermediate and deep-focus earthquakes, the reverse is true. This discrepancy may be related to the Earth models which ISC and CMT use in their depth determinations. ISC uses the Jeffreys and Bullen (1940) model. In the CMT the PREM model is used. At shallow depths the Jeffreys-Bullen model is faster than PREM model, but at upper mantle the opposite is true. An alternative explanation for difference in ISC and CMT depth for shallow focus earthquakes proposed by Dziewonski and Woodhouse (1983) in comparison CMT depths with those determined by NEIC (which uses Jeffreys-Bullen model such as ISC), is that many pP readings are actually reflections from the ocean surface rather than the crust-ocean interface. In addition to reasons cited above, other possible factors are frequency-dependent effects. The high frequency estimates (which ISC uses) reflect the depth at the initiation of rupture, while the lower frequency estimates (which CMT uses) reflect the centroid depth.

In the previous section it was concluded that use of new calibration terms gives a larger value for m_b in comparison with using the Gutenberg-Richter calibration terms. Figure 5.15 shows this discrepancy plotted against focal depth. In this Figure differences between the calculated values of m_b using four different calibration terms, averaged over 5-kilometre-wide intervals and plotted against ISC depth. As Figure 5.15 shows, differences between the two m_b values depend on depth. The averaged values of $m_b^{\text{G-R}} - m_b^{\text{V-C}}$ are positive for all depths and increase with depth, especially for $h < 45$ km and $h > 350$ km. The averaged values of $m_b^{\text{G-R}} - m_b^{\text{L}}$ are approximately zero along depth except at deeper depths. The values of $m_b^{\text{G-R}} - m_b^{\text{New}}$ are approximately zero by about 160 km, then become negative, reaching to a minimum of ≈ -0.2 at $h \approx 350$ km. Therefore, the calculated values of m_b using the Gutenberg-Richter correction, and new calibration terms are approximately the same for $h < 160$ km and $h > 500$ km, but they are systematically different at depth range of $160 < h < 500$. Figure 5.15d shows that $m_b^{\text{New}} - m_b^{\text{V-C}}$ is positive and increases linearly with increasing focal depth, so m_b^{New} is larger than $m_b^{\text{V-C}}$ by 0.1 to 0.5 units. In all cases of Figure 5.15, the scatter in values of $\overline{\delta m_b}$ in the depth range $450 \geq h \geq 250$ km and $h \geq 650$ km are larger because the number of events is smaller (see Fig. 5.9c). To clarify the differences in the mean and standard deviation values shown in Figure 5.15, the raw data for the number of events and their magnitudes as a function of depth, in 20 km depth intervals, for 110,720 events are plotted in Figure 5.16. The concentration of data, particularly at shallow depths, overshadows the discrepancy between $m_b^{\text{G-R}}$, m_b^{L}, and m_b^{New}.

In Figure 5.17 the calibrated m_b scales are cross-plotted using four different corrections. From Figures 5.15, 5.16, and 5.17 it can be concluded that generally $m_b^{\text{New}} \geq m_b^{\text{G-R}} \geq m_b^{\text{L}} \geq m_b^{\text{V-C}}$, when using this study, Gutenberg-Richter, Lilwall, and Veith-Clawson calibration terms. However, one can not justify generalisation of this conclusion through all focal depths.

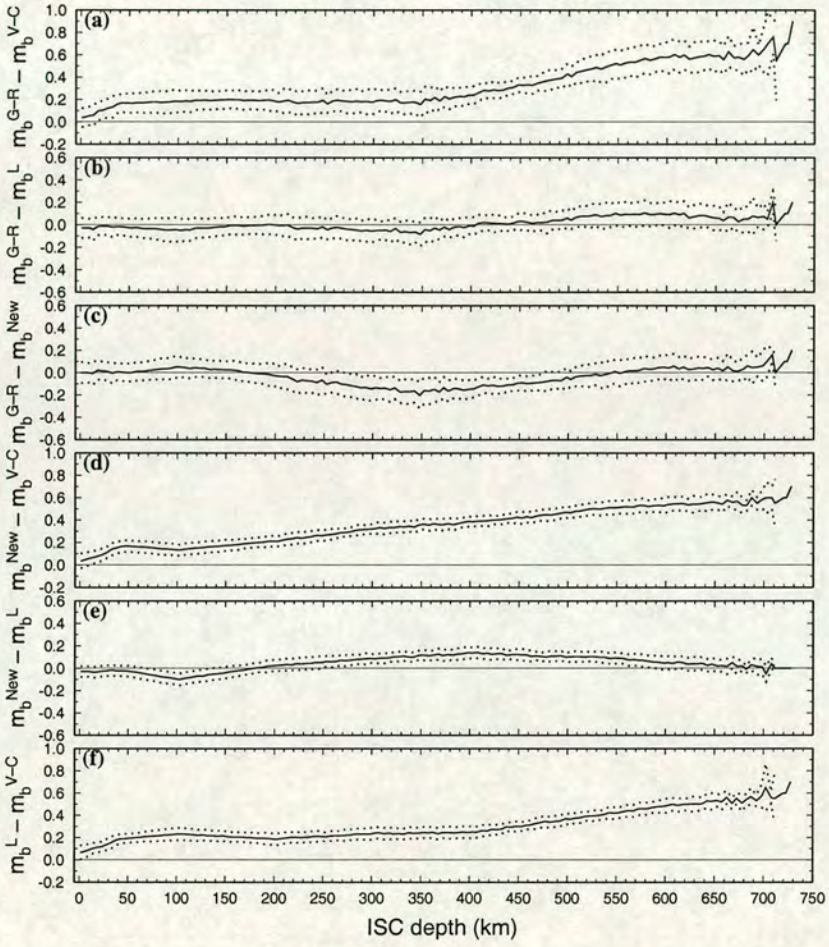

Figure 5.15. Averaged differences of two calculated m_b over 5-kilometres-wide intervals versus the ISC calculated depth, using four different correction terms. $m_b^{\text{G-R}}$, $m_b^{\text{V-C}}$, m_b^{L}, and m_b^{New} represent the mean magnitudes that are estimated using the Gutenberg-Richter, Veith-Clawson, Lilwall, and the new correction terms respectively. In each case the values shown by the solid lines are the averaged differences over the intervals, and dotted lines denote the range of $\pm$ standard deviation.

Kuge (1992), comparing m_b against $\log M_0$ for seven different subduction settings pointed out that for earthquakes around Japan with the same M_0, the body-wave magnitude published in the ISC Bulletin for intermediate earthquakes is larger than that for deep earthquakes by

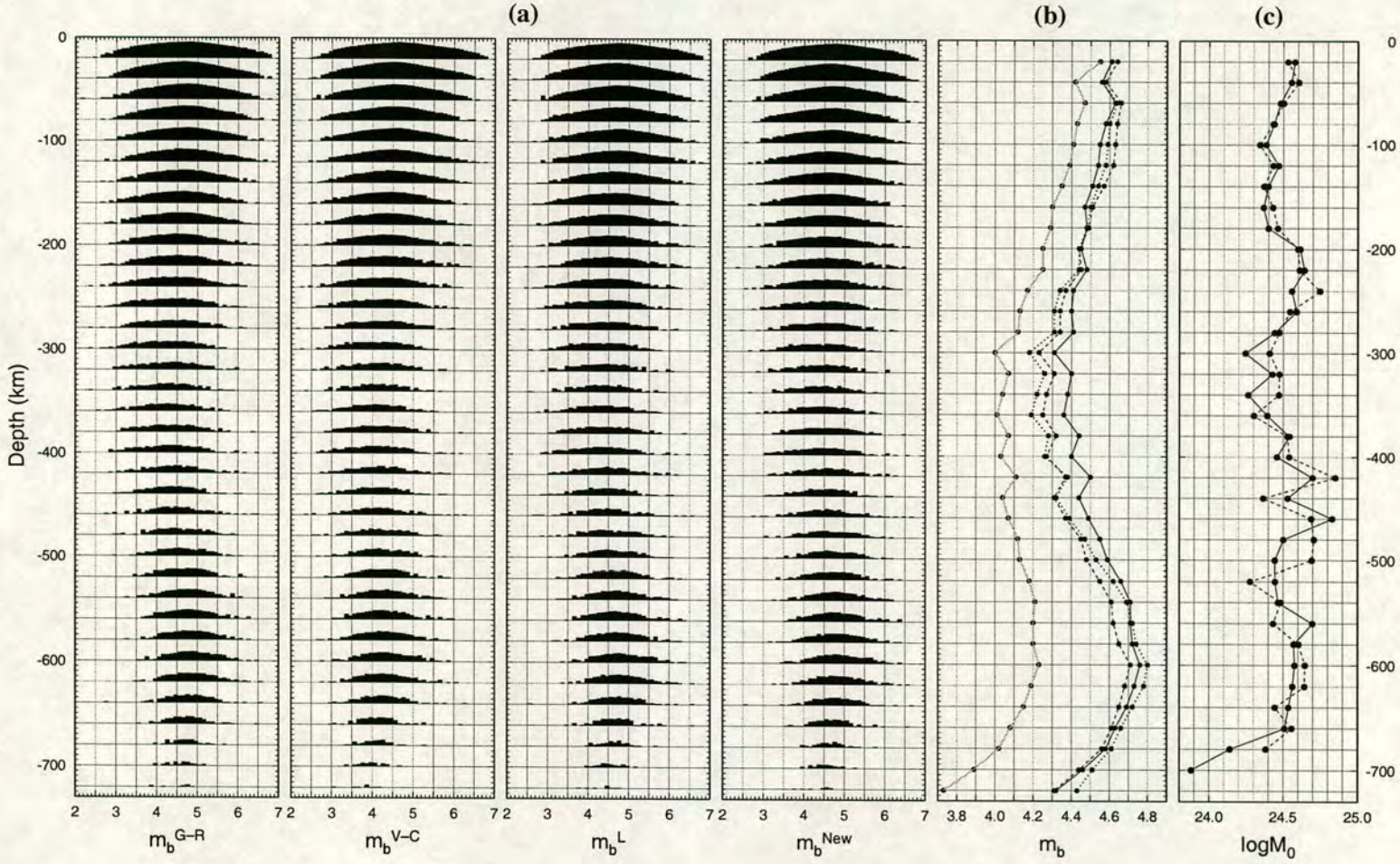

Figure 5.16. Comparison of the number of events and their magnitudes as a function of depth over 20 km depth intervals, for 110,720 events in the ISC Catalogue, when magnitudes are calculated using four different depth-distance correction terms. The height of the histogram bars is a logarithmic measure of the number of events, plotted on the same scale throughout. The shortest bars denote one event and the tallest denotes 3223 events. (b) For each 20-km depth interval the plotted points correspond to the mean magnitude in the corresponding histogram in (a). Dotted, gray, dashed, and solid curves represent the mean values of $m_b^{\text{G-R}}$, $m_b^{\text{V-C}}$, m_b^{L}, and m_b^{New} respectively. (c) For each 20-km depth interval, the mean value of $\log M_0$ for 9949 earthquakes from the Harvard CMT Catalogue is shown. The events are those for which the ISC "prime" location information are almost identical with those in the CMT Catalogue. The solid and dashed lines use the ISC and CMT depths respectively.

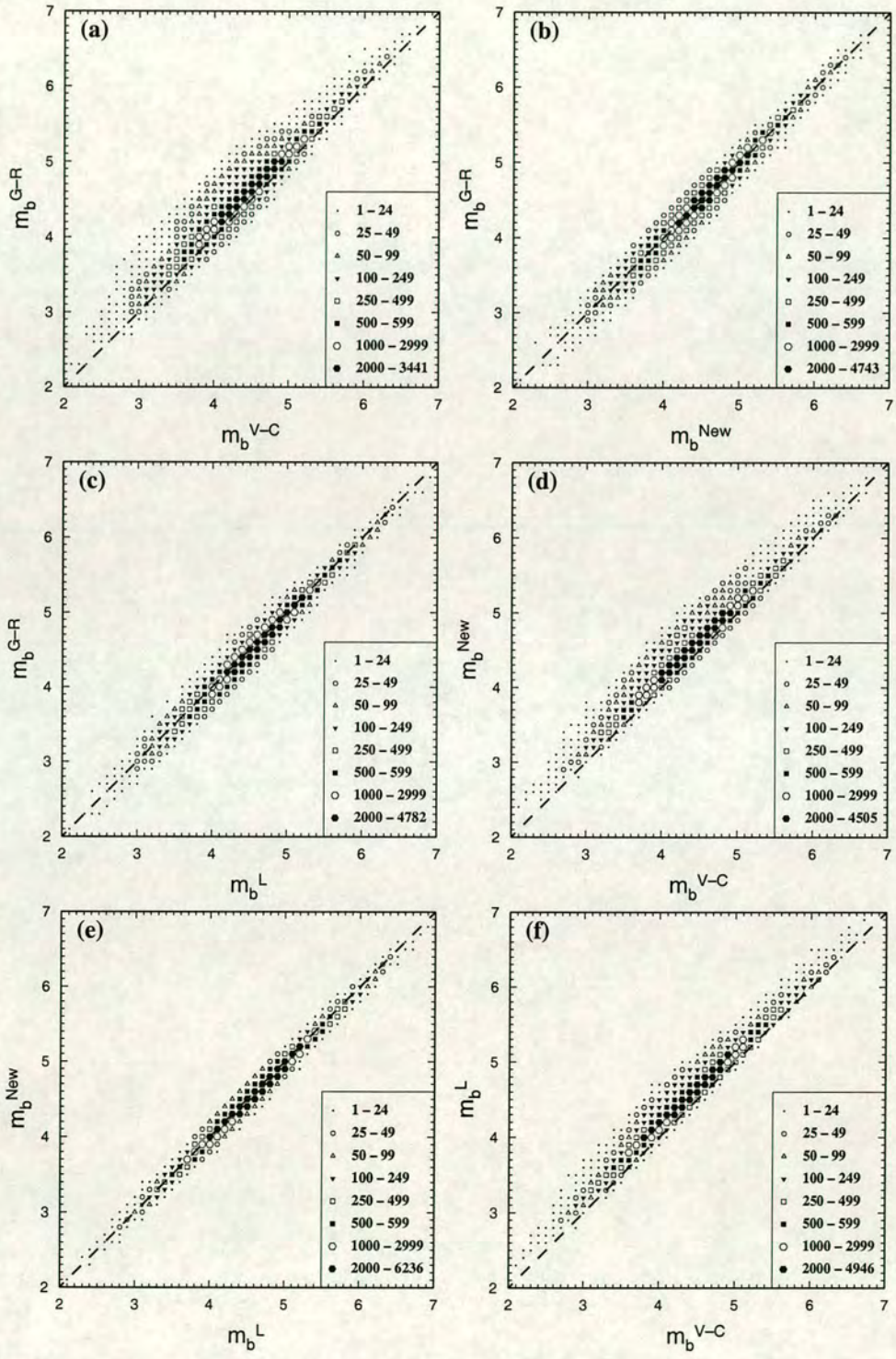

Figure 5.17. Comparison of m_b values calculated using different calibration terms for 110,720 events in the ISC Catalogue between 1978 and 1993. (a) $m_b^{\text{G-R}}$ versus $m_b^{\text{V-C}}$. (b) $m_b^{\text{G-R}}$ versus m_b^{New}. (c) $m_b^{\text{G-R}}$ versus m_b^{L}. (d) m_b^{New} versus $m_b^{\text{V-C}}$. (e) m_b^{New} versus m_b^{L}. (f) m_b^{L} versus $m_b^{\text{V-C}}$. In each case a dashed line shows the locus of equality.

0.2 to 0.3 units, and this discrepancy is independent of epicentral distance. He concluded that this discrepancy is due to a systematic bias introduced by the Gutenberg-Richter calibration terms, which have a depth-distance correction for intermediate earthquakes which is $\approx$ 0.2 magnitude units larger than for deep earthquakes at all distances. Kuge (1992) observed no significant depth-dependent m_b^{ISC} discrepancy in other regions e.g., around Tonga.

Here m_b versus $\log M_0$ is reexamined for the same regions which Kuge studied. However, he used data for the period from 1977 to 1985, while in this study ISC dataset between 1978 and 1993 is used. m_b values in 0.1-wide intervals of $\log M_0$ were averaged and plotted against $\log M_0$ in Figures 5.18 and 5.19, where in each case the red, the blue, and the green lines indicate the regression lines which were fitted to shallow, intermediate, and deep earthquakes respectively.

Contrary to previous definitions for intermediate earthquakes 70 km $\leq h \leq$300 km, the same definition of Kuge 100 km $\leq h \leq$300 km is used for comparison only in Figures 5.18 and 5.19. In some regions the saturation of m_b affects the slope of the regression lines, especially for shallow and intermediate earthquakes. As Figures 5.18 and 5.19 show, m_b using Gutenberg-Richter calibration is more dependent on focal depth than m_b using the new calibration terms.

Contrary to Kuge's result, the discrepancy of m_b for intermediate and deep earthquakes is observed not only in the Japan region but also in other regions, and this discrepancy differs according to the distribution of depths. Therefore the discrepancy of m_b in some regions e.g., around Japan and the South Pacific is large, but in some other regions e.g., around Tonga and South America it is small. For such regional variation, it is likely that the attenuation in the upper mantle and the sources themselves (rise time) have more effect than the other effects along the ray paths.

As a result, the Gutenberg-Richter calibration function gives a systematic bias of m_b with depth (see Figs. 5.12a and 5.18), but the new calibration function gives an m_b almost independent of depth (see Figs. 5.12c and 5.18). As was observed before, the error in the calculation of focal depth directly affects the estimated m_b using any calibration function, and it is well known that the error in focal depth in some cases is very large.

5.6 Station correction

Station correction term mainly includes any effects due to recording instruments and geology of recording station. The lithological composition under the seismic station has an important role in attenuation or enhancing arrival signals. Many studies show that the station correction which is usually referred to as network bias, can be significant. Correcting estimated m_b for station effects reduces the variance of the observations and so improves the precision of the estimates.

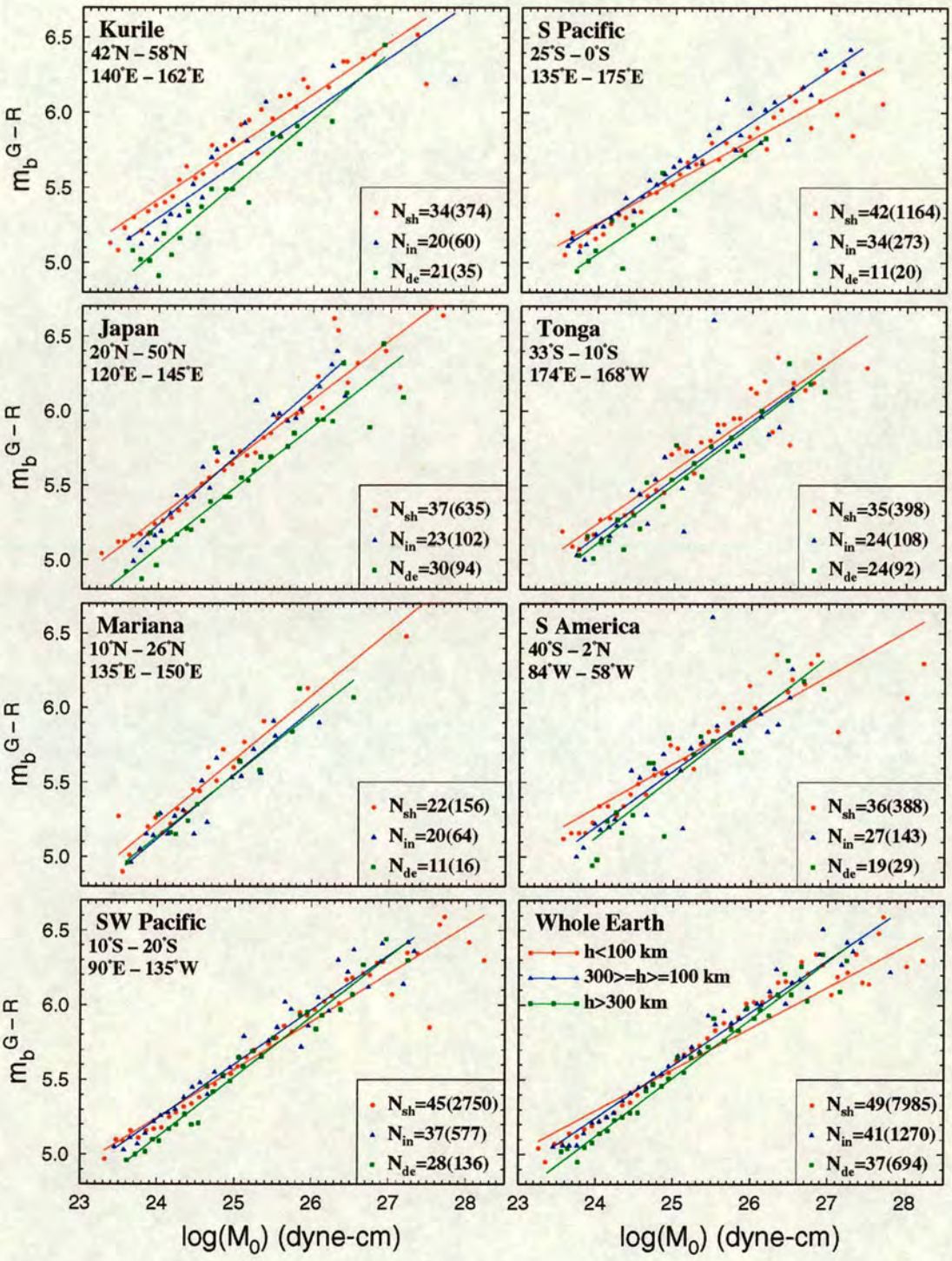

Figure 5.18. The relationship between $m_b^{\text{G-R}}$ (using Gutenberg-Richter calibration terms) and $\log M_0$ for different regions. In each case red, blue, and green lines are the regression lines fitted to shallow, intermediate, and deep earthquakes respectively, and N_{sh}, N_{in}, N_{de} show the relevant binned data points. The numbers inside brackets indicate the individual data points. The circles, triangles, and squares represent the $\overline{\sum m_b}$ for shallow, intermediate, and deep earthquakes respectively. Note, data are grouped according to ISC depth.

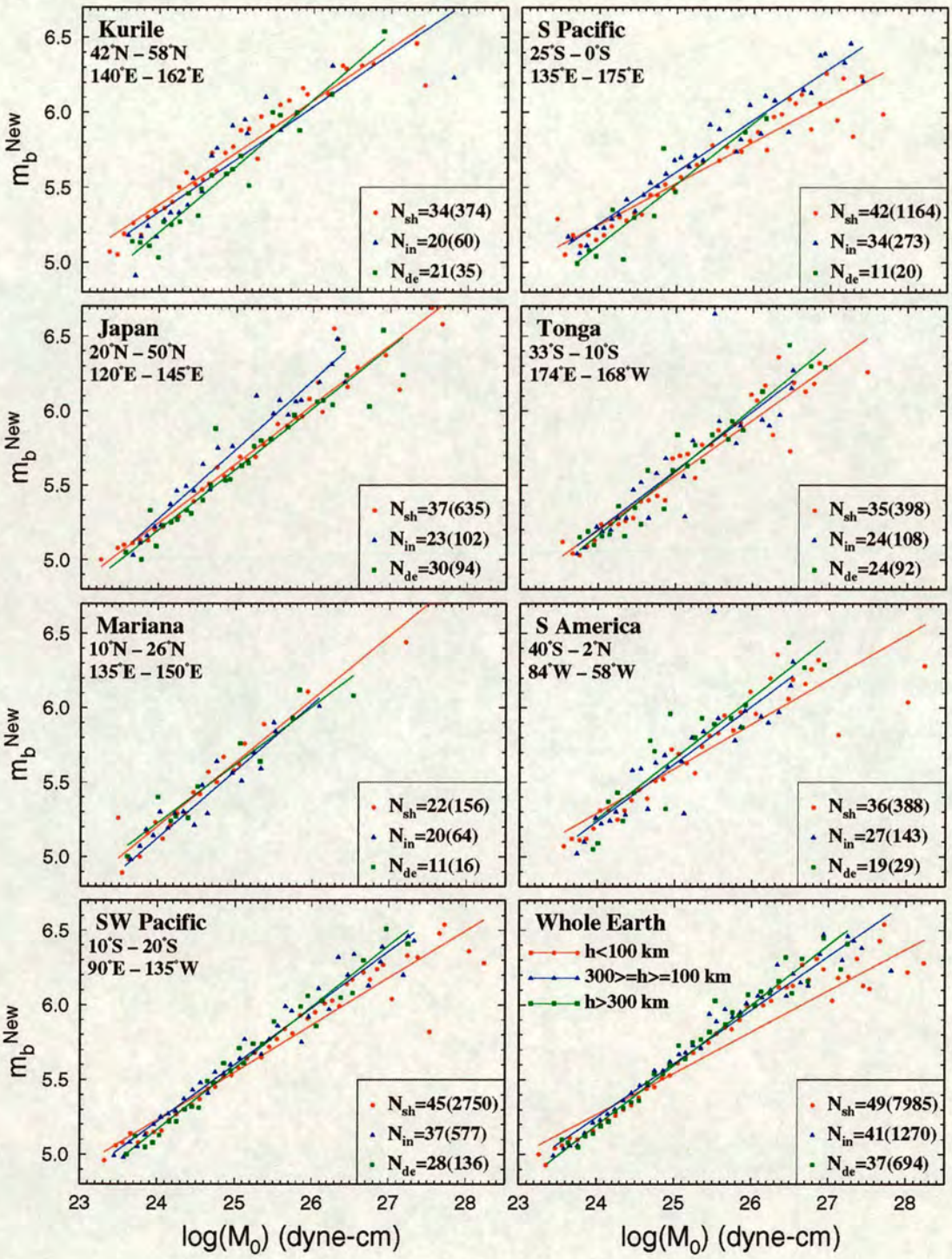

Figure 5.19. The relationship between m_b^{New} (using new calibration terms) and $\log M_0$ for different regions. In each case red, blue, and green lines are the regression lines fitted to shallow, intermediate, and deep earthquakes respectively, and N_{sh}, N_{in}, N_{de} show the relevant binned data points. The numbers inside brackets indicate the individual data points. The circles, triangles, and squares represent the $\overline{\sum m_b}$ for shallow, intermediate, and deep earthquakes respectively. Note, data are grouped according to ISC depth.

Therefore m_b estimated using station correction should give the best relative magnitudes for the sources. Here the station correction was calculated for each station by averaging residuals from event magnitude (events in which more than two stations contributed to the determination of $\overline{m_b}$). For each station, four separate station terms were calculated using magnitudes which were estimated using four different depth-distance correction terms. The resulting station corrections

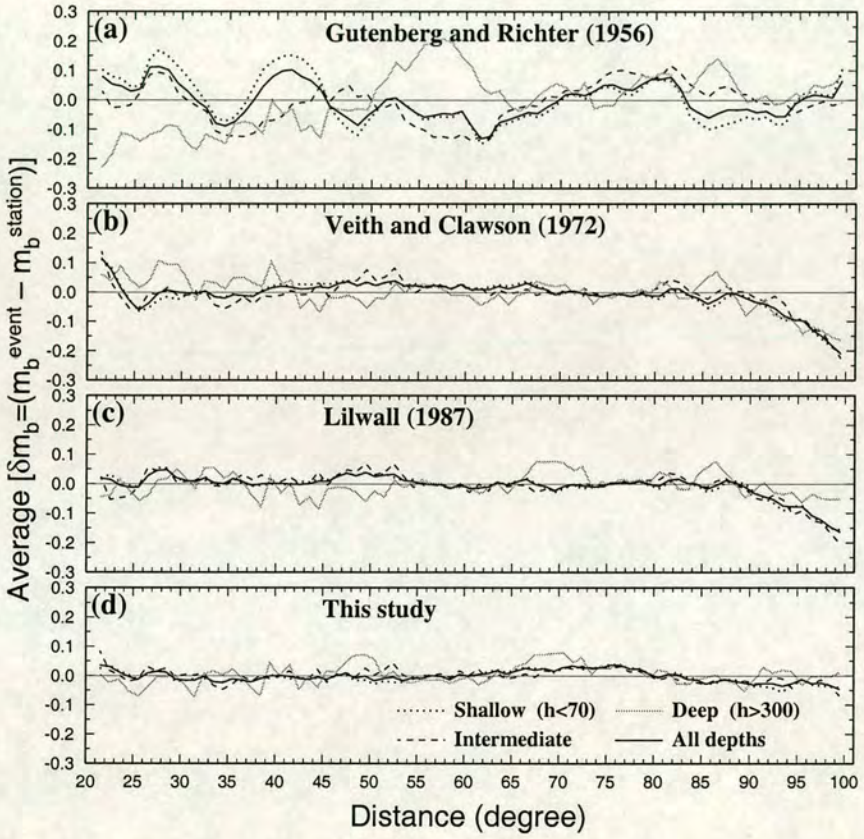

Figure 5.20. Comparison of average residual of station-magnitude from event-magnitude with 1-degree-wide intervals against distance, for 110,720 events using different depth-distance correction terms, and applying station corrections in the determination of m_b.

were then used for determining event magnitude, but only at stations for which the ISC have used more than 200 time observations in calculating event magnitude between 1978 to 1993 (The correction values for these stations (458) are tabulated in Table B.1). For other stations for which ISC has used 200 or less than 200 time observations, magnitudes were estimated without using station corrections. The resulting residuals are shown as a function of epicentral distance in Figure 5.20.

As Figure 5.20 shows, using station corrections reduces the residuals generally in comparison with Figure 5.8 for without station correction. In the distance range of about 40°–80° a variety of residuals which are originally small (without using station correction), do not change much. The negative peak at a distance of about $\Delta = 50°$ for deep earthquakes disappears, but the positive peak of residuals at distance about 87° for deep earthquakes does not (compare Fig. 5.20 with Fig. 5.8). This shows the effect of station residual, combined with non-random source/distance distribution for deep earthquakes. Using station corrections, the residuals at all depths are significantly increased in the negative direction at greater distances, but are slightly increased in the positive direction at closer distances (compare Fig. 5.20 with Fig. 5.8). This result does not change when applying station corrections to the whole dataset without restriction. A possible reason for this deviation could arise from a large bin width (1-degree-wide) which is used here. The residuals of $m_b^{\text{event}} - m_b^{\text{station}}$ were averaged over two small intervals of 0.5° and 0.1°, but again the same result was observed in the averaged residuals. The station correction terms which were used in Figure 5.20 were averaged over 1-degree-wide intervals for each case separately, thus in all four cases the averaged station corrections are approximately independent of distance up to about 88°, but for $\Delta > 88°$ they progressively increase. At $\Delta > 88°$, due to the core shadow zone, the observations quickly reduce with distance. So, the main reason for that increase in the negative direction can be from both of non-random distribution of anomalous station and non-random source/distance distribution.

In Figure 5.21 the standard deviation of the individual mean magnitudes, for events in which two or more amplitude data have been used in calculating the mean magnitude are compared, for the depth-distance correction terms of Gutenberg-Richter, Veith-Clawson, and the new correction terms which are used in the determination of m_b. In Figure 5.21b station corrections have been included, but not in Figure 5.21a. Figure 5.21b shows that inclusion of station corrections reduces the average standard deviations by about 0.07 magnitude units, which is statistically significant.

Figures 5.21a and 5.21b show that standard deviations of event magnitude i.e., $\sigma_{m_b} = \sqrt{\sum_{i=1}^{n}(m_b^{\text{event}} - m_b^{\text{station}})^2/(n-1)}$, in the case of using Gutenberg-Richter calibration terms are larger than others. The histogram of events in which ISC has used more than one station magnitude for calculating event magnitude is shown in Figure 5.21c. As mentioned in Chapter 2, magnitude is a parameter which has a great azimuthal variation due to the radiation pattern etc., and a reliable estimated value (event magnitude) can be made only by averaging many station magnitudes (with a good azimuthal coverage).

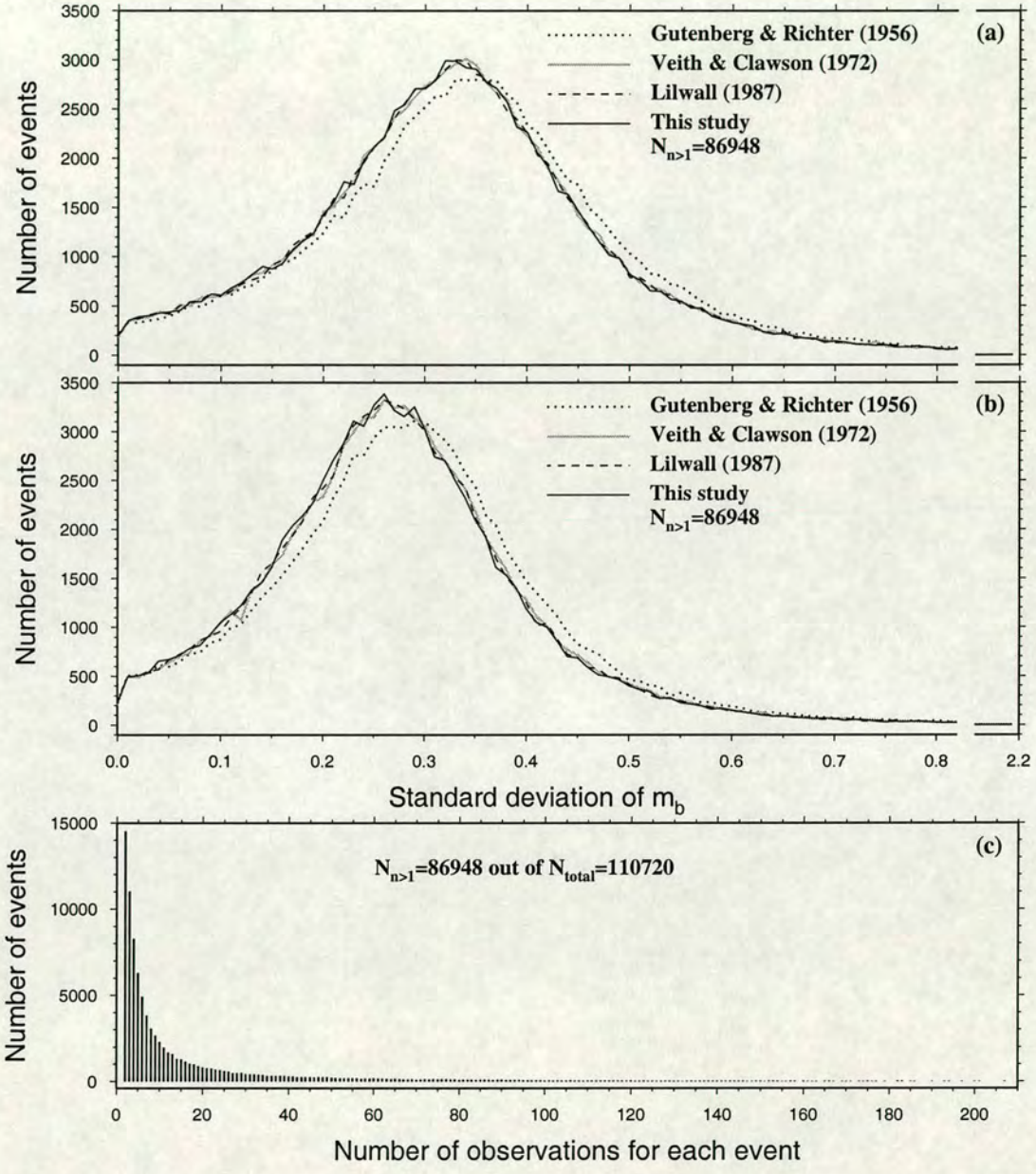

Figure 5.21. (a) Comparison of standard deviation of event magnitude using different depth-distance correction terms without station corrections. (b) as (a) but including station corrections for stations which ISC has used more than 200 time observations in calculating event magnitudes (station correction was not used for other stations). (c) Histogram of events versus number of station observations used in calculating event magnitude in ISC Catalogue between 1978 to 1993. Events with only one observation have been excluded.

5.7 Relation of estimated m_b^{New} and nuclear explosions yield

As described before, the use of the new calibration terms gives a large value of m_b in comparison with using Gutenberg-Richter calibration terms. As a consequence, some empirical relationships such as m_b—yield for nuclear explosions will be different. In this section the m_b^{New}—yield is considered, using yield data from the Oklahoma Catalogue (geopher://wealkaka.okgeosuvey1.gov) of supposed nuclear explosions. In the ISC Catalogue there are 420 events which have been identified as nuclear explosions from 1978 to 1993. On the other hand, for 229 of these explosions actual yields Y in kilotons (no yield ranges) are available in the Oklahoma Catalogue, of which 162, and 66 have been fired by the USSR and France respectively. According to the ISC prime location, 101 of these underground explosions are located at the Semipalatinsk Test Site (STS) in Kazakhstan, and 66 are located at or near Mururora Island. Individual calculated m_b values using the new calibration and the Gutenberg-Richter terms, against $\log Y$ for these explosions are plotted in Figures 5.22. As Figures 5.22a, 5.22b, 5.22c, and 5.22d show, the scatter of observation at STS is less than for Mururora Islands.

One way to estimate the seismic yield of a nuclear explosion is to obtain a calibrated magnitude-yield relationship based on explosions with known yields and magnitudes. However, it is well known that the uncertainties in yield estimates particularly from m_b are significant because of the scatter in magnitudes. Also, conversion from seismic size to yield requires that the coupling factor be known, but unfortunately this information is not generally available.

To reduce the dominance of data at a special part for regression analysis, the m_b^{New} and $m_b^{\text{G-R}}$ values are averaged over 0.1-wide intervals of $\log Y$ units then were plotted against $\log Y$ in Figures 5.22e and 5.22f with standard deviations. Explosions that are shown by asterisk symbol in Figures 5.22c and 5.22d are not used in the averaging and regression analysis. A regression line fitting to averaged m_b^{New} data points, assuming no uncertainty in yield gives:

$$m_b^{\text{New}} = (4.3488 \pm 0.0414) + (0.8997 \pm 0.0291) \log Y \quad \text{for Semipalatinsk Test Site} \tag{5.17}$$

and

$$m_b^{\text{New}} = (4.0562 \pm 0.0630) + (0.8061 \pm 0.0466) \log Y \quad \text{for Mururora Island \& around} \tag{5.18}$$

where Y is explosion yield in kilotons. The above procedure was applied for $m_b^{\text{G-R}}$ and the the

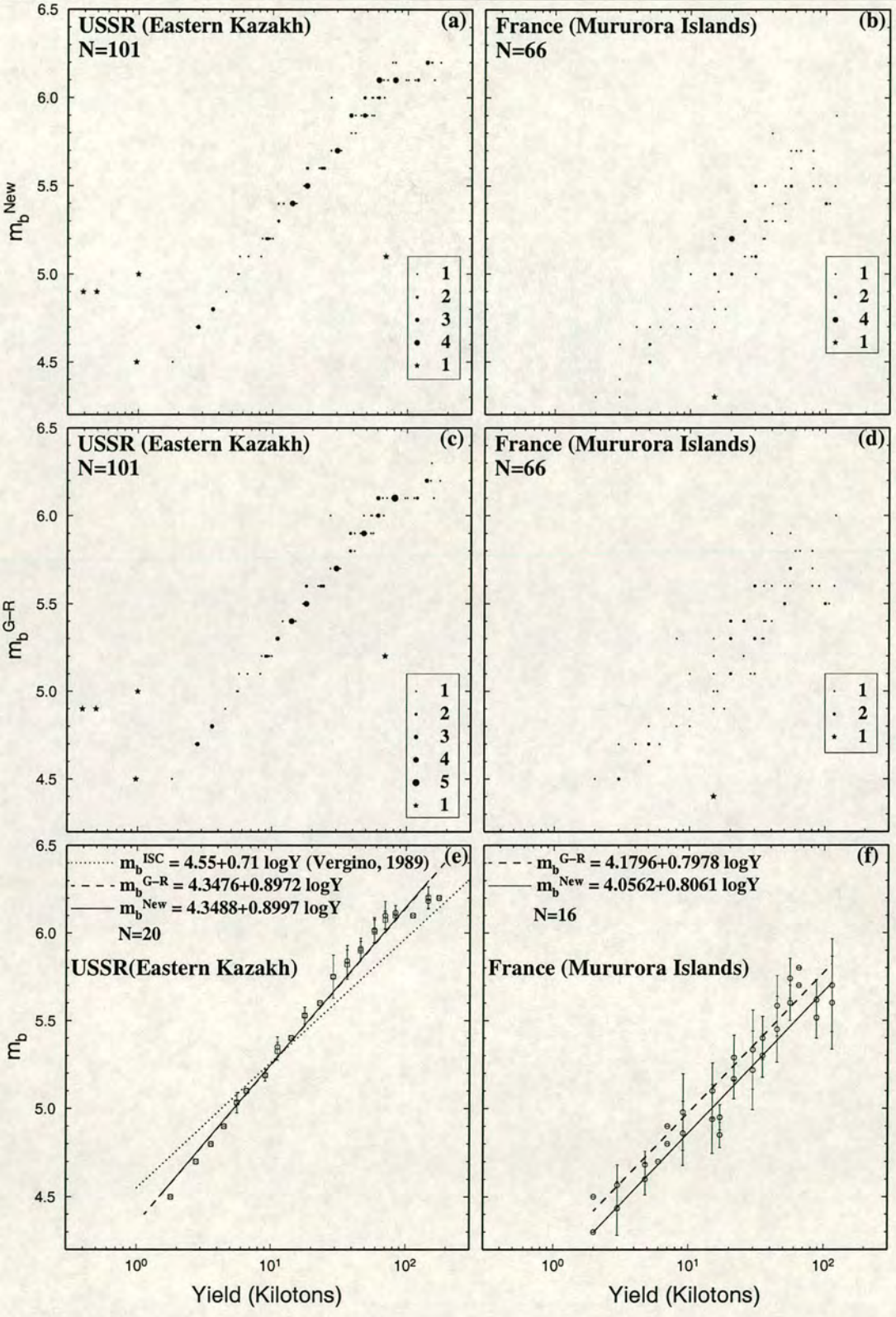

Figure 5.22. (a) m_b^{New} versus $\log Y$ for nuclear explosions in the Semipalatinsk test site. (b) as (a) for Mururora Islands. (c), and (d) as (a), and (b) respectively, but for $m_b^{\text{G-R}}$. (e) Averaged m_b over intervals of 0.1 $\log Y$ units, for the Semipalatinsk test site. (f) as (e) for Mururora Islands. In (e) and (f) the circles and squares show averaged m_b^{New} and m_b^{New} with standard deviations respectively, and the regression lines of these data points have been shown by dashed and solid lines. In (e) the dotted line shows the equation of $m_b = 4.55 + 0.71 \log Y$ (Vergino, 1989).

following regression lines are obtained:

$$m_b^{\text{G-R}} = (4.3476 \pm 0.0380) + (0.8972 \pm 0.0267) \log Y \quad \text{Semipalatinsk Test Site} \tag{5.19}$$

$$m_b^{\text{G-R}} = (4.1796 \pm 0.0703) + (0.7978 \pm 0.0519) \log Y \quad \text{Mururora Island \& around} \tag{5.20}$$

In 1989 Soviet seismologists published details of 96 nuclear explosions conducted between 1961 and 1972 at STS (Bocharov *et al.*, 1989). Vergino (1989) used the ISC m_b and yields of 20 above explosions and obtained a regression line as

$$m_b = 4.55 + 0.71 \log Y \tag{5.21}$$

which is significantly different from those obtained in this study.

As equations (5.17), (5.19) and Figure 5.22e show, the difference between m_b^{New} and $m_b^{\text{G-R}}$ for the Semipalatinsk test site is insignificant, and as mentioned before, in general m_b^{New} is greater than $m_b^{\text{G-R}}$. Figure 5.22f is therefore contrary to what is expected; for the Mururora Islands m_b^{New} is smaller than $m_b^{\text{G-R}}$ by about 0.08 magnitude units (compare Eq. (5.18) with Eq. (5.20)), and the difference between m_b^{New} and $m_b^{\text{G-R}}$ is significant. This discrepancy is due to the heterogeneous distribution of observations over epicentral distance. Figure 5.23 shows the distribution of 9,629 observations from 101 explosions in the Semipalatinsk test site and 1,041 observations from 66 explosions in the Mururora Islands. Also, in this Figure the new calibration terms are compared with the Gutenberg-Richter terms for surface focus events. Figure 5.23 shows that in the Semipalatinsk test site concentration of observations (gray histograms) are high at $30° \lesssim \Delta \lesssim 54°$ and at this range of distances the new calibration terms are larger than the Gutenberg-Richter terms. But for the Mururora Islands concentration of observations (black histograms) are high at $60° \lesssim \Delta \lesssim 90°$ and at this range of distances the new calibration terms are smaller than the Gutenberg-Richter terms.

As a result uncertainty in the relation of m_b—$\log(Y)$ depends not only upon the lithology of regional structure, and the calibration terms used, but also on the non-random distribution of seismic stations around underground nuclear explosions test sites. This uncertainty is greater when the Gutenberg-Richter correction terms are used.

5.8 Conclusions

A large bias has been observed in the estimates of magnitudes at different epicentral distances using the existing Gutenberg-Richter calibration terms. Accordingly, the calibrating terms presently used need to be revised (Fig. 5.8a).

New empirical global depth-distance calibration terms for the determination of body-wave

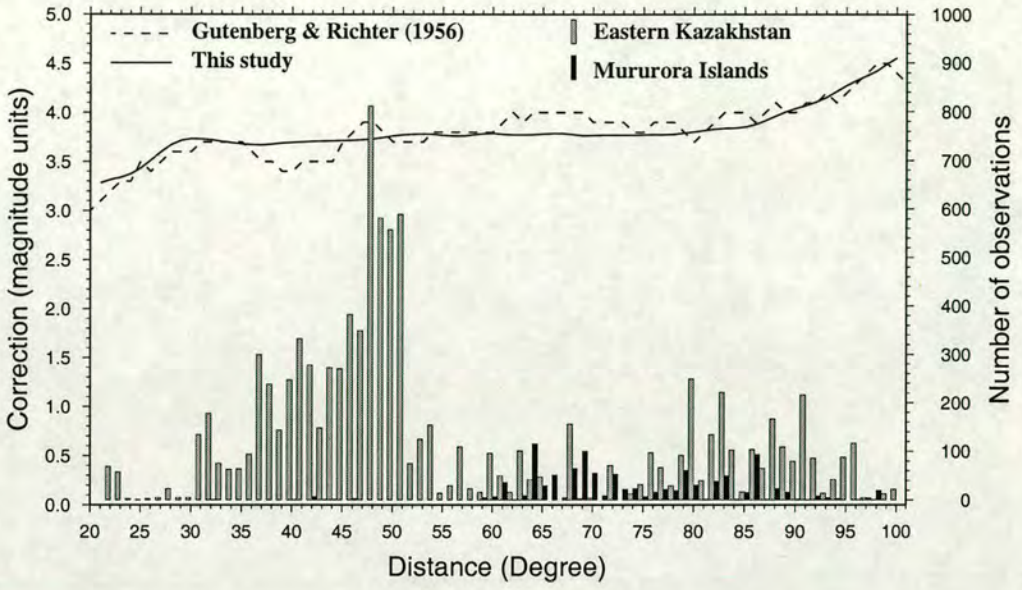

Figure 5.23. Comparison of the new correction terms (solid curve) with the Gutenberg-Richter's terms (dashed curve) for surface focus events. Also, comparison distribution of 9,629 observation from 101 underground nuclear explosions in the Semipalatinsk test site (gray histograms) with distribution of 1,041 observation from 66 underground nuclear explosions in the Mururora Islands (black histograms).

magnitude have been determined using the scalar moment M_0 values of the Harvard CMT Catalogue. Comparison of deviations of station magnitudes from the mean, computed using the calibration terms of this study and major previous studies result in several important conclusions, as follows.

Comparison of the Gutenberg-Richter (1956), Veith-Clawson (1972), Christoskov *et al.* (1979), Marshall *et al.* (1986), and Lilwall (1987b) corrections with those obtained here has shown that m_b is least biased when using the correction terms of Veith-Clawson, Lilwall, and this study (Fig. 5.8).

A systematic bias in the estimated m_b for distance greater than 88° has been shown for the Veith-Clawson corrections and Lilwall's terms. The Veith-Clawson and Lilwall correction terms, underestimate m_b for deep earthquakes by about 0.3–0.5 and 0.1–0.2 magnitude units respectively (Figs. 5.12b and 5.12c).

Application of the new correction terms to the ISC dataset has shown that the estimated m_b is then independent of distance and focal depth, and provides unbiased estimates of m_b in comparison with other depth-distance terms. Also, comparison of event magnitude m_b calculated using the Gutenberg-Richter correction terms, and that of this study, shows that the

new correction terms systematically increase small magnitudes and decrease large magnitudes (see Fig. 5.10). Therefore, for a dataset in seismicity studies, the b-value based on m_b^{New} values will be systematically higher than that for $m_b^{\text{G-R}}$ values.

Comparison of event magnitude values obtained using four different depth-distance correction terms has shown that, $m_b^{\text{New}} \geq m_b^{\text{G-R}} \geq m_b^{\text{L}} \geq m_b^{\text{V-C}}$, although $m_b^{\text{G-R}}$ and m_b^{L} are generally similar. In these last two studies the comparison is governed more by the depth effect (Figs. 5.15, 5.16 and 5.17).

A discrepancy between $m_b^{\text{G-R}}$ for intermediate and deep earthquakes has been observed not only in the Japan region but also in other regions such as the South Pacific (Fig. 5.18). This differs from the result of Kuge (1992), who observed this effect only for Japan region. Also, discrepancy between m_b^{New} for intermediate and deep earthquakes is much smaller than for $m_b^{\text{G-R}}$ (Fig. 5.19).

The standard deviation of m_b values for single events are compared in Figure 5.21a, for each author's correction terms. This has shown that the Gutenberg-Richter standard deviations are consistently larger than those for Veith-Clawson, Lilwall, and this study.

Station corrections obtained from station residuals have been applied using only stations for which ISC have used more than 200 time observations in calculating event magnitudes between 1978 to 1993. The station corrections reduce the average standard deviation of event m_b values by about 0.07 magnitude units, which is statistically significant (Fig. 5.21b).

Comparison of the empirical relation of m_b—$\log(Y)$ using the new correction terms and the Gutenberg-Richter terms, has shown that uncertainty in the m_b—$\log(Y)$ depends on not only lithology of regional structure and the calibration terms used, but also upon the non-random distribution of seismic stations around underground nuclear explosions, especially when the Gutenberg-Richter terms are used.

Chapter 6

Collapsing of surface wave seismograms

6.1 Introduction

In chapters 2 and 3 path effect was identified as one source of bias in the determination of surface-wave magnitude (M_s). Ekström and Dziewonski (1988) showed evidence of systematic deviations in M_s dependent upon tectonic setting. They concluded that M_s tends to overestimate the strength of most continental earthquakes, and to underestimate it for those along mid-ocean ridges. Abercrombie (1994) concluded that surface-wave path type is clearly responsible for the high M_s observed in continental areas, causing systematic overestimation by about 0.2 magnitude units.

The main problem of path in M_s measurements seems to be in allowing for path-dependent dispersion. Marshall and Basham (1972) did this by applying a path correction term in the M_s formula. A better method may be to correct all given digital seismograms to one standard distance and to one type of path. In this chapter the method of collapsing the dispersion on seismograms to a standard distance, or to zero distance is examined with a view to reducing path-dependent bias. In principle, the collapsing of surface wave seismograms to a shorter distance also offers the possibility of improved signal-to-noise ratio, and hence a lower detection threshold. First some characteristics of surface-waves are considered, then some examples of removing dispersion to a standard distance are given.

6.2 Surface waves

In an infinite homogeneous isotropic medium only P- and S- body waves can exist. Body waves travel through Earth's layers and interaction of these waves with free-surface and Earth's layers generate additional waves called surface waves, and they propagate parallel to the Earth's

surface and various underlying boundaries. Surface wave amplitude generally decreases with depth, and they are most distinct at distances farther away from the earthquake source. A detailed theoretical account of how these waves arise has been given in, for example, Aki and Richards (1980), Bullen and Bolt (1985), and Lay and Wallace (1995).

Surface-waves provide an important tool for investigating the velocity structure in the outer part of the Earth, and whole Earth models. For example, from analysis of a large number of dispersion curves, it has been concluded that the S-wave velocity starts to decrease at a depth of approximately 80 km and starts increasing again at around 200-250 km. The detection of this Low-Velocity Zone (LVZ) has probably been the single most important result of surface-wave studies (De Bremaecker, 1985). Comparison of observed periods of different oscillation modes with values computed for different models of Earth's velocity and density structure provides an important check on the validity of the Earth model. Nowadays, seismologists take much notice of surface-waves in extracting seismic moment at the source, because of their longer wave-length and great signal/noise ratio. Two types of elastic surface waves are generated at a free solid surface, sometimes they are known collectively as L-waves, and subdivided into Rayleigh-waves (LR or L_R) and Love-waves, (LQ or L_Q). In the problem of verifying a nuclear test ban treaty, the measurement of surface wave magnitude is important in the application of $m_b : M_s$ discriminant, as discussed in chapter 2.

Rayleigh waves— Each one of P- and SV waves impinging on a free surface, reflects as P- and SV waves, and the amplitude of reflected waves depends on incidence angles and velocity parameters of the radiation medium. For critical incidence angle ($\sin^{-1}(\beta/\alpha)$) the reflected P-wave travels along the free surface. Rayleigh waves develop as a result of the interaction of the curved fronts of body-waves at a solid free surface (Lamb, 1904) and exhibit both dilatational and shear components of motion. They spread cylindrically on the surface and thus have a two-dimensional geometric decrease in amplitude with radius r from the source proportional $1/\sqrt{r}$. So these waves tend to be the largest arrivals on long-period or broadband seismograms. For many rocks, Poisson's ratio $\sigma \approx 0.25$, where $\alpha \approx \sqrt{3}\beta$. This gives $V_R = 0.919\beta = 0.531\alpha$ where V_R is the horizontal Rayleigh-wave velocity (Sheriff and Geldart, 1995).

Love waves— Love waves do not exist in a uniform half-space because it is not possible to satisfy the stress-free boundary condition. There will be a refracted SH wave if the half-space is overlain by a uniform layer of material. As an SH body-wave strikes the reflecting horizon at postcritical angles, all the energy is trapped within the overlying layer, and propagates as guided wave called a Love wave. Love waves are horizontally polarised surface waves which develop in a low-velocity surface layer overlying a faster semi-infinite medium. Suppose there is a low velocity homogeneous layer over a homogeneous half space, and SH waves (from the low velocity layer) radiate onto the half-space interface. For critical angles of incidence and greater, SH reverberations (multiple reflections between the free-surface and half-space)

will be totally trapped in the upper layer. Love-wave velocity depends on frequency and it is dispersed even in a homogeneous structure.

6.3 Dispersion of surface-waves

Almost any seismic source excites waves that comprise a continuous spectrum of frequencies, each harmonic component having a velocity that is called the phase velocity $c(\omega)$. Constructive interference occurs as wave packets propagate along the surface with the group velocity $U(\omega)$.

To summarise, Rayleigh-waves are dispersed except in a homogeneous halfspace, and Love-waves are always dispersed. Rayleigh-waves on the surface of a homogeneous medium do not exhibit dispersion because their velocity is independent of frequency. However, any deviation of the P or S waves velocity structure from a halfspace will create variation of surface-wave velocity with wave length, giving rise to dispersion. Since $\alpha > \beta$ and $k_\alpha > k_\beta$, P-waves attenuate faster with depth than the SV-wave. Differences in dispersion caused by variations in velocity structure along and between different surface-wave paths is a source of M_s bias that has received little attention. Moreover, because dispersion reduces the peak amplitude, it increases the detection threshold for surface waves. Therefore, in a layered medium such as the Earth, in which S-wave velocity generally increases with depth, longer wavelengths, sample more of the higher velocity material, so travel faster. If phase velocity is the same for all frequencies in the pulse, the pulse shape does not change and it is equal to group velocity (energy velocity) $U = c$. In the case of $U \neq c$, the different components travel with different velocities and the medium is dispersive. Figure 6.1 shows a synthetic dispersed vertical surface wave seismogram at three different epicentral distances.

Consider two harmonic waves given by $A_1 = a\cos(\omega_1 t - k_1 x)$ and $A_2 = a\cos(\omega_2 t - k_2 x)$. The superposition of these two waves leads to a pulse given by

$$A_1 + A_2 = 2a\cos\left(\frac{(\omega_1 - \omega_2)}{2}t - \frac{(k_1 - k_2)}{2}x\right)\cos\left(\frac{(\omega_1 + \omega_2)}{2}t - \frac{(k_1 - k_2)}{2}x\right) \quad (6.1)$$

The combined wave changes waveshape and travels at a velocity different from either of them. Equation (6.1) represents two cosine waves, one of which travels with a velocity of $\frac{\omega_1+\omega_2}{k_1+k_2}$, which is the phase or wave velocity. This wave is modulated by another cosine wave with a velocity of $\frac{\omega_1-\omega_2}{k_1-k_2}$, which is the group velocity and is the velocity with which the energy of summed wave travels. If the two waves have similar frequency and wavenumber this tends to $d\omega/dk$.

By defining $\omega_1 + \delta\omega = \omega = \omega_2 - \delta\omega$ and $k = \omega/c$ such that $k_1 + \delta k = k = k_2 - \delta k$

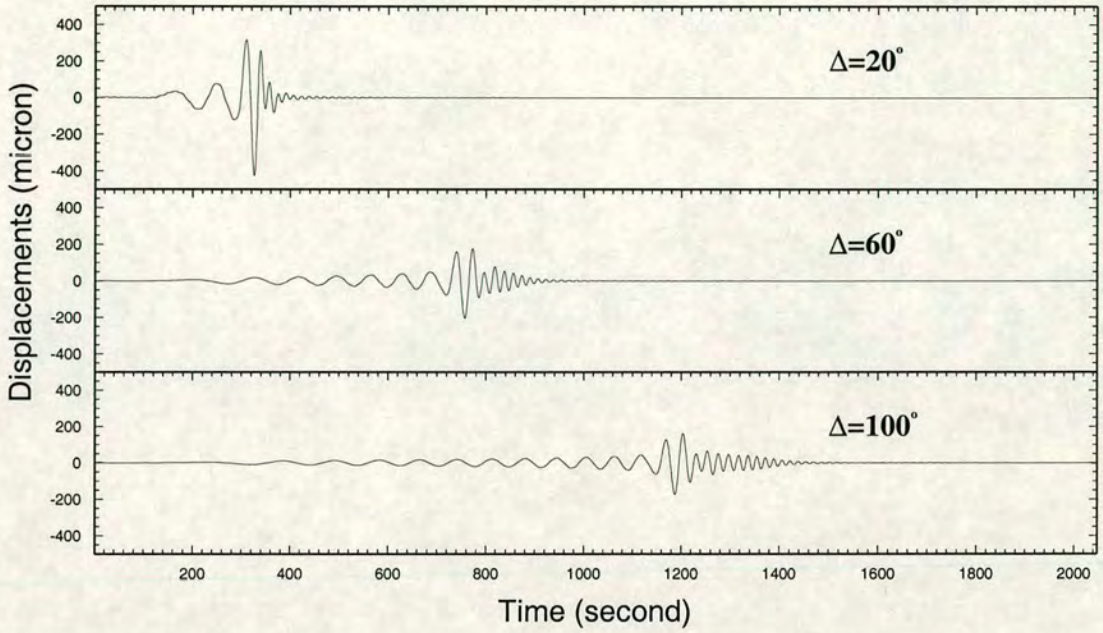

Figure 6.1. Variation of dispersion on vertical synthetic surface-wave seismogram as a function of epicentral distance, resulting from a velocity variation with depth.

Equation (6.1) becomes

$$A_1 + A_2 = 2a\cos(\omega t - kx)\cos(\delta\omega - \delta k x), \tag{6.2}$$

where $\delta\omega \ll \omega$, $\delta k \ll k$. Therefore $U = \frac{\delta\omega}{\delta k}$. In the limits as $\delta\omega \longrightarrow 0$

$$U = \frac{d\omega}{dk} = \frac{d(kc)}{dk} = c + k\frac{dc}{dk} = c - \lambda\frac{dc}{d\lambda}. \tag{6.3}$$

Therefore dispersion of surface-waves depends on phase velocity which is controlled by the velocity structure along the path and variation of phase velocity with wavenumber. When c decreases with frequency, the dispersion is normal and $c > U$; that is, the envelope travels slower than the individual cycles, when c increases with frequency, there will be inverse dispersion $c < U$. Normal dispersion is usual, and phase-velocity curves tend to be monotonic, while group-velocity curves often have a local minimum when $dc/d\lambda$ is greatest (i.e., where dc/dk has its greatest negative value). This minimum in the group-velocity curve implies that significant energy (a nearly pure mixture of signals of long- and short- period components with prominent amplitude) arrives at about the same time which is called an *Airy phase*. For continental paths an Airy phase with about a 20-s period often occurs, so that the presence or

absence of an Airy phase is fundamental to the measurement of M_s, as discussed in chapter 3.

The dispersion information can be used in the estimation of velocity gradients at depth, and for correcting the observed phase back to the source so that the source radiation can be determined. Also, dispersion will vary for different modes, and the excitation of modes as a function of frequency and azimuth depends on the source mechanism.

6.4 Effective factors on amplitude/phase of surface-wave

As a surface-wave passes from source to recording station, many factors affect its amplitude and phase spectrum, and seismogram is result of convolving these factors. Some of these factors are briefly discussed.

Source— Source effect on amplitude/phase spectrum is a function of source dimension and its depth. It is well known that the initial amplitude and phase depend on source orientation and rise-time. Theoretical calculations due to Keilis-Borok (1961) have shown that the most efficient excitation of surface waves occurs at wavelengths approximately four times the dimension of the source; that is, the source region acts as a quarter wavelength antenna (Capon *et al.*, 1969).

Path— The anelastic attenuation, geometrical spreading and non-horizontal interface also affect the passing surface-wave. As previously mentioned, the velocity structure along the path has dispersion effect on waves, therefore according to wave-numbers (group velocity and phase velocity) phase-shift due to path will be different.

Instrument— Any seismometer affects the arrival wave according to its response. No seismometer is capable of recording arrival wave with equal amplitude at all frequencies. For the above effects, the time series $u(r,t)$ of a surface wave recorded at a distance r, can be expressed by:

$$u(r,t) = \frac{1}{2\pi\sqrt{r}} \int_0^\infty A(\omega).\exp\left(\phi_s(\omega) + \phi_g(\omega) + \phi_i(\omega)\right)d\omega \tag{6.4}$$

where $\phi_s(\omega)$ is source phase shift, $\phi_g(\omega)$ is path phase shift, $\phi_i(\omega)$ is instrument phase shift and $A(\omega)$ is an amplitude function. Figure 6.2 shows a schematic representation of these effects which lead to seismogram, therefore there are three basic filters:

$$u(x,t) = s(t) * g(t) * i(t) \tag{6.5}$$

where $u(x,t)$ is the seismogram, $s(t)$ is the signal from the seismic source, $g(t)$ is the path or propagation filter, and $i(t)$ is the seismometer response. Of the three convolution operators used in the calculation of the seismogram, only the instrument response, $i(t)$, is usually well known. The transfer function, $g(t)$, which describe the passage of waves along the whole

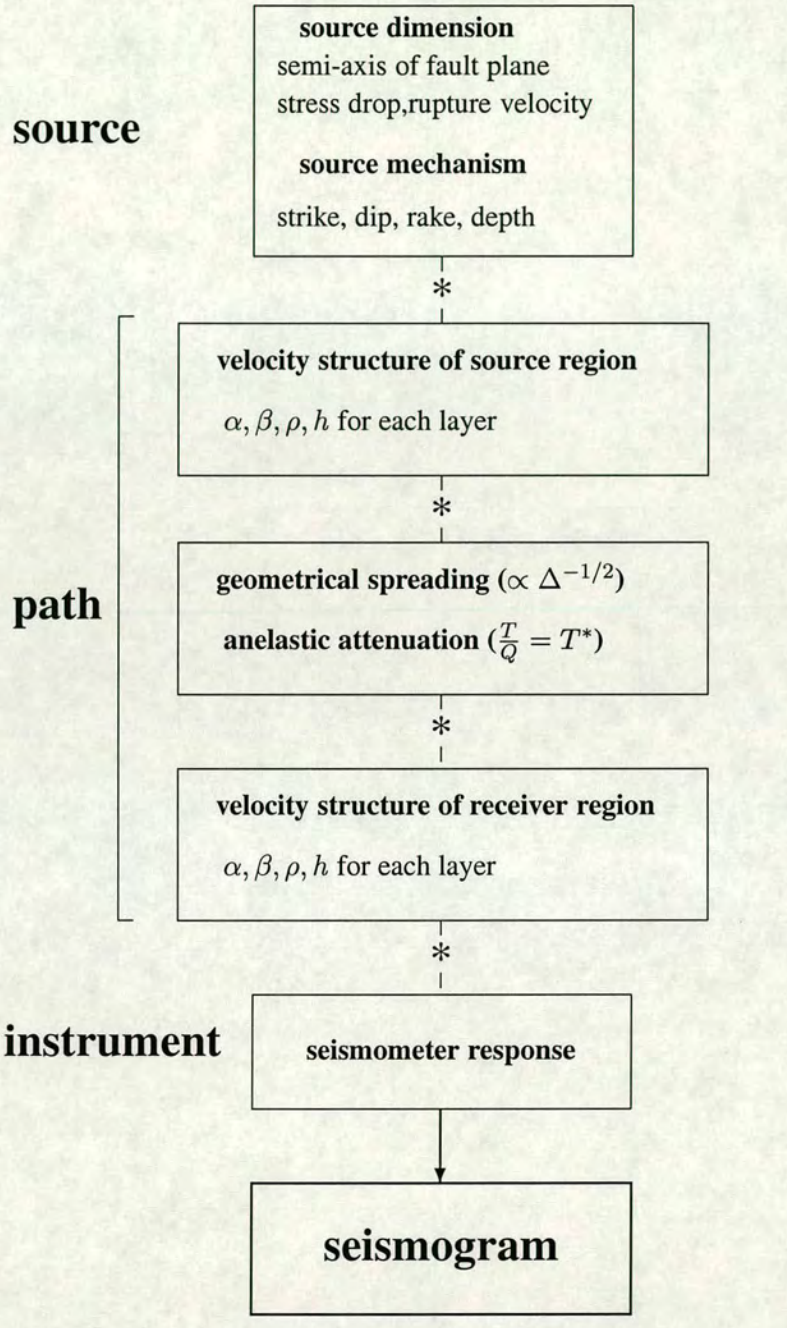

Figure 6.2. Flowchart representation of various effects, which can be convolved to give the seismogram.

path, are rarely well known. In order to describe this path perfectly, it is necessary to have a complete knowledge of the velocity and density structure, both radially and laterally, from source to receiver. This is obviously not, in general, possible. The vertical stratification of the Earth is reasonably well known, but lateral hetrogeneities are poorly understood and are a large source of uncertainty in transfer function.

As Figure 6.2 shows, $s(t)$ and $g(t)$ can be divided into several filters to account for specific effects. For example, $s(t)$ can be divided into filters which take account of the source radiation and fault rupture characteristics. Similarly $g(t)$ can separately take account of the geometrical spreading, anelastic attenuation, velocity structure, etc. This filter is the most complex filter in equation (6.5) which is sometimes called the Earth transfer function.

6.5 Synthetic Rayleigh wave seismograms

In this study to generate synthetic surface-wave seismograms a program developed by Douglas *et. al.*, (1972) is used. Douglas *et. al.*, (1972) used an expression which they derived from Hudson (1969) as:

$$u_z^{q^1} = S_v(\omega) F_z^{q^1}(\phi, \omega)(a \sin \Delta)^{-\frac{1}{2}} \exp\left\{-ik_1 r \pm i\pi/4 - \frac{|\omega| r}{2Q^1 U^1}\right\} \tag{6.6}$$

where the superscript 1 indicates that the parameters are for the fundamental Rayleigh mode. $S_v(\omega)$ is the instrument response, $F_z^{q^1}$ is the amplitude of the displacement of radiated wave with angular frequency ω, at azimuth ϕ from an extended double couple source (Savage 1966). The term $(\sin \Delta)^{-\frac{1}{2}}$ is the geometrical spreading factor for a spherical Earth, a is the radius of the Earth and Δ is the angular distance between source and receiver. The term $\exp(-ik_1 r \pm i\pi/4)$, where k_1 is the wave number at frequency ω, evaluates the phase change due to propagation of surface waves. $\exp(-|\omega| r/2Q^1 U^1)$ accounts for anelastic absorption effects where U^1 is the group velocity and Q is the attenuation factor which is assumed to be frequency independent. In the program $u_z^{q^1}$ is computed over a range of frequencies from 0 to ω_n using Fourier inversion. Also, for surface-wave the layering between source and receiver is taken as constant throughout the path.

6.6 Collapse with removal of standard distance function

In order to remove M_s bias due to path, it is possible to correct all given digital seismograms to one distance (say 50°) and one type of path (using the standard continental and oceanic models of crust). For example, a surface wave recorded at 70° on an oceanic path could be corrected back to zero assuming oceanic dispersion and then re-dispersed using a continental dispersion curve. Similarly a recording for a continental path at say 5 degrees that is not dispersed enough

for M_s to be estimated could be further dispersed to give the record as it would have been recorded at 30 degrees.

The source time function $s(t)$ is usually determined iteratively in generalised source parameter inversion. Another approach is a deconvolution procedure, which is a natural extension of linear filter theory. Therefore by deconvolving the instrument response, and transfer function (path effect), can obtain the source time function or seismogram in a specific distance when the source orientation is known. This inverse approach can be express as:

$$u(\omega) = s(\omega)g(\omega)i(\omega) \quad \Rightarrow \quad s(\omega) = \frac{u(\omega)}{g(\omega)i(\omega)} \tag{6.7}$$

Uncertainty in the Earth transfer function $g(\omega)$ and source orientation is the major problem for this procedure. Here the synthetic transfer function or synthetic seismogram is generated by the method of Douglas *et al.*, (1972) and generates the fundamental mode (zero mode) of Rayleigh-wave. Since surface-waves propagate in the free surface and various underlaying boundaries, in this modelling it is supposed that the structure between source and receiver is the same for continental and oceanic paths. Therefore the transfer function for a given standard continental or a standard oceanic model is calculated and then removed from the seismogram. In the case of mixed path this procedure is separately done for continental and oceanic path. Figures 6.3 and 6.4 show the collapsing procedure of a dispersed synthetic seismogram according to a standard continental crust model (Kanamori, 1967) which has been shown in Table 6.1.

Figure 6.5 shows an example of collapsing for an observed surface-wave seismogram at station FLK from an event to the North of Ascension Island. For generation of transfer function the structure crust model of Raitt (1963) which is shown at Table 6.2 is used. This Figure shows that the collapsing idea for the observed seismogram is not successful.

As observed in Figures 6.3 and 6.4, the procedure of collapsing the dispersion of synthetic surface wave seismograms works satisfactorily, but for the observed surface wave seismogram (Fig. 6.5) the result is under-corrected. This means that the velocity structure used is not close to the true structure, and one cannot collapse the dispersion of the surface wave using a standard oceanic velocity structure. However, no attempt was made to allow for the additional effect of anelastic attenuation.

6.7 Collapse with removal of specific distance function

In Figure 6.4 it was observed that collapsing surface-wave seismogram using standard continental or oceanic structure model is not successful. Therefore in this section a specific structural model is used. Qiu *et. al.*, (1996) introduced a new one dimensional Earth model for

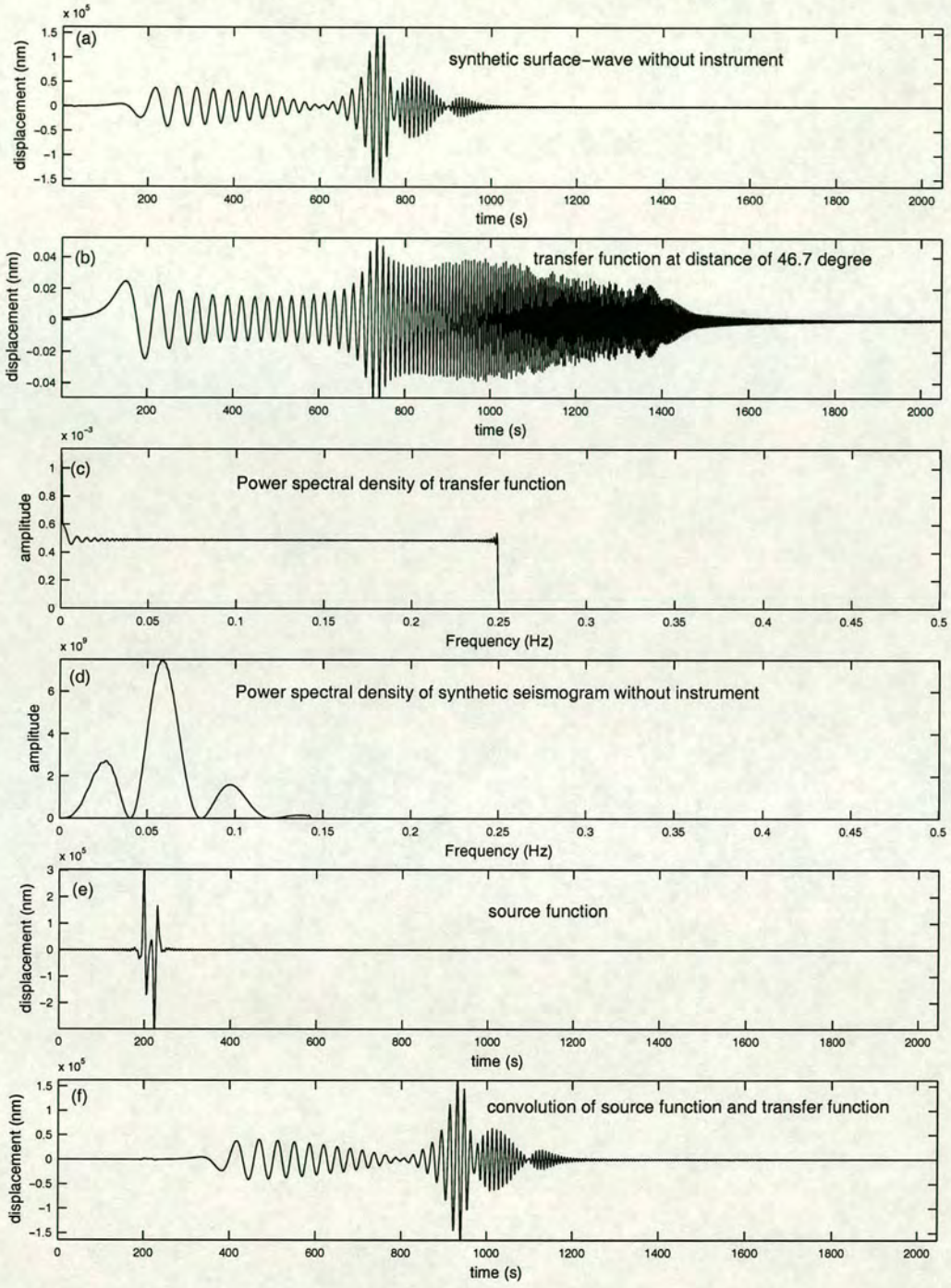

Figure 6.3. Collapsing a synthetic Rayleigh-wave seismogram using a continental structure model. (a) Vertical component of synthetic Rayleigh-wave seismogram $u(x,t) = s(t)*g(t)$ at distance of 46.7° and azimuth 89°, according to a given model in Table 6.1 without instrument. (b) Earth transfer function $g(t)$. (c) Power spectrum of transfer function $|g(\omega)|^2$. (d) Power spectrum of seismogram without instrument response $|u(\omega)|^2$. (e) Source function after deconvolving transfer function $s(t)$. (f) Convolution of source and transfer function $u(t) = g(t)*s(t)$. The deconvolved time series shifted 200 seconds.

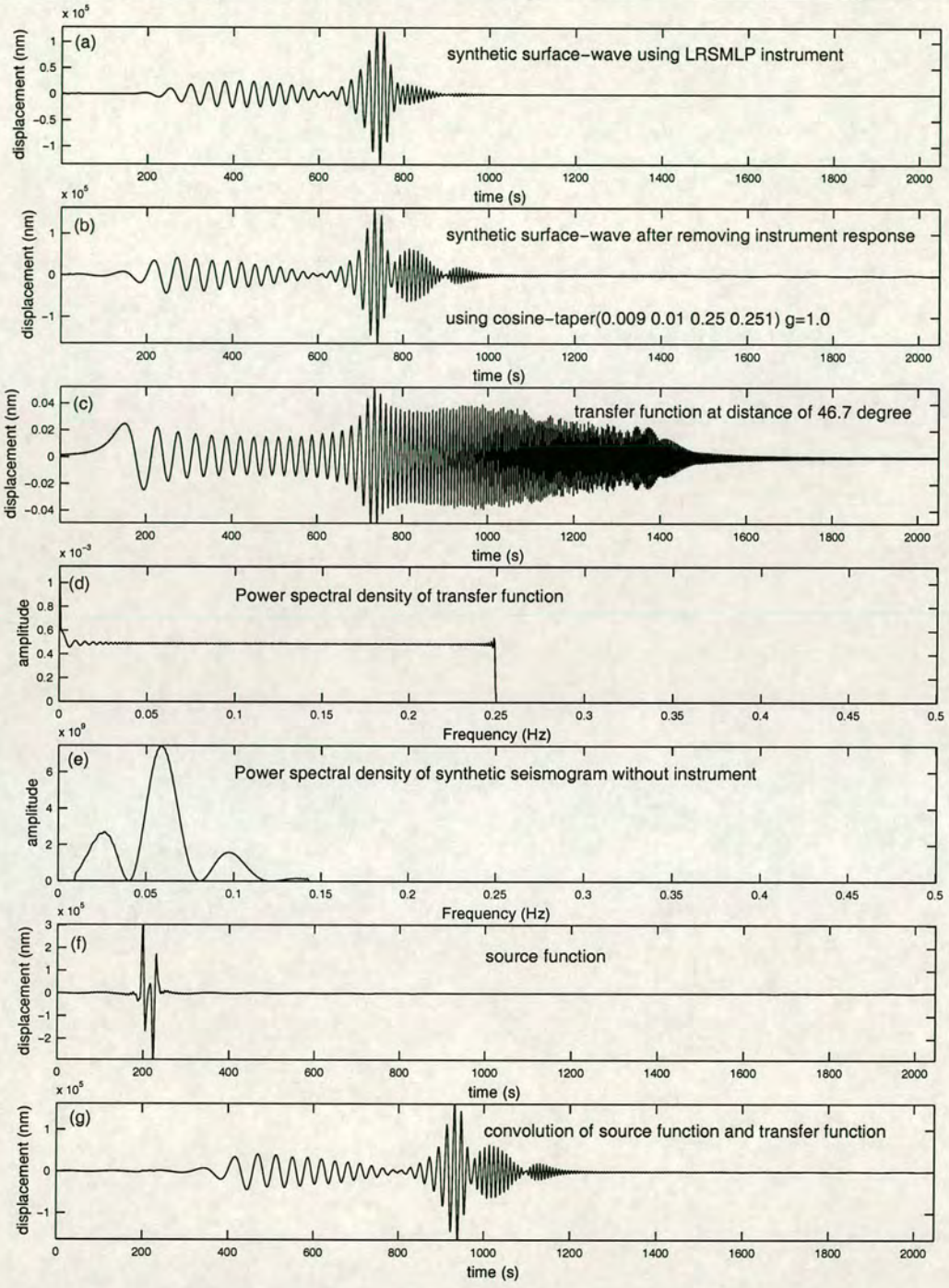

Figure 6.4. Collapsing a synthetic Rayleigh-wave seismogram seismogram using a continental structure model. (a) Vertical component of synthetic surface-wave seismogram $u(x,t) = s(t)*g(t)*i(t)$ at distance of 46.7° and azimuth 89°, according to a given model at Table 6.1 using long-period seismometer of LRSMLP. (b) Seismogram after removing instrument response $u(x,t) = s(t)*g(t)$ and applying a cosine taper (0.009 0.01 0.25 0.251). (c) Earth transfer function $g(t)$. (d) Power spectrum of transfer function $|g(\omega)|^2$. (e) Power spectrum of seismogram without instrument response $|u(\omega)|^2$. (f) Source function after deconvolving transfer function $s(t)$. (g) Convolution of source and transfer function $u(t) = g(t)*s(t)$. The deconvolved time series shifted 200 seconds.

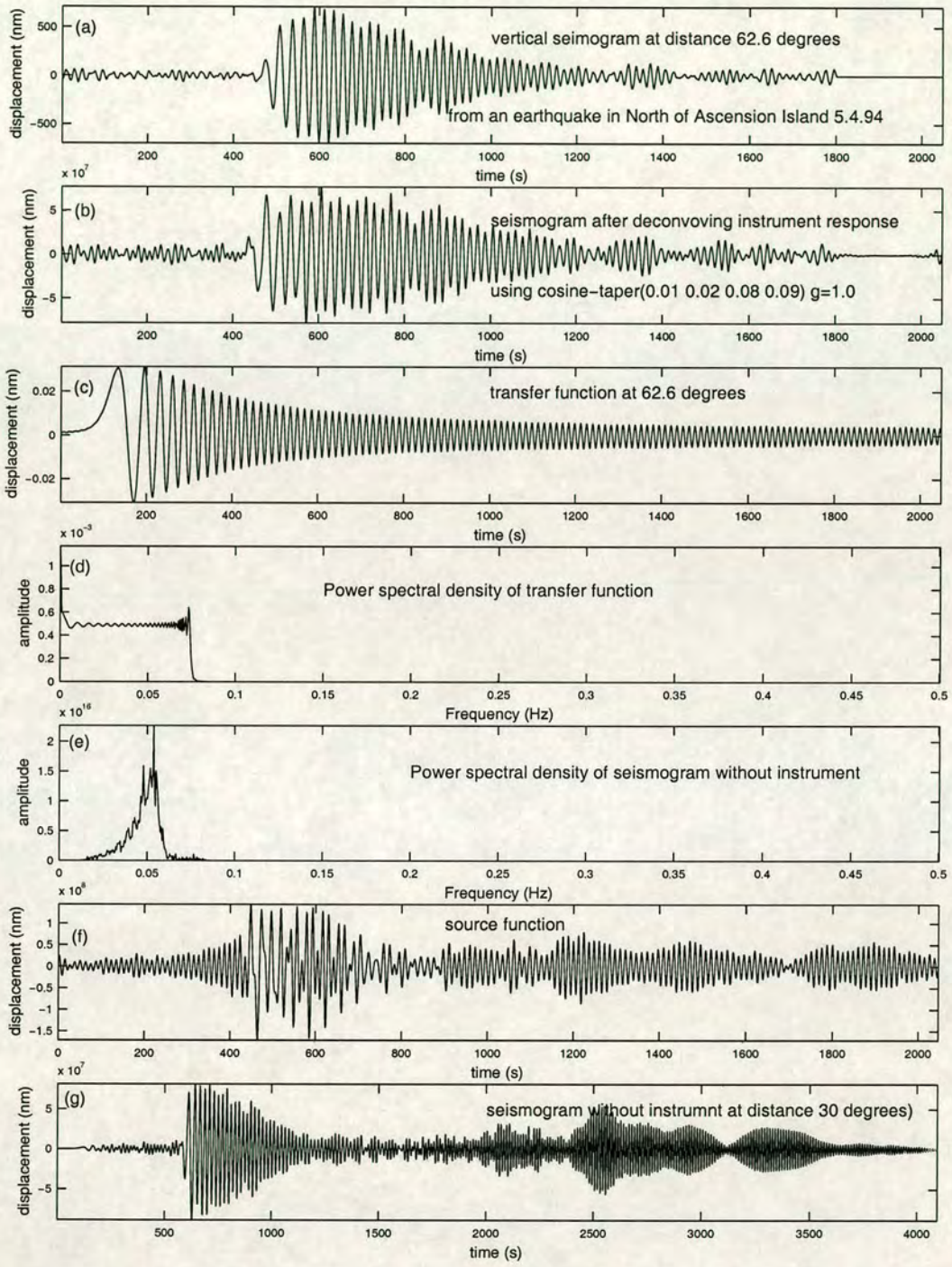

Figure 6.5. (a) Observed vertical component of seismogram recorded at FLK station at distance 62.6° and azimuth 228.6°. (b) Observed seismogram after removing instrument response $u(x,t) = s(t)*g(t)$ and applying a cosine taper (0.01 0.02 0.08 0.09). (c) Earth transfer function $g(t)$ at distance 62.6° and azimuth 228.6°. (d) Power spectrum of transfer function $|g(\omega)|^2$. (e) Power spectrum of seismogram without instrument response $|u(\omega)|^2$. (f) Source function after deconvolving transfer function $s(t)$. (g) Seismogram at distance 30°. The deconvolved time series shifted 200 seconds.

Table 6.1. Standard continental crustal model (based on that of Kanamori, 1967) and focal mechanism parameters.

structure						
layer	α km/s	β km/s	ρ g/cm^3	thickness km	$1/Q_\alpha$	$1/Q_\beta$
1	3.00	1.66	2.35	2.0	0.0	0.0
2	6.10	3.50	2.70	9.0	0.0	0.0
3	6.40	3.68	2.90	9.0	0.0	0.0
4	6.70	3.94	2.90	18.0	0.0	0.0
Half-space	8.15	4.75	2.30	∞	0.0	0.0

focal mechanism				source dimension		Stress
strike	dip	rake	depth	semi-major axe	semi-minor axe	drop
0°	90°	45°	23.0 km	30.0 km	14.0 km	100 bars

Table 6.2. Standard oceanic crustal model (based on that of Raitt, 1963) and focal mechanism parameters

structure						
layer	α km/s	β^a km/s	ρ g/cm^3	thickness km	$1/Q_\alpha$	$1/Q_\beta$
1	1.50	0.0	1.03	4.5	0.0	0.0
2	2.00	$\alpha/\sqrt{3}$	2.10	0.45	0.0	0.0
3	5.00	//	2.80	1.75	0.0	0.0
4	6.70	//	3.30	4.70	0.0	0.0
Half-space	8.09	//	3.30	∞	0.0	0.0

focal mechanism				source dimension		stress
strike	dip	rake	depth	semi-major axe	semi-minor axe	drop
0°	90°	45°	10.0 km	5.0 km	3.0 km	100 bars

[a]Where the S velocity is not specified it is assumed $\beta = \alpha/\sqrt{3}$ where α is the P wave velocity.

the crust and upper mantle in southern Africa. Their structure model is used to examine collapsing of an observed surface-wave seismogram. Here a long-period seismogram from a regional earthquake occurred in southern Africa on 18th August 1986 with origin time 15:07:52 recorded at the digital station SLR is selected to test collapsing. Qiu *et. al.*, (1996) studied this earthquake and they matched synthetic seismogram with observed seismogram at station SLR using their structure model. Figure 6.6 shows collapsing of observed seismogram at station SLR, and Table 6.3 shows the structure model and source mechanism which was used for generating transfer function.

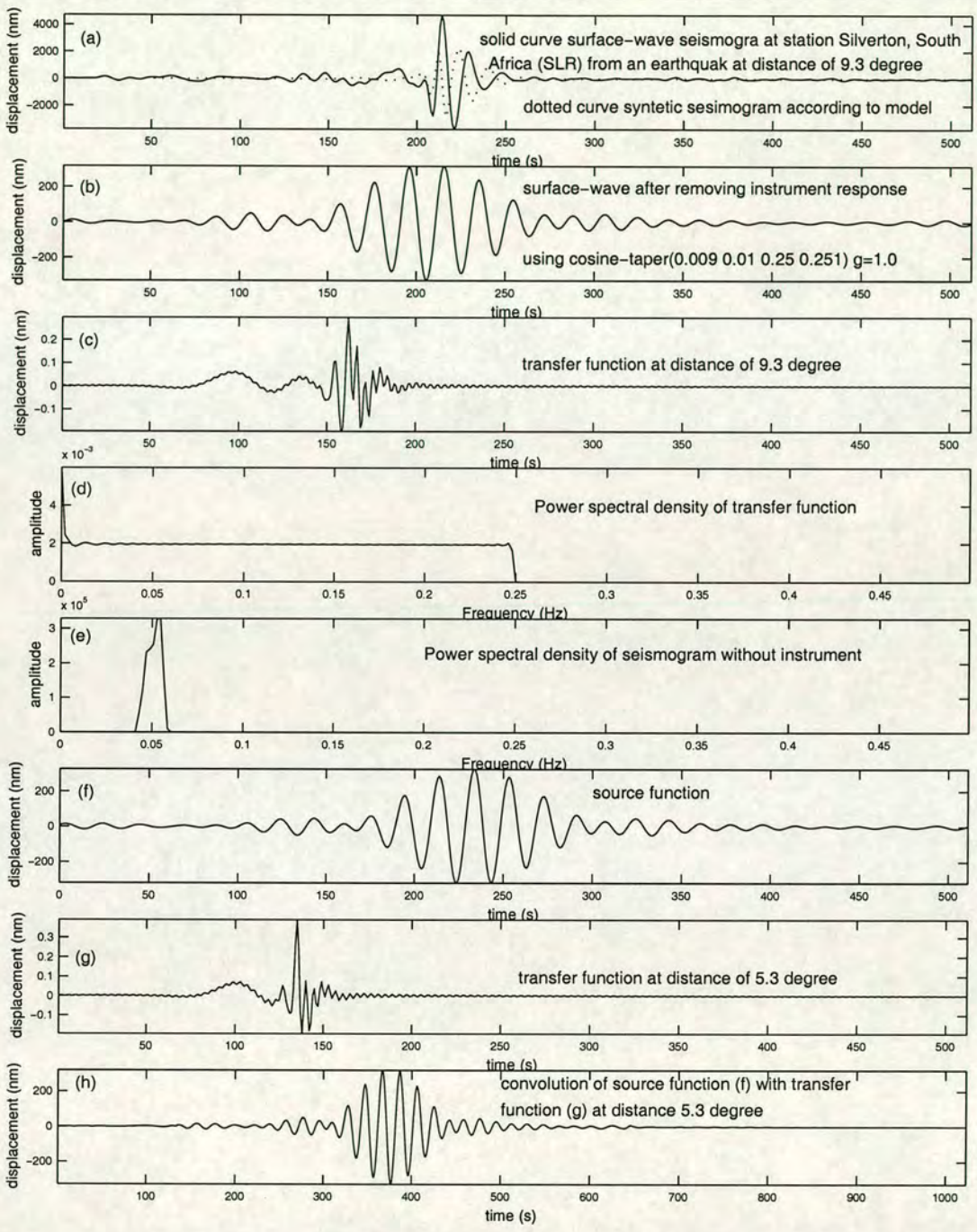

Figure 6.6. Collapsing an observed Rayleigh-wave seismogram using a specific structure model. (a) Vertical component of surface-wave seismogram recorded at station SLR from an earthquake in southern Africa on 18th August 1986, with ISC determined magnitudes of $m_b = 5.4$, $M_s = 4.8$, $\Delta \approx 9.3°$ and azimuth 89°. (b) Seismogram after removing instrument response and applying a cosine taper (0.009 0.01 0.25 0.251). (c) Earth transfer function $g(t)$ according to a given model at Table 6.3. (d) Power spectrum of transfer function $|g(\omega)|^2$. (e) Power spectrum of seismogram without instrument response $|u(\omega)|^2$. (f) Source function after deconvolving the transfer function $s(t)$. (g) Transfer function at $\Delta = 5.3°$. (h) Convolution of source and transfer function at $\Delta = 5.3°$ $u(t) = g(t) * s(t)$. The deconvolved time series shifted by 200 seconds.

Table 6.3. Structure model of Qiu *et. al.*, (1996) for southern Africa and source mechanism used.

structure						
layer	α km/s	β km/s	ρ g/cm^3	thickness km	$1/Q_\alpha$	$1/Q_\beta$
1	4.52	2.44	2.09	1.0	0.0	0.0
2	5.80	3.67	2.31	5.0	0.0	0.0
3	6.45	3.71	2.80	20.0	0.0	0.0
4	6.60	3.92	2.88	14.0	0.0	0.0
5	8.10	4.64	3.35	13.0	0.0	0.0
6	8.12	4.65	3.35	13.0	0.0	0.0
7	8.13	4.67	3.35	13.0	0.0	0.0
8	8.15	4.68	3.35	13.0	0.0	0.0
9	8.17	4.69	3.35	13.0	0.0	0.0
10	8.20	4.72	3.35	13.0	0.0	0.0
11	8.21	4.56	3.35	21.0	0.0	0.0
12	8.24	4.48	3.37	21.0	0.0	0.0
13	8.27	4.41	3.38	21.0	0.0	0.0
14	8.31	4.33	3.40	21.0	0.0	0.0
15	8.34	4.26	3.41	21.0	0.0	0.0
16	8.38	4.14	3.44	21.0	0.0	0.0
17	8.44	4.10	3.45	23.0	0.0	0.0
18	8.53	4.10	3.36	23.0	0.0	0.0
19	8.62	4.10	3.48	23.0	0.0	0.0
20	8.69	4.17	3.49	17.0	0.0	0.0

used mechanism[a]				source dimension		stress
strike	dip	rake	depth	semi-major axe	semi-minor axe	drop
238°	43°	84°	12.0 km	1.7 km	1.0 km	100 bars

[a]Harvard centroid moment tensor catalogue, except depth which was taken from Qiu *et. al.*, (1996)

6.8 Conclusion

The examination of collapsing surface wave seismograms to a shorter distance or zero distance shows that removing the dispersion effect from seismogram using a standard oceanic or continental velocity structure model is not possible. The use of using a specific structure model which is much closer to the true velocity structure of path used, requires more examples to make a definite conclusion. It is concluded that further work on the measurement of M_s on collapsed surface-wave seismograms offers perhaps the most important further improvement in M_s determination.

Chapter 7

Conclusions

In this thesis the bias in the determination of both surface-wave magnitude M_s and body-wave magnitude m_b was investigated using all ISC and NEIC Catalogues between 1978 and 1993. One of the initial aims of this study was to reduce bias caused by inadequacies in the calibration functions of magnitudes by developing new calibration functions.

The review and preliminary analysis of global surface-wave and body-wave magnitude data presented in chapter 2, has demonstrated that there are no systematic differences between the published magnitude datasets of the ISC and the NEIC. This is despite differences such as different period ranges for measuring M_s, different averaging methods, and differences in the average number of contributing stations. Chapter 2 has also revealed that the density function for magnitude against frequency for M_s values is smooth but significantly asymmetric. Surprisingly, that for m_b appears to be symmetric and close to normally distributed. This would be unexpected because the factors governing the fall-off in the density function are apparently different toward high and low magnitude. However, formal tests show that the m_b distribution is not symmetric.

Examination of M_s : m_b for the ISC dataset has revealed some anomalous earthquakes which plot as explosions according to the M_s : m_b discriminant of Nowroozi (1986). Although the number of anomalous earthquakes increases towards increasing depth, the absence of a depth correction is a contributory factor in causing these anomalous values, and the main factor appears to be non-systematic.

The frequency-distance plot for reported surface wave amplitude observations was shown in chapter 3 to exhibit detailed structure of the body-wave amplitude-distance curve at all distances. This censoring via the body waves represents a large deficit in the number of potentially usable surface-wave amplitude observations, particularly in the P-wave shadow zone. It arises because most seismic stations measure surface waves after recognising the first arrival P-wave, and the value of P-wave observation in the core shadow zone ($100° < \Delta < 120°$) is small.

In chapter 3, in order to reduce bias in M_s determination due to inadequate distance function, two new formulae were developed, with constants obtained using all ISC data. In the first formula the Herak and Herak (1993) method was used with different conditions and using a large dataset, and the conventional logarithmic dependence of the distance function was retained. This gave

$$M_s^e = \log(A/T)_{max} + 1.155\log(\Delta) + 4.269. \tag{7.1}$$

In the second formula, the theoretically-known contribution of dispersion and geometrical spreading in propagation of surface-waves was exploited, to obtain

$$M_s^t = \log(A/T)_{max} + \frac{1}{3}\log(\Delta) + \frac{1}{2}\log(\sin\Delta) + 0.0046\Delta + 5.370. \tag{7.2}$$

Comparison of these formulae with other work shows that the distance-dependence term in the Gutenberg (1945a) and Prague (Vaněk *et al.*, 1962) formulae are inadequate. It was shown that M_s^e as well as the formula of Herak and Herak (1993) give less bias at all epicentral distances. M_s^t provides an improved overall distance correction, especially beyond $\Delta = 145°$. Also, there is some evidence that Airy-phase, rather than non-Airy phase distance decay dominates measurements at distances $\Delta \leq 30°$. A global-average apparent $Q^{-1} = 0.00192 \pm 0.00026$ ($Q \approx 500$) was obtained for Rayleigh waves with 20 sec and $U = 3.5$ km/s.

Application of M_s^t for M_s determination provides an opportunity to examine the relation of surface-wave magnitude (which is approximately unbiased due to distance calibration function) with seismic moment. This analysis in chapter 4 has shown that in M_s versus $\log M_0$ relation, there is significantly less scatter in $\log M_0$ for a given M_s when M_s^t is used, than when M_s^{Prague} is used. Moreover, when M_s^t is used, one cannot conclude that the slope of M_s against $\log M_0$ tends to 1.0 towards smaller magnitudes. This suggests that previous claims of M_s data supporting a theoretical slope of 1.0 towards small magnitudes may not be justified. The data used here are more consistent with a linear fit than with the analytical relation of Ekström and Dziewonski (1988).

Reexamination of the conclusions of Ekström and Dziewonski (1988) and Abercrombie (1994) about anomaly in M_s values of different regions such as the New-Hebrides and Tonga-Kermadec shows that most of the anomaly in M_s values for events in these regions are substantially reduced when M_s^t values are used. For the remainder of the anomaly, it is concluded that the path effect is more likely to be responsible than the other possible factors; this is contrary to conclusion of Ekström and Dziewonski (1988) and Abercrombie (1994).

To consider depth bias in M_s formula, a depth correction of $\delta M_s = 0.0025h$ was obtained for earthquakes with depth range of 60 km $\leq h \leq$ 10 km. Also, analysis of non-linear global relationship between surface-wave magnitude and seismic moment has revealed that

the relationship between surface-wave magnitude and $\log M_0$ can be fitted closely to quadratic polynomial given by

$$\log M_0 = (25.1079 \pm 0.2014) - (1.2015 \pm 0.0730)M_s + (0.2052 \pm 0.0066)(M_s)^2 \quad (7.3)$$

This relation is compared with other global linear and non-linear relations.

In Chapter 5, for the determination of m_b, new empirical depth-distance calibration terms $B(\Delta, h)$ were determined using scalar moment values (M_0) from the Harvard CMT Catalogue. In comparison with other published depth-distance terms, the application of the new depth-distance calibration terms for the ISC dataset has shown that the new calibration terms provide estimates of m_b with reduced bias, and estimated m_b is then independent of distance and focal depth. This comparison confirms the inadequacy of the Gutenberg and Richter (1956) correction terms which are presently used by global agencies such as ISC and NEIC. The new calibration terms obtained in this study, for shallow depths are larger than those of Gutenberg-Richter at closer distances, and for greater distances the reverse is true. These differences are gradually changed with increasing depth, i.e., the new calibration terms for greater depths are smaller than those of Gutenberg-Richter at closer distances, and for greater distances the opposite is true.

Comparison of event magnitudes m_b calculated using the commonly-used Gutenberg and Richter (1956) calibration terms with those of this study, shows that the new correction terms increase small magnitudes and decrease large magnitudes. Also, comparison of m_b values and standard deviation of mean magnitude for single events (110,720 events) using different depth-distance correction terms has shown that: (1) $m_b^{\text{New}} \geq m_b^{\text{G-R}} \geq m_b^{\text{L}} \geq m_b^{\text{V-C}}$, (2) the Gutenberg-Richter standard deviations are on average larger than those of Veith-Clawson (1972), Lilwall (1987), and of this study.

In Chapter 6, possible further improvement in M_s determinations is addressed by considering the effect of path. The possibility of collapsing surface-wave seismograms to a standard distance was examined. This was first attempted using standard oceanic and continental dispersion functions, but it was shown that the collapse of surface-wave seismograms to a standard distance is only a realistic possibility with a velocity model, and hence dispersion relation, specific to each path. This is a logical approach now that digital seismograms are widely available. It offers the prospect of reducing the surface-wave detection threshold, as well as a means to remove path-dependent effects on the measured amplitude.

Finally, further work is needed if bias in magnitudes due to radiation pattern, differences in seismometer response, path effect (for M_s), etc. are to be removed.

7.1 Suggestions for further work

Rezapour and Pearce (1998) did not consider M_s distance correction for $\Delta < 20°$. This would require regionalising the correction. There is currently much interest in pursuing this in the context of seismic verification (Stevens and McLaughlin, 1997), and the new M_s^t scale presented here forms a basis for regionalisation of M_s distance correction.

The study of m_b has highlighted deficiencies in depth-distance corrections. The use of maximum-likelihood magnitudes, and further consideration of the detection threshold at individual stations, could further improve the global m_b scale. Following the new results concerning the linearity of the relationship between M_s and $\log M_0$, a further study of m_b against $\log M_0$ is suggested. This would be particularly valuable for providing better seismic moment calibration for the many earthquakes which have magnitude estimates. The relationship between m_b and $\log M_0$ in different regions is also a subject of current study (e.g. Priestly and Patton, 1997).

The study of collapsing surface-waves is a preliminary attempt to investigate collapsing dispersed surface waves to a shorter distance or to a greater distance. To obtain a clear result the method needs further investigation e.g., by analysing more examples with specific structural models, and also using the observed dispersion relation which can be achieved by applying a phase-matched filter. Therefore, use of an observed dispersion relation for examining the collapsing method is suggested. During the course of the present work, the problem of extracting low-amplitude surface waves from noisy seismogram has become prominent in the context of comprehensive nuclear test ban monitoring.

Bibliography

Abercrombie, R. E. (1994). Regional bias in estimates of earthquake M_s due to surface-wave path effects, *Bull. Seism. Soc. Am.* **84**, 377–382.

Adams, R. D. (1992). Effects of heterogeneity on earthquake location at ISC, *Phys. Earth Planet Interiors* **75**, 1–5.

Adams, R. D., A. A. Hughes, and D. M. McGregor (1982). Analysis procedures at the International Seismological Centre, *Phys. Earth Planet Interiors* **30**, 85–93.

Aki, K. (1966). Generation and propagation of G waves from the Niigata earthquake of June 16, 1964, part 2, Estimation of earthquake moment, released energy, and stress-strain drop from the G wave spectrum, *Bull. Earthquake Res. Inst. Univ. Tokyo*, **44**, 73–88.

Aki, K. (1967). Scaling law of seismic spectrum, *J. Geophys. Res.* **72**, 1217–1231.

Aki, K. (1969). Analysis of the seismic coda of local earthquakes as scattered waves, *J. Geophys. Res.* **74**, 615–631.

Aki, K. (1972). Scaling law of earthquake source time-function, *Geophys. J. R. astr. Soc.* **31**, 3–25.

Aki, K. (1987). Magnitude-frequency relation for small earthquakes: a clue to the origin of f_{max} of large earthquakes, *J. Geophys. Res.* **92**, 1349–1355.

Aki, K. and P. G. Richards (1980). *Quantitative seismology: theory and methods, 2 vols.* W. H. Freeman, San Francisco.

Ambraseys, N. N. and R. D. Adams (1996). Large-magnitude Central American earthquakes, 1898–1994, *Geophys. J. Int.* **127**, 665–692.

Anderson, D. L. and R. S. Hart (1978a). Attenuation models of the earth, *Phys. Earth Planet Interiors* **16**, 289–306.

Anderson, D. L. and R. S. Hart (1978b). Q of the Earth, *J. Geophys. Res.* **83**, 5869–5882.

Båth, M. (1952). Earthquake magnitude determination from the vertical component of surface waves, *Trans. Am. Geophys. Union.* **33**, 81–90.

Båth, M. (1958). The energies of seismic body waves and surface waves, *in Contribution in Geophysics: In Honour of Beno Gutenberg,* H. Benioff, M. Ewing, B. F. Howell, Jr., and F. Press, Editors, Pergamon Press, New York, pp. 1–16.

Båth, M. (1977). Teleseismic magnitude relation, *Ann. Geof.* **30**, 299–327.

Båth, M. (1981). Earthquake magnitude — recent research and current trends, *Earth Sci. Rev.* **17**, 315–398.

Båth, M. (1984). Earthquake magnitude based on PKP and SKP waves, *Boll. Geofis. teor. appl.* **26**, 93–108.

Berckhemer, H. (1962). Die ausdehnung der bruchfläche im Erdbeben herd umd ihr Einfluss auf das seismische Wellen spektrum, *Gerlands. Beritr. Geophys.* **71**, 5–26.

Bevington, P. R. and D. K. Robinson (1992). *Data Reduction and Error Analysis for the Physical Science*, 2nd ed, McGraw-Hill, Inc., New York, NY.

Bocharov, V. S., S. A. Zelentsoz, and V. N. Mikhailov. (1989). Characteristics of 96 underground nuclear explosions at the Semipalatinsk test site, *Atomic Energy* **67**, 210–214 (in Russian).

Boore, D. M. and J. Boatwright (1984). Average body-wave radiation coefficients, *Bull. Seism. Soc. Am.* **74**, 1615–1621.

Booth, D. C., P. D. Marshall, and J. B. Young (1974). Long and short period P-wave amplitudes from earthquakes in the range 0°–114°, *Geophys. J. R. astr. Soc.* **39**, 523–537.

Bowers, D. (1997). The October 30, 1994, seismic disturbance in South Africa: Earthquake or large rock burst, *Geophys. J. Res.* **102**, 9843–9857.

Bowers, D. and A. Douglas (1998). The effect of earthquake radiation pattern on m_b—a study using aftershocks in the 1976 Gazli sequence, *Bull. Seism. Soc. Am.* **88**, 523–530.

Brune, J. N. (1968). Seismic moment, seismicity, and rate of slip along major fault zones, *J. Geophys. Res.* **73**, 777–784.

Brune, J. N. (1970). Tectonic stress and the spectra of seismic shear waves from earthquakes, *J. Geophys. Res.* **75**, 4997–5009.

Bullen, K. E. and B. A. Bolt (1985). *An Introduction to the Theory of Seismology,* Cambridge Univ. Press, Cambridge, 4th ed. 499 pp.

Burridge, R. and L. Knopoff (1964). Body force equivalents for seismic dislocations, *Bull. Seism. Soc. Am.* **54**, 1875–1888.

Capon, J., R. J. Greenfield, and R. T. Lacoss (1969). Long-period signals processing results for the large aperture seismic array. *Geophysics 34*, 305–329.

Caputo, M. and R. Console (1980). Statistical distribution of stress drops and faults of seismic regions, *Tectonophysics* **67**, T13–T20.

Caputo, M. (1983). Are there one to one relationships between magnitude, moment, intensity and ground acceleration, *Geophys. J. R. astr. Soc.* **72**, 83–92.

Carpenter, E. W., P. D. Marshall, and A. Douglas (1967). The amplitude-distance curve for short period teleseismic P-wave, *Geophys. J. R. astr. Soc.* **13**, 61–70.

Christoskov, L., N. V. Kondorskaya, and J. Vaněk (1979). *Homogeneous magnitude system of the Eurasian continent: P waves,* Report SE-18, World Data Center A for Solid Earth Geophysics, Boulder, Colorado, 57 pp.

Christoskov, L., N. V. Kondorskaya, and J. Vaněk (1985). Magnitude calibrating function for a multidimensional homogeneous system of reference stations, *Tectonophysics* **118**, 213–226.

Christoskov, L., N. V. Kondorskaya, and J. Vaněk (1991). Homogeneous magnitude system with unified level for using in seismological practice, *Stud. Geophys. Geod.* **35**, 221–223.

Cleary, J. (1967). Analysis of the amplitudes of short-period P-waves recorded by Long Range Seismic Measurements Stations in the distance range 30° to 120°, *J. Geophys. Res.* **72**, 4705–4712.

De Bremaecker, J. C. (1985). *Geophysics: The Earth's Interior*, John Wiley & Sons, Inc.

Douglas, A., J. A. Hudson, and C. Blamey (1972). A quantitative evaluation of seismic signals at teleseismic distance –III. Computed P and Rayleigh wave seismograms, *Geophys. J. R. astr. Soc.* **28**, 385–410.

Douglas, A., J. A. Hudson, and P. D. Marshall (1981a). Earthquake seismograms that show Doppler effects due to crack propagation, *Geophys. J. R. astr. Soc.* **64**, 163–185.

Douglas, A., J. B. Young, and P. D. Marshall (1981b). Some analyses of P- and Rayleigh-wave amplitudes observed at North America stations, *Geophys. J. R. astr. Soc.* **67**, 305–324.

Duda, S. J. (1989). Earthquakes: Magnitude, energy, and intensity. In *"Encyclopedia of Solid Earth Geophysics"* (D. James, ed), pp. 272–288. Van Nostrand-Reinhold, New York.

Duda, S. J., T. B. Yanovskaya, E. N. Its, and R. Nortmann (1989). Preliminary reference calibrating functions for body-wave magnitudes: refracted P-waves, *Tectonophysics* **166**, 189–203.

Dziewonski, A. M. and D. L. Anderson (1981). Preliminary Reference Earth Model. *Phys. Earth Planet Interiors* **25**, 297–356.

Dziewonski, A. M. and D. L. Anderson, (1983). Travel times and station correction for P waves at teleseismic distances, *J. Geophys. Res.* **88**, 3295–3314.

Dziewonski, A. M. and J. H. Woodhouse (1983). An experiment in systematic study of global seismicity: Centroid-moment tensor solutions for 201 moderate and large earthquake of 1981, *J. Geophys. Res.* **88**, 3247–3271.

Ekström, G. and A. M. Dziewonski (1988). Evidence of bias in estimations of earthquake size, *Nature* **332**, 319–323.

Evernden, J. F. (1971). Variation of Rayleigh-wave amplitude with distance, *Bull. Seism. Soc. Am.* **61**, 231–240.

Ewing, W. M., W. S. Jardetzky, and F. Press (1957). *Elastic waves in layered media.* McGraw-hill, New York.

Frohlich, C. and K. D. Apperson (1992). Earthquake focal mechanism, moment tensors, and the consistency of seismic activity near plate boundaries, *Tectonics* **11**, 279–296.

Frohlich, C. and D. Davis (1993). Teleseismic b values: or, much ado about 1.0, *J. Geophys. Res.* **98**, 631–644.

Geller, R. J. (1976). Scaling relations for earthquake source parameters and magnitudes, *Bull. Seism. Soc. Am.* **66**, 1501–1523.

Gilbert, F. and A. M. Dziewonski (1975). An application of normal mode theory to the retrieval of structural parameters and source mechanisms from seismic spectra, *Philos. Trans. R. Soc. (London), Ser. A.* **278**, 187–269.

Gutenberg, B. (1944). Energy ratio of reflected and refracted seismic waves, *Bull. Seism. Soc. Am.* **34**, 85–102.

Gutenberg, B. (1945a). Amplitudes of surface waves and magnitudes of shallow earthquakes, *Bull. Seism. Soc. Am.* **35**, 3–12.

Gutenberg, B. (1945b). Amplitudes of P, PP, and S and magnitude of shallow earthquakes, *Bull. Seism. Soc. Am.* **35**, 57–69.

Gutenberg, B. (1945c). Magnitude determination for deep-focus earthquakes, *Bull. Seism. Soc. Am.* **35**, 117–130.

Gutenberg, B. and C. F. Richter (1939). On seismic waves, *Gerlands Beitr. Geophys.* **54**, 94–136.

Gutenberg, B. and C. F. Richer (1945). Earthquake magnitude, intensity, energy and acceleration, *Bull. Seism. Soc. Am.* **46**, 105–145.

Gutenberg, B. and C. F. Richter (1954). *Seismicity of the Earth and Associated Phenomena*, Princeton Univ. Press, Princeton, NJ.

Gutenberg, B. and C. F. Richter (1956). Magnitude and energy of earthquakes, *Ann. Geof.* **9**, 1–15.

Hanks, T. C. and H. Kanamori (1979). A moment magnitude scale, *J. Geophys. Res.* **84**, 2348–2350.

Haskell, N. A. (1963). Radiation pattern of Rayleigh waves from a fault of arbitrary dip and direction of motion in a homogeneous medium, *Bull. Seism. Soc. Am.* **53**, 619–642.

Haskell, N. A. (1964). Total energy and energy spectral density of elastic wave radiation from propagating faults. *Bull. Seism, Soc. Am.* **56**, 1811-1842.

Heato, T., F. Tajima, and A. W. Mori (1986). Estimating ground motions using recorded accelerograms, *Survey in Geophysics*, **8**, 25–83.

Herak, M. and D. Herak (1993). Distance dependence of M_s and calibrating function for 20 second Rayleigh waves, *Bull. Seism. Soc. Am.* **83**, 1881-1892.

Herrin, E., Chairman (1968). Introduction to "1968 seismological tables for P phases", *Bull. Seism. Soc. Am.* **58**, 1193–1241.

Hudson, J. A. (1969). A quantitative evaluation of seismic signals at teleseismic distances – II, Body waves and surface waves from an earthquake source, *Geophys. J. R. astr. Soc.* **18** 353–370.

Hyndman R. D. and D. H. Weichert (1983). Seismicity and rates of relative motion on the plate boundaries of Western North America, *Geophys. J. R. astr. Soc.* **72**, 59–82.

Jeffreys, H. and K. E. Bullen (1940). *Seismological Tables*, British Association, London. (Reprinted with additions, 1967).

Johnston, A. C. (1996). Seismic moment assessment of earthquakes in stable continental regions –I. Instrumental seismicity, *Geophys. J. Int.* **124**, 381–414.

Kanamori, H. (1967). Attenuation of P wave in the upper and lower mantle, *Bull. earthq. Res. Ins. Tokyo*, **45**, 299-312.

Kanamori, H. (1977). The energy release in great earthquakes, *J. Geophys. Res.* **82**, 2981-2987.

Kanamori, H. (1978a). Quantification of earthquakes, *Nature* **271**, 411–414.

Kanamori, H. (1978b). Quantification of great earthquakes, *Tectonophysics* **49**, 207–213.

Kanamori, H. (1983). Magnitude scale and quantification of earthquakes, *Tectonophysics* **93**, 195–199.

Kanamori, H. and D. Anderson (1975). Theoretical basis of some empirical relations in seismology, *Bull. Seism. Soc. Am.* **65**, 1073–1095.

Kaverina, A. N., A. V. Lander, and A. G. Prozorov (1996). Global creepex distribution and relation to earthquake-source geometry and tectonic origin, *Geophys. J. Int.* **125**, 125–265.

Kawakatsu, H. (1995). Automated near-real-time CMT inversion, *Geophys. Res. Lett.* **22**, 2569–2572.

Keilis-Borok, V. I. (1961). Differences in the spectra of surface waves from earthquakes and from explosions, *Tr. Inst. Fiz. Zemli,* **182**, 88–101.

Kuge, K. (1992). Systematic difference in the ISC body-wave magnitude-seismic moment relationship between intermediate and deep earthquakes, *Bull. Seism. Soc. Am.* **82**, 819–835.

Lamb, H. (1904). On the propagation of tremors over the surface of an elastic solid, *Phil. Trans. A.* **203**, 1–42.

Lay, T. and T. C. Wallace (1995). *Modern global seismology,* Academic Press, USA.

Lienkaemper, J. J. (1984). Comparison of two surface-wave magnitude scales: M of Gutenberg and Richter (1954) and M_s of "Preliminary determination of epicentres", *Bull. Seism. Soc. Am.* **74**, 2357–2378.

Lilwall, R. C. (1987a). Station threshold bias in short-period amplitude distance and station terms used to compute body-wave magnitude m_b, *Geophys. J. R. astr. Soc.* **91**, 1127–1133.

Lilwall, R. C. (1987b). *Empirical amplitude-distance/depth curves for short-period P waves in the distance range 20 to 180°*, AWRE Report No. O 30/86, HMSO, London.

Main, I. G. (1987). A characteristic earthquake model of the seismicity preceding the eruption of Mount St. Helens on 18 May 1980, *Phys. Earth Planet Interiors* **49**, 283–293.

Marshall, P. D. and P. W. Basham (1972). Distribution between earthquakes and underground explosions employing an improved M_s scale, *Geophys. J. R. astr. Soc.* **28**, 431–458.

Marshall, P. D. and P. W. Basham (1973). Rayleigh wave magnitude scale, M_s, *Pure Appl. Geophys.* **103**, 406–414.

Marshall, P. D., J. Bingham, and J. B. Young (1986). An analysis of P-wave amplitudes recorded by seismological stations in the USSR, *Geophys. J. R. astr. Soc.* **84**, 71–91.

Marshall, P. D. and E. W. Carpenter (1966). Estimates of Q for surface Rayleigh waves, *Geophys. J. R. astr. Soc.* **10**, 549–550.

Miyamura, S. (1982). On the importance of continuity of magnitude scales, *Tectonophysics* **84**, 47–55.

Miyamura, S. (1983). Consideration for the body-wave magnitude determination in the recent earthquake data report of the United States Geological Survey, *Tectonophysics* **93**, 313–318.

Noguchi, S. (1979). On the relation between surface-wave magnitude and JMA magnitude, *J. Fac. Sci. Hokkaido Univ. Ser. VII*, **6**, 213–224.

Nolet, G., S. Krueger, and R. M. Clouser (1998). Empirical determination of depth-distance corrections for m_b and M_w from Global Seismograph Network, *Geophys. Res. Lett.* **25**, 1451–1454.

Nortmann, R. and S. L. Duda (1982). The amplitude spectra of P- and S-waves and the body-wave magnitude of earthquakes, *Tectonophysics* **84**, 41–45.

Nortmann, R. and S. L. Duda (1983). Determination of spectral properties of earthquakes from their magnitudes, *Tectonophysics* **93**, 251–275.

Nowroozi, A. A. (1986). On the linear relation between m_b and M_s for discrimination between explosions and earthquakes, *Geophys. J. R. astr. Soc.* **86**, 687–699.

Nuttli, O. W. (1973). Seismic wave attenuation and magnitude relations of eastern North America, *J. Geophys. Res.* **78**, 876–885.

Okal, E. M. (1989). A theoretical discussion of time domain magnitude: The Prague formula for M_s and the mantle magnitude M_m, *J. Geophys. Res.* **94**, 4194–4204.

Orowan, E. (1960). Mechanism of seismic faulting, *Geol. Soc. Amer. Mem.* **79**, 323–345.

Pacheco, J. A., C. H. Scholz, and L. R. Sykes (1992). Changes in frequency-size relationship from small to large earthquakes, *Nature* **355**, 71–73.

Panza, G. F., S. J. Duda, L. Cernobori, and M. Herak (1989). Gutenberg's surface-wave magnitude calibrating function: theoretical basis from synthetic seismograms, *Tectonophysics* **166**, 35–43.

Press, W., S. A. Teukolsky, W. T. Vetterling, and B. P. Flannery (1992). *Numerical Recipes in Fortran 77*, second edition, vol. 1, Cambridge university press.

Priestley K. F. and H. Patton (1997). Calibration of $m_b(P_n)$, $m_b(L_g)$ scales and transportability of the $M_0 : m_b$ discriminant to new tectonic regions, *Bull. Seism. Soc. Am.* **87**, 1083–1099.

Prozorov, A. and A. Hudson (1974). A study of the magnitude difference $M_s - m_b$ for earthquakes, *Geophys. J. R. astr. Soc.* **39**, 551–564.

Purcaru, G. and H. Berckhemer, (1978). A magnitude scale for very large earthquakes, *Tectonophysics* **49**, 189–198.

Purcaru, G., and H. Berckhemer, (1982). Quantitative relations of seismic source parameters and a classification of earthquakes, *Tectonophysics* **84**, 57–128.

Qiu, X., K. Priestley, and D. McKenzie, (1996). Average lithospheric structure of southern Africa, *Geophys. J. Int.* **127**, 563–587.

Raitt, R. W. (1963). The crustal rocks, *The Sea* **3**, ed. M. N. Hill, Interscience Publishers.

Reiter, L. (1990). *Earthquake Hazard Analysis*, Columbia Univ. Press, New York.

Rezapour, M. and R. G. Pearce (1998). Bias in surface wave magnitude M_s due to inadequate distance corrections, *Bull. Seism. Soc. Am.* **88**, 43–61.

Richter, C. F. (1935). An instrumental earthquake magnitude scale, *Bull. Seism. Soc. Am.* **25**, 1–32.

Richter, C. F. (1958). *Elementary Seismology*, Freeman, San Francisco.

Romanelli, F. and G. F. Panza, (1995). Effect of source depth correction on the estimation of earthquake size, *Geophys. Res. Lett.* **22**, 1017–1019.

Rydelek, P. A. and I. S. Sacks (1989). Testing the completeness of earthquake catalogues and the hypothesis of self-similarity. *Nature* **337**, 251–253.

Savage, J. C. (1966). Radiation from a realistic model of faulting, *Bull. Seism. Soc. Am.* **56**, 577–592.

Scheidegger, A. E. (1985). Recent research on the physical aspects of earthquakes, *Earth. Sci. Rev.* **22**, 173–229.

Sheriff, R. E. and L. P. Geldart (1995). *Exploration Seismology*, Cambridge Univ. Press, Cambridge, 2nd ed. 592 pp.

Scholz, C., J. F. Pacheco, and L. R. Sykes (1991). 90-years seismic moment catalogue: break in frequency-size distribution of earthquakes (abstract), *EOS*, **72**(44) Fall Meeting Suppl. 291.

Sipkin, S. A. (1982). Estimation of earthquake source parameters by the inversion derived from moment tensor inversion, *J. Geophys. Res.* **91**, 531–547.

Sipkin, S. A. (1986). Estimation of earthquake source parameters by the inversion of waveform data: global seismicity, 1981–1983, *Bull. Seism. Soc. Am.* **76**, 1515–1541.

Sokal, R. R. and F. J. Rohlf (1995). *Biometry: The principals and practice of statistic in biological research*, third edition, Freeman and Company, New York.

Speidel, D. H. and P. H. Mattson (1993). The polymodal frequency-magnitude relationship of earthquakes, *Bull. Seism. Soc. Am.* **83**, 1893–1901.

S-PLUS software, Version 3.1, (1992) Statistical Sciences, Inc.

Steinhart, J. S. and R. P. Meyer (1961). Explosion studies of continental structure, *Carnegie Inst. Wash. Publ.* **622**, pp 409.

Stevens, J. L. and K. L. McLaughlin (1997). Improved methods for regionalized surface wave analysis, Maxwell Technologies Report No. MFD-TR-97-15887 (http://www.maxwell.com/products/geop/1997_AFTAC_Final/index.html)

Taylor, D. W. A., J. A. Snoke, I. S. Sacks, and T. Takanami (1990). Nonlinear frequency-magnitude relationship for the Hokkaido Corner, Japan, *Bull. Seism. Soc. Am.* **80**, 340–353.

Thatcher, W. and T. C. Hanks (1973). Source parameters of southern California earthquakes, *J. Geophys. Res.* **78**, 8547–8576.

Thomas, J. H., P. D. Marshall, and A. Douglas (1978). Rayleigh-wave amplitudes from earthquakes in the range 0–150°, *Geophys. J. R. astr. Soc.* **53**, 191–200.

Vaněk, J., A. Zatopek, V. Karnik, N. V. Kondorskaya, Y. V. Riznichenko, E. F. Savarensky, S. L. Solov'ev, and N. V. Shebalin (1962). Standardisation of magnitude scales, *Bull. Acad. Sci. USSR, Geophys, Ser. (English Transl.) No.* 2, 108–111.

Vaněk, J., N. V. Kondorskaya, I. V. Fedorova and L. Christoskov (1982). Optimisation of amplitude curves of seismic P-, S- and L-waves in the homogeneous magnitude system of the Eurasian continent, *Tectonophysics* **84**, 41–45.

Veith, K. F. and G. E. Clawson (1972). Magnitude from short-period P-wave data, *Bull. Seism. Soc. Am.* **62**, 435–452.

Vergino, E. S. (1989). Soviet test yields, *EOS, Trans. Am. Geophys.* **70**, 1511.

Vergino, E. S. (1989). Soviet test yields, additions, *EOS, Trans. Am. Geophys.* **70**, 1569.

von Seggern, D. H. (1970). Surface-wave amplitude versus distance relation in the western United States, *SDL Report No.* 249, Teledyne, Geotech, Alexandria, Virginia.

von Seggern, D. H. (1977). Amplitude-distance relation for 20-second Rayleigh waves, *Bull. Seism. Soc. Am.* **67**, 405–411.

Willmore, P. L. and V. Karnik (1970), *Manual of Seismological Practice.* Intern. Seism. Centre, Edinburgh.

York, D. (1966). Least-squares fitting of a straight line, *Can. J. Phys.* **44**, 1079–1086.

Appendix A

Error matrix

Regression uncertainty expresses the degree of confidence with which a given regression relation represents the true parent population of given distribution of data. The error matrix can be used to estimate the uncertainty in a calculated result, including the effects of the correlations of errors. In Chapter 4 for computing regression uncertainty the error propagation equation (Bevington and Robinson, page 43, 1992; Johnston, 1996) was used. The $\sigma^R_{\log M_0}$ depends on both variances and covariances of the regression parameters for least-squares curve fits. So the predicted value of $\log M_0$ should be calculated in the case of second-order fit from

$$\log M_0 = \beta_1 + \beta_2(M_s) + \beta_3(M_s)^2, \tag{A.1}$$

using the parameters determined by the fit to the data. The uncertainty in the calculated value of $\log M_0$, which results from the uncertainty in the regression parameters, is given by

$$\begin{aligned}(\sigma^R_{\log M_0})^2 &= \left(\frac{\partial \log M_0}{\partial \beta_1}\right)^2 \varepsilon_{11} + \left(\frac{\partial \log M_0}{\partial \beta_2}\right)^2 \varepsilon_{22} + \left(\frac{\partial \log M_0}{\partial \beta_3}\right)^2 \varepsilon_{33} + \\ &\quad 2\left[\left(\frac{\partial \log M_0}{\partial \beta_1}\frac{\partial \log M_0}{\partial \beta_2}\right)\varepsilon_{12} + \left(\frac{\partial \log M_0}{\partial \beta_1}\frac{\partial \log M_0}{\partial \beta_3}\right)\varepsilon_{13} + \left(\frac{\partial \log M_0}{\partial \beta_2}\frac{\partial \log M_0}{\partial \beta_3}\right)\varepsilon_{23}\right].\end{aligned} \tag{A.2}$$

From (A.1) we can calculate the partial derivatives with respect to β_i, whence

$$(\sigma^R_{\log M_0})^2 = 1\varepsilon_{11} + (M_s)^2\varepsilon_{22} + (M_s)^4\varepsilon_{33} + 2\left(M_s\varepsilon_{12} + (M_s)^2\varepsilon_{13} + (M_s)^3\varepsilon_{23}\right). \tag{A.3}$$

where ε_{ii} is the variance of the regression parameter β_i, ε_{ij} is the covariance of parameters β_i and β_j. In a least-squares analysis, the parameter variances and covariances are generated in a

covariance or error matrix as

$$\varepsilon = \begin{pmatrix} \varepsilon_{11} & \varepsilon_{12} & \varepsilon_{13} \\ \varepsilon_{21} & \varepsilon_{22} & \varepsilon_{23} \\ \varepsilon_{31} & \varepsilon_{32} & \varepsilon_{33} \end{pmatrix} \tag{A.4}$$

As in equation (A.2) it is clear that, in a least-squares analysis, the off-diagonal terms (covariance terms) are mainly negative, and including them reduces the regression uncertainty. So if we use only the diagonal terms in the error matrix, the predicted uncertainty will be large. It is noteworthy that $\sigma^R_{\log M_0}$ depends not only on parameter variance but also on covariance terms, which are a measure of degree of correlation among regression parameters.

For normally distributed errors, the 68% confidence limit is $\pm\sigma^R_{\log M_0}$, and the 95% confidence limit is $\pm 2\sigma^R_{\log M_0}$. Equation (A.2) was used for computing confidence limits in Figure 4.14.

Equation A.2 represents the total uncertainty of predicted $\log M_0$ if there are no epistemic errors in the input data. Since there is aleatory uncertainty in both of the input data i.e., $\log M_0$ and M_s, it is necessary to account for them in the final prediction uncertainty. An adequate, probably conservative, estimate of their contribution is the standard deviation of the $\log M_0$ residuals, σ_{res}. The total prediction uncertainty in $\log M_0$ is then obtained by adding the variances of $\sigma^R_{\log M_0}$ and σ_{res}, assumed independent, yielding

$$\sigma^P_{\log M_0} = \sqrt{(\sigma^R_{\log M_0})^2 + (\sigma_{res})^2}. \tag{A.5}$$

In case of moment magnitude e.g. the relation of Hanks and Kanamori (1979) (Eq. 2.21), the $\sigma^R_{\log M_0}$ convert to $\sigma^R_{M_w}$ (Johnston, 1996) according to

$$\sigma^R_{M_w} = \frac{2}{3}\sigma^R_{\log M_0}. \tag{A.6}$$

The predicted uncertainty in M_w is then

$$\sigma^P_{M_w} = \sqrt{(\sigma^R_{M_w})^2 + (\sigma_{res})^2}. \tag{A.7}$$

To eliminate outliers, Chauvenet's criterion is used, which assumes that data scatter follows a Gaussian distribution (Bevington and Robinson, 1992, page 58; Johnston, 1996). In Chauvenet's criterion, for a given distribution of events a data point is considered an outlier if less than half an event is expected to lie further from the mean (least-squares fit) than the point under consideration. The probability that any one point is within the Chauvenet outlier limit ($\pm C$ of the least-squares fit) is $P(z, \sigma_{res}) = 1 - \frac{0.5}{N}$, where σ_{res} is standard deviation of residuals in fitting, N is number of data points, z is dimensionless deviation, which is obtained from

standard tables for $P(z, \sigma_{res})$, and it is the numerical multiplier of σ_{res}, such that $C = \pm z\sigma_{res}$.

Removing an outlying point has a greater effect on the standard deviation than on the mean of a data sample, because the standard deviation depends on the square of each deviation. Elimination of one such point will lead to a smaller standard deviation and perhaps another point or points will now become candidates for rejection.

Appendix B

Station corrections from residual of m_b values

Table B.1. Mean deviation $\overline{\delta m_b}$ of all values of $\delta m_b = \overline{m_b} - m_b^{\text{station}}$ for those 458 seismic stations at which the ISC has used more than 200 measurements between 1978 and 1993.

Sta-code	Sta-location	$S^{\text{G-R}}$	$S^{\text{V-C}}$	S^{L}	S^{New}	N
AAI	Seram	0.04±0.53	0.02±0.51	0.00±0.51	0.01±0.51	562
ABM	Madagascar	0.64±0.28	0.64±0.26	0.66±0.26	0.64±0.26	245
ABU	Osaka	-0.21±0.36	-0.21±0.33	-0.23±0.33	-0.21±0.33	1564
ACO	Oklahoma	-0.15±0.35	-0.16±0.35	-0.16±0.36	-0.16±0.35	873
ADE	South Australia	-0.42±0.34	-0.38±0.32	-0.40±0.32	-0.38±0.32	4720
ADK	Alaska and Aleutians	-0.20±0.37	-0.20±0.37	-0.20±0.37	-0.20±0.36	1502
AFR	Moorea	-0.08±0.31	-0.02±0.29	-0.05±0.29	-0.04±0.29	2337
AKU	Iceland	-0.27±0.51	-0.23±0.50	-0.24±0.50	-0.25±0.50	2538
ALE	Northwest Territories	0.17±0.31	0.19±0.30	0.18±0.29	0.18±0.29	6142
ALM	Spain	1.54±0.35	1.53±0.33	1.53±0.33	1.53±0.33	264
ALQ	New Mexico	0.28±0.30	0.25±0.28	0.26±0.28	0.26±0.28	16180
AMN	Tuamotu	-0.12±0.37	-0.05±0.35	-0.07±0.35	-0.07±0.36	302
ANMO	New Mexico	0.18±0.35	0.17±0.34	0.17±0.34	0.18±0.34	1388
ANP	Taiwan	-0.31±0.33	-0.33±0.32	-0.34±0.33	-0.32±0.32	451
ANR	Uzbekistan	-0.47±0.28	-0.42±0.27	-0.44±0.27	-0.43±0.27	1397
APA	Murmanskaya	-0.03±0.32	-0.02±0.32	-0.02±0.31	-0.02±0.31	244
APL	Switzerland	0.07±0.26	0.04±0.25	0.06±0.26	0.05±0.25	215
APO	Sweden	0.11±0.41	0.09±0.41	0.11±0.41	0.09±0.41	820
APP	Sweden	0.00±0.27	-0.01±0.27	0.01±0.26	0.00±0.27	355
ARE	Peru	-0.16±0.36	-0.16±0.33	-0.17±0.33	-0.16±0.33	221
ARMA	New South Wales	0.11±0.29	0.13±0.27	0.11±0.27	0.12±0.27	2112
ARU	Sverdlovskaya	-0.39±0.30	-0.37±0.26	-0.38±0.26	-0.38±0.27	1489
ASH	Turkmeniya	-0.50±0.33	-0.49±0.32	-0.48±0.32	-0.49±0.32	460
ASP	Northern Territory	-0.28±0.34	-0.25±0.31	-0.25±0.31	-0.25±0.31	1270
ASPA	Northern Territory	-0.12±0.38	-0.12±0.35	-0.13±0.35	-0.12±0.36	15664
AVF	Bourgogne	0.09±0.25	0.08±0.24	0.09±0.23	0.09±0.24	11351
AVY	Madagascar	0.61±0.28	0.60±0.28	0.62±0.27	0.60±0.27	579
BAG	Luzon	-0.21±0.35	-0.22±0.35	-0.23±0.35	-0.21±0.34	1162
BAL	Western Australia	0.02±0.32	0.01±0.29	0.00±0.29	0.01±0.29	1428
BCAO	Central African Republic	-0.10±0.38	-0.09±0.36	-0.08±0.35	-0.09±0.35	3421
BDT	Thailand	-0.04±0.38	-0.05±0.37	-0.06±0.36	-0.05±0.36	4907

continued on the next page

continued from previous page

Sta-code	Sta-location	$S^{G\text{-}R}$	$S^{V\text{-}C}$	S^{L}	S^{New}	N
BDW	Wyoming	0.26±0.33	0.24±0.31	0.25±0.32	0.25±0.32	6526
BFD	Victoria	-0.04±0.30	0.00±0.30	-0.01±0.29	0.00±0.29	1298
BFS	Transvaal	-0.25±0.31	-0.27±0.30	-0.27±0.31	-0.27±0.30	560
BFT	Transvaal	-0.15±0.39	-0.15±0.38	-0.14±0.38	-0.15±0.38	338
BGF	Auvergne	0.06±0.24	0.05±0.23	0.06±0.23	0.06±0.23	4394
BHG	Bayern	-0.12±0.25	-0.15±0.23	-0.15±0.23	-0.15±0.23	1110
BHO	Oklahoma	0.12±0.37	0.13±0.37	0.13±0.37	0.13±0.37	1658
BJI	Beijing	0.01±0.36	0.01±0.35	0.00±0.34	0.02±0.34	6376
BKR	Gruziya	-0.29±0.31	-0.31±0.29	-0.30±0.29	-0.32±0.29	1151
BKS	California	-0.21±0.58	-0.23±0.57	-0.23±0.57	-0.23±0.57	3853
BLA	Virginia	-0.06±0.35	-0.07±0.34	-0.07±0.34	-0.07±0.34	1945
BLF	Orange Free State	0.08±0.54	0.06±0.53	0.06±0.53	0.06±0.52	646
BMN	Nevada	0.24±0.35	0.23±0.33	0.23±0.33	0.23±0.33	4799
BNG	Central African Republic	-0.14±0.33	-0.13±0.30	-0.13±0.30	-0.13±0.30	8585
BNH	New Hampshire	0.15±0.34	0.17±0.33	0.18±0.32	0.17±0.33	277
BNS	Nordrhein-Westfalen	0.14±0.87	0.11±0.87	0.11±0.86	0.11±0.87	409
BOD	Irkutskaya	0.05±0.34	0.04±0.32	0.04±0.31	0.05±0.31	2591
BPI	Transvaal	-0.09±0.39	-0.09±0.37	-0.09±0.38	-0.08±0.37	426
BRG	Sachsen	0.06±0.24	0.03±0.23	0.05±0.22	0.03±0.23	9536
BRS	Queensland	0.38±0.41	0.41±0.39	0.38±0.39	0.39±0.39	1948
BRVK	Kazakhstan	-0.10±0.27	-0.09±0.24	-0.09±0.24	-0.09±0.24	221
BSD	Denmark	0.02±0.36	0.01±0.36	0.02±0.35	0.00±0.36	477
BSF	Franche Comte	0.14±0.25	0.13±0.23	0.13±0.23	0.13±0.23	6477
BSI	Sumatera	-0.20±0.42	-0.21±0.43	-0.22±0.42	-0.20±0.43	433
BTO	Nei Monggol Zizhiqu	0.10±0.37	0.09±0.36	0.07±0.36	0.09±0.35	416
BUB	Switzerland	-0.17±0.28	-0.19±0.26	-0.19±0.25	-0.19±0.25	389
BUD	Hungary	-0.08±0.38	-0.13±0.36	-0.12±0.35	-0.13±0.36	528
BUL	Zimbabwe	0.12±0.30	0.10±0.30	0.12±0.29	0.10±0.29	8431
BW06	Wyoming	0.21±0.32	0.20±0.30	0.21±0.30	0.21±0.30	5763
CAF	Midi-Pyrenees	0.08±0.25	0.08±0.24	0.08±0.23	0.09±0.23	6496
CAR	Venezuela	-0.13±0.40	-0.15±0.38	-0.17±0.38	-0.14±0.38	719
CBM	Maine:USA	0.06±0.40	0.08±0.38	0.07±0.39	0.07±0.38	731
CCM	Missouri	-0.01±0.32	-0.02±0.32	-0.03±0.31	-0.03±0.31	205
CD2	Sichuan	-0.24±0.30	-0.24±0.28	-0.26±0.28	-0.25±0.29	1909
CDF	Alsace	0.20±0.25	0.18±0.24	0.19±0.24	0.18±0.24	6359
CEH	North Carolina	-0.18±0.31	-0.22±0.32	-0.20±0.31	-0.21±0.32	696
CER	Cape Province	-0.07±0.38	-0.10±0.37	-0.08±0.37	-0.10±0.37	597
CGP	Mindanao	-0.04±0.42	-0.03±0.41	-0.04±0.40	-0.05±0.41	790
CHG	Thailand	0.11±0.32	0.10±0.31	0.09±0.30	0.09±0.30	9431
CHTO	Thailand	0.25±0.36	0.24±0.34	0.23±0.34	0.24±0.34	8390
CIR	Zimbabwe	0.29±0.29	0.30±0.26	0.31±0.27	0.29±0.26	1418
CLE	Ohio	0.67±0.38	0.67±0.36	0.67±0.35	0.68±0.35	861
CLK	Malawi	0.27±0.29	0.29±0.28	0.30±0.28	0.29±0.28	1507
CLL	Sachsen	-0.06±0.23	-0.09±0.23	-0.08±0.22	-0.09±0.23	8985
CMB	California	0.20±0.35	0.19±0.33	0.19±0.32	0.19±0.33	1042
CMS	New South Wales	0.04±0.36	0.07±0.33	0.07±0.32	0.09±0.32	1913
CN2	Jilin	0.14±0.45	0.15±0.44	0.14±0.43	0.15±0.43	2721
CNB	ACT	-0.09±0.35	-0.04±0.28	-0.07±0.29	-0.04±0.29	1510
COL	Alaska and Aleutians	-0.03±0.32	-0.05±0.30	-0.05±0.30	-0.05±0.30	7626
COO	New South Wales	-0.17±0.37	-0.08±0.34	-0.13±0.34	-0.11±0.33	1046
COOL	Western Australia	0.20±0.32	0.18±0.30	0.18±0.30	0.19±0.30	932
COP	Denmark	-0.27±0.25	-0.30±0.24	-0.29±0.24	-0.30±0.24	1832
CRO	Oklahoma	-0.14±0.33	-0.13±0.32	-0.12±0.31	-0.13±0.31	349
CSY	Wilkes Land	-0.02±0.40	0.02±0.39	0.02±0.39	0.00±0.39	998
CTA	Queensland	-0.04±0.35	0.00±0.33	-0.01±0.33	0.01±0.32	9768
CTAO	Queensland	-0.01±0.33	0.04±0.31	0.03±0.31	0.05±0.31	3606
CVF	Corse	0.07±0.30	0.07±0.28	0.08±0.28	0.09±0.28	1716
CVP	Luzon	0.01±0.38	0.01±0.36	-0.01±0.37	0.00±0.37	427
CWF	England	0.26±0.31	0.23±0.28	0.24±0.28	0.23±0.28	444
CYP	Poland	-0.98±0.45	-1.00±0.45	-0.98±0.45	-0.99±0.45	2793
DAG	Greenland	-0.01±0.32	0.00±0.31	0.00±0.30	-0.01±0.31	10274
DAV	Mindanao	-0.47±0.35	-0.48±0.33	-0.49±0.33	-0.48±0.33	275
DCN	Ireland	-0.31±0.26	-0.33±0.24	-0.32±0.24	-0.33±0.24	1419

continued on the next page

continued from previous page

Sta-code	Sta-location	$S^{G\text{-}R}$	$S^{V\text{-}C}$	S^{L}	S^{New}	N
DDK	Ireland	-0.19±0.23	-0.21±0.22	-0.20±0.22	-0.20±0.22	658
DIX	Switzerland	-0.11±0.39	-0.12±0.39	-0.11±0.39	-0.11±0.39	4261
DKM	Ireland	-0.20±0.23	-0.24±0.23	-0.22±0.22	-0.23±0.22	547
DL2	Liaoning	-0.24±0.32	-0.23±0.30	-0.25±0.29	-0.24±0.29	949
DLE	Ireland	-0.24±0.26	-0.26±0.26	-0.25±0.26	-0.26±0.26	1521
DLF	Ireland	-0.40±0.29	-0.41±0.29	-0.39±0.29	-0.41±0.28	213
DMN	Nepal	-0.29±0.28	-0.26±0.26	-0.27±0.26	-0.26±0.26	8202
DMU	Ireland	-0.27±0.27	-0.28±0.26	-0.27±0.25	-0.28±0.26	1732
DOU	Belgium	-0.12±0.30	-0.12±0.29	-0.13±0.29	-0.13±0.30	1271
DUG	Utah	0.22±0.33	0.22±0.32	0.21±0.32	0.22±0.31	2240
EAB	Scotland	-0.04±0.29	-0.05±0.30	-0.04±0.29	-0.05±0.29	1078
EAU	Scotland	-0.12±0.29	-0.11±0.28	-0.11±0.27	-0.12±0.27	905
EBH	Scotland	-0.10±0.28	-0.10±0.28	-0.09±0.27	-0.10±0.27	1112
EBL	Scotland	0.01±0.31	0.02±0.29	0.02±0.29	0.02±0.29	938
ECB	Ireland	-0.27±0.27	-0.28±0.26	-0.27±0.25	-0.28±0.26	749
ECP	Ireland	-0.36±0.28	-0.37±0.26	-0.37±0.26	-0.37±0.26	1345
EDI	Scotland	-0.02±0.32	-0.02±0.33	-0.01±0.33	-0.02±0.32	640
EDM	Alberta	-0.41±0.27	-0.40±0.26	-0.40±0.25	-0.40±0.25	2499
EDU	Scotland	-0.10±0.29	-0.11±0.28	-0.10±0.28	-0.11±0.28	895
EGL	Scotland	-0.04±0.33	-0.04±0.31	-0.03±0.31	-0.04±0.30	483
EKA	Scotland	0.10±0.30	0.09±0.29	0.10±0.28	0.09±0.28	9785
ELO	Scotland	0.01±0.26	0.00±0.25	0.01±0.25	0.00±0.25	969
ELT	Altayskiy	-0.09±0.32	-0.10±0.31	-0.11±0.31	-0.10±0.31	2153
EMM	Maine:USA	-0.11±0.36	-0.09±0.34	-0.09±0.34	-0.08±0.34	413
EMS	Switzerland	-0.32±0.28	-0.32±0.27	-0.31±0.27	-0.31±0.28	1531
ENN	Netherlands	-0.02±0.28	-0.04±0.28	-0.03±0.27	-0.04±0.28	4356
EPF	Aquitaine	0.13±0.29	0.13±0.28	0.14±0.28	0.14±0.28	4659
ESK	Scotland	-0.11±0.27	-0.12±0.27	-0.11±0.27	-0.12±0.27	1020
ESY	Scotland	-0.02±0.29	-0.02±0.27	-0.02±0.27	-0.02±0.27	475
ETA	Ireland	-0.28±0.28	-0.29±0.27	-0.28±0.27	-0.29±0.27	797
EUR	Nevada	0.15±0.55	0.14±0.54	0.15±0.54	0.15±0.54	10700
EVA	Transvaal	-0.08±0.34	-0.08±0.33	-0.08±0.34	-0.07±0.33	372
FBA	Alaska and Aleutians	0.06±0.37	0.05±0.36	0.05±0.36	0.05±0.36	9623
FBAS	Alaska and Aleutians	0.22±0.32	0.22±0.30	0.22±0.29	0.22±0.29	494
FCC	Manitoba	-0.18±0.31	-0.17±0.30	-0.18±0.29	-0.17±0.30	472
FFC	Manitoba	-0.02±0.32	-0.02±0.30	-0.02±0.29	-0.02±0.30	11903
FHC	California	-0.29±0.34	-0.30±0.33	-0.31±0.33	-0.30±0.32	300
FLN	Basse-Normandie	0.00±0.25	-0.01±0.24	-0.01±0.24	-0.01±0.24	6700
FORR	Western Australia	-0.33±0.31	-0.32±0.30	-0.31±0.30	-0.32±0.30	1701
FORT	Western Australia	-0.13±0.32	-0.12±0.30	-0.11±0.30	-0.12±0.30	396
FRB	Northwest Territories	-0.16±0.35	-0.12±0.32	-0.14±0.32	-0.13±0.32	1652
FRF	Provence-Cote d'Azur	0.01±0.24	0.02±0.22	0.03±0.22	0.03±0.22	3272
FRS	Orange Free State	0.00±0.34	-0.03±0.34	-0.02±0.34	-0.02±0.34	539
FRT	Tuamotu	-0.06±0.34	0.00±0.33	-0.02±0.33	-0.01±0.33	291
FRU	Kirgiziya	-0.24±0.31	-0.21±0.30	-0.24±0.30	-0.22±0.30	1421
FSJ	British Columbia	0.00±0.31	-0.01±0.32	-0.01±0.32	-0.01±0.32	282
FUR	Bayern	-0.25±0.30	-0.28±0.28	-0.27±0.28	-0.27±0.28	1743
FVM	Missouri	-0.15±0.36	-0.15±0.32	-0.15±0.32	-0.15±0.32	3457
GAM	Tadzhikistan	-0.18±0.34	-0.13±0.32	-0.14±0.32	-0.14±0.33	328
GAR	Tadzhikistan	-0.26±0.36	-0.21±0.35	-0.22±0.35	-0.22±0.35	977
GBA	Karnataka	0.19±0.35	0.22±0.33	0.22±0.33	0.22±0.33	19055
GDH	Greenland	0.02±0.31	0.06±0.30	0.05±0.30	0.05±0.30	1724
GEC2	Bayern	0.51±0.29	0.48±0.29	0.50±0.28	0.48±0.28	4269
GIL	Alaska and Aleutians	0.17±0.39	0.12±0.35	0.10±0.34	0.11±0.35	649
GKN	Nepal	-0.34±0.28	-0.31±0.27	-0.32±0.27	-0.32±0.27	3812
GLD	Colorado	-0.18±0.31	-0.18±0.29	-0.18±0.29	-0.18±0.29	2780
GOL	Colorado	0.16±0.36	0.15±0.35	0.15±0.35	0.15±0.35	6588
GRF	Bayern	-0.12±0.26	-0.16±0.26	-0.14±0.25	-0.15±0.26	6907
GRI	Italy	-0.22±0.30	-0.20±0.28	-0.20±0.27	-0.20±0.27	207
GRM	Cape Province	-0.16±0.37	-0.19±0.36	-0.19±0.35	-0.20±0.35	413
GRO	Checheno-Ingushskaya	-0.48±0.27	-0.50±0.26	-0.49±0.26	-0.50±0.25	357
GRR	Pays de la Loire	-0.04±0.24	-0.06±0.23	-0.05±0.23	-0.05±0.23	7532
GRS	Armeniya	-0.15±0.27	-0.18±0.26	-0.16±0.26	-0.18±0.26	719

continued on the next page

continued from previous page

Sta-code	Sta-location	$S^{G\text{-}R}$	$S^{V\text{-}C}$	S^{L}	S^{New}	N
GTA	Gansu	0.06±0.38	0.06±0.37	0.05±0.37	0.06±0.37	5885
GUA	Mariana Islands	-0.36±0.34	-0.35±0.33	-0.36±0.32	-0.38±0.33	2709
GUMO	Mariana Islands	-0.39±0.37	-0.38±0.37	-0.40±0.37	-0.41±0.37	1423
GUN	Nepal	-0.44±0.27	-0.42±0.25	-0.43±0.26	-0.42±0.25	3991
GYA	Guizhou	0.00±0.38	0.00±0.36	-0.01±0.36	0.00±0.36	2182
GZH	Guangdong	0.01±0.34	-0.01±0.33	-0.03±0.32	-0.01±0.32	295
HAU	Lorraine	0.16±0.24	0.15±0.23	0.15±0.23	0.15±0.23	6651
HDM	Connecticut	0.04±0.39	0.06±0.38	0.05±0.38	0.06±0.37	201
HFS	Sweden	0.02±0.33	0.02±0.32	0.03±0.33	0.01±0.33	25239
HHC	Nei Monggol Zizhiqu	-0.02±0.34	-0.02±0.34	-0.03±0.33	-0.01±0.33	2561
HOF	Bayern	-0.03±0.25	-0.06±0.25	-0.05±0.25	-0.06±0.25	1146
HPK	England	0.10±0.28	0.10±0.27	0.10±0.27	0.10±0.27	441
HRV	Massachusetts	-0.05±0.33	-0.02±0.32	-0.03±0.32	-0.02±0.31	205
HYB	Andhra Pradesh	-0.20±0.29	-0.16±0.27	-0.18±0.27	-0.17±0.27	6710
ILT	Magadanskaya	-0.03±0.32	-0.06±0.29	-0.05±0.29	-0.06±0.29	1700
IMA	Alaska and Aleutians	0.23±0.33	0.21±0.31	0.21±0.31	0.21±0.31	6700
INK	Northwest Territories	-0.03±0.38	-0.03±0.36	-0.02±0.36	-0.03±0.36	4885
IPM	Peninsular Malaysia	-0.04±0.32	-0.06±0.31	-0.06±0.30	-0.06±0.30	5628
IRK	Irkutskaya	0.09±0.30	0.10±0.29	0.09±0.29	0.11±0.29	1744
ISA	California	0.10±0.34	0.09±0.33	0.10±0.33	0.10±0.33	695
ISQ	Queensland	-0.22±0.30	-0.19±0.29	-0.22±0.28	-0.20±0.27	307
JAY	Irian Jaya	-0.12±0.46	-0.05±0.42	-0.07±0.41	-0.08±0.43	619
JCT	Texas	0.03±0.31	0.05±0.30	0.06±0.30	0.05±0.30	4500
JFWS	Wisconsin	-0.21±0.32	-0.23±0.31	-0.23±0.30	-0.22±0.30	219
JOS	Hungary	0.00±0.33	-0.04±0.32	-0.01±0.32	-0.03±0.32	1633
KAF	Finland	0.03±0.29	0.05±0.28	0.05±0.28	0.04±0.28	3206
KBA	Austria	0.00±0.30	-0.04±0.31	-0.03±0.30	-0.04±0.31	5874
KBS	Svalbard	-0.06±0.34	-0.03±0.31	-0.06±0.31	-0.04±0.30	472
KDC	Alaska and Aleutians	0.05±0.34	0.02±0.32	0.02±0.32	0.02±0.32	795
KEDI	Sumba	-0.05±0.33	-0.04±0.31	-0.05±0.30	-0.04±0.31	240
KEV	Finland	-0.01±0.38	0.02±0.38	0.01±0.37	0.01±0.38	4693
KGM	Peninsular Malaysia	-0.16±0.39	-0.17±0.38	-0.19±0.37	-0.18±0.37	1273
KHC	K Czech Republic	0.16±0.26	0.12±0.26	0.14±0.26	0.13±0.26	5976
KHE	Arkhangel'skaya	-0.30±0.31	-0.30±0.30	-0.32±0.30	-0.30±0.30	666
KHZ	South Island	0.00±0.37	0.08±0.35	0.04±0.35	0.05±0.33	266
KIC	Ivory Coast	-0.25±0.32	-0.25±0.31	-0.24±0.31	-0.26±0.31	2880
KIR	Sweden	-0.55±0.25	-0.53±0.25	-0.53±0.24	-0.53±0.24	3200
KIS	Moldaviya	-0.60±0.24	-0.65±0.25	-0.62±0.24	-0.64±0.25	250
KIV	Stravropol'skiy	-0.32±0.37	-0.31±0.34	-0.29±0.34	-0.32±0.35	381
KJF	Finland	-0.15±0.33	-0.14±0.33	-0.13±0.32	-0.14±0.32	9172
KKM	Sabah	-0.10±0.38	-0.08±0.37	-0.09±0.36	-0.08±0.36	1512
KKN	Nepal	-0.26±0.28	-0.23±0.27	-0.24±0.27	-0.23±0.27	10480
KLB	Western Australia	0.02±0.33	0.01±0.30	0.00±0.30	0.02±0.30	2197
KLG	Western Australia	-0.02±0.37	0.01±0.36	-0.01±0.36	0.02±0.35	536
KMI	Yunnan	-0.16±0.52	-0.16±0.52	-0.17±0.52	-0.16±0.52	3217
KNA	Western Australia	-0.22±0.29	-0.23±0.29	-0.21±0.28	-0.24±0.29	1496
KOD	Tamil Nadu	-0.19±0.35	-0.18±0.34	-0.19±0.33	-0.18±0.34	704
KOI	Arunachal Pradesh	-0.01±0.34	-0.02±0.34	-0.03±0.34	-0.02±0.34	332
KRA	Poland	-0.27±0.26	-0.30±0.26	-0.28±0.25	-0.29±0.25	4816
KRI	Zimbabwe	0.21±0.29	0.20±0.28	0.21±0.28	0.19±0.28	4432
KRP	North Island	-0.34±0.34	-0.32±0.33	-0.34±0.33	-0.33±0.33	673
KSH	Xinjiang Uygur Zizhiqu	-0.21±0.36	-0.18±0.35	-0.20±0.35	-0.20±0.35	920
KSP	Poland	0.01±0.51	-0.02±0.50	-0.01±0.50	-0.02±0.50	2509
KSR	Transvaal	0.04±0.39	0.04±0.39	0.04±0.39	0.04±0.39	917
KTG	Greenland	0.08±0.29	0.12±0.28	0.11±0.28	0.11±0.28	813
KUPT	Timor	-0.31±0.38	-0.35±0.39	-0.38±0.38	-0.36±0.38	262
KUR	Sakhalinskaya	-0.44±0.29	-0.41±0.29	-0.43±0.28	-0.42±0.29	211
LBF	Bourgogne	0.19±0.24	0.18±0.23	0.19±0.23	0.19±0.23	9040
LD3	Montana	-0.09±0.32	-0.09±0.30	-0.08±0.30	-0.08±0.30	982
LDF	Basse-Normandie	0.03±0.23	0.02±0.22	0.02±0.22	0.02±0.22	4936
LEM	Jawa	-0.05±0.37	-0.04±0.36	-0.05±0.35	-0.05±0.35	1894
LFF	Aquitaine	-0.06±0.24	-0.06±0.23	-0.06±0.22	-0.06±0.22	7322
LGP	Luzon	-0.36±0.45	-0.33±0.43	-0.35±0.42	-0.35±0.43	286

continued on the next page

continued from previous page

Sta-code	Sta-location	$S^{G\text{-}R}$	$S^{V\text{-}C}$	S^{L}	S^{New}	N
LHC	Ontario	-0.27±0.29	-0.27±0.28	-0.29±0.28	-0.27±0.28	803
LIC	Ivory Coast	-0.10±0.29	-0.09±0.27	-0.08±0.28	-0.10±0.28	1285
LKO	Ivory Coast	-0.15±0.30	-0.16±0.29	-0.14±0.29	-0.16±0.28	829
LLS	Switzerland	-0.30±0.31	-0.32±0.31	-0.30±0.31	-0.31±0.31	2744
LMR	Provence-Cote d'Azur	0.02±0.27	0.02±0.25	0.03±0.25	0.04±0.25	3989
LON	Washington	0.29±0.42	0.29±0.39	0.29±0.38	0.29±0.39	664
LOR	Bourgogne	0.13±0.25	0.12±0.24	0.12±0.24	0.12±0.24	11505
LPB	Bolivia	-0.22±0.33	-0.23±0.32	-0.24±0.32	-0.23±0.32	2360
LPF	Bretagne	0.00±0.24	-0.02±0.23	-0.01±0.23	-0.01±0.23	6716
LPG	Rhone-Alpes	0.04±0.24	0.03±0.24	0.04±0.23	0.04±0.24	6168
LPL	Rhone-Alpes	0.04±0.26	0.04±0.25	0.05±0.25	0.05±0.25	3199
LPO	Midi-Pyrenees	0.04±0.25	0.03±0.24	0.04±0.24	0.04±0.24	6350
LPS	El Salvador	-0.14±0.34	-0.13±0.32	-0.15±0.33	-0.12±0.33	301
LRG	Provence-Cote d'Azur	-0.05±0.25	-0.05±0.25	-0.04±0.24	-0.03±0.24	3943
LSA	Xizang Zizhiqu	0.10±0.42	0.12±0.41	0.10±0.40	0.12±0.41	1024
LSF	Limousin	0.03±0.25	0.03±0.24	0.03±0.24	0.03±0.24	6857
LSZ	Zambia	0.09±0.59	0.07±0.57	0.08±0.58	0.07±0.57	336
LTX	Texas	0.27±0.33	0.26±0.33	0.26±0.33	0.26±0.33	1349
LTZ	South Island	-0.11±0.34	-0.08±0.35	-0.09±0.34	-0.08±0.33	391
LZH	Gansu	-0.17±0.41	-0.17±0.40	-0.18±0.40	-0.17±0.40	9293
MAF	Auvergne	0.02±0.26	0.02±0.24	0.02±0.24	0.02±0.24	5506
MAIO	Iran	0.27±0.31	0.27±0.31	0.28±0.30	0.27±0.30	1144
MAN	Luzon	-0.61±0.52	-0.58±0.49	-0.60±0.49	-0.60±0.49	224
MAT	Nagano	0.09±0.34	0.09±0.32	0.08±0.32	0.09±0.32	9093
MAW	Mac Robertson Land	0.07±0.31	0.03±0.29	0.03±0.29	0.03±0.29	2039
MBC	Northwest Territories	0.01±0.33	0.02±0.32	0.03±0.31	0.02±0.32	21074
MBL	Western Australia	0.03±0.33	-0.02±0.32	-0.03±0.31	-0.02±0.31	3562
MDJ	Jilin	-0.04±0.33	-0.02±0.31	-0.04±0.31	-0.02±0.31	1515
MEEK	Western Australia	-0.09±0.36	-0.09±0.32	-0.11±0.32	-0.09±0.31	317
MEK	Western Australia	-0.04±0.36	-0.04±0.32	-0.05±0.32	-0.03±0.32	1413
MEKA	Western Australia	0.04±0.38	0.02±0.33	0.01±0.33	0.02±0.32	691
MEO	Oklahoma	-0.03±0.34	0.00±0.32	0.00±0.32	-0.01±0.33	304
MFF	Poitou-Charentes	0.03±0.24	0.02±0.23	0.02±0.23	0.02±0.23	7134
MGD	Magadanskaya	-0.14±0.31	-0.14±0.29	-0.15±0.28	-0.15±0.28	1175
MHI	Iran	-0.07±0.32	-0.07±0.31	-0.07±0.31	-0.08±0.31	236
MIAR	Arkansas	0.00±0.31	0.02±0.29	0.02±0.29	0.02±0.30	644
MIM	Maine:USA	0.10±0.37	0.11±0.35	0.11±0.34	0.11±0.34	643
MIR	Queen Mary Land	-0.17±0.31	-0.17±0.29	-0.15±0.30	-0.18±0.30	304
MIZ	Iwate	0.33±0.35	0.34±0.35	0.32±0.35	0.34±0.34	268
MJZ	South Island	-0.21±0.39	-0.18±0.37	-0.20±0.37	-0.18±0.38	301
MKS	Sulawesi	-0.18±0.60	-0.16±0.59	-0.18±0.59	-0.16±0.59	229
MMK	Switzerland	-0.39±0.29	-0.40±0.29	-0.38±0.29	-0.39±0.29	2315
MNG	North Island	-0.10±0.37	-0.06±0.35	-0.08±0.35	-0.07±0.35	722
MNI	Sulawesi	-0.27±0.45	-0.27±0.46	-0.29±0.44	-0.28±0.44	219
MNT	Quebec	-0.17±0.37	-0.13±0.34	-0.14±0.35	-0.13±0.34	948
MOS	Moskovskaya	-0.47±0.28	-0.47±0.26	-0.47±0.26	-0.48±0.26	676
MOTA	Austria	-0.09±0.25	-0.12±0.25	-0.11±0.25	-0.11±0.25	294
MOX	Thuringen	-0.02±0.23	-0.05±0.22	-0.03±0.22	-0.04±0.22	6298
MOY	Buryatskaya	-0.08±0.29	-0.06±0.29	-0.08±0.28	-0.06±0.29	1322
MRWA	Western Australia	0.22±0.35	0.21±0.31	0.20±0.31	0.22±0.31	2396
MSO	Montana	0.03±0.39	0.04±0.37	0.05±0.37	0.05±0.37	1554
MSZ	South Island	-0.30±0.30	-0.25±0.30	-0.27±0.29	-0.26±0.29	653
MTA	Gruziya	-0.16±0.76	-0.18±0.76	-0.17±0.76	-0.20±0.76	228
MTD	Zimbabwe	0.21±0.29	0.21±0.28	0.23±0.28	0.21±0.28	3906
MTN	Northern Territory	-0.36±0.34	-0.35±0.33	-0.33±0.33	-0.35±0.33	1236
MUD	Denmark	0.08±0.32	0.07±0.32	0.07±0.32	0.06±0.31	1481
MUN	Western Australia	-0.10±0.40	-0.10±0.38	-0.11±0.38	-0.09±0.38	1623
MZF	Auvergne	0.07±0.26	0.07±0.25	0.07±0.25	0.07±0.25	4427
NAI	Kenya	-0.07±0.37	-0.06±0.36	-0.07±0.36	-0.06±0.36	1826
NANU	Western Australia	0.01±0.32	-0.03±0.31	-0.03±0.30	-0.03±0.30	1499
NAO	Norway	0.19±0.29	0.18±0.28	0.19±0.28	0.18±0.28	4169
NAU	Western Australia	0.01±0.32	-0.03±0.32	-0.03±0.32	-0.02±0.32	1456
NB2	Norway	0.22±0.29	0.20±0.27	0.22±0.27	0.20±0.28	25788

continued on the next page

continued from previous page

Sta-code	Sta-location	$S^{G\text{-}R}$	$S^{V\text{-}C}$	S^{L}	S^{New}	N
NBO	Norway	0.25±0.28	0.24±0.26	0.25±0.26	0.23±0.26	426
NDI	Delhi	-0.11±0.49	-0.08±0.47	-0.10±0.48	-0.09±0.47	3831
NEW	Washington	0.03±0.35	0.04±0.34	0.04±0.34	0.04±0.34	4235
NIE	Poland	-0.07±0.26	-0.10±0.25	-0.08±0.25	-0.09±0.25	3735
NJ2	Jiangsu	0.07±0.38	0.06±0.36	0.05±0.36	0.06±0.36	1137
NNA	Peru	0.15±0.46	0.14±0.45	0.13±0.45	0.13±0.44	1139
NRI	Krasnoyarskiy	0.06±0.33	0.04±0.30	0.04±0.29	0.04±0.29	1615
NUR	Finland	-0.08±0.41	-0.06±0.40	-0.05±0.40	-0.06±0.40	10968
NVL	Dronning Maud Land	-0.14±0.33	-0.15±0.31	-0.14±0.30	-0.15±0.30	853
NVS	Novosibirskaya	-0.03±0.36	-0.04±0.35	-0.06±0.34	-0.04±0.34	917
NWAO	Western Australia	0.08±0.36	0.08±0.32	0.07±0.32	0.09±0.32	2296
OBN	Kaluzhskaya	-0.32±0.30	-0.33±0.29	-0.32±0.28	-0.33±0.28	3206
OGA	Austria	-0.04±0.23	-0.07±0.23	-0.06±0.23	-0.06±0.23	1731
OHR	Macedonia	0.60±1.37	0.57±1.38	0.59±1.38	0.59±1.38	803
OJC	Poland	-0.32±0.25	-0.35±0.24	-0.33±0.23	-0.35±0.24	499
OPO	Madagascar	0.63±0.29	0.62±0.28	0.64±0.27	0.62±0.27	500
OSS	Switzerland	-0.25±0.28	-0.28±0.26	-0.26±0.26	-0.26±0.27	1578
OTP	Tuamotu	-0.25±0.35	-0.18±0.35	-0.20±0.34	-0.20±0.35	341
OTT	Ontario	-0.07±0.34	-0.04±0.31	-0.04±0.32	-0.03±0.31	1542
PAE	Tahiti	-0.01±0.31	0.04±0.31	0.01±0.29	0.02±0.30	2506
PAS	California	-0.29±0.39	-0.29±0.39	-0.29±0.38	-0.29±0.38	300
PCI	Sulawesi	0.87±0.34	0.86±0.33	0.86±0.33	0.87±0.33	640
PCT	Thailand	0.29±0.40	0.28±0.38	0.26±0.37	0.28±0.38	1936
PEC	California	0.20±0.35	0.20±0.34	0.20±0.34	0.20±0.33	1103
PET	Kamchatskaya	-0.17±0.33	-0.14±0.34	-0.15±0.33	-0.15±0.33	667
PGC	British Columbia	-0.05±0.32	-0.05±0.31	-0.06±0.31	-0.05±0.31	521
PGF	Corse	-0.05±0.28	-0.04±0.26	-0.03±0.26	-0.03±0.26	995
PGP	Mindoro	-0.11±0.49	-0.09±0.49	-0.11±0.48	-0.11±0.50	313
PGZ	North Island	-0.10±0.32	-0.08±0.32	-0.09±0.31	-0.08±0.30	247
PHC	British Columbia	-0.15±0.30	-0.14±0.29	-0.15±0.30	-0.14±0.29	228
PKI	Nepal	-0.11±0.29	-0.08±0.28	-0.09±0.28	-0.09±0.28	9537
PLP	Leyte	0.09±0.42	0.11±0.40	0.08±0.40	0.09±0.40	381
PME	Alaska and Aleutians	0.06±0.34	0.05±0.32	0.04±0.32	0.05±0.32	1796
PMG	Papua New Guinea	-0.31±0.34	-0.23±0.29	-0.25±0.28	-0.23±0.28	2351
PMO	Tuamotu	-0.05±0.34	-0.01±0.33	-0.03±0.32	-0.02±0.33	4175
PMR	Alaska and Aleutians	0.03±0.35	0.02±0.32	0.02±0.32	0.02±0.32	8423
PMS	Alaska and Aleutians	-0.08±0.34	-0.10±0.31	-0.10±0.30	-0.10±0.31	295
PNT	British Columbia	-0.02±0.29	-0.03±0.27	-0.03±0.27	-0.03±0.27	8712
POF	Cape Province	0.06±0.34	0.03±0.35	0.03±0.35	0.03±0.34	239
POO	Maharashtra	-0.14±0.34	-0.09±0.32	-0.10±0.31	-0.11±0.32	1187
PPI	Sumatera	-0.02±0.39	-0.02±0.37	-0.04±0.37	-0.02±0.37	1794
PPN	Tahiti	0.07±0.32	0.12±0.32	0.10±0.30	0.10±0.31	2551
PPR	Palawan	-0.05±0.42	-0.02±0.40	-0.05±0.40	-0.03±0.40	616
PPT	Tahiti	-0.12±0.31	-0.06±0.30	-0.10±0.29	-0.09±0.29	2583
PRA	Czech Republic	-0.06±0.26	-0.08±0.24	-0.07±0.24	-0.08±0.24	2478
PRE	Transvaal	-0.02±0.34	-0.01±0.33	0.00±0.33	-0.01±0.33	612
PRU	Czech Republic	0.09±0.26	0.06±0.24	0.07±0.24	0.06±0.24	3396
PRY	Orange Free State	0.14±0.37	0.14±0.35	0.14±0.35	0.14±0.35	723
PRZ	Kirgiziya	-0.25±0.31	-0.22±0.29	-0.25±0.29	-0.23±0.30	1248
PSI	Sumatera	-0.02±0.35	-0.04±0.33	-0.04±0.33	-0.03±0.33	5074
PUL	Leningradskaya	-0.39±0.27	-0.37±0.27	-0.37±0.27	-0.37±0.27	565
PYA	Stravropol'skiy	-0.40±0.25	-0.40±0.25	-0.39±0.25	-0.42±0.25	368
QIS	Queensland	0.05±0.37	0.04±0.38	0.03±0.37	0.04±0.36	1333
QIZ	Hainan Dao	0.15±0.30	0.16±0.30	0.15±0.29	0.15±0.30	309
QLP	Queensland	-0.44±0.35	-0.39±0.31	-0.40±0.31	-0.39±0.31	572
QUE	Pakistan	-0.33±0.57	-0.29±0.56	-0.30±0.56	-0.30±0.56	332
QZH	Fujian	-0.08±0.34	-0.09±0.33	-0.10±0.32	-0.09±0.33	421
RES	Northwest Territories	0.06±0.33	0.09±0.31	0.08±0.31	0.08±0.31	4079
RJF	Limousin	0.08±0.25	0.08±0.24	0.08±0.23	0.08±0.24	6265
RKG	Western Australia	0.04±0.36	0.04±0.33	0.02±0.33	0.04±0.33	1103
RKT	Gambier Islands	0.06±0.33	0.12±0.32	0.10±0.32	0.10±0.31	986
RMQ	Queensland	-0.20±0.34	-0.14±0.32	-0.18±0.32	-0.17±0.32	1910
RSCP	Tennessee	-0.23±0.35	-0.22±0.33	-0.23±0.33	-0.24±0.33	772

continued on the next page

continued from previous page

Sta-code	Sta-location	$S^{G\text{-}R}$	$S^{V\text{-}C}$	S^{L}	S^{New}	N
RSNT	Northwest Territories	-0.04±0.34	-0.04±0.33	-0.03±0.32	-0.04±0.32	1461
RSNY	New York	0.02±0.34	0.05±0.31	0.05±0.31	0.06±0.31	1689
RSON	Ontario	-0.08±0.32	-0.06±0.30	-0.07±0.30	-0.05±0.30	3198
RSSD	South Dakota	0.07±0.31	0.06±0.30	0.07±0.29	0.07±0.30	4254
RUV	Tuamotu	-0.06±0.32	-0.02±0.30	-0.03±0.30	-0.02±0.30	4251
SAX	Switzerland	-0.16±0.25	-0.18±0.24	-0.17±0.24	-0.17±0.24	1493
SBA	Victoria Land	-0.15±0.46	-0.15±0.41	-0.16±0.42	-0.16±0.41	2047
SBF	Provence-Cote d'Azur	-0.15±0.24	-0.15±0.22	-0.14±0.22	-0.14±0.22	2353
SCH	Quebec	-0.19±0.32	-0.16±0.30	-0.18±0.31	-0.17±0.30	1733
SCO	Greenland	0.05±0.40	0.08±0.40	0.07±0.40	0.06±0.40	1261
SDN	Alaska and Aleutians	-0.45±0.34	-0.48±0.33	-0.46±0.33	-0.48±0.33	486
SDV	Venezuela	-0.19±0.38	-0.21±0.39	-0.22±0.38	-0.20±0.38	490
SEK	Orange Free State	-0.05±0.36	-0.07±0.35	-0.06±0.35	-0.06±0.35	1038
SES	Alberta	-0.35±0.30	-0.36±0.29	-0.35±0.28	-0.35±0.29	2623
SEY	Magadanskaya	-0.08±0.29	-0.09±0.28	-0.10±0.27	-0.10±0.27	883
SHE	Azerbaydzhan	-0.22±0.29	-0.24±0.29	-0.23±0.28	-0.24±0.28	215
SHK	Hiroshima	-0.27±0.36	-0.25±0.34	-0.27±0.33	-0.25±0.33	390
SIT	Alaska and Aleutians	0.11±0.35	0.10±0.33	0.10±0.33	0.10±0.33	434
SJG	Puerto Rico	-0.06±0.34	-0.04±0.31	-0.06±0.32	-0.04±0.31	601
SKO	Macedonia	-0.32±0.40	-0.34±0.38	-0.34±0.38	-0.34±0.38	1239
SLE	Switzerland	-0.22±0.26	-0.23±0.25	-0.21±0.25	-0.22±0.25	2002
SLL	Sweden	-0.05±0.35	-0.09±0.36	-0.05±0.34	-0.09±0.35	2118
SLR	Transvaal	-0.09±0.34	-0.10±0.34	-0.09±0.34	-0.09±0.34	2069
SMF	Bourgogne	0.05±0.24	0.04±0.24	0.04±0.23	0.04±0.23	10666
SMY	Alaska and Aleutians	-0.41±0.30	-0.39±0.27	-0.39±0.27	-0.39±0.27	374
SNA	Dronning Maud Land	-0.24±0.35	-0.23±0.34	-0.23±0.34	-0.23±0.34	932
SNG	Thailand	0.05±0.68	0.05±0.67	0.03±0.67	0.04±0.67	1239
SNY	Liaoning	-0.03±0.34	-0.03±0.34	-0.05±0.34	-0.03±0.33	1679
SOB1	Bahia	0.11±0.43	0.14±0.41	0.14±0.41	0.15±0.41	305
SOC	Krasnodarskiy	-0.24±0.30	-0.26±0.28	-0.23±0.27	-0.25±0.28	326
SOP	Hungary	-0.11±0.33	-0.15±0.32	-0.14±0.31	-0.15±0.32	691
SPA	Antarctica:Land	-0.01±0.35	-0.02±0.34	-0.01±0.34	-0.02±0.34	15116
SPF	Provence-Cote d'Azur	0.16±0.30	0.16±0.27	0.17±0.27	0.17±0.26	515
SQTA	Austria	-0.08±0.26	-0.10±0.25	-0.08±0.24	-0.09±0.25	933
SRDI	Jawa	-0.16±0.35	-0.14±0.34	-0.14±0.33	-0.14±0.33	231
SSC	Basse-Normandie	0.09±0.25	0.08±0.24	0.09±0.24	0.08±0.24	1754
SSE	Jiangsu	0.18±0.53	0.16±0.51	0.15±0.51	0.16±0.51	4380
SSF	Bourgogne	0.14±0.24	0.13±0.23	0.14±0.23	0.14±0.23	10868
STJ	Newfoundland	-0.35±0.34	-0.32±0.32	-0.33±0.33	-0.32±0.32	245
STK	New South Wales	0.25±0.45	0.25±0.42	0.25±0.42	0.26±0.42	6641
STU	Baden-Wurttemberg	-0.06±0.30	-0.09±0.28	-0.09±0.28	-0.09±0.28	611
SUF	Finland	0.04±0.30	0.05±0.28	0.06±0.28	0.05±0.28	13582
SUR	Cape Province	-0.16±0.36	-0.19±0.35	-0.18±0.35	-0.19±0.35	619
SVE	Sverdlovskaya	-0.28±0.30	-0.25±0.28	-0.26±0.27	-0.26±0.27	1453
SVW	Alaska and Aleutians	-0.08±0.34	-0.10±0.32	-0.10±0.32	-0.10±0.32	1499
SWZ	Transvaal	-0.08±0.35	-0.08±0.35	-0.08±0.35	-0.08±0.35	292
TAS	Uzbekistan	-0.45±0.28	-0.42±0.28	-0.43±0.28	-0.43±0.28	806
TBI	Tubuai	-0.08±0.31	-0.02±0.31	-0.05±0.30	-0.05±0.30	1132
TCF	Limousin	0.15±0.24	0.15±0.23	0.15±0.23	0.15±0.23	8762
THZ	South Island	0.04±0.30	0.11±0.29	0.09±0.28	0.09±0.28	250
TIA	Shandong	-0.04±0.36	-0.04±0.34	-0.05±0.34	-0.04±0.34	873
TIC	Ivory Coast	-0.04±0.30	-0.03±0.28	-0.03±0.28	-0.04±0.28	1091
TIK	Yakutskaya	0.00±0.36	-0.01±0.33	-0.01±0.33	-0.01±0.34	2483
TIY	Shanxi	0.11±0.74	0.11±0.74	0.10±0.74	0.12±0.73	978
TLG	Kazakhstan	0.15±0.36	0.17±0.34	0.15±0.34	0.17±0.34	1671
TMA	Switzerland	-0.45±0.26	-0.47±0.25	-0.45±0.25	-0.46±0.26	2062
TNP	Nevada	0.22±0.32	0.21±0.29	0.21±0.29	0.21±0.29	3880
TOL	Spain	-0.06±0.65	-0.06±0.65	-0.06±0.64	-0.06±0.65	1585
TOO	Victoria	-0.13±0.32	-0.08±0.30	-0.10±0.30	-0.09±0.30	3125
TOV	Venezuela	0.01±0.42	0.01±0.43	-0.02±0.42	0.01±0.42	255
TPNV	Nevada	0.07±0.32	0.07±0.31	0.07±0.31	0.07±0.31	696
TPT	Tuamotu	-0.06±0.32	-0.02±0.31	-0.03±0.31	-0.02±0.31	4189
TRN	Trinidad and Tobago	-0.02±0.36	-0.04±0.37	-0.05±0.35	-0.04±0.36	356

continued on the next page

continued from previous page

Sta-code	Sta-location	$S^{G\text{-}R}$	$S^{V\text{-}C}$	S^{L}	S^{New}	N
TRT	Jawa	-0.14±0.37	-0.12±0.37	-0.13±0.35	-0.13±0.36	1363
TSI	Sumatera	-0.37±0.44	-0.37±0.43	-0.38±0.42	-0.37±0.43	209
TSK	Ibaraki	0.16±0.36	0.17±0.33	0.15±0.33	0.16±0.33	206
TTA	Alaska and Aleutians	0.20±0.32	0.18±0.30	0.18±0.29	0.18±0.29	2319
TUC	Arizona	0.16±0.33	0.13±0.32	0.13±0.32	0.13±0.32	1074
TUL	Oklahoma	-0.11±0.33	-0.10±0.32	-0.10±0.32	-0.10±0.32	10426
TVO	Tahiti	-0.14±0.30	-0.09±0.29	-0.12±0.28	-0.11±0.29	2690
UCT	Connecticut	-0.08±0.39	-0.07±0.39	-0.06±0.39	-0.06±0.39	266
UER	Tuvinskaya	0.03±0.35	0.05±0.33	0.04±0.32	0.04±0.32	312
UPA	Panama	0.01±0.40	0.00±0.39	-0.01±0.38	0.01±0.38	363
UPP	Sweden	-0.48±0.26	-0.47±0.24	-0.47±0.24	-0.48±0.24	3333
UZH	Ukraina	-0.16±0.34	-0.20±0.35	-0.16±0.33	-0.19±0.35	1308
VAH	Tuamotu	0.04±0.32	0.08±0.32	0.06±0.31	0.07±0.31	3821
VAL	Ireland	-0.21±0.27	-0.22±0.26	-0.21±0.26	-0.21±0.26	1021
VAY	Macedonia	0.27±1.12	0.24±1.12	0.25±1.11	0.25±1.11	503
VDL	Switzerland	-0.45±0.24	-0.47±0.24	-0.45±0.24	-0.46±0.24	1597
VIE	Austria	-0.31±0.39	-0.34±0.37	-0.35±0.36	-0.35±0.36	205
VKA	Austria	-0.26±0.31	-0.29±0.29	-0.28±0.28	-0.28±0.28	952
VLA	Primorskiy	-0.17±0.35	-0.15±0.32	-0.18±0.32	-0.15±0.32	288
VRAC	Czech Republic	-0.25±0.47	-0.28±0.46	-0.26±0.46	-0.28±0.46	370
VTY	Madagascar	0.63±0.28	0.61±0.27	0.63±0.27	0.61±0.27	556
VUN	Fiji	-0.01±0.44	0.00±0.43	-0.01±0.43	-0.01±0.43	246
WARB	Western Australia	0.06±0.32	0.05±0.31	0.06±0.31	0.06±0.30	2563
WB2	Northern Territory	-0.10±0.40	-0.08±0.39	-0.09±0.39	-0.09±0.39	5392
WBN	Western Australia	-0.13±0.30	-0.14±0.29	-0.13±0.29	-0.14±0.30	1764
WDC	California	0.07±0.35	0.06±0.33	0.06±0.32	0.07±0.32	343
WEL	North Island	-0.46±0.34	-0.37±0.32	-0.40±0.31	-0.40±0.31	304
WES	Massachusetts	-0.85±0.52	-0.82±0.51	-0.81±0.51	-0.82±0.51	219
WET	Bayern	-0.02±0.25	-0.05±0.24	-0.04±0.24	-0.05±0.24	1741
WHN	Hubei	0.01±0.57	0.00±0.57	-0.01±0.56	0.00±0.56	1643
WIN	Namibia	-0.05±0.34	-0.06±0.33	-0.05±0.33	-0.05±0.33	1065
WLF	Luxembourg	0.30±0.29	0.30±0.27	0.31±0.27	0.30±0.28	205
WMOK	Oklahoma	-0.05±0.34	-0.06±0.35	-0.05±0.34	-0.04±0.34	496
WMQ	Xinjiang Uygur Zizhiqu	-0.01±0.38	0.02±0.37	0.00±0.37	0.01±0.37	2774
WOL	England	-0.30±0.28	-0.33±0.28	-0.32±0.28	-0.32±0.27	774
WR2	Northern Territory	-0.07±0.40	-0.06±0.39	-0.07±0.39	-0.07±0.39	1644
WRA	Northern Territory	0.24±0.36	0.25±0.35	0.25±0.35	0.25±0.35	31859
WTS	Netherlands	0.00±0.28	-0.02±0.27	-0.01±0.27	-0.02±0.27	4343
WTTA	Austria	-0.09±0.25	-0.13±0.25	-0.12±0.24	-0.12±0.25	1087
XAN	Shaanxi	0.08±0.33	0.07±0.31	0.07±0.31	0.08±0.31	2989
YAK	Yakutskaya	-0.40±0.31	-0.39±0.29	-0.40±0.28	-0.40±0.28	2771
YKA	Northwest Territories	0.35±0.35	0.34±0.33	0.36±0.33	0.34±0.33	7338
YKC	Northwest Territories	-0.03±0.32	-0.02±0.31	-0.02±0.30	-0.02±0.30	5125
YSS	Sakhalinskaya	-0.07±0.38	-0.05±0.37	-0.06±0.36	-0.05±0.37	1140
ZAK	Buryatskaya	0.13±0.31	0.13±0.30	0.12±0.30	0.14±0.30	3629
ZLA	Switzerland	-0.55±0.24	-0.57±0.24	-0.56±0.23	-0.56±0.24	1022
ZOBO	Bolivia	0.13±0.36	0.11±0.34	0.11±0.34	0.11±0.34	2958
ZST	Slovak Republic	0.08±0.27	0.02±0.26	0.04±0.24	0.02±0.25	350
ZUL	Switzerland	-0.35±0.27	-0.37±0.26	-0.36±0.26	-0.36±0.26	2840

$S^{G\text{-}R}$, $S^{V\text{-}C}$, S^{L}, and S^{New} are station correctin which obtaned using magnitude values when applying calibration terms of the Gutenberg-Richter, Vieth-Clawson, Lilwall, and this study respectively. N is the number of observation/events from a especefic sation which ISC has used for the determination of $m_b^{station}$ between 1978 and 1993.

Bulletin of the Seismological Society of America, Vol. 88, No. 1, pp. 43–61, February 1998

Bias in Surface-Wave Magnitude M_s due to Inadequate Distance Corrections

by Mehdi Rezapour and Robert G. Pearce

Abstract We investigate bias in surface-wave magnitude using the complete ISC and NEIC datasets from 1978 to 1993. We conclude that although there are some small differences between the ISC and NEIC magnitudes, there is no major difference between these agencies for this presentation of the global dataset. The frequency–distance plot for reported surface-wave amplitude observations exhibits detailed structure of the body-wave amplitude–distance curve at all distances; the influence of the surface-wave amplitude decay with distance is much less apparent. This censoring via the body waves represents a large deficit in the number of potentially usable surface-wave amplitude observations, particularly in the *P*-wave shadow zone between $\Delta = 100°$ and 120°. We have obtained two new modified M_s formulas based upon analysis of all ISC data between 1978 and 1993. In the first, the conventional logarithmic dependence of the distance correction is retained, and we obtain

$$M_s^e = \log(A/T)_{\max} + 1.155 \log(\Delta) + 4.269.$$

In the second, we make allowance for the theoretically known contribution of dispersion and geometrical spreading, to obtain

$$M_s^t = \log(A/T)_{\max} + \frac{1}{3}\log(\Delta) + \frac{1}{2}\log(\sin\Delta) + 0.0046\Delta + 5.370.$$

Comparison of these formulas with other work confirms the inadequacy of the distance-dependence term in the Gutenberg and Prague formulas, and we show that our first formula, as well as that of Herak and Herak, gives less bias at all epicentral distances to within the scatter of the observed dataset. Our second formula provides an improved overall distance correction, especially beyond $\Delta = 145°$. We show evidence that Airy-phase distance decay predominates at shorter distances ($\Delta \leqq 30°$), but for greater distances, we are unable to resolve whether this or non-Airy-phase decay predominates. Assuming 20-sec surface waves with $U = 3.6$ km/sec, we obtain a globally averaged apparent Q^{-1} of 0.00192 ± 0.00026 ($Q \approx 500$). We argue that our second formula not only improves the distance correction for surface-wave magnitudes but also promotes the analysis of unexplained amplitude anomalies by formally allowing for those contributions that are theoretically predictable. We conclude that there remains systematic bias in station magnitudes and that this includes the effects of source depth, different path contributions, and differences in seismometer response. For intermediate magnitudes, M_s^t shows less scatter against log M_0 than does M_s calculated using the Prague formula.

Introduction

Magnitude M is a measure of earthquake size determined from the amplitude and period of a certain type of seismic wave using an empirical formula that contains several constants whose values are chosen to maximize internal consistency between different observations. There is a limitation in the use of any magnitude scale for the quantification of earthquakes because magnitude is unrelated to source physics. Nevertheless, magnitude scales are so widely used that it is difficult to imagine that they would be easily abandoned. Moreover, archived magnitude data provide the only quantitative determinations of size for most historical earthquakes. Most studies in earthquake seismology use magni-

tude data as a guide to the strength of an earthquake. So biases in magnitude estimates, caused by incorrect allowance for any effects other than earthquake strength, directly affect the result of any study in which magnitude data are used. Such uses cover a wide range of seismology. Reduction of bias when comparing recent data (for which seismic moments can be determined) with historical data (for which only magnitudes are available) will improve estimates of the size of historical earthquakes, improve discrimination between earthquakes and nuclear explosions, and will give us a better measure of the overall rate of seismic energy release.

The problem of magnitude scale became very complex as many different scales were introduced to accommodate different situations such as the use of teleseismic surface and body waves, extension of the scale to intermediate and deep earthquakes, changes in seismic instrumentation, and extension of the scale to very small and very large earthquakes. Moreover, the standard magnitude estimates are meaningless for very large events (Aki, 1967; Kanamori, 1978) as the scale becomes saturated.

Earthquake magnitude is routinely estimated by the global agencies in two frequency bands: high-frequency body waves with periods around 1 sec (for m_b) and low-frequency surface waves with periods around 20 sec (for M_s). However, the period of the wave with maximum ground motion depends upon the source spectrum, the source depth, the dispersion characteristics and the absorption properties of the propagation path, and the magnification of the seismograph in the passband.

In this article, we consider bias in surface-wave magnitude M_s. There are two primary motivations. First, the M_s:m_b criterion is a widely used seismic discriminant between earthquakes and nuclear explosions, and it has potential to identify explosions under the Comprehensive Nuclear Test Ban Treaty. Second, the quantification of earthquake size requires a parameter that has a physical basis (e.g., seismic moment); such parameters for historical earthquakes must usually be derived from archived magnitude data. As the body of global magnitude data increases with the passage of time, there is more scope for understanding, and hence allowing for, its biases and scatter.

We begin by highlighting some theoretical points. We then compare m_b and M_s determinations for the two largest global agencies, the ISC (International Seismological Centre) and the NEIC (National Earthquake Information Center). We then examine M_s:m_b for the ISC data, and point out the large number of earthquakes that plot as explosions according to the M_s:m_b discriminant when ISC magnitudes are used. We then use the ISC global dataset to derive an optimum M_s distance-correction function, first assuming the "log(Δ)" distance dependence of conventional magnitude scales, and second after allowing for those parts of the distance dependence that are known from theory. These approaches are compared with each other and with other work. We also show the distribution of M_s against log M_0 for the Prague formula and for our second formula using 6553 earthquakes in the Harvard Centroid Moment Tensor (CMT) Catalogue. We then briefly consider the origins of the scatter remaining in M_s values.

Surface-Wave Magnitude Scales

Gutenberg Formula. Surface-wave magnitude was originally defined by Gutenberg (1945) as the first attempt to measure the strength of shallow earthquakes at teleseismic distances. As such, it was an extension of the local magnitude scale, M_L, introduced by Richter (1935) for the rating of regional earthquakes in California. The M_s scale was adjusted to agree with M_L and is based on 20-sec surface waves from shallow earthquakes in the distance range $15° \leqq \Delta \leqq 130°$. Richter introduced the universally accepted basis of magnitude as log (amplitude). However, there was no absolute scaling between the maximum amplitudes on instruments with different frequency responses, and the correction for distance was constrained to be logarithmic, without theoretical justification. Scales obtained from different instruments can be matched at one magnitude level, but they will then diverge at other levels (Scheidegger, 1985). The final formula of Gutenberg (1945) is

$$M_s^{\text{Gutenberg}} = \log A + 1.656 \log \Delta + 1.818 + S_c, \quad (1)$$

where S_c is a station correction, Δ is the epicentral distance in degrees, and A is the maximum amplitude on the horizontal component seismogram in microns for a surface wave with period of about 20 sec. This formula was originally designed to use amplitude data from horizontal seismographs, but when vertical-component systems came into general use, it became common practice to measure displacements on the vertical component.

Prague Formula. Vaněk *et al.* (1962) proposed the so-called "Prague formula":

$$M_s^{\text{Prague}} = \log (A/T)_{\max} + 1.66 \log \Delta + 3.3, \quad (2)$$

where A is the vertical or resultant horizontal amplitude in microns and T is the mean period in seconds. In equation (2), $(A/T)_{\max}$ is the maximum of all A/T (amplitude/period) values of wave groups on a record. However, it is not clear whether all the seismic stations that report data to the ISC measure $(A/T)_{\max}$ or $(A_{\max}/T)$. In practice, it seems improbable that $\log(A/T)_{\max}$ and $\log(A_{\max}/T)$ will differ greatly for classical long-period observations, though the difference may be very large on broadband seismograms, which are of course becoming more common. The Prague formula employed a geographic average of various distance-normalizing terms, and incorporated T in the formula to account for those cases, particularly for continental propagation and using broadband (Kirnos-type) seismographs, for which the

maximum trace amplitude does not occur at a period near 20 sec (Marshall and Basham, 1972).

The recommendations on magnitude made by the IASPEI (International Association of Seismology and Physics of the Earth's Interior) Assembly at Zürich in 1967 (Båth, 1981) concerned surface-wave magnitude determination using the Prague formula with conditions $20° \leqq \Delta \leqq 160°$, and 17 sec $\leqq T \leqq$ 23 sec for shallow earthquakes with a calculated depth $h < 50$ km. The ISC uses the Prague formula for shallow events with a calculated depth of $h \leqq 60$ km in the distance range 20° to 160° and in the period range 10 sec $\leqq T \leqq 60$ sec. ISC uses either the vertical component or the vector sum of the horizontals, but NEIC uses only the vertical component.

Modified M_s Formulas. Several authors have pointed out difficulties with the above scales for $\Delta \leqq 20°$ (e.g., von Seggern, 1970; Evernden, 1971). A modification of the Prague formula applicable to closer ranges was proposed by Marshall and Basham (1972). They suggested a modified formula for M_s as

$$M_s = \log A_{\max} + B'(\Delta) + P(T) + 3, \qquad (3)$$

where A is the maximum amplitude in microns of the Raleigh wave train, $B'(\Delta)$ is a tabulated epicentral distance correction term, and $P(T)$ is the path correction varying with the period of the wave measured and tabulated for different lithospheric structures. Marshall and Basham proposed that for distances up to 25°, the distance-dependence term, $B'(\Delta)$, is proportional to $0.8\log(\Delta)$, and at large teleseismic distances, it is the same as Gutenberg's distance-dependence term. Marshall and Basham have adjusted the absolute level of $B'(\Delta)$, so that magnitude determinations give results essentially the same as the Gutenberg and Prague formulas at large epicentral distances.

Herak and Herak (1993) found a new empirical formula for determining M_s as

$$M_s = \log (A/T) + 1.094 \log(\Delta) + 4.429 \qquad (4)$$

based on an analysis of surface-wave magnitudes of 250 selected earthquakes published in the ISC and NEIC Catalogues. They conclude that the Prague formula is inappropriate for magnitude determination because of bias in the distance calibration function.

The general form of most formulas for determining surface-wave magnitude has remained as

$$M_s = \log(A/T) + B(\Delta) + C,$$

where $B(\Delta)$ is a correction for the decay of amplitude with distance and C is a correction for effect of the station structure or path correction, which in some formulas has been omitted. Later we shall compute an M_s formula similar to equation (4), using a much larger dataset from the ISC.

Use of Theoretical Distance Corrections. The second and subsequent terms on the right of equations (1) to (4) attempt to correct individual observations for effects other than the earthquake strength, to ensure that the magnitude database is internally consistent and consistent with other magnitude scales. Okal (1989) considered the theoretical issues of magnitude corrections in some detail. He compared a theoretical distance correction with that of the Prague formula and found that the difference between these corrections never exceeds ± 0.05 magnitude units for $20° < \Delta < 150°$. Okal found that, compared with the theoretical distance correction, the Prague distance correction overestimates M_s by between 0.02 and 0.04 magnitude units in the distance range 20° to 110°. Nevertheless, he concluded that the distance correction of the Prague formula was adequate except at very short distances.

None of the above formulas incorporate corrections that are theoretically predicted, despite the fact that the main contributions to both distance and depth corrections are known from seismological theory, as pointed out by Nuttli (1973). Theoretically the distance-correction term is not logarithmic with distance, so there is a limit to the distance range over which the conventional correction can be applicable. This explains, at least in part, the difficulties with previous M_s distance-correction terms at short ($\Delta \leqq 20°$) and very long ($\Delta \geqq 140°$) distances. More importantly, in order to isolate those contributions to magnitude residuals that are unexplained, we must first correctly remove those components whose contribution is predictable from theory.

For a spherical Earth, and assuming that the wavelength is small compared with the Earth's radius, the distance dependence of Rayleigh-wave amplitude $A(\Delta,T)$ is given by (see, e.g., Marshall and Carpenter, 1966)

$$A(\Delta,T) \propto \Delta^{-\frac{1}{2}} (\sin \Delta)^{-\frac{1}{2}} \exp(-\pi^2 E\Delta/180QUT), \qquad (5)$$

where again Δ is the distance in degrees between source and receiver, U is the group velocity (which is assumed to be increasing monotonically with period T), E is the Earth's radius, and Q is the path-averaged apparent absorption coefficient for surface waves of period T. Here the three terms represent respectively the contributions of dispersion (Ewing *et al.,* 1957, p. 164), geometrical spreading on the surface of a sphere, and anelastic attenuation. For an observation at a known distance and period, this formula has only two unknowns—the product QU and the constant of proportionality. Near a group velocity minimum (corresponding to an Airy phase), the first term becomes $\Delta^{-1/3}$ (Ewing *et al.,* 1957, p. 165). Hence, the correction for dispersion depends upon whether or not the measured amplitude is at a period close to a group velocity minimum.

Thomas *et al.* (1978) examined the fit of a distance-correction function of this form and found that the Airy-phase dependence better fitted observations, which suggested that most of their observations were made from the

Airy phase. However, their data are restricted to stations of the Long Range Seismic Measurement (LRSM) program. Douglas *et al.* (1981) studied this in more detail and were unable to discriminate between non-Airy-phase decay and Airy-phase decay from the statistics of their regression lines.

Herak and Herak (1993) also considered a theoretical correction similar to equation (5), but they assumed non-Airy-phase observation in their dispersion term. Also, the formula they proposed did not include terms of a form corresponding to the theoretical corrections. Imposition of a distance dependence of the form of equation (5) does not increase the number of unknown constants to be determined by least-squares fitting of observations. Later we determine a distance correction function based on this form.

None of the commonly used surface-wave magnitude formulas include a depth-dependent correction, yet the effect of depth is known from theory to vary by about 1.0 magnitude units between 0 and 60 km for Love waves (e.g., Panza *et al.*, 1989); this corresponds to the range of computed values over which surface-wave magnitudes are determined by the ISC. It appears that failure to include such a correction results from the poor accuracy of depth determinations; it is not that the effect of depth is insignificant. Moreover, for earthquake/explosion discrimination, it is argued that the M_s:m_b criterion must work without a depth correction.

Comparison of Magnitudes Determined by ISC and NEIC

Magnitude is routinely estimated by different agencies, such as the ISC, NEIC, and by many national agencies, and at individual stations. For global comparison of magnitudes reported by the ISC and the NEIC, and for investigation of the M_s:m_b relation, we used the ISC Catalogue data from 1978 (when consistent ISC M_s determination began) to 1993. We use data from all earthquakes for which the ISC uses its own determination in the ISC Catalogue (i.e., where the ISC location is the "prime" location). The M_s:m_b statistics can be used for comparison of source properties only over a limited range of magnitudes since it is not linear over a large magnitude range. Figure 1 shows a comparison of magnitudes determined by the ISC and the NEIC in that period. Each graph includes those earthquakes (i.e., excluding events reported as explosions) for which the relevant two parameters are reported. ISC and NEIC compute M_s for earthquakes with a computed depth h of $\leqq 60$ km and < 50 km, respectively. To improve comparability, we impose a limit of $h < 50$ km for both agencies.

Many authors have given linear approximations to the relation between surface-wave and body-wave magnitudes. However, there is a great deal of scatter about the straight lines because of source effects and because of large variations, both random and systematic, in the empirical signals. These may be caused by differences in recording apparatus, the nonuniform distribution of seismic stations, and differences in the method of determination of magnitudes (Prozorov and Hudson, 1974). In Figures 1a and 1b, M_s versus m_b has been plotted for ISC and NEIC data, respectively. Regression lines have been determined assuming the same variance in M_s and m_b, and we obtain

$$M_s^{\mathrm{ISC}} = (1.8782 \pm 0.0222)m_b^{\mathrm{ISC}} - (4.6046 \pm 0.1102), \quad (6)$$

$$M_s^{\mathrm{NEIC}} = (1.8030 \pm 0.0216)m_b^{\mathrm{NEIC}} - (4.3655 \pm 0.1101). \quad (7)$$

Due to progressive increase in network sensitivity, the regression coefficient and regression constant in the linear regression line between M_s and m_b change significantly over time; we would expect this even if we imposed a magnitude cutoff and minimum number of reporting stations, because of the characteristic evolution of the global network. From the regression lines in Figures 1a and 1b, it is seen that in the ISC Catalogue, the values are equal at magnitude (M) about 5.2; for $M < 5.2$, surface-wave magnitude is less than body-wave magnitude, while for $M > 5.2$, the reverse is true. In the NEIC Catalogue, the values are equal at magnitude about 5.4. Correlation in Figure 1b (NEIC) is a little better than in Figure 1a (ISC).

In Figures 1c and 1d, a comparison is made between data for the two agencies, separately for body-wave and surface-wave magnitudes. The equations of the regression lines in Figures 1c and 1d are

$$m_b^{\mathrm{NEIC}} = (1.0053 \pm 0.0025)m_b^{\mathrm{ISC}} + (0.0166 \pm 0.0117), \quad (8)$$

$$M_s^{\mathrm{NEIC}} = (1.0089 \pm 0.0036)M_s^{\mathrm{ISC}} - (0.0743 \pm 0.0175). \quad (9)$$

In both Figures 1c and 1d, the correlation is good, but it seems that for body-wave magnitude, the correlation is higher for the NEIC than for the ISC. For surface-wave magnitude, the reverse is true. The correlation coefficient in equation (9) is higher than in equation (8). We conclude that although there are some small differences between the ISC and NEIC magnitudes, there is no major difference between these agencies for this presentation of the global earthquake data.

M_s:m_b for ISC Data

The relation M_s:m_b is widely used as a discriminant to identify underground nuclear explosions. The M_s:m_b discriminant is essentially empirical, with several effects contributing to its success. A number of studies have been carried out on the variation of M_s and m_b with geographical location. Marshall and Basham (1972) showed that the

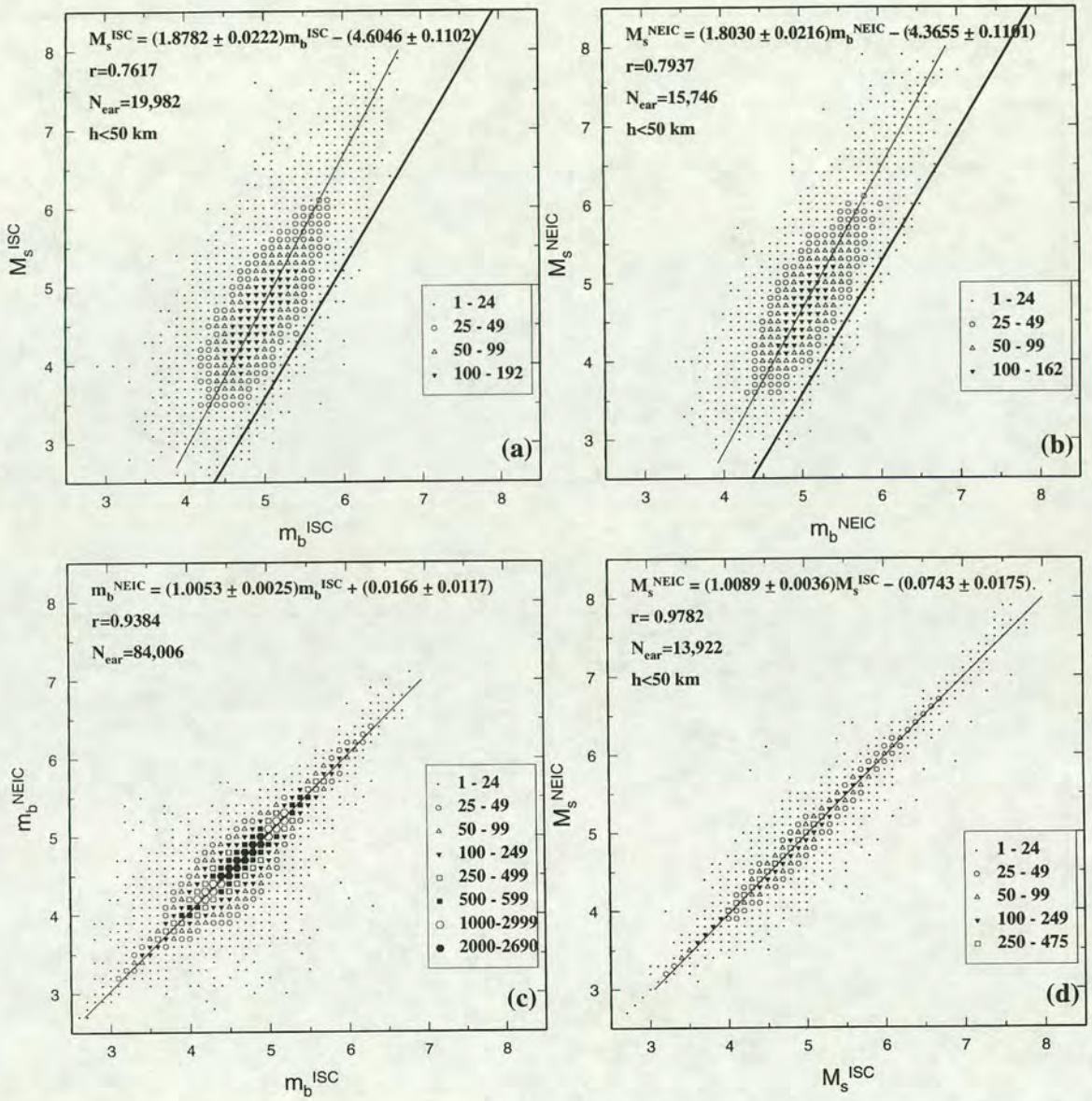

Figure 1. Relation between body-wave magnitude and surface-wave magnitude for earthquakes reported by ISC and NEIC from 1978 to 1993. (a) and (b) show surface-wave magnitude against body-wave magnitude. In (c), m_b^{ISC} versus m_b^{NEIC} and in (d), M_s^{ISC} versus M_s^{NEIC} is shown. Each plot includes all events for which the relevant two parameters have been reported, and the ISC is the ''prime'' location. In each case the regression line is shown by a thin solid line. r = correlation coefficient; N_{ear} = number of earthquakes; h = depth. Symbols indicate the number of data points as shown. In (a) and (b), the thick solid line shows the equation of $m_b = 0.595\ M_s + 2.872$ (Nowroozi, 1986), which is used as a discrimination line for earthquakes and underground nuclear explosions.

M_s:m_b relationship varies between different nuclear test sites. Although they found no such variation for earthquakes in the same regions, many workers have confirmed the geographical variation of M_s:m_b.

Examination from the viewpoint of the discrimination of earthquakes and explosions in the ISC and NEIC Catalogues shows that, respectively, about 0.2% and 0.84% of reported earthquakes used in Figures 1a and 1b are located to the right of the discrimination line formulated by Nowroozi (1986):

$$m_b = 0.595M_s + 2.872. \qquad (10)$$

This line is marked in Figures 1a and 1b.

Figure 2a shows all the earthquakes that plot as explosions using ISC magnitudes. Because we are not comparing

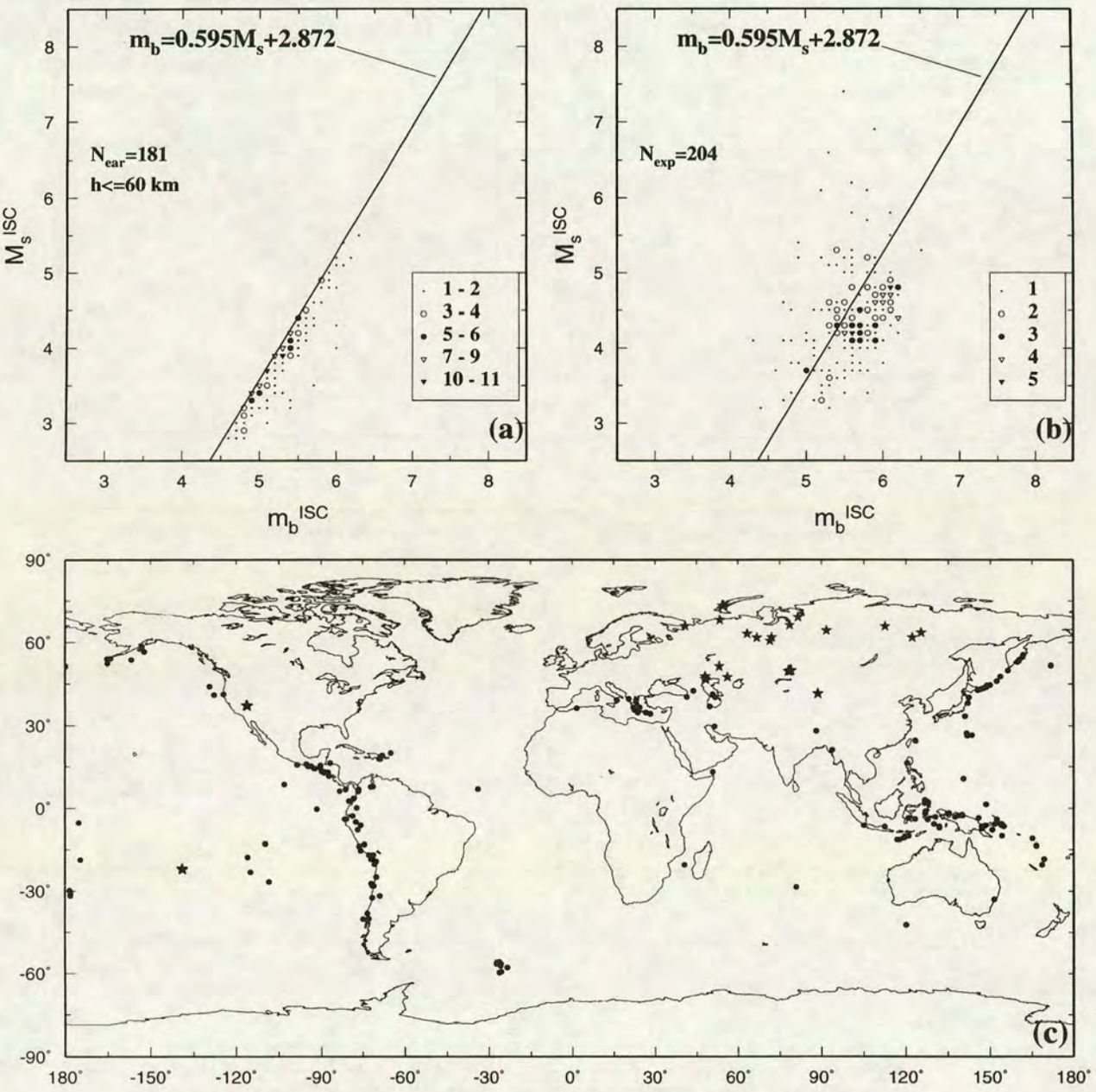

Figure 2. (a) Distribution of those events reported by the ISC as earthquakes that lie to the right of the discrimination line of Nowroozi (1986) in Figure 1a (including only earthquakes with a reported depth $h \leqq 60$ km); (b) Distribution all of events reported as underground nuclear explosions in the ISC Catalogue for which M_s is available; and (c) location of these earthquakes and explosions. In (a) and (b), symbols indicate the number of data points as shown; in (c), circles and asterisks denote the events in (a) and (b), respectively.

with NEIC data in this figure, we have included all earthquakes with a computed depth $h \leqq 60$ km. There are 181 earthquakes (0.82%) in Figure 2a out of a total of 22,080 ISC determinations with $h \leqq 60$ km. The worldwide distribution of these ''anomalous'' earthquakes is shown in Figure 2c; most are located in subduction zones. Figure 2b shows all events identified as nuclear explosions in the ISC Catalogue. For United States of America explosions, the ''prime'' determination is not that of the ISC, but these events have been included in the figure.

The question arises whether the absence of a depth correction in M_s is a major factor in these anomalous earthquake M_s:m_b ratios; this cannot be the case for the explosions because their depths are all close to zero. Because Figure 2a includes earthquakes with an ISC computed depth of $\leqq$60 km, the true depth of some of these events will be >60 km.

This implies failure to apply a depth correction to M_s for earthquakes with depths as great as (say) 80 km in some cases. Regression of M_s against depth for the anomalous earthquakes (without attention to errors in either parameter) gives a line of negative slope corresponding to an average M_s that is 0.2 units lower at $h = 60$ km than at zero depth. We expect the calculated M_s to be lower toward greater depth in the absence of a depth correction, but this result is only significant under the assumption that the true magnitude distribution is constant over this depth range. A histogram of these earthquakes against computed depth shows a steady increase in number with depth, whereas a histogram of all earthquakes for which M_s^{ISC} is available differ in that the number decreases for depths greater than 40 km. This shows that there are more anomalous earthquakes for depths at which the correction would be larger. We conclude that the absence of a depth correction is a contributory factor in these earthquakes, but the main factor appears to be nonsystematic.

The application of a depth correction to a given M_s value would always make events more earthquakelike, because observed surface-wave amplitude always decreases with true focal depth. However, as already pointed out, this would not assist discrimination by M_s:m_b; this must be achieved without a depth correction, because assignment of a nonzero depth itself implies prior identification of the source as an earthquake. Because explosions have a lower M_s:m_b ratio than earthquakes, the average distance of M_s observations will tend to be smaller for an explosion than for an earthquake with the same m_b. It follows that an inappropriate distance correction applied to surface-wave amplitudes will itself create bias in M_s:m_b ratios.

Kaverina *et al.* (1996) showed that the global distribution of "creepex" (difference between M_s and the orthogonal regression of M_s on m_b) has an evident pattern of dominance of negative values in subduction zones and positive ones in mid-ocean ridges. The name "creepex" was coined by combining two words: creep and explosion, which indicate the closeness of a seismic event by its spectral content either to ultra-low-frequency creep events or to high-frequency explosive ones (Kaverina *et al.,* 1996). A further clue to the problem of M_s:m_b using ISC data is given by Figure 2b, which shows all events reported as explosions by the ISC (and as such have a zero depth constraint).

Empirical Distance-Correction Function

To investigate the effect of distance on M_s determination, we determined station magnitudes (M_s^{STA}) from ISC Bulletin data using the Prague formula, for earthquakes with a published surface-wave magnitude (M_s^{ISC}) equal to 4, 4.5, 5, 5.5, 6, and 6.5 (M_s^{ISC} is essentially M_s averaged over contributing stations.) There are 851, 1383, 1039, 519, 229, and 82 earthquakes with estimated M_s of 4, 4.5, 5, 5.5, 6, and 6.5, respectively; and 89.5% of the measurements contributing to these data are from the vertical component. The difference ($M_s^{ISC} - M_s^{STA}$) is shown for these data in Figure 3. We do not attempt to reduce bias either by excluding poorly recorded earthquakes or by further limiting the distance range, because we wish to illuminate, rather than obscure, any factors that contribute to M_s values.

The differences in magnitude value established for

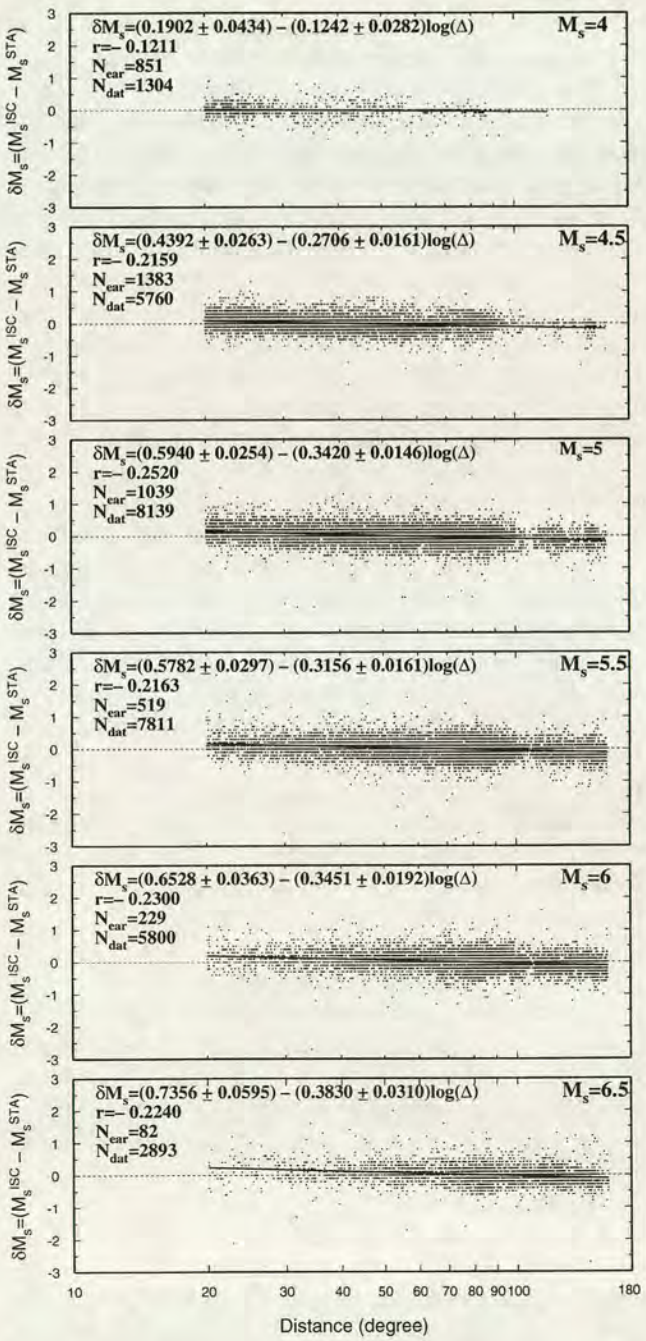

Figure 3. Deviation of individual station magnitudes from average magnitude, against distance for earthquakes with M_s^{ISC} equal to 4, 4.5, 5, 5.5, 6, and 6.5, which have been reported by the ISC from 1978 to 1993. N_{ear} = number of earthquakes; r = correlation coefficient; N_{dat} = number of station records.

waves of the same type at different stations are mainly due to different local conditions at the station, path effects, source effects, and instrumentation. In Figure 3, the slope of all regression lines is negative, which means that $M_s^{ISC} - M_s^{STA}$ decreases with increasing distance. In other words, M_s^{STA} for larger distances is overestimated, and for closer distances, is underestimated. Confirming the results of Herak and Herak (1993), this result indicates that M_s values obtained by the Prague formula are significantly distance dependent and that the numerical value of the constant 1.66 in the Prague formula is too large.

The regression lines in Figure 3 also show a systematic increase in negative slope with increasing magnitude. There are several possible reasons for this. First, the change in slope could arise from the different distribution of observations with distance at different magnitudes. If the distance term were correct, then all "ideal" M_s^{STA} values for earthquakes of the same magnitude would lie on a horizontal line, so that their mean (M_s^{ISC}) for any earthquake, and hence all values of $M_s^{ISC} - M_s^{STA}$, would be equal. Any error in the distance term (whether linear or nonlinear in log Δ) would cause M_s^{ISC} to depend on distance distribution, causing a scatter in values of $M_s^{ISC} - M_s^{STA}$. The systematic difference between station distance distributions at each magnitude would then cause a difference in the slope of the regression lines drawn through values of $M_s^{ISC} - M_s^{STA}$ at each magnitude. It follows that when the correct value of the constant in log Δ is applied, any nonlinear effect in log Δ can be revealed, and once an adequate correction is applied, any true dependence of the distance correction on magnitude can be isolated.

Second, M_s^{STA} values close to the maximum detection distance may be biased in favor of sensitive stations ($M_s^{ISC} - M_s^{STA}$ low), while for large earthquakes, the closest observations may be biased in favor of less-sensitive stations because of instrument saturation. These effects would cause similar slope changes as observed in Figure 3. We investigated this by replotting Figure 3, showing mean values of $M_s^{ISC} - M_s^{STA}$ for data binned in equal increments of distance. At each magnitude, we looked for curving downward or upward of those points near to the maximum and minimum of the distance range. There is some evidence of this at the upper distance limit for $M_s = 4$ and $M_s = 4.5$, and possibly at the lower end for $M_s = 6.5$. However, we conclude that the effect is unsufficient to contribute significantly to the changes in slope observed in Figure 3.

Third, it may be that the required distance-correction term is truly magnitude dependent, as a result of the magnitude dependence of source spectrum, the variation of different instrument response with period T, and a failure of the A/T term to compensate fully these effects when determining M_s^{STA}. We cannot distinguish between this and the first possibility until we have determined the optimum value for the log Δ correction.

In all the graphs of Figure 3, it is clear that, due to the P-wave shadow zone, the number of stations reporting to the ISC with epicentral distances between 100° and 120° is less than for other epicentral distances. The histogram of Figure 4 illustrates a limitation implicit in surface-wave observations in the ISC and most other agencies. Although the ISC will accept unassociated surface-wave observations, in practice, a surface wave is usually reported only if a direct P wave has already been identified. When the station is located in the shadow zone, the P-wave information is not usually reported; consequently, neither is the surface wave. (The distribution of body-wave observations is also shown in Fig. 4.) It follows that the form of the frequency–distance relation for single-station surface waves used in M_s determination is dominated by the structure of the body-wave amplitude–distance curve. The core shadow zone, PKP amplitude peak, and other features of the curve are closely reproduced, and this modulates the true surface-wave amplitude–distance effect, which tilts the distribution down toward increasing distance. A large proportion of data are located between $\Delta = 70°$ and 90°. This observed concentration is mainly due to the larger number of stations per unit distance at epicentral distances close to 90°, and to some extent on the nonrandom pattern of source–station distances over the Earth.

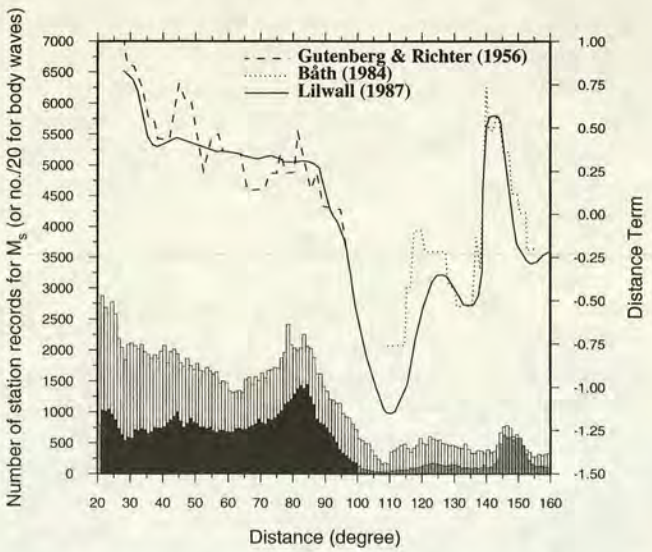

Figure 4. White histogram shows epicentral-distance distribution of 166,733 station records used in M_s^{ISC} determination for 22,080 earthquakes with ISC depth $\leqq$ 60 km, between 1978 and 1993 (left scale). This is overlain by a histogram showing the epicentral-distance distribution of reported short-period P-wave amplitudes during the same period. This is shown in black for the range $21° \leqq \Delta \leqq 100°$ that is used for m_b determination (1,268,101 station records for 110,300 earthquakes) and for other distances in gray (216,632 station records for 43,777 earthquakes). For this histogram, multiply the left scale by 20. The white and black histograms both exclude records outside the period limitation for the respective magnitude determination. Smoothed and unsmoothed published body-wave amplitude–distance curves are shown for comparison (right scale).

To re-examine the calibration function $B(\Delta)$, we used the method of Herak and Herak (1993), but for the whole ISC Catalogue data and using different conditions. In this study, we determined the parameters (α,β) of the regression line of station magnitude versus epicentral distance, for every earthquake with three or more stations in the computation of M_s^{ISC}.

To correct the calibration function $B(\Delta)$, we selected those data in the regression–coefficient range -2.5 to $+3.5$ with a standard error of fitting less than 0.5, and we plotted the difference between individual station magnitude and reference magnitude at $\Delta = 83°$ (M_{83}^j) versus the epicentral distance of the reporting station in Figure 5. As Figures 4 and 5 show, data are concentrated around $\Delta = 83°$, so the reference magnitude is defined as

$$M_{83}^j = \alpha^j + \beta^j \log(83°) \qquad (11)$$

for the jth earthquake ($j = 1 \ldots 9966$). The difference between individual station magnitude and relevant computed M_{83}^j is given by

$$\delta M_i(\Delta) = M_i^j(\Delta) - M_{83}^j, \qquad (12)$$

where i is the ith reported M_s for the jth earthquake ($j = 1 \ldots 9966$, $i = 1 \ldots N_j$). The results show that from 10,894 regression coefficients (β^j), only 2728 are negative, so that 75% of the data have a positive value. As Herak and Herak have pointed out, this indicates that M_s^{Prague} values are significantly distance dependent; consequently, the mean magnitude obtained by averaging all reported magnitude values is not a representative estimate of the earthquake's strength.

Equation (12) is plotted against epicentral distance for all data in Figure 5. The regression line is

$$\delta M_s = (0.5051 \pm 0.0037) \log \Delta - (0.9689 \pm 0.0066), \qquad (13)$$

so the modified Prague formula M_s^e (empirically corrected) becomes

$$M_s^e = \log(A/T)_{\max} + 1.555 \log \Delta + 4.269. \qquad (14)$$

Regression of mean observations binned in intervals of Δ had no significant effect on these regression parameters.

For $\Delta = 83°$, the Prague formula M_s (equation 2) and our M_s^e (equation 14) are equivalent, but for $\Delta = 20°$, equation (2) underestimates M_s by 0.31, whereas for $\Delta = 160°$, M_s is overestimated by 0.14 magnitude units. This result is not surprising; similar results have already been obtained by other workers such as von Seggern (1977), Thomas *et al.*, (1978), and Herak and Herak (1993). This study, which uses a much larger number of ISC data (from 1978 to 1993 over the full range of M_s^{ISC}), further emphasises the need to revise the Prague formula, which most agencies, including the ISC and NEIC, use to determine surface-wave magnitude. The value of the constant in equation (14) is dependent solely upon the choice of reference magnitude (or other condition imposed in the comparison of magnitude scales). It is now clear from Figure 5, as well as from theory, that the correction is not linear in log Δ.

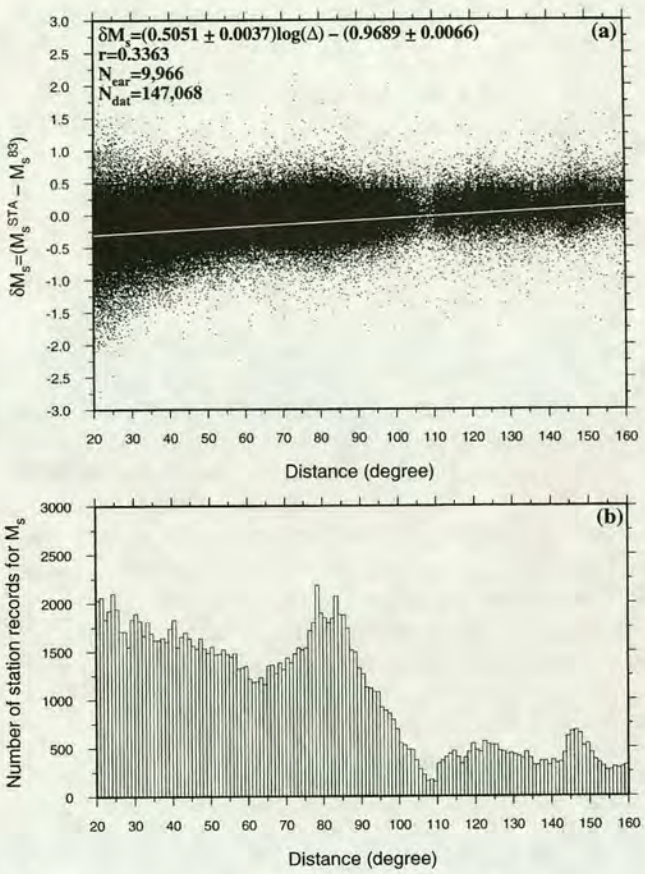

Figure 5. (a) Distribution of the differences between individual station magnitude and reference magnitude M_s^{83} against epicentral distance for 9966 earthquakes. The plot includes those earthquakes for which at least three observations have been used, and for which the regression line of station magnitudes against distance have a slope of between -2.5 and $+3.5$ and a standard error of less than 0.5. r = correlation coefficient; N_{ear} = number of earthquakes; N_{dat} = number of station records. The regression line (shown in white) is for δM_s against log Δ, although the graph is plotted linearly against Δ for clarity. (b) Histogram of distances of the constituent observations.

Empirical Distance Correction Function with Theoretical Constraints

In order to devise a magnitude M_s^t that incorporates theoretically predicted constraints in the distance-dependence terms in equation (5), we correct each A/T observation according to

$$(A/T)_{\text{corrected}} = (A/T)_{\text{observed}}(K\Delta^{-\alpha}\sin^{-\frac{1}{2}}\Delta e^{-k\Delta})^{-1}, \quad (15)$$

where α is either ½ (non-Airy-phase measurement) or ⅓ (Airy-phase measurement) and K and k are constants to be determined. The M_s^t definition becomes

$$M_s^t = \log(A/T) - \log K + \alpha\log\Delta + \frac{1}{2}\log(\sin\Delta) + k(\log_{10}e)\Delta. \quad (16)$$

Because the constant of proportionality in the log Δ term is not a free parameter, we still have only two constants to determine, as for previous formulas.

In order to estimate K and k, we choose the total distance-correction term for an individual observation as the difference between M_s^{ISC} for the corresponding earthquake and $\log(A/T)_{\text{station}}$ for the individual observation. We first use M_s^{ISC} because this is our best available estimate of M_s on the Prague scale. We set this distance correction to be the sum of the correction terms in equation (16), and rearranging, we obtain

$$M_s^{\text{ISC}} - \log(A/T)_{\text{station}} - \alpha\log\Delta - \frac{1}{2}\log(\sin\Delta) = k(\log_{10}e)\Delta - \log K. \quad (17)$$

This should correspond to a straight line of slope $k(\log_{10} e)$ and intercept $\log K$ if the left-hand side is plotted against Δ, and deviations from this straight line will represent additional effects not accounted for theoretically.

This procedure must be applied iteratively, replacing M_s^{ISC} by the average of the M_s^t values for each earthquake, $\overline{M_s^t}$, using equation (16) with K and k as determined. After three iterations, no further reduction was seen in the mean deviation of data from the regression line. The iteration procedure was repeated using $\overline{M_s^e}$ values for each earthquake as the initial values, computed using our equation (14). In this case, no iteration was required to reach minimum deviation. Figures 6a and 6b show this relationship for all station data (152,539 records from 10,894 earthquakes) with α = ⅓ and ½, respectively. The regression lines are shown in white, and the regression parameters are also shown. We see that there is an excellent linear trend over all distances. The fit is equally good in Figures 6a and 6b, so it appears that we cannot resolve from the observed data whether Airy-phase or non-Airy-phase measurements predominate. A similar conclusion was drawn by Douglas *et al.* (1981). Okal (1989) suggested that the assumption of Airy-phase observations made by some authors is probably invalid at periods close to 20 sec. In reality, the mixture of continental, oceanic, and mixed paths in global station magnitudes makes it difficult to make any prediction as to which, if either, type of observation will predominate over the period range of interest. However, our choice of α affects the value of k that is obtained, so the uncertainty in k must be increased to encompass values obtained with ⅓ ≦ α ≦ ½.

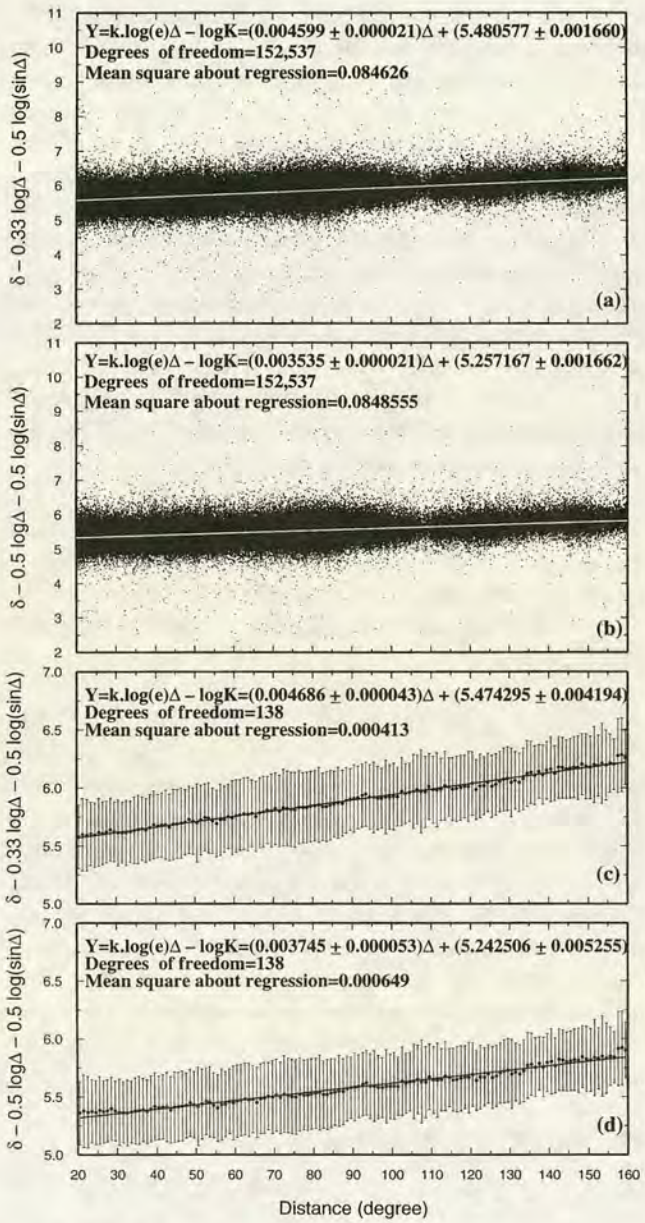

Figure 6. (a) The distance correction with the theoretically predicted parts removed assuming Airy-phase dispersion, plotted against epicentral distance. (b) as for (a) but assuming non-Airy-phase dispersion. (c) and (d), as for (a) and (b), respectively, but showing amplitude averaged in 1-deg bins with standard deviation. On all four graphs, $\delta = M_s^{\text{ISC}} - \log(A/T)_{\text{station}}$.

To examine the detail of the observed fit to the relationship represented in equation (17), we show in Figures 6c and 6d the mean of data in Figures 6a and 6b, respectively, binned for each 1° increment in Δ. Although the deviations are small compared with the standard error of each point, it is clear that adjacent values are not independent, so

that there are some details in the deviation that are systematic with distance. There is also a suggestion of an upward deviation for $\Delta < 30°$ in Figure 6d, which represents the only noticeable difference between Figures 6c and 6d. This suggests that at these close distances, Airy-phase measurements predominate (giving a straight line in Fig. 6c). We therefore chose $\alpha = \frac{1}{3}$, implying the overall predominance of observations close to an Airy phase. The random scatter in Figure 6a about the regression line is greater than ± 0.3 magnitude units. The absence of a depth correction should not directly affect the scatter in Figure 6 since these are differences between event-average and station measurements.

The value of K in equation (17) determines only the relationship between this and other scales, and it may be chosen to maximize consistency with them. The most compelling condition to impose would be equality at $\Delta = 20°$, to maintain consistency with M_L as originally intended by Gutenberg. However, this is unhelpful in practice because it would result in large corrections to the established scale over a large range of distances beyond 20° and, hence, a large correction to most existing magnitude determinations. An alternative condition is to leave the constant as it is; this corresponds to an agreement with the Prague formula at close to $\Delta = 83°$. Although this value was originally chosen because it represents the distance with greatest data density, a more appropriate condition for scale comparison is to set the constant so that the sum-squares correction needed to all ISC event magnitudes so far determined is minimized, i.e., we set K to $K - \delta$, where δ is chosen to minimize $\Sigma[M_s^{\mathrm{ISC}} - (\overline{M_s^t} + \delta)]^2$, where the sum is over all earthquakes. We find $\delta = 0.111$, so that the initial K value of 5.481 becomes $K = 5.370$. We then obtain the relation

$$M_s^t = \log(A/T)_{\max} + \frac{1}{3}\log(\Delta) + \frac{1}{2}\log(\sin\Delta) + 0.0046\Delta + 5.370. \quad (18)$$

According to the regression coefficient, i.e., $k \log_{10} e$ (see Fig. 6a), k is equal to 0.01050 ± 0.00005 deg^{-1}, and assuming 20-sec surface waves with group velocity of $U = 3.6$ km/sec, the globally averaged apparent Q^{-1} becomes 0.00218 ± 0.00001. Since we are unclear whether Airy-phase or non-Airy-phase measurements predominate (and, in general, we may expect a mixture), our best estimate and true error of Q^{-1} must include the uncertainty introduced by changing α from $\frac{1}{3}$ to $\frac{1}{2}$. We then obtain $Q^{-1} = 0.00192 \pm 0.00026$ ($Q \approx 500$), which is slightly higher than $Q = 405$ (with 95% confidence limits of 700 and 285) found by Marshall and Carpenter (1966) for the Northern Hemisphere. Von Seggern (1977) and Herak and Herak (1993) obtained somewhat higher values of $Q = 605 \pm 20$ and $Q = 704$, respectively, assuming $U = 3.5$ km/sec for 20-sec Rayleigh waves. The value of $Q = 297$ used by Okal (1989) is much lower because it was calculated assuming the Prague constant 1.66.

Comparison of Formulas

In Figures 7a and 7b, the distance calibration $B(\Delta)$ of different empirical formulas for determining M_s at 20-sec period are compared, and in Figure 7c, we show the differences between the distance corrections of our formulas and that of Prague. The differences in the slope of the calibration functions of Gutenberg, Prague, Herak and Herak, and our

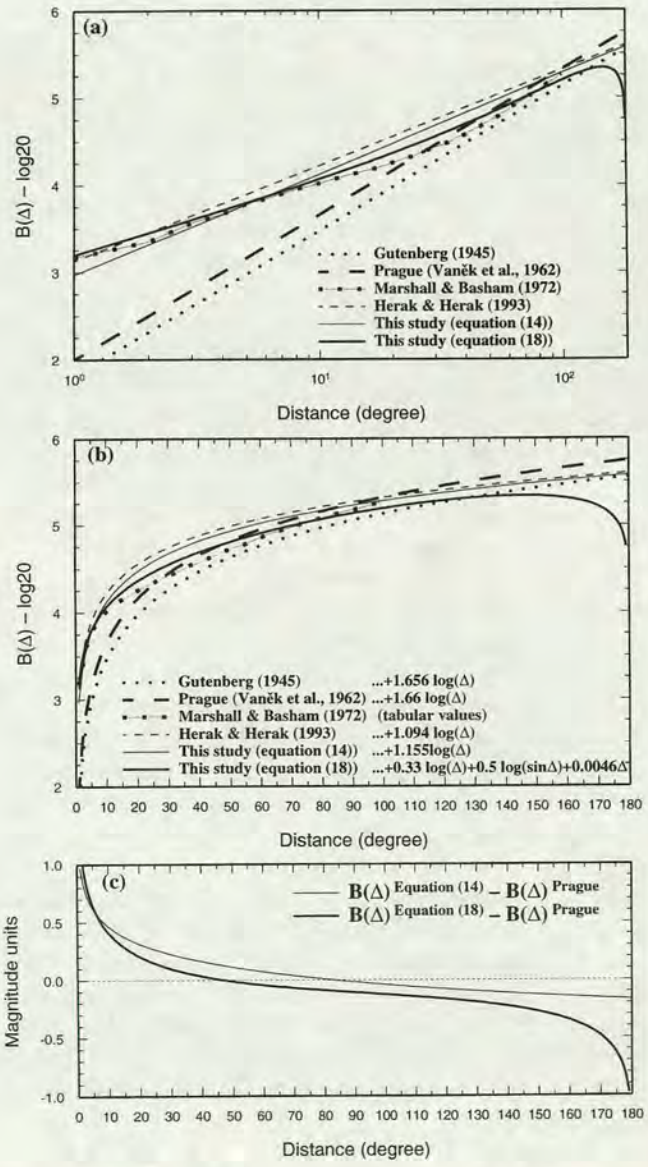

Figure 7. Distance-calibration functions $B(\Delta)$ for the determination of surface-wave magnitude using observations of 20-sec period for calibration functions of the following: Gutenberg without station correction, Prague, Marshall and Basham without path correction, Herak and Herak, our equation (14) (M_s^e), and our equation (18) (M_s^t). (a) On a log scale. (b) The same distance-calibration functions on a linear scale for more clarity. (c) Residual of our distance corrections for M_s^e and M_s^t compared with that of M_s^{Prague}.

M_s^e must be due to differences in the type of data used. For example, Gutenberg (1945) and Vaněk *et al.* (1962) used measurements made from horizontal components, whereas Herak and Herak (1993) used measurements of the vertical component. Here we use both types of measurement, of which only a small fraction of data (11.8% and 10.8% for the first and second formulas, respectively) were measured on horizontal components. Horizontal-component data may be either Love- or Rayleigh-wave amplitudes or a mixture of both. The specific quality factor for Love waves is less than for Rayleigh waves. So if most of the data are Love-wave amplitudes, a steeper slope is expected for the calibration function. Most importantly, we have used a distribution of data used by the ISC in its own magnitude determinations.

Comment is required on the vertical position of each curve in Figures 7a and 7b, which is governed solely by the constant term in the respective formula. We have pointed out that this depends only on the condition used to establish a comparison between the scales. The Prague formula is related to the Gutenberg formula by putting $T = 20$ sec, then using a different constant. The Marshall and Basham formula has the form 1.66 log Δ + constant for $\Delta > 40°$ and is approximately 0.8 log Δ + constant for $\Delta < 25°$. The Herak and Herak formula is set equal to the Prague formula at $\Delta = 100°$ by definition. Our first formula (M_s^e, equation 14) is equivalent to the Prague formula at $\Delta = 83°$ because of our different choice reference magnitude. Our second formula (M_s^t, equation 18) has been chosen to require minimum least-squares change in existing ISC magnitudes as explained in the previous section. (From Fig. 7, it is seen to equal M_s^{Prague} at $\Delta \approx 50°$ and to equal $M_s^{\text{Gutenberg}}$ at $\Delta \approx 130°$.)

To examine the accuracy of our formulas and other empirical formulas for the determination of M_s, 166,733 individual surface-wave magnitudes of 22,080 earthquakes recorded by 343 seismic stations were calculated. The deviation of individual station magnitudes from the average magnitude of the relevant earthquake computed using the same formula averaged in 1-deg-wide bins in distance, is shown in Figure 8. As observed in Figures 8c, 8d, and 8e, values of M_s determined by the Herak and Herak formula and our formulas are almost independent of distance within the range $20° \leqq \Delta \leqq 145°$. Our second formula (Fig. 8e) is independent of distance at least throughout the range $20° \leqq \Delta \leqq 160°$; this indicates an absence of distance bias when this formula is used.

By comparison with Figure 2a, the application of our M_s^t formula (equation 18) results in 149 earthquakes plotting in the explosion region, compared with 181 for the ISC Catalogue. For the explosion population, 63 explosions plot in the earthquake region, compared with 68 in Figure 2b. Because of our method of determining K, we expect the discrimination line of Nowroozi (1986) to behave similarly. We conclude that M_s^t:m_b may provide a small improvement in earthquake/explosion discrimination compared with M_s^{ISC}:m_b.

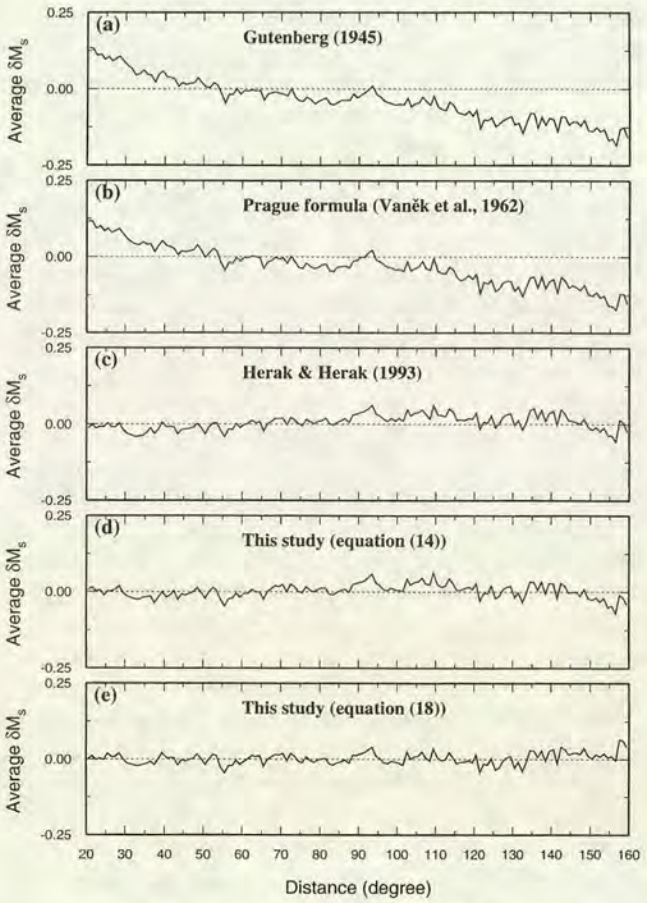

Figure 8. Observations of average magnitude residual for all earthquakes, binned at 1-deg distance intervals with individual magnitude calculated using (a) Gutenberg formula, (b) Prague formula, (c) Herak and Herak formula, (d) this study according to equation (14), and (e) this study according to equation (18). In all five cases, 166,733 station records were used from 22,080 earthquakes between 1978 and 1993. In all cases, the standard error of each point is approximately 0.25.

Relation between Seismic Moment M_0 and Magnitudes M_s^{Prague} and M_s^t

Ekström and Dziewonski (1988) studied bias in M_s by comparison with seismic moment M_0 and showed evidence of systematic deviations in M_s dependent upon tectonic setting. They concluded that M_s tends to overestimate the strength of most continental earthquakes and to underestimate it for those along mid-ocean ridges. They also concluded that estimates of seismic versus aseismic strain release may suffer because seismic moments determined from magnitudes can be wrong by as much as a factor of 4.

We now compare the relationship between seismic moment M_0 and two M_s scales, M_s^{Prague} and M_s^t (equation 18), using M_0 values obtained from the Harvard Centroid Moment Tensor (CMT) Catalogue that is available for a subset of earthquakes having body-wave magnitude of about 5 and

greater from 1977. In the CMT Catalogue, the prime location information is that of the NEIC PDE (*Preliminary Determination of Epicenters*), or in 23.5% of cases from its monthly listing. Where NEIC determinations are included in the ISC Catalogue, they are always from the monthly listing. We matched earthquakes by comparing the NEIC location in the ISC Catalogue to the CMT Catalogue, and imposing an origin time difference of $\leqq \pm 5$ sec and a latitude/longitude difference of $\leqq \pm 0.2°$. We matched 6553 earthquakes with a computed ISC depth $h \leqq 60$ km in this way, for the time period 1978 to 1993. This is of course a small number compared with the 22,080 we have used in previous sections.

To consider the difference in scatter of M_s about given values of M_0 when applying the Prague formula and our M_s^t, we plot in Figure 9 (a) mean $\overline{M_s^{\text{Prague}}}$ and (b) mean $\overline{M_s^t}$, against log M_0 binned in increments of 0.1 for these 6553 earthquakes from the CMT Catalogue. To show the range of M_0 values contributing to a given M_s value, Figures 9c and 9d present surface-wave magnitude binned against log M_0 using the same two M_s formulas, respectively. Here $\overline{M_s^{\text{Prague}}}$ and $\overline{M_s^t}$ are the magnitudes obtained for each earthquake to two decimal places using the contributing station amplitude and period values taken from ISC Bulletin data. Values of log M_0 are derived from M_0 values in the CMT Catalogue and are also expressed to two decimal places. ($\overline{M_s^{\text{Prague}}}$ differs from $\overline{M_s^{\text{ISC}}}$ only in some minor details of computation.)

Factors contributing to the relationship between M_s^{Prague} and M_0 observed in Figure 9a have been discussed by Hanks and Kanamori (1979) and by Ekström and Dziewonski (1988), whose analytical relationships are included as dashed and solid lines in Figure 9. Here we focus on the differences between the relationship observed using M_s^{Prague} and our M_s^t.

First, the differences between Figures 9c and 9d at the largest M_s values are not significant, as they result from small differences between M_s values for a small number of very large earthquakes. Second, from Figures 9a and 9b, M_s values are generally lower in 9b than 9a. This is because the figure includes only the larger earthquakes in the ISC Catalogue, whereas we have normalized our M_s^t scale to minimize differences over whole ISC dataset. Third, in 9b, the slope does not tend to 1.0 toward smaller magnitudes. Fourth, it is clear that the *b*-value obtained using the Prague formula on a large dataset will be different when we use instead our M_s^t (equation 18). Finally, there is significantly less scatter in log M_0 for a given M_s when M_s^t is used. This can be seen from Figures 9a′ to 9d′, which show differences between successive values in the histograms of 9a to 9d, respectively. This is particularly noticeable in the magnitude range 4.3 to 6.3 (compare Figs. 9c′ and 9d′).

Remaining Sources of Scatter and Bias in M_s

We now consider the scatter remaining in M_s^t values. We first reconsider the question posed by Figure 3, in which the distance dependence changed with magnitude. All the graphs in Figure 3 have been recomputed using our equation (18), so that the ordinate becomes $\overline{M_s^t} - M_s^t$. In all cases, the gradient of the regression line was $\leqq \pm 0.03$, with no systematic difference. We therefore conclude that there is no significant magnitude dependence in the distance-correction term of equation (18) over the whole distance range $20° \leqq \Delta \leqq 160°$.

Second, we re-examine the possible systematic effect arising from the absence of a depth correction to M_s. Romanelli and Panza (1995) conclude that this effect is significant. One way to examine it is to use CMT depth as a reference. Strictly, this approach is flawed in that centroid depth and depth of nucleation (deduced from travel-time data) are not coincident especially for large earthquakes. However, this difference will be insignificant compared with depth error for earthquakes below $M_s \approx 6.0$, because CMT depth is resolved to no better than 10 km, and the minimum error in ISC depth is similar. When the data in Figures 9c and 9d are plotted as separate curves for earthquakes with CMT depth in 20-km ranges, we see no significant difference between the curves for $0 \leqq h \leqq 20$ km and $20 < h \leqq 40$ km, but the curve for $40 < h \leqq 60$ km shows a systematic lower value of average M_s corresponding to 0.1 ± 0.05 magnitude units, throughout the magnitude range $4.7 \leqq M_s \leqq 6.3$. Above and below this range, the scatter increases, and any effect is obscured.

Third, the Prague formula has no station correction. Station correction may be influenced by seismograph type as well as local geological conditions. Historically, there has been a tendency for specific instrument types to be concentrated in specific regions—e.g., in the former Soviet Union; these regional differences are disappearing with the new generation of digital broadband instrumentation and the tendency toward more global mixing of seismograph types. It is therefore important to consider the extent to which regional differences in station magnitude residuals may be the result of regional clustering of common instrumentation.

From 1978 to 1993, the ISC has determined M_s for 22,080 earthquakes with $h \leqq 60$ km, using measurements from 343 seismic stations. There are 10,894 earthquakes for which three or more observations have been used in the calculation of M_s^{ISC}. For all 343 stations, the value of $\overline{M_s} - M_s^{\text{STA}}$ averaged over all earthquakes was computed using the Prague formula (M_s^{Prague}) and equation (18) (M_s^t). Values for those 231 seismic stations that have contributed M_s observations for more than 25 earthquakes are listed in Table 1. The absolute values of the average deviation for most (84%) of the stations is less than 0.2 magnitude units, but at some stations, this value is very high (see Table 1). Station BRS with the largest negative average ($\overline{\delta M_s}$) has been measured on vertical-component amplitudes, and for all its 52 readings, δM_s is negative. For station ALM where measurements have all been made on horizontal components, the reverse is true.

In Figure 10, the distribution of the deviation obtained

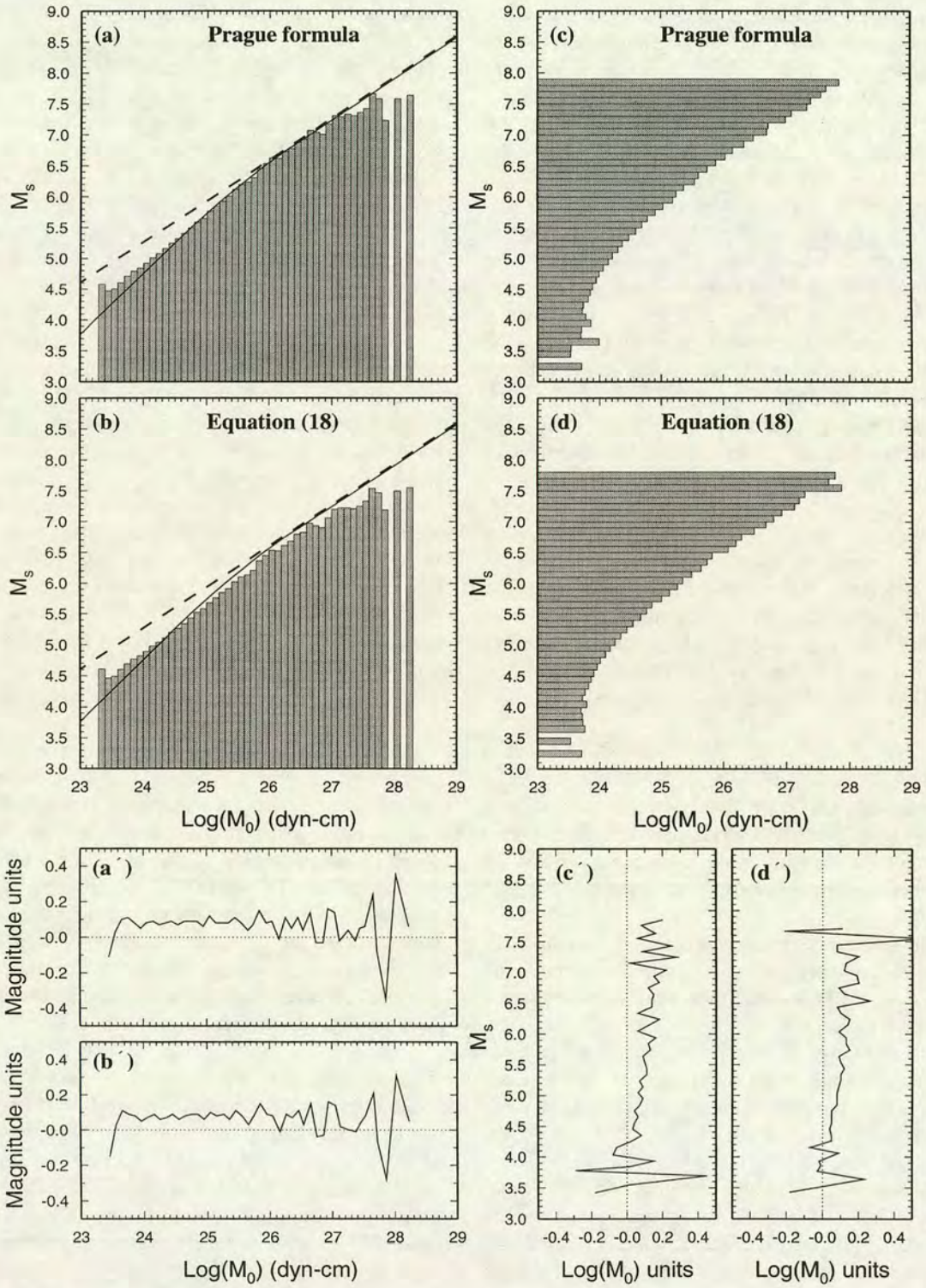

Figure 9. (a) Distribution of $\overline{M_s^{\text{Prague}}}$ averaged in 0.1-unit-wide ranges of log M_0 for 6553 earthquakes in the CMT Catalogue used in this study. (b) Shows the same using our $\overline{M_s'}$ (equation 18). (c) and (d) Distribution of log M_0 for the same data, averaged in 0.1-unit-wide ranges of (c) $\overline{M_s^{\text{Prague}}}$ and (d) our $\overline{M_s'}$. In (a) and (b), the dashed line shows the relationship obtained by Hanks and Kanamori (1979) under the assumption that the relationship is linear, and the solid line shows the analytical relationship developed by Ekström and Dziewonski (1988). (a′)–(d′) Difference between successive values in the histograms of (a)–(d), respectively.

Table 1

Mean Deviation $\overline{\delta M_s}$ of All Values of $\delta M_s = \overline{M_s} - M_s^{STA}$ for 231 Seismic Stations that ISC Has Used Measurements from for More Than 25 Earthquakes from 1978 to 1993

1*	2†	3‡	4§	1	2	3	4	1	2	3	4
AAA	−0.05 ± 0.20	−0.06 ± 0.20	42	HAU	0.11 ± 0.27	0.16 ± 0.26	1276	PPT	0.18 ± 0.56	0.08 ± 0.53	164
AAS	−0.20 ± 0.31	−0.26 ± 0.30	87	HFS	0.03 ± 0.31	0.07 ± 0.31	2677	PRA	−0.11 ± 0.26	−0.06 ± 0.23	750
ADK	0.12 ± 0.31	0.07 ± 0.27	49	HHC	−0.03 ± 0.20	−0.07 ± 0.20	2378	PRE	−0.11 ± 0.31	−0.07 ± 0.33	120
AKU	−0.05 ± 0.25	−0.05 ± 0.23	160	HLW	0.23 ± 0.42	0.22 ± 0.40	65	PRU	−0.11 ± 0.23	−0.06 ± 0.21	3684
ALM	1.10 ± 0.41	1.10 ± 0.42	35	HOF	−0.13 ± 0.23	−0.11 ± 0.21	229	PRZ	−0.17 ± 0.25	−0.20 ± 0.25	211
ALQ	0.01 ± 0.28	0.04 ± 0.28	3510	HON	0.17 ± 0.32	0.15 ± 0.30	893	PUL	−0.06 ± 0.26	−0.04 ± 0.25	536
ANMO	0.01 ± 0.31	0.03 ± 0.28	174	HRV	0.00 ± 0.25	0.04 ± 0.24	618	PYA	−0.11 ± 0.25	−0.08 ± 0.22	284
ANN	0.10 ± 0.21	0.12 ± 0.19	139	ILT	0.10 ± 0.33	0.08 ± 0.30	541	QIZ	0.09 ± 0.21	0.01 ± 0.21	583
ANR	−0.11 ± 0.27	−0.11 ± 0.25	378	IRK	0.05 ± 0.25	0.01 ± 0.25	1112	QZH	0.18 ± 0.21	0.10 ± 0.21	735
ANTO	0.18 ± 0.46	0.21 ± 0.47	35	ISA	0.01 ± 0.23	0.03 ± 0.23	448	RAC	−0.12 ± 0.28	−0.08 ± 0.28	213
APA	−0.13 ± 0.24	−0.11 ± 0.25	300	JCT	−0.04 ± 0.27	−0.02 ± 0.25	1219	RIV	0.38 ± 0.45	0.21 ± 0.47	95
APP	0.01 ± 0.30	0.07 ± 0.30	47	JFWS	−0.02 ± 0.23	0.00 ± 0.22	151	RJF	0.08 ± 0.30	0.14 ± 0.29	1100
ARC	0.10 ± 0.29	0.07 ± 0.29	46	KAT	−0.12 ± 0.34	−0.09 ± 0.32	242	RSCP	0.01 ± 0.36	0.01 ± 0.33	168
ARU	−0.12 ± 0.25	−0.10 ± 0.24	1082	KBS	−0.28 ± 0.84	−0.31 ± 0.81	58	RSNT	0.07 ± 0.24	0.05 ± 0.24	71
ASH	−0.15 ± 0.28	−0.15 ± 0.27	149	KEV	−0.07 ± 0.27	−0.06 ± 0.27	795	RSNY	0.04 ± 0.28	0.06 ± 0.28	908
ASPA	0.08 ± 0.35	0.00 ± 0.39	1672	KHC	−0.03 ± 0.27	0.02 ± 0.24	2335	RSON	0.03 ± 0.34	0.05 ± 0.33	369
BAK	−0.35 ± 0.38	−0.36 ± 0.36	103	KHE	−0.11 ± 0.29	−0.09 ± 0.28	432	RSSD	0.10 ± 0.31	0.12 ± 0.30	645
BCAO	0.10 ± 0.33	0.18 ± 0.31	76	KHO	0.05 ± 0.27	0.05 ± 0.26	54	SAM	−0.05 ± 0.27	−0.04 ± 0.26	259
BER	0.01 ± 0.71	0.02 ± 0.71	73	KIS	−0.10 ± 0.31	−0.05 ± 0.28	464	SAO	0.00 ± 0.27	0.00 ± 0.27	233
BINY	−0.07 ± 0.22	−0.01 ± 0.20	88	KIV	0.08 ± 0.27	0.14 ± 0.26	216	SBA	0.10 ± 0.26	0.04 ± 0.24	44
BJI	0.10 ± 0.23	0.07 ± 0.22	3402	KJF	−0.19 ± 0.22	−0.18 ± 0.22	867	SCO	−0.26 ± 0.41	−0.25 ± 0.39	46
BKR	−0.12 ± 0.31	−0.10 ± 0.30	42	KMI	−0.01 ± 0.25	−0.04 ± 0.24	1727	SDN	−0.01 ± 0.43	−0.02 ± 0.40	362
BKS	0.02 ± 0.33	−0.01 ± 0.33	1431	KOD	0.06 ± 0.22	0.00 ± 0.22	34	SEM	−0.08 ± 0.21	−0.08 ± 0.20	37
BLA	0.03 ± 0.29	−0.02 ± 0.28	211	KON	−0.24 ± 0.58	−0.26 ± 0.57	31	SEY	0.05 ± 0.31	0.00 ±0.26	199
BNS	−0.23 ± 0.29	−0.20 ± 0.27	360	KRA	−0.18 ± 0.26	−0.15 ± 0.24	2385	SHE	−0.05 ± 0.32	−0.04 ± 0.31	148
BOCO	0.17 ± 0.26	0.22 ± 0.25	40	KRV	0.14 ± 0.30	0.13 ± 0.29	82	SIM	0.03 ± 0.29	0.06 ± 0.27	355
BRG	−0.11 ± 0.22	−0.06 ± 0.21	1146	KSH	−0.26 ± 0.26	−0.25 ± 0.25	924	SIT	0.04 ± 0.35	0.03 ± 0.33	642
BRK	0.00 ± 0.31	−0.03 ± 0.30	151	KTG	−0.13 ± 0.26	−0.11 ± 0.27	77	SJG	0.06 ± 0.29	0.06 ± 0.27	433
BRS	−0.73 ± 0.29	−0.84 ± 0.33	52	KUL	−0.19 ± 0.26	−0.19 ± 0.27	49	SKO	−0.11 ± 0.38	−0.06 ± 0.37	1264
BRVK	0.00 ± 0.23	0.03 ± 0.22	72	KUR	0.10 ± 0.32	0.03 ± 0.29	262	SKR	0.18 ± 0.39	0.10 ± 0.37	84
BTO	−0.06 ± 0.21	−0.10 ± 0.21	2270	LBNH	−0.11 ± 0.21	−0.05 ± 0.22	102	SLL	−0.08 ± 0.37	−0.02 ± 0.36	102
BUL	−0.16 ± 0.33	−0.14 ± 0.34	230	LEN	0.21 ± 0.31	0.20 ± 0.29	59	SLM	0.02 ± 0.31	0.05 ± 0.30	367
CAR	0.05 ± 0.38	0.06 ± 0.39	182	LIC	0.11 ± 0.39	0.17 ± 0.38	700	SLR	−0.30 ± 0.36	−0.26 ± 0.35	1072
CBM	−0.05 ± 0.23	0.00 ± 0.21	348	LOR	0.06 ± 0.37	0.12 ± 0.36	1633	SMY	−0.01 ± 0.36	−0.05 ± 0.33	666
CCM	0.23 ± 0.33	0.25 ± 0.32	97	LPA	−0.02 ± 0.27	−0.02 ± 0.27	638	SNG	0.23 ± 0.40	0.10 ± 0.40	47
CD2	0.01 ± 0.21	−0.02 ± 0.21	1512	LPB	−0.10 ± 0.27	−0.07 ± 0.29	1647	SNY	0.02 ± 0.20	−0.02 ± 0.19	1792
CEH	0.08 ± 0.25	0.11 ± 0.24	565	LRG	0.05 ± 0.30	0.11 ± 0.29	491	SOC	−0.01 ± 0.30	0.01 ± 0.28	313
CHG	0.26 ± 0.38	0.22 ± 0.36	65	LSA	0.05 ± 0.30	0.01 ± 0.29	422	SPA	−0.03 ± 0.36	−0.05 ± 0.35	1757
CHTO	0.46 ± 0.49	0.45 ± 0.45	104	LSCT	−0.14 ± 0.21	−0.07 ± 0.22	86	SPC	−0.30 ± 0.39	−0.29 ± 0.38	122
CIT	−0.04 ± 0.27	−0.13 ± 0.28	126	LTX	0.05 ± 0.51	0.07 ± 0.50	193	SRO	−0.14 ± 0.31	−0.12 ± 0.30	563
CLL	−0.02 ± 0.22	0.02 ± 0.20	926	LVV	−0.20 ± 0.31	−0.16 ± 0.29	306	SSE	0.12 ± 0.26	0.07 ± 0.25	3226
CMB	0.04 ± 0.25	0.05 ± 0.25	425	LZH	−0.02 ± 0.24	−0.04 ± 0.24	3873	SSPA	0.21 ± 0.48	0.25 ± 0.47	35
CN2	0.01 ± 0.23	−0.01 ± 0.22	2292	MAK	−0.04 ± 0.32	−0.04 ± 0.30	248	STAN	0.10 ± 0.25	0.05 ± 0.25	34
COL	0.00 ± 0.29	−0.02 ± 0.27	668	MAT	0.22 ± 0.27	0.17 ± 0.25	2741	STU	0.04 ± 0.24	0.06 ± 0.22	269
COP	−0.06 ± 0.27	−0.03 ± 0.26	776	MAW	−0.08 ± 0.33	−0.10 ± 0.35	263	SUR	−0.32 ± 0.32	−0.31 ± 0.31	232
CTA	−0.02 ± 0.37	−0.17 ± 0.37	280	MCWV	−0.10 ± 0.27	−0.07 ± 0.24	333	SVE	−0.10 ± 0.29	−0.08 ± 0.29	974
CTAO	0.15 ± 0.43	0.07 ± 0.44	26	MDJ	0.01 ± 0.23	−0.03 ± 0.23	1053	TAS	−0.08 ± 0.27	−0.07 ± 0.26	523
DAG	−0.05 ± 0.30	−0.04 ± 0.30	308	MGD	0.17 ± 0.34	0.13 ± 0.29	472	TIA	0.07 ± 0.21	0.02 ± 0.21	1514
DBN	0.09 ± 0.29	0.11 ± 0.28	1133	MHC	0.09 ± 0.44	0.06 ± 0.42	163	TIK	−0.02 ± 0.27	−0.03 ± 0.26	842
DL2	0.16 ± 0.27	0.11 ± 0.26	976	MIAR	0.13 ± 0.25	0.17 ± 0.22	362	TIY	−0.08 ± 0.22	−0.09 ± 0.20	2963
DOU	−0.04 ± 0.22	−0.01 ± 0.21	458	MIN	0.16 ± 0.51	0.13 ± 0.52	40	TLG	0.12 ± 0.31	0.10 ± 0.31	331
DSH	−0.05 ± 0.29	−0.05 ± 0.29	62	MIR	0.04 ± 0.26	0.00 ± 0.28	133	TPNV	−0.18 ± 0.30	−0.18 ± 0.29	191
DUG	0.10 ± 0.23	0.13 ± 0.23	230	MNK	−0.24 ± 0.22	−0.20 ± 0.20	179	TUC	0.06 ± 0.26	0.08 ± 0.26	404
ELT	−0.15 ± 0.31	−0.16 ± 0.31	254	MOS	−0.17 ± 0.28	−0.16 ± 0.26	512	TUL	0.09 ± 0.37	0.11 ± 0.35	2828
ERE	0.11 ± 0.28	0.12 ± 0.28	96	MOX	−0.04 ± 0.24	0.00 ± 0.24	2764	UER	0.02 ± 0.33	−0.03 ± 0.34	72
FLN	0.05 ± 0.28	0.10 ± 0.28	1089	MSO	0.00 ± 0.48	0.00 ± 0.48	119	UKR	0.02 ± 0.20	−0.01 ± 0.18	29
FRU	−0.06 ± 0.24	−0.06 ± 0.23	677	MTA	0.32 ± 0.36	0.35 ± 0.36	140	UPA	0.12 ± 0.32	0.13 ± 0.29	496
FUR	−0.06 ± 0.29	−0.03 ± 0.28	582	MUN	−0.01 ± 0.32	−0.12 ± 0.34	363	UZH	−0.21 ± 0.30	−0.16 ± 0.27	435
FVM	−0.14 ± 0.33	−0.11 ± 0.30	479	NAI	0.23 ± 0.37	0.25 ± 0.37	180	VKA	0.07 ± 0.22	0.10 ± 0.21	713
GAC	−0.15 ± 0.75	−0.16 ± 0.76	27	NDI	0.11 ± 0.33	0.07 ± 0.32	373	VLA	0.37 ± 0.47	0.29 ± 0.46	77

(*continued*)

Table 1—*Continued*

1*	2†	3‡	4§	1	2	3	4	1	2	3	4
GAM	−0.43 ± 0.99	−0.45 ± 1.01	28	NEW	−0.11 ± 0.35	−0.11 ± 0.34	663	WAR	−0.23 ± 0.24	−0.21 ± 0.23	447
GAR	0.06 ± 0.37	0.05 ± 0.36	56	NJ2	0.16 ± 0.25	0.11 ± 0.24	1332	WDC	0.05 ± 0.28	0.07 ± 0.28	402
GDH	−0.04 ± 0.25	−0.03 ± 0.25	269	NNA	0.26 ± 0.42	0.26 ± 0.42	419	WEL	−0.09 ± 0.29	−0.21 ± 0.27	170
GLD	−0.04 ± 0.31	−0.03 ± 0.29	1249	NRI	−0.21 ± 0.31	−0.22 ± 0.29	505	WET	−0.12 ± 0.24	−0.09 ± 0.22	337
GOGA	0.04 ± 0.22	0.08 ± 0.20	81	NRN	−0.29 ± 0.36	−0.31 ± 0.36	36	WHN	0.04 ± 0.22	−0.01 ± 0.22	1554
GOL	0.06 ± 0.28	0.08 ± 0.27	1817	NUR	−0.03 ± 0.27	0.00 ± 0.27	2696	WIN	−0.29 ± 0.34	−0.26 ± 0.34	367
GRA1	−0.09 ± 0.63	−0.08 ± 0.62	26	NVL	−0.06 ± 0.30	−0.06 ± 0.30	360	WMOK	−0.05 ± 0.24	−0.01 ± 0.22	251
GRB1	0.10 ± 0.51	0.14 ± 0.50	70	NVS	−0.14 ± 0.26	−0.16 ± 0.26	357	WMQ	−0.12 ± 0.24	−0.10 ± 0.23	2684
GRF	0.10 ± 0.28	0.15 ± 0.27	3938	NWAO	0.22 ± 0.38	0.17 ± 0.40	629	WOL	−0.10 ± 0.83	−0.05 ± 0.82	81
GRM	0.02 ± 0.40	0.04 ± 0.40	179	OBN	−0.13 ± 0.26	−0.08 ± 0.25	1695	XAN	−0.02 ± 0.23	−0.05 ± 0.22	1358
GRO	−0.28 ± 0.32	−0.26 ± 0.33	306	OJC	−0.12 ± 0.30	−0.07 ± 0.28	105	YAK	0.05 ± 0.26	0.00 ± 0.24	595
GRS	0.16 ± 0.29	0.17 ± 0.28	272	ORV	0.19 ± 0.25	0.19 ± 0.24	53	YBH	0.09 ± 0.21	0.08 ± 0.22	50
GTA	−0.12 ± 0.22	−0.12 ± 0.22	3216	PAS	0.12 ± 0.27	0.10 ± 0.25	300	YSNY	−0.06 ± 0.22	−0.01 ± 0.21	101
GUA	0.32 ± 0.27	0.17 ± 0.28	457	PET	0.19 ± 0.29	0.14 ± 0.25	431	YSS	0.16 ± 0.29	0.12 ± 0.26	721
GUMO	0.48 ± 0.34	0.39 ± 0.34	526	PME	0.07 ± 0.40	0.04 ± 0.38	201	ZAK	−0.04 ± 0.23	−0.08 ± 0.23	1188
GYA	0.02 ± 0.21	−0.02 ± 0.22	1599	PMG	0.02 ± 0.40	−0.08 ± 0.41	127	ZOBO	0.12 ± 0.28	0.20 ± 0.29	1475
GZH	0.09 ± 0.22	0.02 ± 0.23	756	PMR	0.10 ± 0.32	0.10 ± 0.30	1849	ZST	−0.27 ± 0.40	−0.23 ± 0.39	173

*Station code.
†Mean deviation with standard error ($\overline{\delta M_s} \pm \sigma_{\text{mean}}$) according to the Prague formula.
‡Mean deviation with standard error ($\overline{\delta M_s} \pm \sigma_{\text{mean}}$) according to equation (18).
§Number of readings.

using the Prague formula for these stations has been plotted on a world map. Stations located in southern Africa, the eastern part of Europe, and in the former Soviet Union have negative deviations. This means that the sizes of events have been overestimated relative to other seismic stations, and for some other stations, the reverse is true. Therefore, corrections are essential to improve the measure of earthquake size obtained from M_s. This is not unexpected, and station magnitude residuals have long been used as an indicator of regional seismic attenuation. However, we would like to differentiate between true near-station effects caused by subsurface conditions, and any purely instrumental effect that may result from biases due to the prevalence of different recording instruments in different regions of the world. Unfortunately, comprehensive information on the type of instrument used is not easily available for most stations. From future studies using exclusively digital data transformed to a common instrument response, it will be possible to isolate any contribution of instrumentation, from which we will be able to decide whether an investigation into this aspect of previous data would be worthwhile.

Fourth, the Prague formula has no path correction, although the substantial effect on M_s^{STA} of surface-wave propagation path has long been well known. From our equation (18), it follows that the appropriate way to introduce a path correction into our M_s' scale would be to determine a path-specific value of K, since this constant reflects both the average anelastic attenuation along the path and the average velocity structure. This implies that the path correction would be linear in distance Δ.

Fifth, we know that azimuthal variation in surface-wave radiation pattern must contribute significantly to scatter in M_s^{STA}. It has long been recognized that station M_s determinations must not require prior focal mechanism determination and that source radiation effects are expected to remain as a contributory factor in M_s scatter.

Finally, there is a scatter implicit in the observatory practice of measuring surface-wave amplitude. Figure 11 shows the distribution of amplitude and period values among observations. Similar to the data of Douglas *et al.* (1981), we see a predominance of "round number" values in A and T for the ISC data, which is evident from the peaks at multiples of 0.1 μm and 2 sec in amplitude and period, respectively, in Figure 11a. This is made clear in the magnified section of 11a, shown in 11b. It is known that the most important source of this type of effect is associated with recording system. In particular, many WWSSN stations recorded at 0.5 mm/sec, while many observers read times to the nearest millimeter. This measurement practice results in various preferred $\log(A/T)$ values. The effect of this on larger-magnitude values is insignificant, but the effect becomes progressively larger toward smaller magnitudes. For example, it seems the precision of most amplitude measurements is ± 0.05 μm. For a measured value of 0.1 μm ($M_s \approx 4$), this implies an error of ± 0.18 magnitude units, whereas at 0.01 μm ($M_s \approx 3$), this gives an error of ± 0.8 magnitude units.

Conclusions

A global comparison of magnitude determinations by the ISC and NEIC shows some small differences, but there are no systematic differences between reported magnitudes of ISC and NEIC. A least-squares fit of 19,982 M_s and m_b values reported by the ISC for the period 1978 to 1993 gives

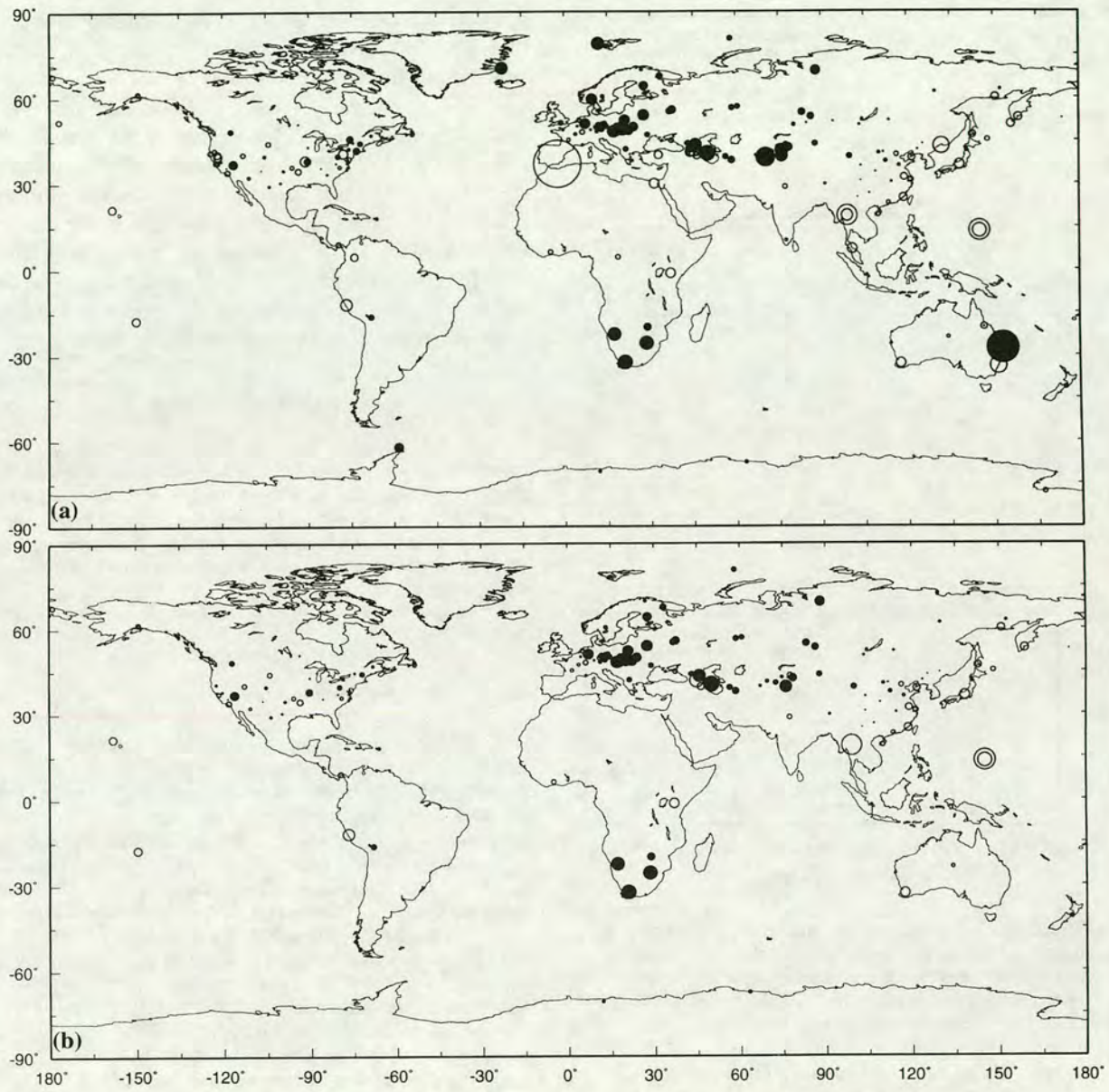

Figure 10. Global maps showing the average value of $\overline{M_s} - M_s^{STA}$ for all earthquakes recorded at individual stations. (a) Includes those stations that have contributed more than 25 earthquakes. (b) Stations that have contributed more than 100 earthquakes. Filled circles show positive deviations ($\overline{M_s} > M_s^{STA}$), and open circles show negative deviations. The size of each circle is proportional to the absolute value of the mean deviation; the largest symbol corresponds to a deviation of 1.12 magnitude units.

$$M_s^{ISC} = (1.8782 \pm 0.0222)m_b^{ISC} - (4.6046 \pm 0.1102),$$

and the relation of M_s and m_b values of 15,746 earthquakes reported by the NEIC in that period is

$$M_s^{NEIC} = (1.8030 \pm 0.0216)m_b^{NEIC} - (4.3655 \pm 0.1101).$$

The number of reported surface-wave amplitude observations at distances corresponding to the *P*-wave shadow zone ($100° \leqq 120°$) is less, because most seismic stations measure surface waves after recognizing the first-arrival *P* wave. Indeed, the frequency–distance relation for surface-wave amplitude measurements is dominated by the body wave amplitude–distance curve. It follows that many potentially useful observations of surface-wave amplitude are missing from the datasets.

In an investigation of the distance calibration function, we conclude that in the Herak and Herak formula and our

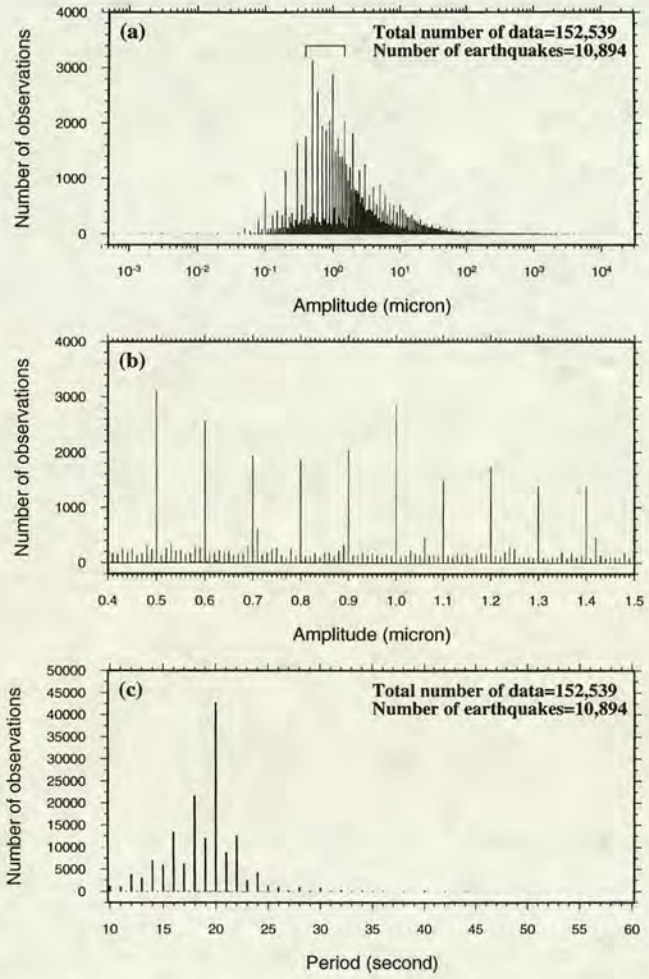

Figure 11. Histograms of measured amplitude and period of surface waves for all observations of earthquakes for which three or more reported observations have been used in the calculation of M_s^{ISC}: (a) for amplitude (in microns) on logarithmic scale, (b) for a small part of the amplitude range identified in Figure 11a plotted on a linear scale for more clarity, and (c) for period in seconds.

M_s^e and M_s^t formulas, the residuals of individual station magnitudes from the mean magnitudes are less than for other formulas. Our M_s^e (equation 14) was obtained using the whole ISC data from 1978 to 1993 and over the whole range of M_s. By deriving a formula containing theoretical distance-dependence terms, we have provided a means (M_s^t, equation 18) to reduce systematic errors in the distance correction over the full range of distances. There is some evidence that Airy-phase, rather than non-Airy-phase, distance dependence dominates measurements for $\Delta < 35°$.

Deviations in M_s determinations made using our M_s^t formula isolate those remaining sources of scatter that are unexplained. It appears that the absence of a depth correction and of station and path corrections all contribute to this remaining scatter but that there is no discernible magnitude dependence remaining in our M_s^t distance correction. It is possible that regional variations in instrumentation are distorting the perceived regional differences in M_s station residuals, but further investigation of this must await more seismic moment data from the global digital networks. We have shown that there is less scatter in the relationship between our M_s^t and CMT M_0 than when M_s^{Prague} is used.

The kind of study reported here is important in the removal of bias in M_s. It is also important in the correct application of the M_s:m_b discriminant, and in confirming the need to modify the formula for M_s calculation. In particular, we have shown the importance of applying a suitable distance-correction term that is theoretically valid.

Acknowledgments

We thank Professor A. Douglas and Drs. D. Bowers and D. McCormack for their valuable comments. We also thank associate editor Dr. Lind Gee, reviewer Dr. Göran Ekström, and one anonymous reviewer, for suggesting improvements to the original manuscript. One of us (M.R.) was supported by a scholarship from the Ministry of Culture and Higher Education of Iran. The figures were prepared using Generic Mapping Tools (Wessel and Smith, 1995).

References

Aki, K. (1967). Scaling law of seismic spectrum, *J. Geophys. Res.* **72,** 1217–1231.

Båth, M. (1981). Earthquake magnitude—recent research and current trends, *Earthquake Sci. Rev.* **17,** 315–398.

Båth, M. (1984). Earthquake magnitude based on *PKP* and *SKP* waves, *Boll. Geofis. Teor. Appl.* **26,** 93–108.

Douglas, A., J. B. Young, and P. D. Marshall (1981). Some analyses of *P*- and Rayleigh-wave amplitudes observed at North America stations, *Geophys. J. R. Astr. Soc.*, **67,** 305–324.

Ekström, G. and A. M. Dziewonski (1988). Evidence of bias in estimations of earthquake size, *Nature* **332,** 319–323.

Evernden, J. F. (1971). Variation of Rayleigh-wave amplitude with distance, *Bull. Seism. Soc. Am.* **61,** 231–240.

Ewing, W. M., W. S. Jardetzky, and F. Press (1957). *Elastic Waves in Layered Media,* McGraw-Hill, New York.

Gutenberg, B. (1945). Amplitudes of surface waves and magnitudes of shallow earthquakes, *Bull. Seism. Soc. Am.* **35,** 3–12.

Gutenberg, B. and C. F. Richter (1956). Magnitude and energy of earthquakes, *Ann. Geofisica.* **9,** 1–15.

Hanks, T. C. and H. Kanamori (1979). A moment magnitude scale, *J. Geophys. Res.* **84,** 2348–2350.

Herak, M. and D. Herak (1993). Distance dependence of M_s and calibrating function for 20 second Rayleigh waves, *Bull. Seism. Soc. Am.* **83,** 1881–1892.

Kanamori, H. (1978). Quantification of earthquakes, *Nature* **271,** 411–414.

Kaverina, A. N., A. V. Lander, and A. G. Prozorov (1996). Global creepex distribution and relation to earthquake-source geometry and tectonic origin, *Geophys. J. Int.* **125,** 125–265.

Lilwall, R. C. (1987). Station threshold bias in short-period amplitude distance and station terms used to compute body-wave magnitude m_b, *Geophys. J. R. Astr. Soc.* **91,** 1127–1133.

Marshall, P. D. and P. W. Basham (1972). Distribution between earthquakes and underground explosions employing an improved M_s scale, *Geophys. J. R. Astr. Soc.* **28,** 431–458.

Marshall, P. D. and E. W. Carpenter (1966). Estimates of Q for surface Rayleigh waves, *Geophys. J. R. Astr. Soc.* **10,** 549–550.

Nowroozi, A. A. (1986). On the linear relation between m_b and M_s for discrimination between explosions and earthquakes, *Geophys. J. R. Astr. Soc.* **86,** 687–699.

Nuttli, O. W. (1973). Seismic wave attenuation and magnitude relations of eastern North America, *J. Geophys. Res.* **78,** 876–885.

Okal, E. A. (1989). A theoretical discussion of time domain magnitude: the Prague formula for M_s and the mantle magnitude M_m, *J. Geophys. Res.* **94,** 4194–4204.

Panza, G. F., S. J. Duda, L. Cernobori, and M. Herak (1989). Gutenberg's surface-wave magnitude calibrating function: theoretical basis from synthetic seismograms, *Tectonophysics* **166,** 35–43.

Prozorov, A. and J. A. Hudson (1974). A study of the magnitude difference $M_s - m_b$ for earthquakes, *Geophys. J. R. Astr. Soc.* **39,** 551–564.

Richter, C. (1935). An instrumental earthquake magnitude scale, *Bull. Seism. Soc. Am.* **25,** 1–32.

Romanelli, F. and G. F. Panza (1995). Effect of source depth correction on the estimation of earthquake size, *Geophys. Res. Lett.* **22,** 1017–1019.

Scheidegger, A. E. (1985). Recent research on the physical aspects of earthquakes, *Earth. Sci. Rev.* **22,** 173–229.

Thomas, J. H., P. D. Marshall, and A. Douglas (1978). Rayleigh-wave amplitudes from earthquakes in the range 0–150°, *Geophys. J. R. Astr. Soc.* **53,** 191–200.

Vaněk, J., A. Zatopek, V. Karnik, N. V. Kondorskaya, Y. V. Riznichenko, E. F. Savarensky, S. L. Solov'ev, and N. V. Shebalin (1962). Standardization of magnitude scales, *Bull. Acad. Sci. USSR, Geophys. Ser.*, no. 2, 108–111 (English Translation).

von Seggern, D. H. (1970). Surface-wave amplitude versus distance relation in the western United States, SDL Report No. 249, Teledyne Geotech, Alexandria, Virginia.

von Seggern, D. H. (1977). Amplitude-distance relation for 20 second Rayleigh waves, *Bull. Seism. Soc. Am.* **67,** 405–411.

Wessel, P. and W. H. F. Smith (1995). New version of the Generic Mapping Tools released, *EOS* **76,** 329.

Department of Geology and Geophysics
University of Edinburgh
Grant Institute
West Mains Road
Edinburgh EH9 3JW, United Kingdom

Manuscript received 18 February 1997.

Relation between seismic moment M_0 and surface wave magnitude M_s

by Mehdi Rezapour and Robert G. Pearce

Abstract

The relation between M_s and $\log M_0$ is examined using Harvard CMT M_0, with both M_s^{Prague} and the improved surface wave magnitude scale M_s^t of Rezapour and Pearce (1998) applied to ISC data. Although M_s^t shows less scatter than M_s^{Prague}, neither dataset supports a slope of M_s against $\log M_0$ which tends to 1.0 towards smaller magnitudes or $\frac{2}{3}$ at larger magnitudes. Instead, a good linear fit of slope 0.76 using M_s^t is found throughout the fitted range of M_0 (2.0×10^{24} to 1.26×10^{27} dyne-cm), and this linearity extends down to $M_0 = 2.5 \times 10^{23}$ dyne-cm. This suggests that previous proposals that M_s data support a theoretical slope of 1.0 and $\frac{2}{3}$ in the low and high ranges of magnitude respectively, which may be expected from established relationships, is not justified.

1 Introduction

The objective of this article is to reassess the empirical relationship between surface-wave magnitude M_s and seismic moment M_0. This study was prompted by the introduction of a surface wave magnitude scale with improved distance correction (M_s^t) by Rezapour and Pearce (1998). Magnitude, especially M_s, as a measure of earthquake strength, forms the basic dataset of much research in seismology. However, nowadays seismologists consider the seismic moment as a more reliable measure of earthquake size. Seismic moment is in theory a direct measure of earthquake size, whereas all magnitude scales are empirical and unrelated to source physics. M_s is available for most significant earthquakes in the twentieth century and some historical earthquakes, but routine estimates of M_0 by the Harvard group as Centroid Moment Tensor (CMT) solutions are available since about 1977 for earthquakes having body-wave magnitude m_b of about 5 and greater. Therefore development of a reliable relationship between magnitude and seismic moment is of fundamental importance for integrating historical data into earthquake catalogues e.g., for seismic hazard analysis.

Most global agencies such as the International Seismological Centre (ISC) and the National Earthquake Information Center (NEIC) routinely determine M_s using an empirical formula, the so-called "Prague formula", given by

$$M_s^{Prague} = \log(\frac{A}{T})_{max} + 1.66 \log \Delta + 3.3, \tag{1}$$

where A is the vertical or resultant horizontal amplitude in microns, T is the period in seconds, and Δ is the epicentral distance in degrees (Vaněk *et al.*, 1962).

Rezapour and Pearce (1998) considered the theoretically-known contribution of dispersion and geometrical spreading, and introduced a modified M_s formula given by

$$M_s^t = \log(A/T)_{max} + \frac{1}{3}\log(\Delta) + \frac{1}{2}\log(\sin\Delta) + 0.0046\Delta + 5.370. \tag{2}$$

They concluded that the M_s^t formula gives reduced bias for M_s in comparison with the Prague formula, and that there is less scatter in $\log M_0$ for a given M_s when M_s^t is used. Ekström and Dziewonski (1988), here referred to as ED88, presented evidence of systematic deviation in M_s dependent upon tectonic setting; they also fitted an analytical relationship to the M_s versus $\log M_0$ dataset.

In the CMT Catalogue the prime location information is that of the NEIC PDE (Preliminary Determination of Epicenters) or from its Monthly Listing. Where NEIC determinations are included in the ISC Catalogue, they are always from the Monthly Listing. Here the NEIC epicentral location and origin time (in the ISC Bulletin) were compared with those in the CMT Catalogue. Those epicentral estimates whose positions are the same within 0.2 degree in both latitude and longitude and whose times of origin are the same within 5 seconds are assumed to be the same earthquake. 6,533 earthquakes with available M_s and M_0 were matched in this way, for the time period 1978 to 1993.

In this paper the relationship between seismic moment M_0 and two M_s scales, M_s^{Prague} (ISC) and M_s^t, are compared using M_0 values obtained from the CMT Catalogue for the above dataset and the conclusions of ED88 are reexamined.

2 Analysis

Most earlier studies have assumed a linear relation between surface-wave magnitude and the log of seismic moment. Under the hypothesis of constant stress drop, theoretical models predict that $\log M_0$ and M_s are indeed related linearly:

$$\log M_0 = A + BM_s. \tag{3}$$

The slope (B) commonly found in the literature (e.g., Kanamori and Anderson, 1975; Purcaru and Berckhemer, 1978; Hanks and Kanamori, 1979; Caputo and Console, 1980; Hyndman and Weichert, 1983; Dziewonski and Woodhouse (1983)) is around 1.5. However, the data and the range of magnitudes used by different authors were slightly different. Moreover, this slope has often been obtained using M_L rather than M_s (e.g., Aki, 1969; Thatcher and Hanks, 1973). An attempt at a relation between magnitude and seismic moment (Kanamori, 1977; Hanks and Kanamori, 1979) resulted in the "moment magnitude" scale, M_w:

$$M_w = \frac{2}{3}\log M_0 - 10.7, \tag{4}$$

where M_0 is seismic moment in dyne-cm. According to the Kanamori and Anderson (1975) model (constant stress drop), if the correlation coefficient in equation (3) is large, then the dataset contains events with almost constant stress drop, and in the case of low correlation the reverse is true.

Because a theoretical slope of 1.0 is only predicted from instantaneous moment release at a point, a different slope is to be expected for real data. Moreover, it has been argued (e.g. Aki, 1967; Kanamori and Anderson, 1975) that the slope should decrease towards larger magnitude on account of the decreasing corner frequency, remembering that magnitude estimates are derived at a standard frequency.

ED88 chose to use a two-segment linear model (with a quadratic transition between the segments) to fit the global M_s versus $\log M_0$ data. They attempted a fit of the averaged magnitude data from 2,341 earthquakes, to a hypothesised M_s:$\log M_0$ relation. In their analytical relation between M_s (as the dependent variable) and $\log M_0$ (as the independent

variable) they imposed a slope of unity for small events, and $\frac{2}{3}$ for moderate to large events.

We use the above dataset of 6,553 earthquakes between 1978 and 1993. Magnitudes (M_s^{Prague} and M_s^t) have been recomputed from amplitude and period measurements in the ISC Catalogue to two decimal places, and corresponding M_0 values are taken from the CMT Catalogue. The individual data are plotted in Figures 1a and 1a′ for M_s^{Prague} and M_s^t respectively. The event magnitudes are averaged within each 0.1-wide interval of $\log M_0$ units, and are plotted in Figures 1b, and 1b′.

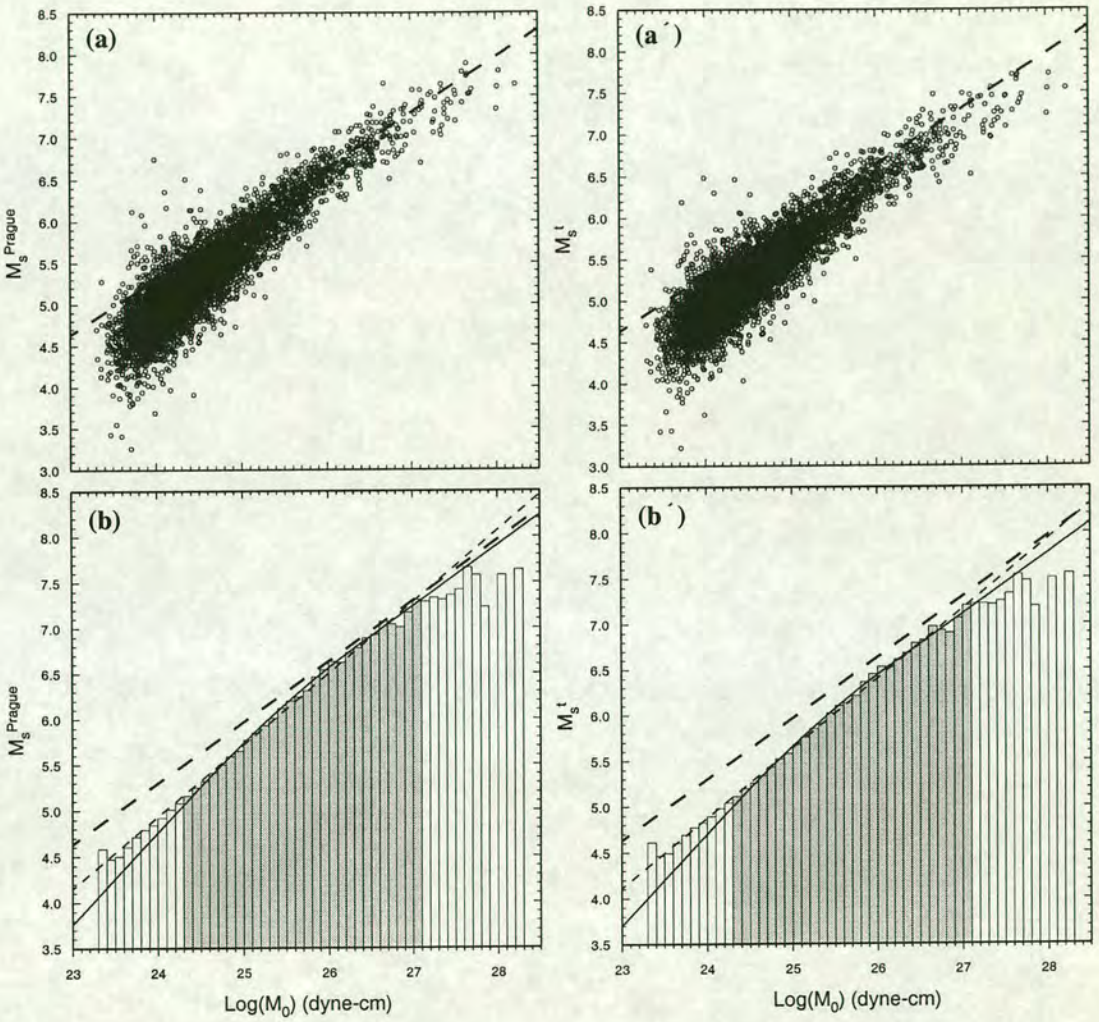

Figure 1: Distribution of M_s values against $\log M_0$ for 6,553 earthquakes. (a) individual data points for M_s^{Prague} values. (b) average M_s^{Prague} values over 0.1-unit-wide intervals of $\log M_0$. (a′) and (b′), are as for (a) and (b) respectively, but for M_s^t values. In (b) and (b′) the solid curves represents the ED88's analytical relation (their equation 2) and our equation (6) respectively, and the thin dashed lines show the linear regression fit to the same data. The relationship of Hanks and Kanamori (1979) (our equation 4) is shown by a thick dashed line in all the graphs. In (b) and (b′) the range of data used in the fits is highlighted in grey.

There are some minor differences between this dataset and that of ED88 resulting from their use of NEIC rather than ISC data. They used M_s^{NEIC} values from events for which both h^{NEIC} and h^{CMT} are less than 50 km, whereas here data from events with $h^{ISC} \leq 60$ km are used. Also, their data window was 1977–1987 whereas here 1978–1993 is used (consistent ISC M_s determination began in 1978). Although we use the same lower

M_0 limit of 2.0×10^{24} dyne-cm for fitting, a more restrictive upper limit of $M_0 = 1.26 \times 10^{27}$ dyne-cm is imposed because saturation and incompleteness in this dataset appear at this lower value.

The analytic relation has three free parameters and is most easily represented using the formulation of ED88 (their equation 1), except that we control the limits of the segments by constants A and B in units of M_0 (rather than $\log M_0$), in order to relate the constants to the graph more easily. We obtain

$$\bar{M}_s = \begin{cases} k - \frac{(\log A + \log B)}{6} + \log M_0 & M_0 < A \\ k - \frac{(\log A + \log B)}{6} + \log M_0 - \frac{(\log M_0 - \log A)^2}{6(\log B - \log A)} & A \leq M_0 \leq B \\ k + \frac{2}{3} \log M_0 & M_0 > B \end{cases} \quad (5)$$

We first attempt to fit an analytical function of the form proposed by ED88 using M_s^t. The results of our analysis are shown in Table 1. Row 1 shows the resulting fit when the Residual Sum Squares Error (RSSE) is minimised in k, A and B using M_s^t and the specified range of M_0. It is seen that A is equal to 2.0×10^{24} dyne-cm, which corresponds to the lower limit of the fitted range. Hence, no segment with a slope of 1.0 remains when the least-squares fit to the function in equation (5) is optimised. The full relation is given by

$$M_s^t = \begin{cases} -19.30 + \log M_0 & M_0 < 2.0 \times 10^{24} \\ -19.30 + \log M_0 + 0.09(\log M_0 - 24.31)^2 & 2.0 \times 10^{24} \leq M_0 \leq 1.45 \times 10^{26} \\ -10.89 + \frac{2}{3} \log M_0 & M_0 > 1.45 \times 10^{26} \end{cases} \quad (6)$$

Table 1: Fitting parameters obtained when applying the analytical relation of equation (5) to the M_s^{Prague} and M_s^t datasets. Details are given in the text.

	M_s formula	Parameters			Residual Sum Squares Error (RSSE)[a]				No. of data points[b]			
		k	A	B	r1	r2	r3	R	n1	n2	n3	N
1	M_s^t	−10.89	2.00×10^{24}	1.45×10^{26}	0.0000	0.0239	0.0275	0.0514	0	18	10	28
2	M_s^{Prague}	−10.78	2.00×10^{24}	2.57×10^{26}	0.0000	0.0158	0.0243	0.0401	0	21	7	28
3	M_s^t	−10.89	2.88×10^{24}	1.29×10^{26}	0.0108	0.0179	0.0275	0.0563	2	16	10	28
4	M_s^{Prague}	−10.78	2.88×10^{24}	2.09×10^{26}	0.0047	0.0134	0.0245	0.0426	2	18	8	28

$M_s = \alpha \log M_0 + \beta$						
	M_s	α	β	RSSE	Correlation coefficient	N
5	M_s^t	0.763518±0.011680	−13.448340±0.300357	0.064944	0.996971	28
6	M_s^{Prague}	0.783727±0.012359	−13.875954±0.317816	0.072714	0.996783	28

[a] r1, r2, and r3, and respectively the Residual Sum Squares Error of the three sections of the relationship in equation (5), and R is that for the total relation.

[b] n1, n2, n3, and N are the number of data points used to compute the four RSSE values respectively.

In view of this result we next reassess the fit to equation (5) using M_s^{Prague} (Row 2 of Table 1). Again we see that no segment of slope 1.0 remains, although the RSSE is smaller than when M_s^t values are used. This fit differs from that of ED88, possibly because ED88 did not determine a formal least-squares fit.

The above results suggest that the observed data for M_s^t and even M_s^{Prague} do not provide evidence of a slope of unity for small events. If a minimum of two points are required to lie along a slope of 1.0 (Rows 3 and 4 of Table 1), then for M_s^{Prague} the values of k, A, and B are then almost equivalent to those given by ED88.

The analytical relation of ED88 (their equation 2) and our fit (our equation (6)) are plotted with solid curves in Figures 1b and 1b′ respectively, and the relationship of Hanks and Kanamori (1979) is shown by a thick dashed line. Dark histogram bars are used to highlight the range of data used to compute the fit. These plots show visually that the evidence in support of the analytical relation proposed by ED88 is even weaker when the improved M_s^t scale is used.

It is important to compare the success of testing different hypotheses. The decreased quality of fit observed in Figure 1b′ is now compared with the quality of fit obtained using a standard linear regression (Rows 5 and 6 of Table 1). A better fit is obtained for M_s^t than for M_s^{Prague} as shown by thin dashed lines in Figures 1b′ and 1b respectively. Moreover, it is apparent from both Figures 1b and 1b′ that the good fit extends to smaller moments which were excluded from the fit because of possible incompleteness of earthquake catalogue, and also because of possible upward bias in M_s values close to the detection threshold. It is apparent that the goodness of fit strongly depends on the upper limit of fitted data, because the progressively smaller number of earthquakes towards higher moment create greater scatter, and because of the onset of magnitude saturation.

ED88's main reason for imposing a lower limit of 2.0×10^{24} dyne-cm when fitting their relation was the well-known upward biasing of M_s values caused by station threshold effects. Of course, this specific source of bias is governed by magnitude rather than moment. Figures 1a and 1a′ show a large scatter in the $\log M_0$:M_s relation for individual events, particularly at smaller magnitude. If data points below, say, $M_s = 4.5$ are affected by station threshold bias, then this would have only a marginal effect on Figures 1b and 1b′, because averaged moments are predominantly occupied by higher magnitude events down to the lower limit of the data. We therefore conclude that this source of bias does not contribute significantly to these histograms. (If it did, the use of maximum-likelihood M_s values (e.g. as used by Stevens and McLaughlin, 1997) could possibly be used to reduce it.)

We conclude that these data are more consistent with a linear fit than with the more complicated analytic relation of equation (5), and that this is so over the wider moment range from 2.5×10^{23} to 1.26×10^{27} dyne-cm. This conclusion implies that $\log M_0$ is proportional to about $1.3M_s$ over this wider magnitude range (or M_s is proportional to $0.76 \log M_0$).

The observed linear relationship suggests that the spectral fall-off above the corner frequency is not influencing M_s measurements at least up to $M_s \lesssim 7.2$. We can only speculate on the origin of the 0.76 gradient. We can be confident that it is not caused by inadequate distance correction since we are using M_s^t (Table 1 Row 5) although the difference between this value and the 0.78 obtained for M_s^{Prague} (Table 1 Row 6) may represent such an effect. One possibility is that the deviation of our gradient from 1.0 represents a dependence of stress drop $\Delta\sigma$ upon M_0. If this were so, a relation $\Delta\sigma \propto {M_0}^{0.14}$ is implied, which corresponds to a reduction in stress drop towards larger earthquakes.

To compare average M_s in different tectonic settings defined as "oceanic ridges and fracture zones", "continental", and "subduction zones" (broadly following ED88), the data were classified using Flinn-Engdahl seismic region number, and M_s values were averaged over 0.1-wide intervals of $\log M_0$. In Figure 2 average M_s versus $\log M_0$ are compared for different tectonic regions. This Figure shows that the continental earthquakes have a larger M_s than corresponding earthquakes along mid-oceanic ridges and subduction zones with the same seismic moment. However, the largest earthquakes occur in subduction zones. For a given M_0 value, mid-oceanic ridge earthquakes have a smaller M_s than earthquakes in other regions. The difference between these regions is not constant and it increases

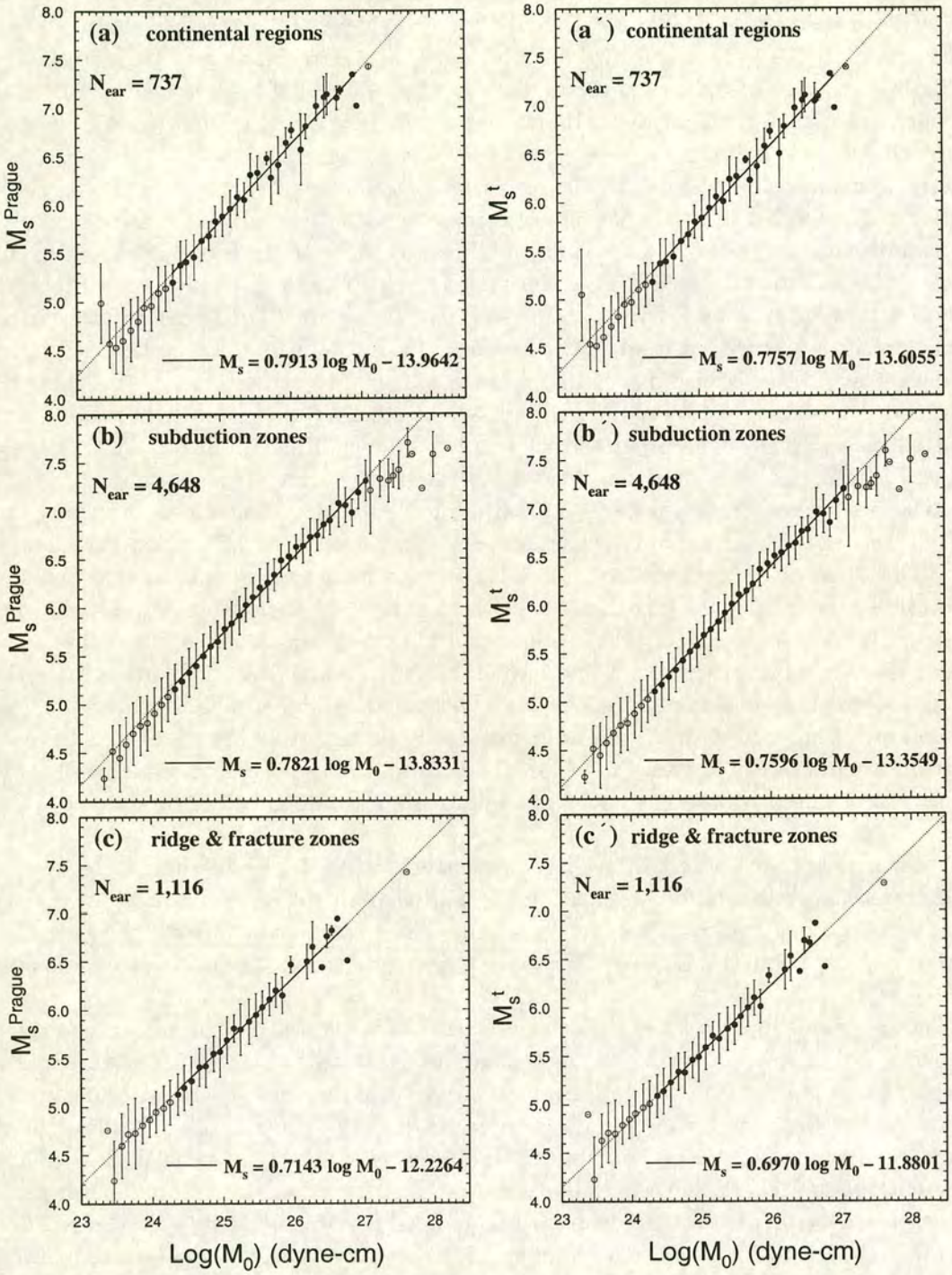

Figure 2: Average M_s over 0.1-wide intervals of $\log M_0$ against $\log M_0$ with standard deviations in different tectonic regions. (a) Continental regions. (b) Subduction zones. (c) Mid-oceanic ridge including fracture zones. (a′)–(c′) are as (a)–(c) but for M_s^t formula. In each case the solid line represents a linear regression line to the data points in the seismic moment range 2.5×10^{23} to 1.26×10^{27} dyne-cm. The data points in this range are shown by filled symbols. N_{ear} shows the number of earthquakes in each region which have been classified using Flinn-Engdahl seismic region number.

with increasing seismic moment. Also, the number of individual data points controls the scatter of averaged data.

Comparison of M_s^t with M_s^{Prague} for different regions in Figure 2 shows that the scatter for M_s^t is less than that for M_s^{Prague}, and that in all regions the standard deviation of data points is less than those for M_s^{Prague}. This confirms conclusions of Rezapour and Pearce (1998).

3 Conclusions

In the relation of M_s with $\log M_0$ the observed data do not provide evidence of a slope of unity towards smaller events when either the M_s^t or M_s^{Prague} scales are used. A simple linear regression gives a slope of 0.76 for M_s^t over a wide range of moments from 2.5×10^{23} to 1.26×10^{27} dyne-cm extending below the range used for fitting. The linear regression is less good for M_s^{Prague}. It is concluded that a linear fit of gradient 0.76 is preferable to the analytical relation of equation (5), making $\log M_0$ proportional to about $1.3M_s$ over this wider moment range. Comparison of M_s^t with M_s^{Prague} for different tectonic settings shows that the scatter for M_s^t is less than that for M_s^{Prague}.

Acknowledgements: We thank Professor A. Douglas, Dr D. Bowers and Dr I. Main for their valuable comments. One of us (M. R.) was supported by a scholarship from the Ministry of Culture and Higher Education of Iran. The Figures were prepared using Generic Mapping Tools (Wessel and Smith, 1995).

References

Aki, K. (1967). Scaling law of seismic spectrum, *J. Geophys. Res.* **72**, 1217–1231.

Aki, K. (1969). Analysis of the seismic coda of local earthquakes as scattered waves, *J. Geophys. Res.* **74**, 615–631.

Caputo, M. and R. Console (1980). Statistical distribution of stress drops and faults of seismic regions, *Tectonophysics* **67**, T13–T20.

Dziewonski, A. M. and J. H. Woodhouse (1983). An experiment in systematic study of global seismicity: Centroid-moment tensor solutions for 201 moderate and large earthquake of 1981, *J. Geophys. Res.*, **88**, 3247–3271.

Ekström, G. and A. M. Dziewonski (1988). Evidence of bias in estimations of earthquake size, *Nature* **332**, 319–323.

Hanks, T. C. and H. Kanamori (1979). A moment magnitude scale, *J. Geophys. Res.* **84**, 2348–2350.

Kanamori, H. (1977). The energy release in great earthquakes, *J. Geophys. Res.* **82**, 2981-2987.

Hyndman R. D. and D. H. Weichert (1983). Seismicity and rates of relative motion on the plate boundaries of Western North America, *Geophys. J. R. astr. Soc.* **72**, 59–82.

Kanamori, H. and D. Anderson (1975). Theoretical basis of some empirical relations in seismology, *Bull. Seism. Soc. Am.* **65**, 1073–1095.

Purcaru, G., and H. Berckhemer (1978). A magnitude scale for very large earthquakes, *Tectonophysics* **49**, 189–198.

Rezapour, M. and R. G. Pearce (1998). Bias in surface wave magnitude M_s due to inadequate distance corrections, *Bull. Seism. Soc. Am.* **88**, 43–61.

Stevens, J. L. and K. L. McLaughlin (1997). Improved methods for regionalized surface wave analysis, Maxwell Technologies Report No. MFD-TR-97-15887 (http://www.maxwell.com/products/geop/1997_AFTAC_Final/index.html)

Thatcher, W. and T. C. Hanks (1973). Source parameters of southern California earthquakes, *J. Geophys. Res.*, **78**, 8547–8576.

Vaněk, J., A. Zatopek, V. Karnik, N. V. Kondorskaya, Y. V. Riznichenko, E. F. Savarensky, S. L. Solov'ev, and N. V. Shebalin (1962). Standardisation of magnitude scales, *Bull. Acad. Sci. USSR, Geophys, Ser. (English Transl.) No.* 2, 108–111.

Wessel, P. and W. H. F. Smith (1995). New version of the Generic Mapping Tools released, *EOS Trans. Amer. Geophys. U.* **76**, 329.

Department of Geology & Geophysics,
University of Edinburgh,
Grant Institute,
West Mains Road,
Edinburgh EH9 3JW
United Kingdom